SANDIA REPORT
SAND2020-2331
Printed February 2020

Sandia National Laboratories

Optimal Distribution System Voltage Regulation using State Estimation and DER Grid-Support Functions

Jay Johnson, Adam Summers, Rachid Darbali-Zamora, Clifford Hansen, Matthew J. Reno, Anya Castillo, Sigifredo Gonzalez, Javier Hernandez-Alvidrez, Nicholas S. Gurule
Sandia National Laboratories

Boqi Xie, Chiyang Zhong, A. P. Meliopoulos
Georgia Institute of Technology

Chad Showalter, Terry Rohrer, Mark Rupnik
Connected Energy

Jithendar Anandan, Nicholas Heine, Miguel E. Hernandez F., Davis Montenegro Martinez, Brian Seal
Electric Power Research Institute

Tom Tansy, Bob Fox, Anil Pochiraju, Suzanne Martinez
SunSpec Alliance

Harmony Smith, Samer Arafa, Justin Woodard
National Grid

Jon Hawkins
Public Service Company of New Mexico

Philip Rothblum, Miles Bintz, Patrick Chapman
SunPower Corporation

Prepared by
Sandia National Laboratories
Albuquerque, New Mexico
87185 and Livermore,
California 94550

Issued by Sandia National Laboratories, operated for the United States Department of Energy by National Technology & Engineering Solutions of Sandia, LLC.

NOTICE: This report was prepared as an account of work sponsored by an agency of the United States Government. Neither the United States Government, nor any agency thereof, nor any of their employees, nor any of their contractors, subcontractors, or their employees, make any warranty, express or implied, or assume any legal liability or responsibility for the accuracy, completeness, or usefulness of any information, apparatus, product, or process disclosed, or represent that its use would not infringe privately owned rights. Reference herein to any specific commercial product, process, or service by trade name, trademark, manufacturer, or otherwise, does not necessarily constitute or imply its endorsement, recommendation, or favoring by the United States Government, any agency thereof, or any of their contractors or subcontractors. The views and opinions expressed herein do not necessarily state or reflect those of the United States Government, any agency thereof, or any of their contractors.

Printed in the United States of America. This report has been reproduced directly from the best available copy.

Available to DOE and DOE contractors from
U.S. Department of Energy
Office of Scientific and Technical Information
P.O. Box 62
Oak Ridge, TN 37831

Telephone: (865) 576-8401
Facsimile: (865) 576-5728
E-Mail: reports@osti.gov
Online ordering: http://www.osti.gov/scitech

Available to the public from
U.S. Department of Commerce
National Technical Information Service
5301 Shawnee Rd
Alexandria, VA 22312

Telephone: (800) 553-6847
Facsimile: (703) 605-6900
E-Mail: orders@ntis.gov
Online order: https://classic.ntis.gov/help/order-methods/

ABSTRACT

Increasing solar energy penetrations may create challenges for distribution system operations because production variability can lead to large voltage deviations or protection system miscoordination. Instituting advanced management systems on distribution systems is one promising method for combating these challenges by intelligently controlling distribution assets to regulate voltage and ensure protection safety margins. While it is generally not the case today, greater deployment of power system sensors and interoperable distributed energy resources (DER)—e.g., photovoltaic (PV) inverters, energy storage systems (ESS), electric vehicles (EVs)—will enable situational awareness, control, and optimization of distribution systems. In this work, a control system was created which measures power system parameters to estimate the status of a feeder, forecasts the distribution state over a short-term horizon, and issues optimal set point commands to distribution-connected equipment to regulate voltage and protect the system. This two-year project integrated multiple research innovations into a management system designed to safely allow PV penetrations of 50% or greater. The integrated software was demonstrated through extensive real-time (RT) and power hardware-in-the-loop studies and a field demonstration on a live power system with a 684 kVA PV system.

ACKNOWLEDGEMENTS

The team would like to thank Trimark Associates for configuring communication and control functionality at the Old Upton Rd PV Site for the field demonstrations. The team would also like to acknowledge the support from Opal-RT to integrate simulated DER devices in the power simulations using Data Bus.

The "Voltage Regulation and Protection Assurance using DER Advanced Grid Functions" project was funded by the Department of Energy (DOE) Energy Efficiency and Renewable Energy (EERE) Solar Energy Technologies Office (SETO) through the Enabling Extreme Real-time Grid Integration of Solar Energy (ENERGISE) funding program.

CONTENTS

LIST OF FIGURES

LIST OF TABLES

This page left blank

ACRONYMS AND DEFINITIONS

Abbreviation	Definition
AC	Alternating Current
AMI	Advanced Metering Infrastructure
API	Application Programming Interface
ARIMA	autoregressive integrated moving average
BPS	Bulk Power System
IEC	International Electrotechnical Commission
IEEE	Institute of Electrical and Electronics Engineers
CPUC	California Public Utilities Commission
DC	Direct Current
DDoS	Distributed Denial of Service
DER	Distributed Energy Resource(s)
DERMS	Distributed Energy Resource Management System
DETL	Distributed Energy Technology Laboratory
DNP	Distribution Network Protocol
DNP3	Distributed Network Protocol
DOE	Department of Energy
DR	Demand Response
EBP	Estimation-Based Protection
EMS	Energy Management System
ENERGISE	Enabling Extreme Real-time Grid Integration of Solar Energy
EPRI	Electric Power Research Institute
EPS	Electric Power System
EERE	Energy Efficiency and Renewable Energy
ESS	Energy Storage System
ESC	Extremum Seeking Control
EV	Electric Vehicle
FDEMS	Facilities DER Energy Management System
FEMS	Facility Energy Management System
FERC	Federal Energy Regulatory Commission
FW	Frequency-Watt
GIS	Geographic Information System
HAN	Home Area Network
HIL	Hardware-in-the-Loop

HMI	Human-Machine Interface
IEC	International Electrotechnical Commission
IEEE	Institute of Electrical and Electronics Engineers
IoT	Internet of Things
IOU	Investor-Owned Utility
IP	Internet Protocol
IT	Information Technology
JSON	JavaScript Object Notation
LAN	Local Area Network
LTC	Load Tap Changer
NG	National Grid
NERC	North American Electric Reliability Corporation
NIST	National Institute of Standards and Technology
OE	Office of Electric Delivery and Energy Reliability
OMS	Outage Management System
OpenDSS	Open Distribution System Simulation
OT	Operational Technology
PCC	Point of Common Coupling
PCS	Power Conditioning System
PDC	Phasor Data Concentrator
PHIL	Power Hardware-in-the-Loop
PLC	Programmable Logic Controller
PMU	Phasor Measurement Unit
PNM	Public Service Company of New Mexico
ProDROMOS	Programmable Distribution Resource Open Management Optimization System
PSO	Particle Swarm Optimization
PUC	Public Utilities Commission
PV	Photovoltaic
QSTS	Quasi-State Time-Series
R&D	Research and Development
RT	Real-Time
RTU	Remote Terminal Unit
SCADA	Supervisory Control and Data Acquisition
SDO	Standards Development Organization
SCAQCF	State and Control Algebraic Quadratic Companion Form
SEP	Smart Energy Profile

SETO	Solar Energy Technology Office
SNL	Sandia National Laboratories
SSL	Secure Socket Layer
TCP	Transmission Control Protocol
TLS	Transport Layer Security
UDP	User Datagram Protocol
UL	Underwriters Laboratories
US	United States
VPN	Virtual Private Network
VV	Volt-Var
WAN	Wide Area Network
WinIGS	Integrated Grounding System Analysis program for Windows

1. INTRODUCTION

State-of-the-art distribution management systems generally provide limited visibility into real-time (RT) feeder operations, do not fully consider solar forecasts, and issue the same DER command or autonomous function to the entire fleet of inverters. This project investigated a future in which ubiquitous sensors produce granular, RT feeder data so that the management system could address the full spectrum of distribution circuit and DER management, including: state estimation, voltage regulation, protection, optimization, communications, and cybersecurity. The solution provided RT visibility into the distribution circuit and optimized reactive power DER settings and protection equipment operations to meet voltage regulation, protection, and economic objectives in the presence of forecast uncertainty. The cross-cutting nature of the effort offers far-reaching benefits to electricity grid controls, protection, forecasting, distribution system optimization, and DER interoperability. It can also dramatically reduce utility capital expenditures by shifting the voltage regulation and protection control actions to DER. To demonstrate the scalability and versatility of the system, multiple demonstrations were conducted:

1. Estimation Based Protection laboratory experiments were conducted to determine the response time and accuracy of a novel protection technology.
2. A power hardware-in-the-loop environment with dozens of physical and virtual DERs were connected to multiple simulated RT distribution models.
3. The control system was constructed in a commercial software vendor's cloud-based environment for a field demonstration on a live feeder in Grafton, MA. The controller issued power factor setpoints to 28 inverters at a 684 kW PV site to improve the feeder voltage profile.

The integrated collection of control and optimization software, called the Programmable Distribution Resource Open Management Optimization System (ProDROMOS)[1], provided the world's first live demonstration of a resilient distribution co-optimization platform for dispatching DERs to provide voltage regulation based on a feeder state estimation. This functionality was provided by running a particle-swarm optimization (PSO) of reduced-order Open Distribution System Simulation (OpenDSS) time-series feeder simulations populated with DER forecasts and state estimation load data. The following major contributions were provided by this project:

1. A persistence DER power forecasting tool was created and open-sourced in Python[2].
2. Opal-RT compatible reduced-order models of multiple utility feeders with advanced DER equipment at >50% of circuit capacity were created and open-sourced.
3. A multi-objective particle swarm optimization wrapper for OpenDSS was created with forecasting and state estimation interfaces.
4. Estimation Based Protection algorithms were expanded for new distribution feeder topologies.
5. A "digital twin" methodology was created to provided model-based measurements for sparse/nonconvergent state estimation problems.
6. Direct comparisons of volt-var (VV), extremum seeking control (ESC), and estimation-based PSO voltage regulation techniques using RT and power hardware-in-the-loop (PHIL) 4-hour simulations of two utility feeders were completed using high-variability solar conditions.

[1] Prodromos is Greek for "forerunner" and the prodromoi were a light cavalry army unit in ancient Greece used for scouting missions.

[2] ProDROMOS GitHub Repository, URL: https://github.com/sunspec/prodromos/

The project showed that under balanced conditions, VV, ESC, and PSO methods were well suited to improve the feeder voltage profile; but in cases with imbalanced phases, three-phase inverters could not substantially improve the imbalance. In those cases, controlling a fleet of single-phase DER equipment is necessary to impudently improve the voltage profiles of each phase. Unfortunately, the field demonstration using a 684 kVA PV system in Grafton, MA, did not demonstrate a substantial improvement in the voltage profile of that feeder because of significant phase imbalance. However, the field demonstration did illustrate that ESC and PSO optimization methods can run on live power systems for multiple hours with results that closely match RT PHIL simulation results.

2. PRODROMOS ARCHITECTURE

ProDROMOS is a partially open-source software platform[3] that addresses the spectrum of distribution circuit and DER management to safely allow PV penetrations of 50% or greater by providing RT visibility into distribution circuits and optimizing the active and reactive (P/Q) DER settings to meet voltage regulation, protection, and economic objectives in the presence of forecast uncertainty. The software system provides RT protection, voltage regulation and visualization by integrating the following modules, shown in Figure 2-1:

1. The Georgia Tech Distribution System Distributed Quasi-Dynamic **State Estimator** (DS-DQSE) takes IEEE C37.118 feeder telemetry from phasor measurement units (PMUs) and generates a power flow estimation and validates the RT model. This information is used to populate the OpenDSS quasi-state time-series (QSTS) simulations within the optimization engine.
2. The Georgia Tech **Estimation-Based Protection** (EBP) detects faults and protects the system by isolating the faulted section of the distribution circuit by recloser/breaker/switching operations. The EBP solves the issues associated with the present protection schemes for distribution circuits with distributed resources.
3. The **forecasting** component provides short-term (e.g., 5-minute) forecasts of PV power output and load using recent system states and statistical irradiance modeling in conjunction with PV performance models.
4. An **optimization engine** determines the necessary active and reactive power settings for the DER to maintain voltage and distribution protection systems for the time horizon (e.g., 15 minutes). The optimization evaluates circuit performance given the state estimate loads and DER power forecasts to minimize the risk of voltage or protection violations while also maximizing economic value.
5. The **communications system** monitors and control thousands of DER devices via internet channels. VV, power factor (PF), and active power curtailment commands were issued to the DERs SunSpec Modbus, IEEE 1815 (DNP3), and proprietary protocols. **Cybersecurity** was paramount to the interoperable operations and was considered for all operations in the project.

The actual RT simulation and field implementations decoupled the protection functionality and voltage regulation using DER optimization. This was done because the voltage regulation could be accomplished using a centralized control methodology, but the protection system needed to be distributed so that the response time of the state-estimation protection commands could not tolerated the added latency of the centralized approach to respond within 10 cycles.[4] The voltage regulation optimization controlled the DER reactive power output to minimize the risk of exceeding the ANSI C84.1 Range A voltage limits. Since inverter specified power factor commands can reduce active power and PV owner revenue, the control system was designed to minimize lost PV production as well.[5] Co-optimizing DER operations to meet multiple objectives is novel in distribution system management.

---

[3] ProDROMOS GitHub Repository, URL: https://github.com/sunspec/prodromos

[4] ProDROMOS protection requirements were aligned with IEEE 1547-2018, which includes a 0.16 s default "must trip" clearing time requirement for low voltage sags below 0.45 pu for Category I DER devices.

[5] While there are some incentives (payment structures) in the wholesale markets for reactive power capacity and output, this is not typically the case at the distribution level. In the future, there may be new regulatory models that incentivize reactive power supply on feeders—in which case the optimization problem would be redesigned to account for this additional revenue stream.

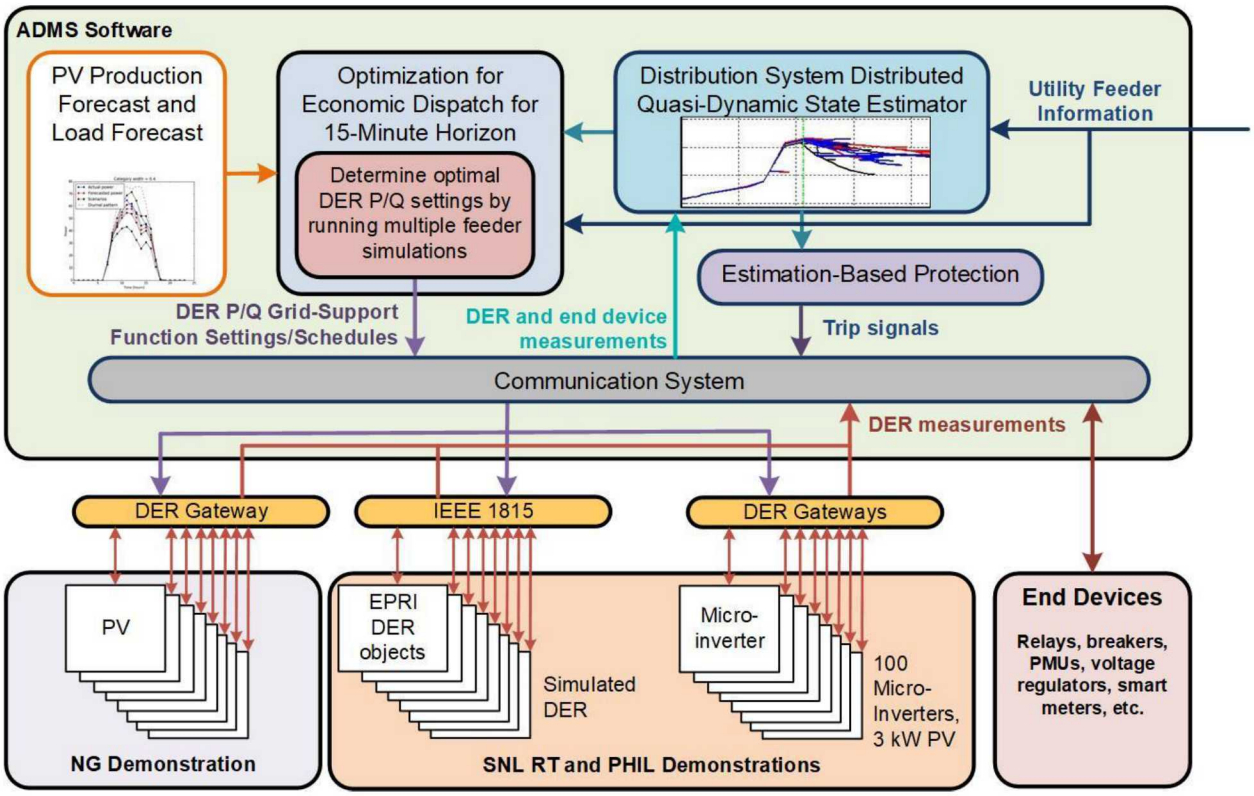

Figure 2-1. High-level ProDROMOS components and data interfaces.

2.1. Interoperability

Utilities and distribution system operators generally do not have the sensor infrastructure or Distributed Energy Resource Management System (DERMS) communication network to execute centralized control of DER devices. One of the objectives of this project was to define the information exchanges shown in Figure 2-2 so that deployment of these systems could become "plug-and-play" in the future.

In the configurational stages of ProDROMOS deployments, a utility will likely contract with a 3rd party software vendor to provide distribution services. The utility will then provide the ProDROMOS vendor with feeder information (e.g., OpenDSS, CYME, models) and access to the field data by creating the associated APIs and/or firewall rules to allow access to the devices. The ProDROMOS vendor will likely establish a login for the utility to visualize the data. In some cases, the ProDROMOS vendor would also provide the utility with APIs to pull data back into their SCADA environment.

In the operational stages of the ProDROMOS deployment, the system would connect to and control DER and field devices. This may or may not require routing this data through the utility. The target operation speeds for each of the components is listed in

Table 2-1. To demonstrate market maturity, the ProDROMOS software was operated with a utility to demonstrate the robustness of the solution to live PV power profiles.

Table 2-1. ProDROMOS component update and response times.

Component	**Update Rate**
State Estimation	Up to 60 Hz update rates, as described in Section 2.3.
PV Forecasts	5-min forecasts updated upon request (every 1 min).
Economic Optimization	Every minute with a 15-min planning horizon.
DER Dispatch	DER set points issued at 1-min intervals.
Feeder Protection	Estimation Based Protection (EBP) operating on two sampled values at a time. Time response depends on sampling rate; typically, < 1 ms.

In terms of defining standardized data exchanges for establishing a ProDROMOS system from scratch, this project took an approach based on the available equipment interfaces to demonstrate the ProDROMOS functionality, but we will not go so far as to say this is the best approach. These distribution services and DER control capabilities are much too nascent to provide definitive recommendations about standardization at this point. This said, based on the experiences of this project, the following information exchanges were found to work well:

- OpenDSS was the preferred feeder exchange format (likely because EPRI and Sandia have extensive experience working with those simulations and file formats).
- DER monitoring and control via DNP3 or Modbus was straightforward, though any of the IEEE 1815-2018 protocols (DNP3, IEEE 2030.5, and SunSpec Modbus) are likely to work well in the future once DER device support these protocols.
- Collecting field data using DNP3 or C37.1118 for PMUs was found to be straightforward and effective, through other protocols supported by field equipment should be considered.
- Custom APIs that exchanged JavaScript Object Notation (JSON) data were highly effective at moving data between internal components of the ProDROMOS system.

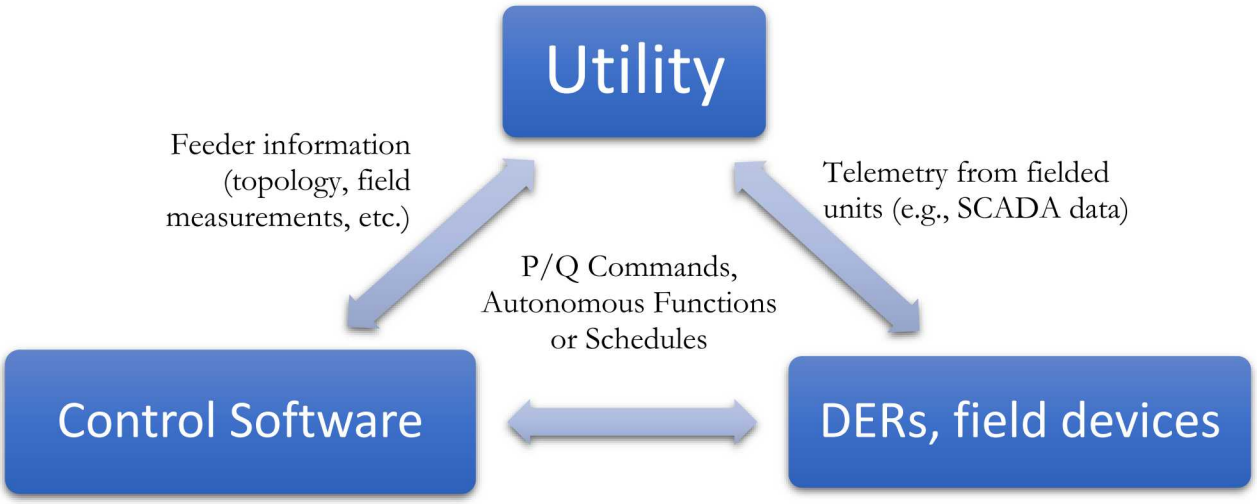

Figure 2-2. Information exchanges required to perform distribution voltage and protection optimization.

2.1.1. Commercial Implementation

The ProDROMOS system was constructed on the Connected Energy CNRG software system in a cloud environment. The DER, PMU, and other device communications were established from the Amazon Web Services (AWS) environment to the end devices using different communication protocols and application specific interfaces (APIs) with associated firewall exemptions at Sandia National Laboratories, National Grid, and Trimark Associates.

During the project, Connected Energy connected the ProDROMOS software to thousands of DER devices and field measurement equipment. The PV equipment included SMA inverters in the field demonstration, EPRI PV simulators, 100 microinverters and one 3 kW residential string inverter at Sandia National Laboratories' Distributed Energy Technologies Laboratory (DETL). Connected Energy also gathered PMU data from the RT and PHIL experiments for the state estimation and field data from a SEL-734 Advanced Metering System for the field demonstrations.

2.1.2. Interoperability Experiments

A component of the project was to show scalability of solutions, so the ProDROMOS software was connected to 1,200 DER devices for multiple hours. Four instances of the EPRI PV simulator were started with 300 DER devices with unique port numbers. Connected Energy then connected to the DNP3 interfaces of each of the PV inverters and collected data from each of the emulated DER devices. By instantiating the DERMS/ProDROMOS system in the AWS cloud computing platform, much of the scaling could be completed by changing the size and processing power of the virtual machines and servers used for the monitoring and control functionality.

2.2. Forecasting

Short-term forecasts of PV output power can be made using several different models and techniques—each with their own data requirements. For this project, short-term forecasts are made using a persistence method that requires only the DER location, PV system AC and DC capacity and historical power. The ability to map forecasts to other DER devices was also established, so that, if power data was not collected by some of the DER equipment, forecasts could still be created by scaling the production forecasts based on the capacities of each system. The forecasting code is in Python and is open source.[6]

2.2.1. Persistence Forecasts

Conceptually, a persistence forecast projects future values of power by assuming that recent weather conditions persist through the forecast period. Persistence forecasts for PV output also account for the systematic movement of the sun and the system's DC and AC capacities.

Denoted by t_1,K,t_N, the future time points at which a forecast is desired, and $P(t_{-K}),K,P(t_{-1})$ the system's recent observed power. The clear-sky power index K quantifies the system output as a fraction of possible output in clear-sky conditions, calculated as $K(t)=P(t)/CSP(t)$ where $CSP(t)$ is the clear-sky power of the system. Clear-sky power is calculated by first using a clear-sky irradiance model and an irradiance transposition model from `pvlib python` to obtain irradiance in the PV

[6] https://github.com/sunspec/prodromos/tree/master/forecasting

system's plane $\mathrm{POA}(t)$, then estimating power as $\mathrm{CSP}(t) = \min\left\{\left(\mathrm{POA}(t)/1000\ \mathrm{W/m^2}\right)\times \mathrm{DC}, \mathrm{AC}\right\}$ where DC and AC are the system capacities, and the DC capacity is determined at irradiance of 1000 W/m^2. We applied this persistence approach to forecast the expected value of power as $P(t_i) = \mathrm{CSP}(t_i)\times\frac{1}{N}\sum_{j=-K}^{j=-1} K(t_j), i = 1,K,N$. The PV power forecast is used to determine power factor settings to minimize the average voltage deviation from a target value over a period of time (Section 2.5). An appropriate forecast quantity for the optimization is the expected value of PV power output over the forecast period.

Special handling is necessary for forecast periods using data prior to sunrise, because clear-sky power before sunrise is zero. For these periods, the forecast power is the observed power for the same time period on the preceding day.

Forecasts for systems without data or with missing data are made by identifying a surrogate PV system, forecasting for the surrogate system, then scaling the forecast by the ratio of AC capacities. The assigned surrogate system should be nearby, to avoid large errors from different irradiance conditions, and should have a similar ratio of DC to AC capacity.

2.2.2. Forecasts using ARIMA Model

One potential shortcoming of the persistence forecast approach is the requirement to know DC and AC capacities. In operations, PV system capacity varies from its design value due to system losses, equipment maintenance, failure and repair of components, or external factors such as local shading. An alternative approach is to fit a statistical model to the recent power data over rolling periods and use the model to forecast power. Fitting to rolling periods ensures that the model reflect the system's condition for each forecast.

We implemented this approach by fitting an autoregressive integrated moving average (ARIMA) model to the clear-sky power index. For intervals (time between data or forecast points) less than 15 minutes we used an AR(1) model with first differencing (ARIMA order (1, 1, 0)) reasoning that any diurnal pattern remaining in the clear-sky power index is removed by first differencing, and favoring a parsimonious model. In this fitting, the capacities used to calculate the clear-sky power index serve to set a fixed reference for system power; reasonable but inaccurate values suffice since the model adapts to system's actual state. When the model was successfully fit we found the forecasts to be a minor improvement over the persistence forecast described above. However, during testing, fitting the model over rolling periods of recorded data would occasionally fail due to numerical problems that are not automatically handled in the available tools. Because the ARIMA model offered only minor improvement in accuracy and this project's focus is not developing forecast methods, we chose the persistence forecast approach for its reliability rather than developing methods that guarantee a forecast using a rolling ARIMA approach.

2.3. State Estimation

Distribution system state estimation has recently gained substantial interest in the international research community for its ability to enable a range of distribution services.[7] The *Integrated Grounding System Analysis program for Windows* (WinIGS) Software developed by Georgia Institute of Technology and provided by Advanced Power Concepts was used to complete the state estimation in this project.

[7] A. Primadianto and C. Lu, "A Review on Distribution System State Estimation," in IEEE Transactions on Power Systems, vol. 32, no. 5, pp. 3875-3883, Sept. 2017.

This software generated the best estimate of the distribution power flows (bus and device current and voltage phasors) based on a set of filed measurements. However, before running the state estimation, the power system topology, locations of DER and other feeder end-devices, and the models of distribution circuits were required. This information was provided by the utilities and reconstructed from the utility data into State and Control Algebraic Quadratic Companion Form (SCAQCF). To do this for each feeder model, first a Compact Component Model consisting of set of algebraic and differential linear and nonlinear equations and inequalities was created. This model was then converted to a Quadratized Model with second order equations and inequalities and then into SCAQCF. The format of the SCAQCF formulation is shown in Figure 2-3. Given the measurements and the device SCAQCF models in a feeder section, the DS-DSE created the measurement mathematical model at the device-level. Then, with the help of network formulation techniques, the measurement mathematical models from device-level were converted to network level measurement models. The state estimation algorithm worked directly with the measurement mathematical model at the network level. The results of a DS-DSE are the best estimate of the states and the validated model of that feeder section. Finally, the output of each DS-DSE for each section was sent to the distribution management system where the states and RT model of the entire feeder were constructed. The whole procedure was solved in previous work for an example feeder.[8] The PNM and NG models were updated as WinIGS models with the DER for RT and PHIL simulations and the NG field demonstration.

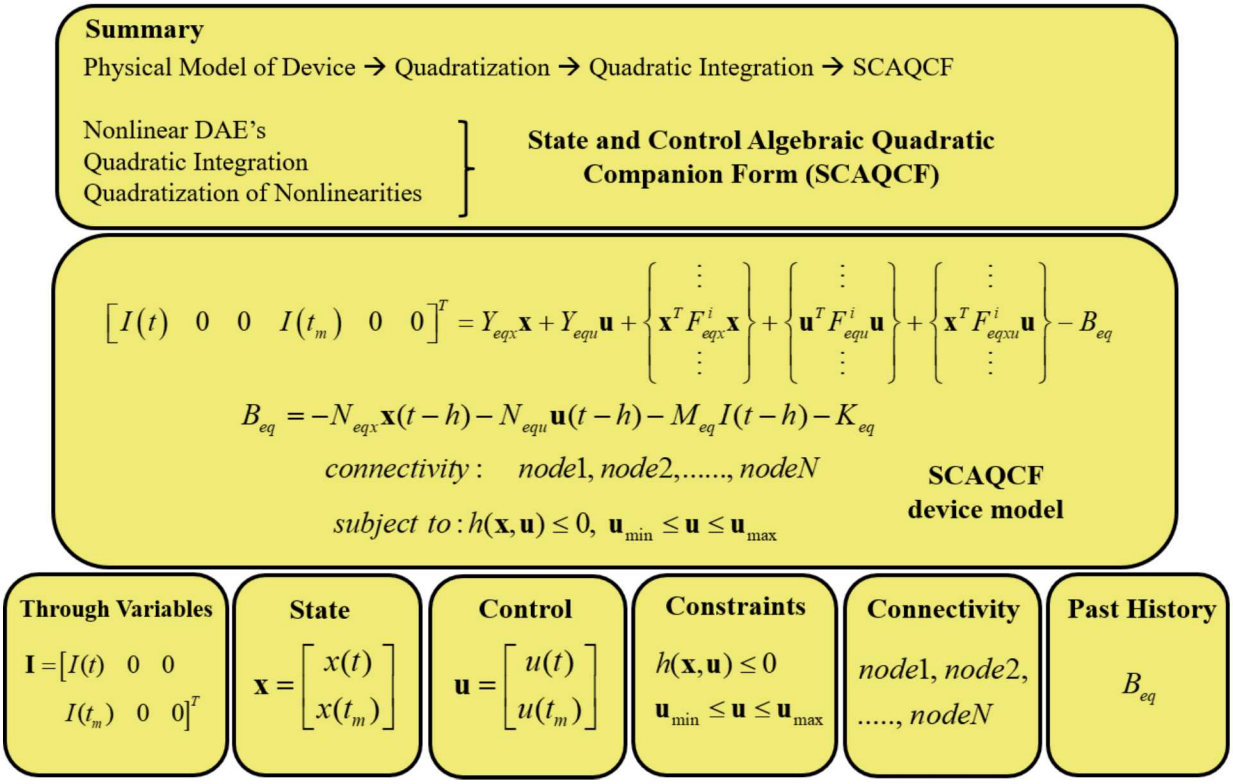

Figure 2-3. State and Control Algebraic Quadratic Companion Form (SCAQCF).

[8] A.P. Meliopoulos, G. Cokkinides, B. Xie, C. Zhong, J. Johnson, "Full State Feedback Control for Virtual Power Plants," Sandia Technical Report, SAND2017-10178, September 2017.

To generate the state estimation, measured values from the PV devices and other field data must be passed to the state estimator via C37.118 streams or COMTRADE files. For this project, only virtualized μPMU devices where used; they instantiated created on each of the buses of the feeder model and passed voltage and/or current phasor data as C37.118 streams to the WinIGS state estimation tool. The distribution state estimator passed the system state to the optimization tools, which determined the best set points for the DER devices.

2.3.1. Formulation for PNM Feeder

This subsection introduces the details of the formulation for PNM feeder model in WinIGS. Since the feeder model is given in OpenDSS format, the Georgia Tech team developed a filter that converted the OpenDSS models to WinIGS models. The flow chart of the procedure is shown in Figure 2-5. The filter first read the model OpenDSS files and a bus coordinate OpenDSS files and stores them in the specific arrays in each device class (e.g., load class, transformer class, line class, etc.). Then, the filter processes the buses by 1) renaming these buses in WinIGS format, 2) creating a mapping list between the original bus names from OpenDSS and the renamed buses, and 3) scaling bus coordinates. After the bus processing procedure, the filter converts all devices into WinIGS format with all the original parameters (device name, bus name, bus coordinates, rated voltage, rated power, etc.). Lastly, the filter outputs the translated models into a WinIGS readable file (WinIGS NMF file).

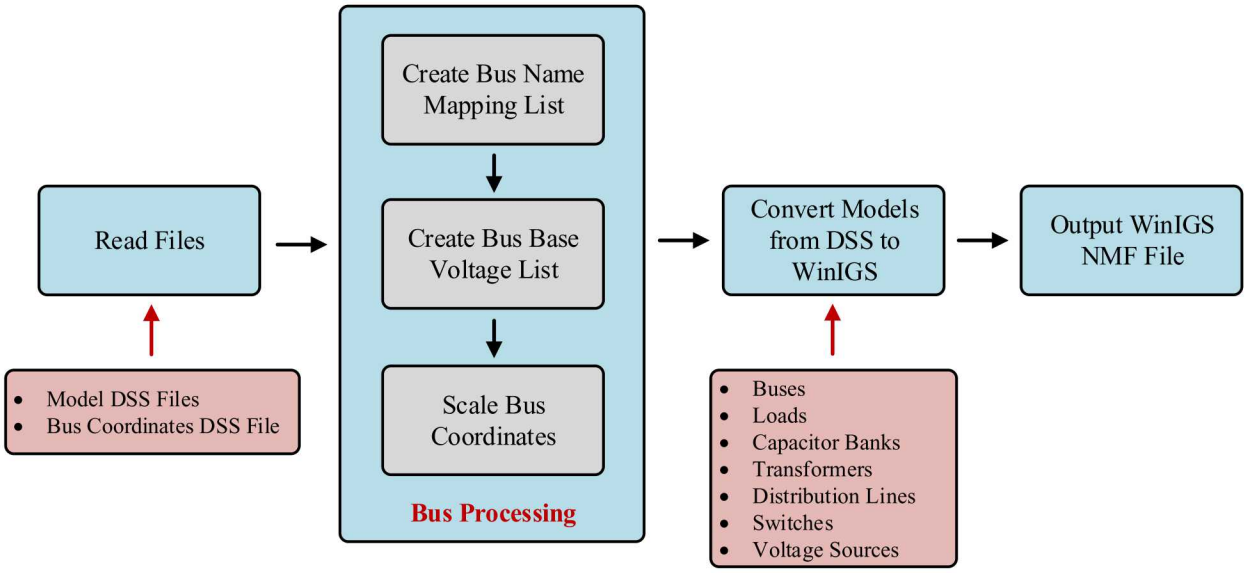

Figure 2-4. Program Flow Chart for Model Conversion from OpenDSS to WinIGS.

The converted PNM feeder model in WinIGS is shown in Figure 2-6. This reduced feeder model has 15 three-phase buses. The anonymized GPS coordinates of the buses were available, which allowed visualization of the feeder topology. The feeder model was debugged in the WinIGS software. The case was solvable, and the convergence was achieved in 6 iterations.

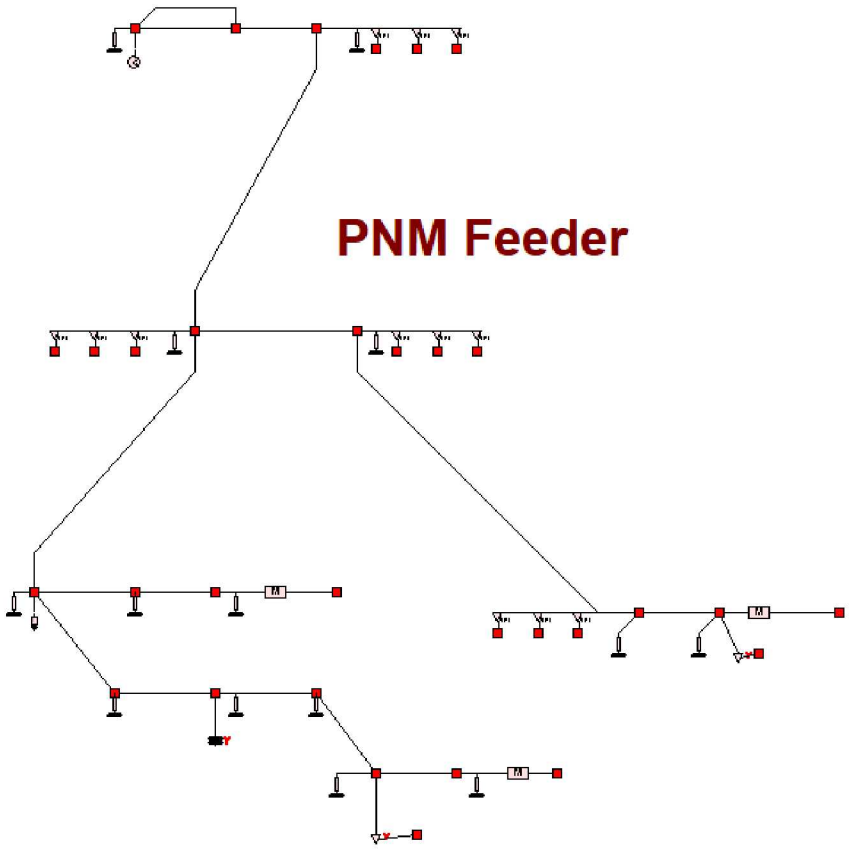

Figure 2-5. Single-Phase Diagram of PNM Feeder Model.

PNM feeder model consisted of loads (three-phase, single-phase), capacitor banks, three-phase two-winding transformers, three-phase distribution lines, equivalent sources, PV sources, etc. Table 2-2 describes these types of devices in this feeder. Specifically, the feeder consists of 2 three-phase loads, 12 single-phase loads. The real and reactive power consumption of these loads is 2568.60 kW and 1418.71 kVAr, respectively. The detailed parameters of these loads are listed in Table 2-3. Table 2-4, Table 2-5, Table 2-6, and Table 2-7 describe the detailed parameters of capacitor banks, transformers, distribution lines, equivalent sources, and PV sources, respectively.

Table 2-2. Devices in PNM Feeder Model.

Device Type		Number
Constant Power Load	Three-Phase Load	2
	Single-Phase Load	12
Capacitor Bank	Three-Phase	2
Transformer	Three-Phase Two-Winding	2
Distribution Line	Three-Phase	12
Equivalent Source	Three-Phase	1
PV Source	Three-Phase	3

Table 2-3. Parameters of Load Models in PNM Feeder Model.

Three-Phase Load						
#	Device Name	Bus Name	Phase Number	Rated Voltage (L-L, kV)	Real Power (kW)	Reactive Power (kVar)
1	Load19	B15	3	0.48	25.5	19.2
2	Load20	B04	3	12.47	1885	1292
Single-Phase Load						
1	Load136	B11_A	1	7.19956	-0.03183	0.003439
2	Load137	B11_B	1	7.19956	3.86034	0.489472
3	Load138	B11_C	1	7.19956	2.67042	0.302451
4	Load139	B05_A	1	7.19956	0.028182	-0.00895
5	Load140	B05_B	1	7.19956	2.28829	0.413719
6	Load141	B05_C	1	7.19956	0.393999	0.15441
7	Load142	B09_A	1	7.19956	97.1185	22.0604
8	Load143	B09_B	1	7.19956	100.58	22.4071
9	Load144	B09_C	1	7.19956	116.318	25.6155
10	Load133	B10_A	1	7.19956	107.384	11.5588
11	Load134	B10_B	1	7.19956	108.562	11.9113
12	Load135	B10_C	1	7.19956	118.93	12.6054

Table 2-4. Parameters of Capacitor Bank Models in PNM Feeder Model.

Capacitor Bank					
#	Device Name	Bus Name	Rated Reactive Power (kVar)	Rated Voltage (L-L, kV)	Connection Type
1	Capa1	B07	1800	12.47	WYE

Table 2-5. Parameters of Three-Phase Two-Winding Transformers in PNM Feeder Model.

Three-Phase Two-Winding Transformer					
#	Device Name	Bus Name	Rated Power (MVA)	Rated Voltage (kV)	Connection Type
1	Tran1	B01, B02	30	115/12.47	DELTA/WYE
2	Tran20	B10, B15	0.5	12.47/0.48	WYE/WYE

Table 2-6. Parameters of Three-Phase Equivalent Source in PNM Feeder Model.

Three-Phase Equivalent Source				
#	Device Name	Bus Name	Rated Voltage (kV)	Rated Power (MVA)
1	feeder	B01	115	100

Table 2-7. Parameters of Three-Phase PV Sources in PNM Feeder Model.

Three-Phase PV Source					
#	Device Name	Bus Name	Rated Voltage (kV)	Rated Power (MVA)	Power factor
1	PVSy1	B12	12.47	1	1.0
2	PVSy2	B14	12.47	10	1.0
3	PVSy3	B15	0.48	0.258	1.0

The simulation data (line-to-neutral voltages at each bus) are compared between WinIGS and OpenDSS to validate the converted feeder model. Figure 2-6, Figure 2-7, and Figure 2-8 depict the

line-to-neutral voltage magnitude differences at all 15 buses between the simulation result from OpenDSS and WinIGS at phase A, B, and C, respectively. Notice that all the errors are within 0.001 p.u., which is acceptable and a result of different configuration/parameters of the models between WinIGS and OpenDSS.

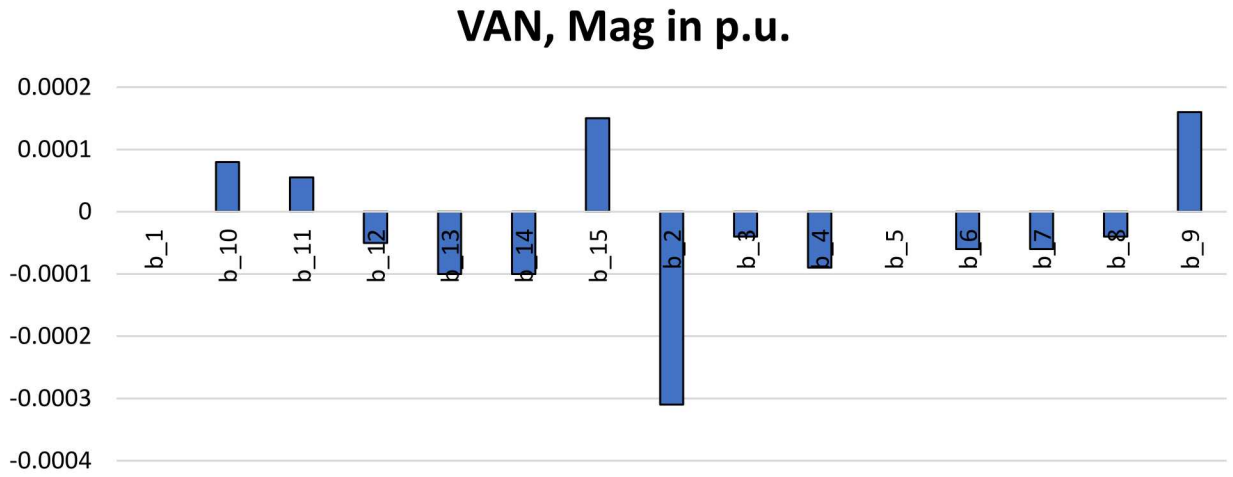

Figure 2-6. V_{AN} mismatch between WinIGS and OpenDSS.

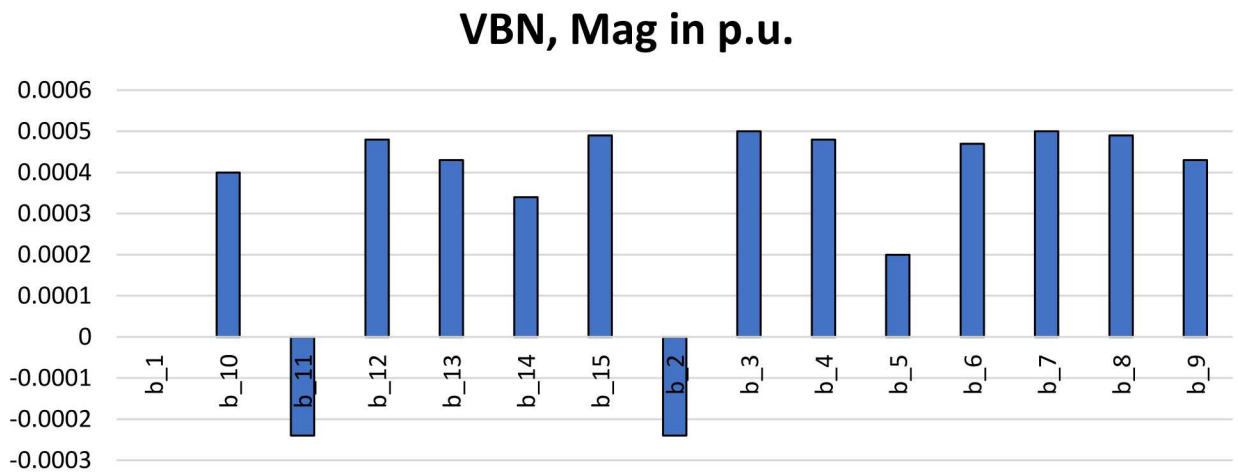

Figure 2-7. V_{BN} mismatch between WinIGS and OpenDSS.

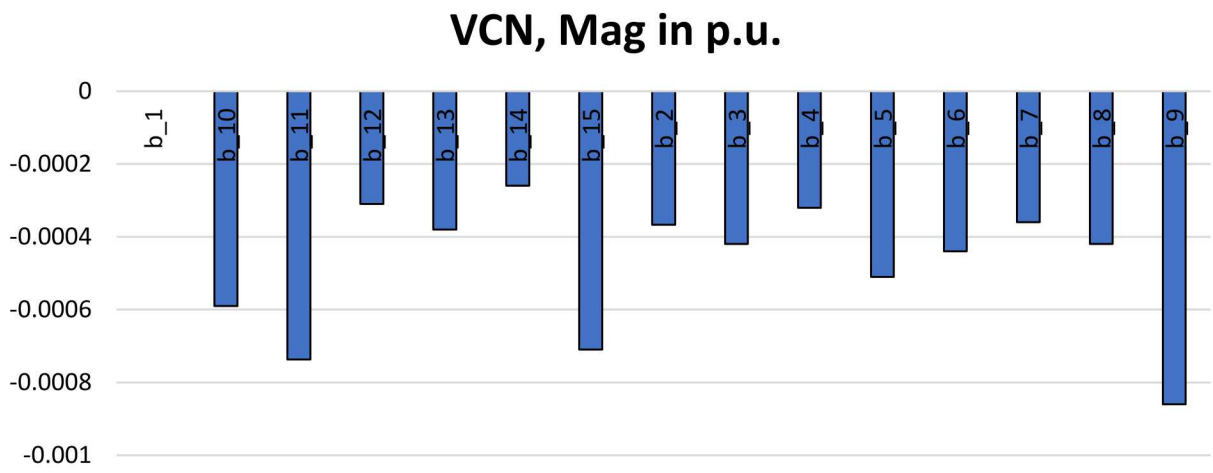

Figure 2-8. V_{CN} mismatch between WinIGS and OpenDSS.

2.3.2. Validation of PNM Feeder State Estimation

This subsection introduces the overall approach of validation of PNM feeder state estimation. The validation is performed by the DS-DSE in WinIGS. As shown in Figure 2-9, a distribution system is arbitrarily partitioned into several sections, each having a local distributed state estimator, which performs quasi-dynamic state estimation (QDSE) by using the measurements collected only in the corresponding section. Each local state estimator streams the data to the data control center, where estimated states and validated model for the whole feeder are synthesized for further RT applications. Such a procedure requires at least one GPS-synchronized intelligent electronic device (IED) in each section, accelerates the speed of state estimation, and dramatically reduces the data traffic between the IEDs and the control center.

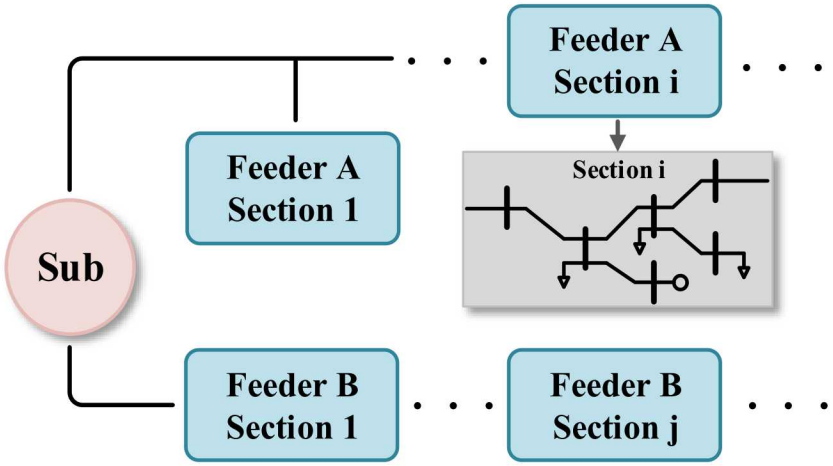

Figure 2-9. Partitioned Sections in a Distribution System.

The infrastructure of the DS-DSE is an object-oriented high-fidelity device modeling approach. The modeling approach starts from a physically-based model, which is a set of equations describing the physical characteristics of a device with states and control variables. Then, a quadratization procedure

is applied so that the highest order in the model equations is ≤2. Since the physically-based model may contain differential terms that reflect the dynamics, the quadratic integration method is applied to transform the differential equations to algebraic equations. The final result of this procedure is an object-oriented interoperable syntax called State and Control Algebraic Quadratic Companion Form (SCAQCF). The network measurement model formulation process and quasi-dynamic state estimation algorithm introduced in the following paragraphs are all based on the models in such standard without any other inputs.

The state estimator requires measurements obtained from the distribution system to perform the dynamic state estimation. Any measurements, irrespectively of the source of the measurements, i.e., actual, virtual, derived, or pseudo (described in Section 2.3.2.2), can be expressed as functions of the states in the SCAQCF syntax and in this form are utilized by the state estimator to perform the quasi-dynamic state estimation. Specifically, given a measurement set and all the SCAQCF device models, the measurement models are first developed at the device-level, i.e., they are expressed as functions of the state variables of individual devices. Subsequently, the mapping between devices and the network is developed and the measurement models are converted from device-level to network-level by the mapping plus adding additional virtual measurements based on the Kirchhoff's current law (KCL) equations at common nodes.

The quasi-dynamic state estimation algorithm works directly on the measurement mathematical models at the network-level. The state estimator provides a quantitative probabilistic consistency between the network measurement model and the network model. Specifically, the DS-DSE provides the best estimate of the states, the differences (residuals) between measurements and estimated measurements, and the expected standard deviation of these quantities. Finally, the output of each distributed state estimator for each section is sent to the control center where the states and model of the entire distribution system is constructed from the states and model of each section at a specific time stamp, which is referred as RT operating conditions and model.

2.3.2.1. Object-Oriented Device Modeling

This subsection describes a high-fidelity standardized modeling approach for power devices that enables object-oriented analysis in the distribution system. As shown in Figure 2-10, the modeling approach starts from physical based model of a power device referred as compact device model, which is a set of equations describing the physical and mathematical properties of the device. Any existing model can be expressed as a compact device model, and it is in terms of states and control variables. A quadratization procedure is then applied to the compact model. This procedure consists of introducing additional variables to reduce higher order terms to nonlinear terms of highest order two. The end result is a state and control quadratized device model (SCQDM), which in general is also in terms of states and controls with other device information (connectivity, etc.). The SCQDM form is shown below. Notice that in SCQDM, equation set one and two are linear, and equation set three is quadratic.

Model Description: *Type*, *Code*, *ID*, *Title*

$$i(t) = Y_{eqx1}\mathbf{x}(t) + Y_{equ1}\mathbf{u}(t) + D_{eqxd1}\frac{d\mathbf{x}(t)}{dt} + C_{eqc1}$$

$$0 = Y_{eqx2}\mathbf{x}(t) + Y_{equ2}\mathbf{u}(t) + D_{eqxd2}\frac{d\mathbf{x}(t)}{dt} + C_{eqc2}$$

$$0 = Y_{eqx3}\mathbf{x}(t) + Y_{equ3}\mathbf{u}(t) + \left\{\begin{matrix}\vdots \\ \mathbf{x}(t)^T \left\langle F^i_{eqxx3} \right\rangle \mathbf{x}(t) \\ \vdots\end{matrix}\right\} + \left\{\begin{matrix}\vdots \\ \mathbf{u}(t)^T \left\langle F^i_{equu3} \right\rangle \mathbf{u}(t) \\ \vdots\end{matrix}\right\} + \left\{\begin{matrix}\vdots \\ \mathbf{u}(t)^T \left\langle F^i_{equx3} \right\rangle \mathbf{x}(t) \\ \vdots\end{matrix}\right\} + C_{eqc3}$$

$$\mathbf{h}(\mathbf{x},\mathbf{u}) = Y_{hfeqx}\mathbf{x}(t) + Y_{hfequ}\mathbf{u}(t) + \left\{\begin{matrix}\vdots \\ \mathbf{x}(t)^T F^i_{hfeqxx}\mathbf{x}(t) \\ \vdots\end{matrix}\right\} + \left\{\begin{matrix}\vdots \\ \mathbf{u}(t)^T F^i_{hfequu}\mathbf{u}(t) \\ \vdots\end{matrix}\right\} + \left\{\begin{matrix}\vdots \\ \mathbf{u}(t)^T F^i_{hfequx}\mathbf{x}(t) \\ \vdots\end{matrix}\right\} + C_{hfeqc}$$

Constraints : $\mathbf{h}(\mathbf{x},\mathbf{u}) \le \mathbf{0},\ \mathbf{u}_{\mathbf{hmin}} \le \mathbf{u} \le \mathbf{u}_{\mathbf{hmax}},\ |\mathbf{du}| \le \mathbf{u}_{\mathbf{hllim}}$

Model Dimensions : $\mathrm{n}_{equ1}, n_{equ2}, n_{equ3}, n_{state}, n_{control}, n_{Feqxx}, n_{Fequu}, n_{Fequx}, n_{fconst}, n_{Ffeqxx}, n_{Ffequu}, n_{Ffequx}$

Connectivity : $nn_t, ivn, inn, onn, S_{st}$

Normalization Factors: $x_{NF}, e_{NF}, u_{NF}, h_{NF}$

where: $i(t)$ is the terminal through variable vector, $\mathbf{x}(t)$ is the state variable vector, Y matrices are linear coefficients, D matrices are differential coefficients, C vectors are constants, F matrices are nonlinear coefficients, $\mathbf{h}$ denotes functional constraints, $\mathbf{u}_{\mathbf{hmin}}$, $\mathbf{u}_{\mathbf{hmax}}$ are lower and upper bounds for control variables, $\mathbf{u}_{\mathbf{hlim}}$ denotes the maximum permissible control variable excursions to maintain linearization error below a threshold. Besides, the SCQDM also provides additional information for this model including model type, model ID, model title, model dimensions, connectivity information, normalization factors, and units.

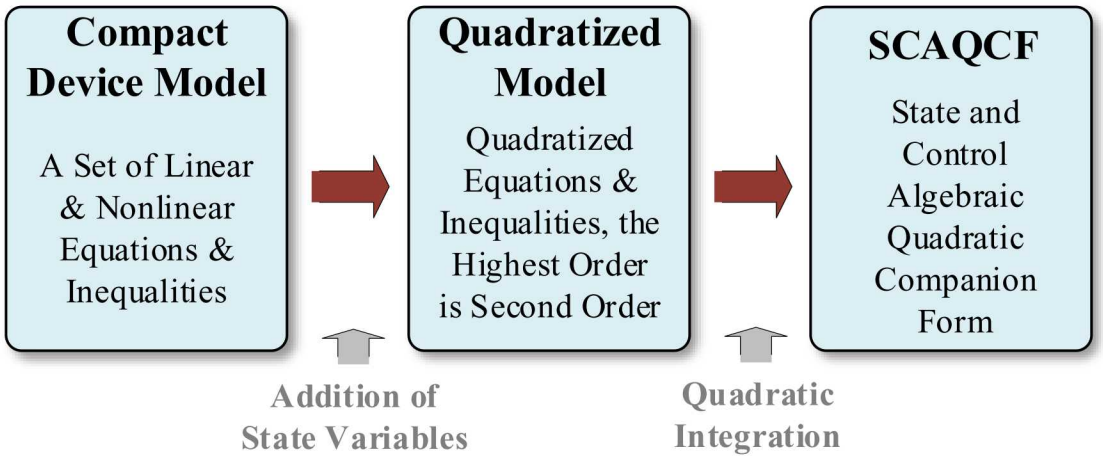

Figure 2-10. Object-Oriented Device Modeling Approach.

The SCQDM is then integrated for the purpose of converting it into an algebraic model. The quadratic integration method is adopted, and the integration process transforms the SCQDM into a state and control algebraic quadratic companion form (SCAQCF) as shown below. The state estimator works directly on this SCAQCF syntax.

Model Description: *Type*, *Code*, *ID*, *Title*

$$\begin{Bmatrix} i(t) \\ 0 \\ 0 \\ i(t_m) \\ 0 \\ 0 \end{Bmatrix} = \mathbf{e}_{\mathbf{lhs}} = Y_{eqx}\mathbf{x} + \begin{Bmatrix} \vdots \\ \mathbf{x}^T \left\langle F^i_{eqxx} \right\rangle \mathbf{x} \\ \vdots \end{Bmatrix} + Y_{equ}\mathbf{u} + \begin{Bmatrix} \vdots \\ \mathbf{u}^T \left\langle F^i_{equu} \right\rangle \mathbf{u} \\ \vdots \end{Bmatrix} + \begin{Bmatrix} \vdots \\ \mathbf{u}^T \left\langle F^i_{equx} \right\rangle \mathbf{x} \\ \vdots \end{Bmatrix} - B_{eq}$$

$$B_{eq} = -N_{eqx}\mathbf{x}(t-h) - N_{equ}\mathbf{u}(t-h) - M_{eq}I(t-h) - K_{eq}$$

$$\mathbf{h}(\mathbf{x},\mathbf{u}) = Y_{feqx}\mathbf{x} + Y_{fequ}\mathbf{u} + \begin{Bmatrix} \vdots \\ \mathbf{x}^T \left\langle F^i_{feqxx} \right\rangle \mathbf{x} \\ \vdots \end{Bmatrix} + \begin{Bmatrix} \vdots \\ \mathbf{u}^T \left\langle F^i_{fequu} \right\rangle \mathbf{u} \\ \vdots \end{Bmatrix} + \begin{Bmatrix} \vdots \\ \mathbf{u}^T \left\langle F^i_{fequx} \right\rangle \mathbf{x} \\ \vdots \end{Bmatrix} + C_{feqc}$$

Constraints : $\mathbf{h}(\mathbf{x},\mathbf{u}) \le \mathbf{0}, \mathbf{u}_{\mathbf{min}} \le \mathbf{u} \le \mathbf{u}_{\mathbf{max}}, \ |\mathbf{du}| \le \mathbf{u}_{\mathbf{llim}}$

Model Dimensions: n_{equ}, n_{state}, $n_{control}$, n_{Feqxx}, n_{Fequu}, n_{Fequx}, n_{fconst}, n_{Ffeqxx}, n_{Ffequu}, n_{Ffequx}

Connectivity: nn_t, *ivn*, *inn*, *onn*, S_{st}

Normalization Factor: x_{NF}, e_{NF}, u_{NF}, h_{NF}

Units: *xUnit*, *eUnit*, *uUnit*, *hUnit*

2.3.2.2. Network-Level Measurement Model Formulation

This subsection introduces the procedure that formulates the network-level measurement model using SCAQCF devices and measurements from a partitioned section. With increasing deployment of DER, smart meters, and other grid sensors in the distribution system, the amount of available measurements is growing. These measurements construct the network-level measurement model that improves the observability of the distribution system and increases the accuracy of the state estimation results. To construct the network-level measurement model, three tasks are performed:

1) construct the network-level SCAQCF model and form the mapping lists (states, control, equations) from devices to the network
2) create the network-level actual measurement model based on the given measurements from all IEDs and the mapping lists
3) create the network-level derived, pseudo, and virtual measurement model.

Given *n* device SCAQCF models in a selected section, the first task is to create the network-level SCAQCF syntax as shown in Figure 2-11. In general, a device SCAQCF model consists of three types of equations: a) equations corresponding to the network interface nodes, b) equations corresponding to the network common nodes, and c) device internal equations. To formulate the network SCAQCF model, we keep types a and c equations and replace the states and controls in terms of devices by the

states and controls in terms of the network. For type b equations from different devices but corresponding to a same common node, we apply KCL at each node which provides one equation for each node and which eliminates the through variables. These equations are in terms of the states and controls of the network. During this task, we first create the mapping lists (states, controls, equations) from devices to the network based on the device connectivity. Then, the network SCAQCF model is automatically created by device SCAQCF models in this network and the mapping lists. The output of this step is the network SCAQCF model listed in Figure 2-12. Note that in the network SCAQCF model, the equations with the current i on the left-hand side denote the through variables flowing into the network through the interface nodes, and all the other equations with zero value on the left-hand side are the device internal equations and the zero sum of equations at the common nodes derived from KCL.

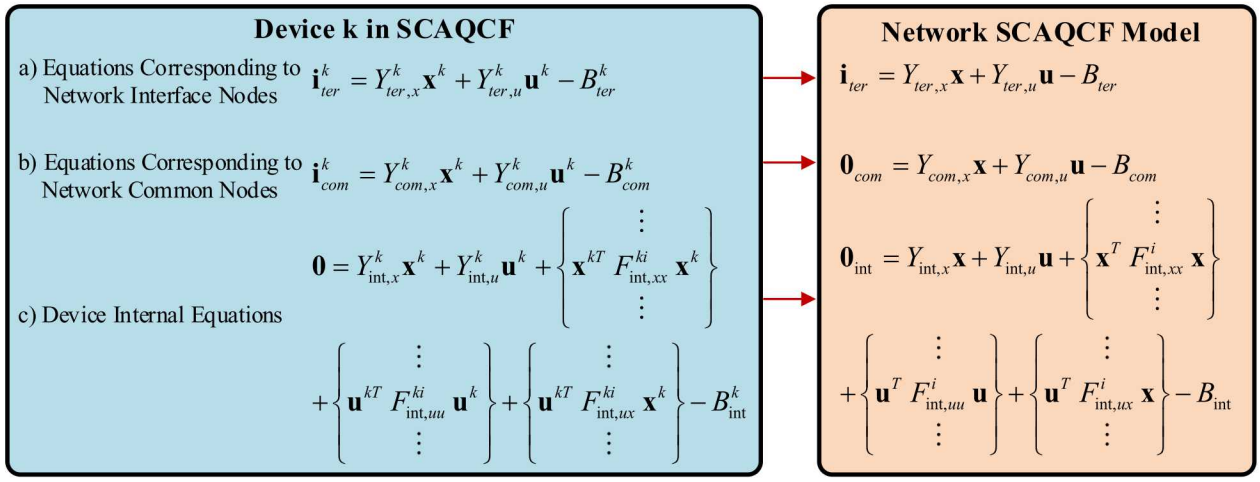

Note:

1) the superscript k denotes the device number k;

2) "ter" refers to terminal, "com" refers to common node, "int" refers to internal.

Figure 2-11. Network SCAQCF Model Formulation.

The second task is to form the network-level actual measurement model. Given the measurements from all IEDs and all device SCAQCF models, we first construct the device-level measurement model. For an across measurement, its measurement model is simply a linear combination of the states of the measured device plus a measurement error from this IED, i.e.,

$$z(t) = A\mathbf{x}(t) + \eta \tag{2.4.1}$$

where $z(t)$ is the measurement, A is the linear coefficient matrix, $\mathbf{x}(t)$ is the device state vector at time t, and η is the noise introduced by this IED. For a through measurement, its measurement model is obtained directly from the corresponding equations of the device SCAQCF model, i.e.,

$$z(t) = Y_{zx}\mathbf{x} + Y_{zu}\mathbf{u} + \left\{ \begin{matrix} \vdots \\ \mathbf{x}^{T} F_{zx}^{i} \mathbf{x} \\ \vdots \end{matrix} \right\} + \left\{ \begin{matrix} \vdots \\ \mathbf{u}^{T} F_{zu}^{i} \mathbf{u} \\ \vdots \end{matrix} \right\} + \left\{ \begin{matrix} \vdots \\ \mathbf{u}^{T} F_{zux}^{i} \mathbf{x} \\ \vdots \end{matrix} \right\} - B_{z} + \eta \tag{2.4.2}$$

$$B_{z} = -N_{zx}\mathbf{x}(t-h) - N_{zu}\mathbf{u}(t-h) - M_{z}i(t-h) - K_{z}$$

where Y, N, M matrices are linear coefficient matrices, F matrices are nonlinear coefficient matrices, and K is the constant term. Once the device-level actual measurement model is formed, the network-level actual measurement model is easily obtained by using the formulated mapping lists that map the states, controls, and equations in the device-level actual measurement model to those in the network-level actual measurement model.

To realize the observability and increase redundancy, four other measurement types are introduced:

1) type I derived measurement: derived from actual measurements based on the system topology
2) type II derived measurement: generated for missing through variable measurements in any multi-terminal device
3) pseudo measurement: quantities that are approximately known
4) virtual measurements: equations with zero value defined by physical or mathematical laws.

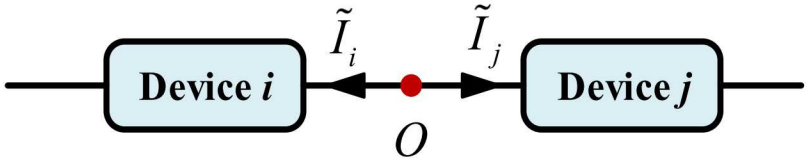

Figure 2-12. Illustration of Type I Derived Measurement.

Type I derived measurement is created by derivation from actual measurements based on the network topology. For instance, as shown in Figure 2-12, devices i and j are connected at node O with available current phasor measurement $\tilde{I}_i$. Since no other devices are connected at point O, the current flowing into device j is simply derived as $z = \tilde{I}_j + \eta = -\tilde{I}_i + \eta$, which is a type I derived measurement. Type I derived measurement can also be created based on the device topology. For example, as a distribution line is usually short, its shunt capacitance is quite small. Therefore, if a current measurement at one terminal of this line is available, we can derive a current measurement that has the same magnitude but is with an opposite phase angle at the other terminal of this line. Such measurement is also considered as a type I derived measurement. By using formulated mapping lists, type I derived measurement model is expressed in terms of variables at network-level as listed in (2.4.3), where subscript dI denotes type I derived measurement.

$$z_{dI}(t) = Y_{dI,x}\mathbf{x} + Y_{dI,u}\mathbf{u} + \begin{Bmatrix} \vdots \\ \mathbf{x}^T F^i_{dI,x}\mathbf{x} \\ \vdots \end{Bmatrix} + \begin{Bmatrix} \vdots \\ \mathbf{u}^T F^i_{dI,u}\mathbf{u} \\ \vdots \end{Bmatrix} + \begin{Bmatrix} \vdots \\ \mathbf{u}^T F^i_{dI,ux}\mathbf{x} \\ \vdots \end{Bmatrix} - B_{dI} + \eta \qquad (2.4.3)$$

$$B_{dI} = -N_{dI,x}\mathbf{x}(t-h) - N_{dI,u}\mathbf{u}(t-h) - M_{dI}i(t-h) - K_{dI}$$

Type II derived measurement is generated for missing through variable measurements in any multi-terminal device that has at least one through quantity actual measurement. Specifically, for an n-terminal device with m terminals having through measurements, the state estimator creates type II derived measurements for the other n-m terminals. Type II derived measurement model is directly obtained from the device SCAQCF model. However, its measurement value is computed from the

device SCAQCF model using the estimated states from the last time step. Since the measurement value is not obtained from the current time step, the state estimator assigns a relatively higher measurement error to type II derived measurement compared to the actual measurements from this device (e.g., five times larger than the actual measurement error of this device). By using the mapping lists between devices and the network, type II derived measurement model is expressed in terms of variables at network level in (2.4.4), where *dII* denotes type II derived measurement.

$$z_{dII}(t) = Y_{dII,x}\mathbf{x} + Y_{dII,u}\mathbf{u} + \left\{\begin{array}{c}\vdots\\ \mathbf{x}^T F^i_{dII,x}\mathbf{x}\\ \vdots\end{array}\right\} + \left\{\begin{array}{c}\vdots\\ \mathbf{u}^T F^i_{dII,u}\mathbf{u}\\ \vdots\end{array}\right\} + \left\{\begin{array}{c}\vdots\\ \mathbf{u}^T F^i_{dII,ux}\mathbf{x}\\ \vdots\end{array}\right\} - B_{dII} + \eta \qquad (2.4.4)$$
$$B_{dII} = -N_{dII,x}\mathbf{x}(t-h) - N_{dII,u}\mathbf{u}(t-h) - M_{dII}i(t-h) - K_{dII}$$

Pseudo measurement models are not directly measured but are quantities for which we know their approximate values. For example, the voltage at a neutral is around zero during normal operations. This voltage can be introduced as a pseudo measurement. Since we do not know the exact value of pseudo measurements, a relatively higher measurement error compared to the actual measurement model is introduced. Pseudo measurement models are also expressed in terms of variables at network level as listed in (2.4.5), where subscript *p* denotes pseudo measurement.

$$z_p(t) = Y_{p,x}\mathbf{x} + Y_{p,u}\mathbf{u} + \left\{\begin{array}{c}\vdots\\ \mathbf{x}^T F^i_{p,x}\mathbf{x}\\ \vdots\end{array}\right\} + \left\{\begin{array}{c}\vdots\\ \mathbf{u}^T F^i_{p,u}\mathbf{u}\\ \vdots\end{array}\right\} + \left\{\begin{array}{c}\vdots\\ \mathbf{u}^T F^i_{p,ux}\mathbf{x}\\ \vdots\end{array}\right\} - B_p + \eta \qquad (2.4.5)$$
$$B_p = -N_{p,x}\mathbf{x}(t-h) - N_{p,u}\mathbf{u}(t-h) - M_p i(t-h) + K_p$$

Virtual measurement models are provided by the network internal equations reflecting the physical property (e.g., KCL, etc.) of the network. These are directly obtained from the equations with zero value on the left-hand side in the network-level SCAQCF model with a relatively small measurement error compared to actual measurement models as shown in (2.4.6), where subscript *v* refers to virtual measurement model.

$$0 = Y_{v,x}\mathbf{x} + Y_{v,u}\mathbf{u} + \left\{\begin{array}{c}\vdots\\ \mathbf{x}^T F^i_{v,x}\mathbf{x}\\ \vdots\end{array}\right\} + \left\{\begin{array}{c}\vdots\\ \mathbf{u}^T F^i_{v,u}\mathbf{u}\\ \vdots\end{array}\right\} + \left\{\begin{array}{c}\vdots\\ \mathbf{u}^T F^i_{v,ux}\mathbf{x}\\ \vdots\end{array}\right\} + \eta \qquad (2.4.6)$$

By following all these three tasks and combining network-level actual, derived I and II, pseudo, and virtual measurement models, the final expression of the network measurement model with a similar syntax as the network SCAQCF model is obtained:

$$\mathbf{z}(t) = h(\mathbf{x}) + \boldsymbol{\eta} = Y_{zx}\mathbf{x} + Y_{zu}\mathbf{u} + \left\{\begin{array}{c}\vdots\\ \mathbf{x}^T F^i_{zx}\mathbf{x}\\ \vdots\end{array}\right\} + \left\{\begin{array}{c}\vdots\\ \mathbf{u}^T F^i_{zu}\mathbf{u}\\ \vdots\end{array}\right\} + \left\{\begin{array}{c}\vdots\\ \mathbf{u}^T F^i_{zux}\mathbf{x}\\ \vdots\end{array}\right\} - B_z + \boldsymbol{\eta} \qquad (2.4.7)$$
$$B_z = -N_{zx}\mathbf{x}(t-h) - N_{zu}\mathbf{u}(t-h) - M_z i(t-h) - K_z$$

2.3.2.3. Quasi-Dynamic State Estimation Algorithm

The quasi-dynamic state estimation algorithm is applied on the formulated network measurement model and provides the best estimate of the network model at each time step by applying weighted least square method. The optimization problem is expressed to minimize the sum of the residual squares between measurements and estimated measurements as follows:

$$Minimize \quad J = \left(h(\mathbf{x},\mathbf{u}) - \mathbf{z}\right)^T W \left(h(\mathbf{x},\mathbf{u}) - \mathbf{z}\right) \tag{2.4.8}$$

where W is the weight matrix with the weights defined as the inverse of the squared standard deviation δ_i for each measurement: $W = diag\left\{1/\delta_1^2, 1/\delta_2^2, ..., 1/\delta_n^2\right\}$.

Then we substitute the control vector $\mathbf{u}$ in $h(\mathbf{x},\mathbf{u})$ with actual values from the control center, yielding $h(\mathbf{x})$. The unknown state vector $\mathbf{x}$ is obtained by the optimal condition:

$$dJ/d\mathbf{x} = 0 \tag{2.4.9}$$

To obtain the solution of the nonlinear optimization problem above, we linearize the nonlinear equations by assuming an initial guess $\mathbf{x}^n$, and the residual between the measurements and the linearized measurement model is:

$$\mathbf{r} = h\left(\mathbf{x}^n\right) + H\left(\mathbf{x}^n\right)\left(\mathbf{x} - \mathbf{x}^n\right) - \mathbf{z} = H\left(\mathbf{x}^n\right)\mathbf{x} - \mathbf{z}' \tag{2.4.10}$$

where $\mathbf{z}' = -h\left(\mathbf{x}^n\right) + H\left(\mathbf{x}^n\right)\mathbf{x}^n + \mathbf{z}$, $H\left(\mathbf{x}^n\right)$ is the Jacobian matrix of $h(\mathbf{x})$ at $\mathbf{x}^n$, and it is denoted as H for simplicity in the following paragraphs.

Now the objective function is in a linear form:

$$Minimize \quad J = \left(H\mathbf{x} - \mathbf{z}'\right)^T W \left(H\mathbf{x} - \mathbf{z}'\right) \tag{2.4.11}$$

where the optimal solution is obtained when $dJ/d\mathbf{x} = 0$. Therefore, the solution is achieved by the iterative equation:

$$\mathbf{x}^{n+1} = (H^T W H)^{-1} H^T W \mathbf{z}' = \mathbf{x}^n - (H^T W H)^{-1} H^T W (\mathbf{h}\left(\mathbf{x}^n\right) - \mathbf{z}) \tag{2.4.12}$$

Notice that the algorithm performs state estimation using two consecutive measurements (time t and tm). In addition, the past history terms $\mathbf{x}(t\text{-}h)$ and i(t-h) are updated by $\mathbf{x}(t)$ and i(t) at each time step.

After the solution is obtained, the chi-square test is performed immediately. The chi-square test is a mathematical method to check the consistency between the measurements and the network model.

The procedure is as follows. First, the chi-square is computed, then the confidence level is obtained as shown in (2.4.13).

$$\xi = \sum_i \left(h_i(\mathbf{x}) - z_i / \delta_i \right)^2 \qquad \mathrm{P} = 1 - \Pr(\xi, \nu) \tag{2.4.13}$$

where ξ is the chi-square, ν is the degree of freedom (the difference between the number of measurements and states), Pr() is the probability function, P is the confidence level evaluating the consistency between the measurements and the system model. A high value (e.g., 100%) indicates the measurements matching the system model, and the estimated states and measurements are trustworthy. A low value (e.g., 0%) implies the occurrence of some bad data or hidden failures in the system.

2.3.2.4. Demonstration Case – State Estimation on PNM Feeder Model

As shown in Figure 2-13, the state estimator separates the feeder model into two sections. Each section has several IEDs that collect voltage and current measurements from the devices in this section. To be more specific, section 1 has 7 IEDs, and section 2 has 10 IEDs. The total number of phasor measurement is 90. Each measurement channel is defined by IED's instrumentation channel in detail. The installed IEDs and their measurements in section 1 and 2 are listed in Table 2-8 and Table 2-9, respectively. A local state estimator is installed in each section. The local state estimator automatically collects the measurement information (measurement definition) and measurement data in this section, then performs quasi-dynamic state estimation for this section. Meanwhile, a master state estimator collects the data from the local state estimators and synthesizes the states and the validated model for the whole feeder.

For this demonstration case, we use WinIGS to define events, simulate events, and store the results in COMTRADE format. The sampling rate was 60 samples per second, and the simulation was executed for a period of 1 minute. Since the generated data was very large, we present the data obtained from some specific IEDs as shown in Figure 2-14 and Figure 2-15. Figure 2-14 presents the three-phase voltage and current phasor measurements from IED 2 on bus 11 (IED2_B11) and IED 3 on bus 5 (IED3_B05) from section 1. Figure 2-15 presents the three-phase voltage and current phasor measurements from IED9_B14 and IED14_B12. Notice that since no dynamics exist in the system, the system is in steady state. Therefore, the measurements obtained from IEDs keep constant during the whole event.

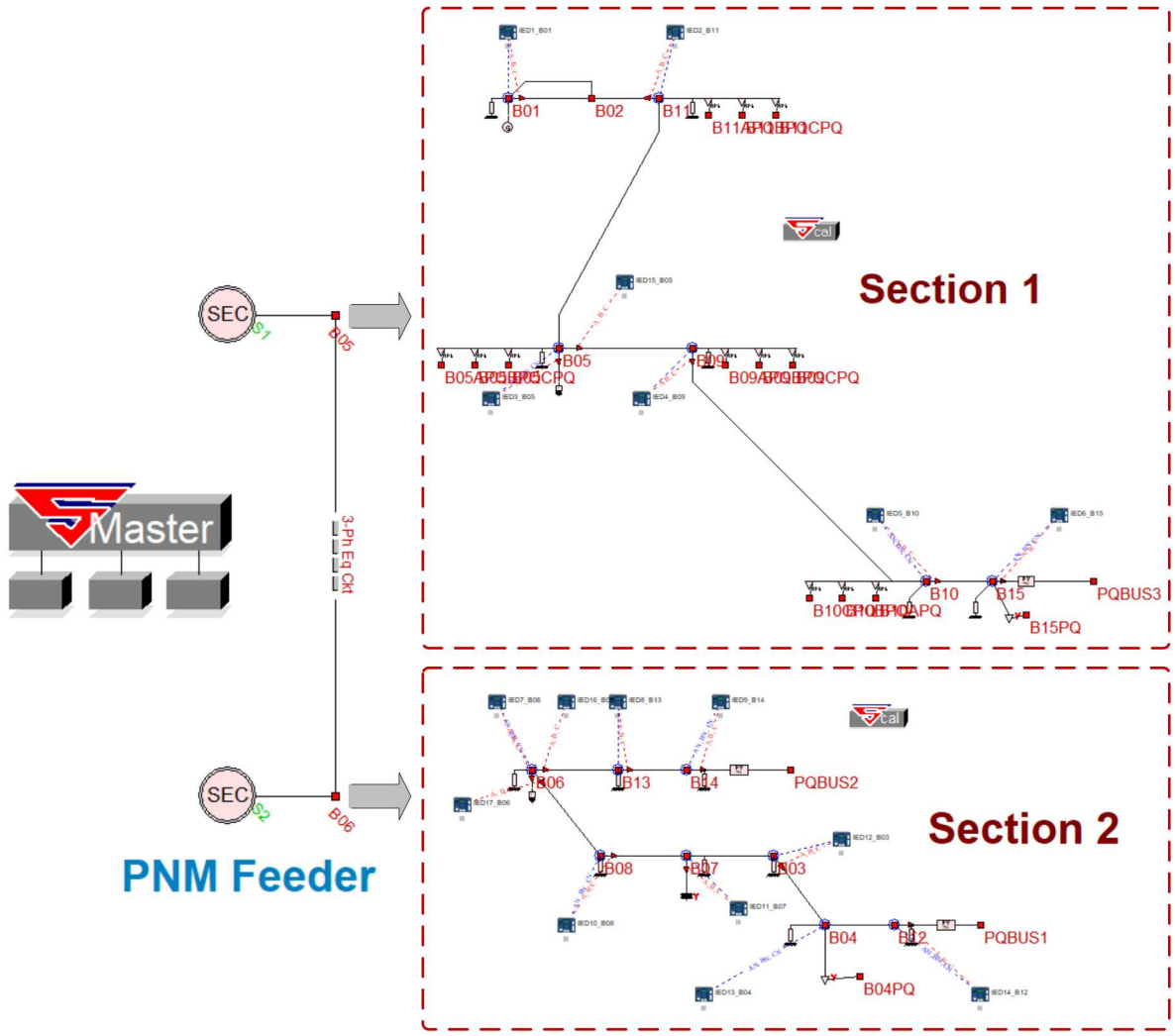

Figure 2-13. Single-Line Diagram with IEDs and State Estimators of PNM Feeder Model.

Table 2-8. Measurements of IEDs in Section 1.

IED Name	Voltage Measurements	Current Measurements	# of Measurements
IED1_B01	AN, BN, CN at B01	A, B, C at B01, from B01 to B02 (Tran1)	6
IED2_B11	AN, BN, CN at B11	A, B, C at B11, from B11 to B02 (Line149)	6
IED3_B05	AN, BN, CN at B05	A, B, C at B05, from B05 to B06 (Line59)	6
IED4_B09	AN, BN, CN at B09	A, B, C at B09, from B09 to B10 (Line105)	6
IED5_B10	AN, BN, CN at B10	A, B, C at B10, from B10 to B15 (Tran20)	6
IED6_B15	AN, BN, CN at B15	A, B, C at B15, into the PV Source (PVSy3)	6
IED15_B05		A, B, C at B05, from B05 to B09 (Line135)	3

Table 2-9. Measurement of IEDs in Section 2.

IED Name	Voltage Measurements	Current Measurements	# of Measurements
IED7_B06	AN, BN, CN at B06	A, B, C at B06, from B06 to B05 (Line59)	6
IED8_B13	AN, BN, CN at B13	A, B, C at B13, from B13 to B14 (Line196)	6
IED9_B14	AN, BN, CN at B14	A, B, C at B14, into the PV Source (PVSy2)	6
IED10_B08	AN, BN, CN at B08	A, B, C at B08, from B08 to B07 (Line97)	6
IED11_B07	AN, BN, CN at B07	A, B, C at B07, into the capacitor bank (Capa1)	6
IED12_B03	AN, BN, CN at B03	A, B, C at B03, from B03 to B04 (Line4)	6
IED13_B04	AN, BN, CN at B04		3
IED14_B12	AN, BN, CN at B12	A, B, C at B12, into the PV Source (PVSy1)	6
IED16_B06		A, B, C at B06, from B06 to B13 (Line167)	3
IED17_B06		A, B, C at B06, from B06 to B08 (Line188)	3

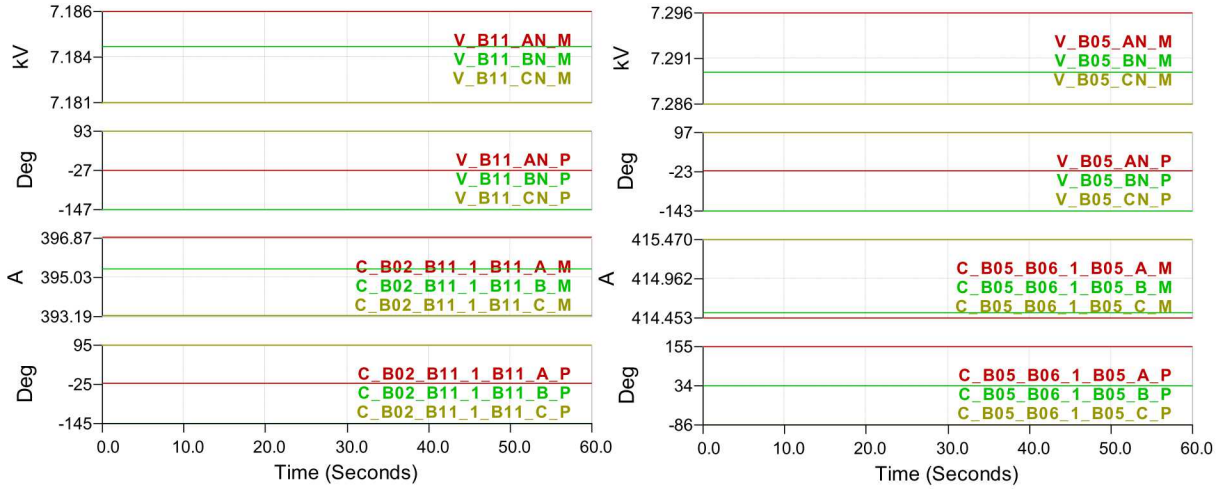

Figure 2-14. Measurements from IED2_B11 and IED3_B05.

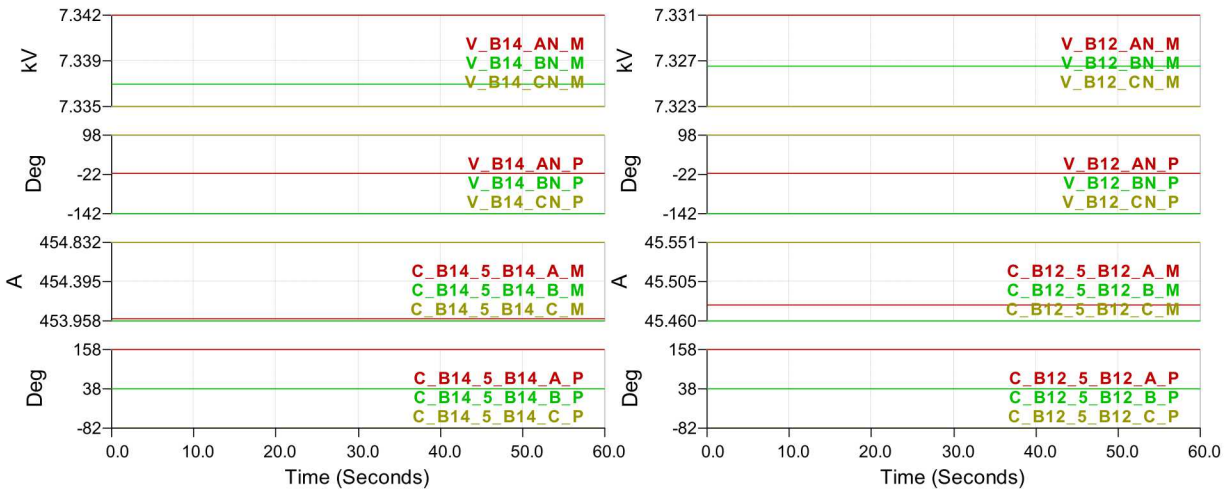

Figure 2-15. Measurements from IED9_B14 and IED14_B12.

Each local state estimator performs quasi-dynamic state estimation for this local section independently. In section 1, we have 18 voltage phasor measurements and 21 current phasor measurements collected from IEDs. Since the state estimator divides each phasor measurement into real and imaginary parts, we have 78 actual measurements in total. Furthermore, the state estimator automatically creates type I derived, type II derived, pseudo, and virtual measurements: 1) 120 type I derived measurements, 2) 30 type II derived measurements, 3) 42 virtual measurements, and 4) 14 pseudo measurements. In summary, we have 284 measurements at time *t*. Since section 1 consists of 114 states at time *t*, the redundancy is 284/114 = 249.12%.

The local state estimator at section 1 uses section-wise measurements to estimate the states of the whole section. Since the generated data are very large in size, we depict the state estimation results by some specific data. Figure 2-16 depicts the estimated states (voltage at each bus and internal states of devices) of this section. Figure 2-17 snapshots the actual and estimated measurements and the differences of all the actual measurements (voltage and current phasor measurements from IEDs) in section 1. Notice that all the errors are small. Figure 2-18 shows the performance evaluation (confidence level) of section 1 at one time stamp. As shown in Figure 2-18, the confidence level is 100% when k equals to 1. As a matter of fact, the confidence level of the whole section remains at 100% during the event, which indicates a strong consistency between the measurements and the system model, i.e., the estimated states of this section are trustworthy, and the system model of this section is validated.

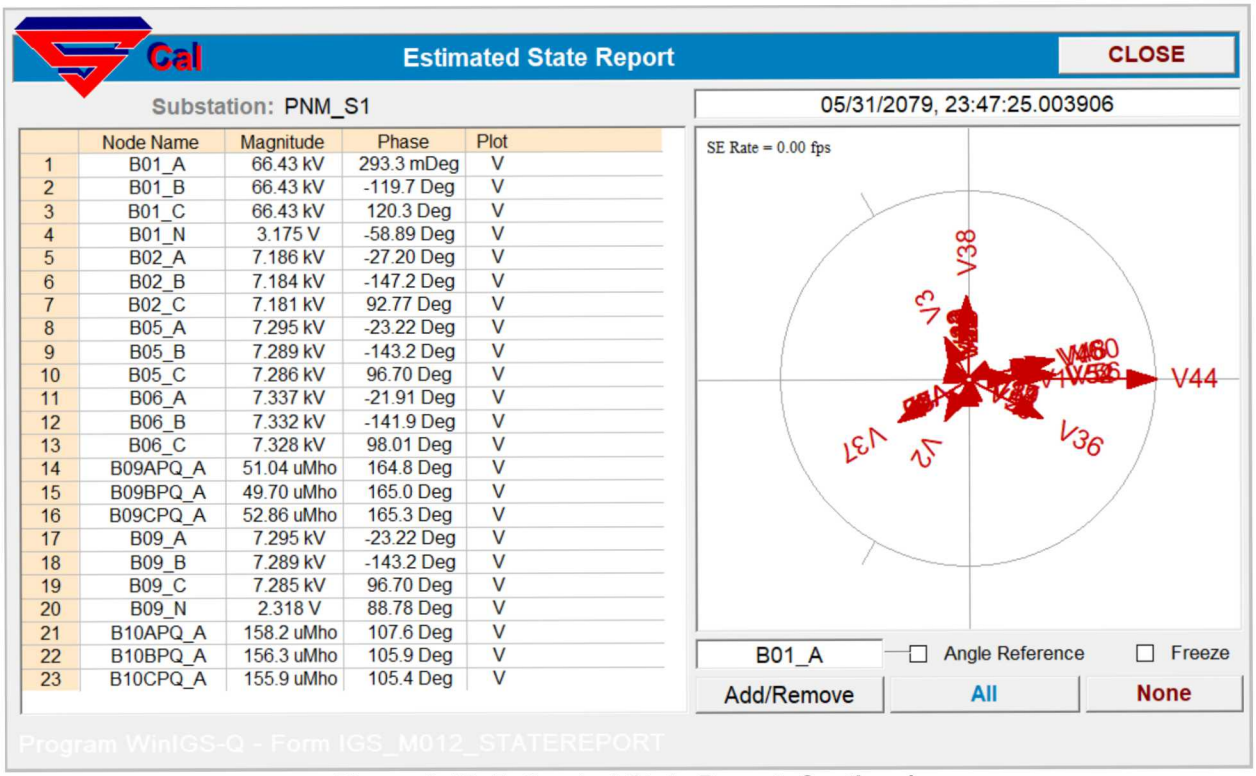

	Node Name	Magnitude	Phase	Plot
1	B01_A	66.43 kV	293.3 mDeg	V
2	B01_B	66.43 kV	-119.7 Deg	V
3	B01_C	66.43 kV	120.3 Deg	V
4	B01_N	3.175 V	-58.89 Deg	V
5	B02_A	7.186 kV	-27.20 Deg	V
6	B02_B	7.184 kV	-147.2 Deg	V
7	B02_C	7.181 kV	92.77 Deg	V
8	B05_A	7.295 kV	-23.22 Deg	V
9	B05_B	7.289 kV	-143.2 Deg	V
10	B05_C	7.286 kV	96.70 Deg	V
11	B06_A	7.337 kV	-21.91 Deg	V
12	B06_B	7.332 kV	-141.9 Deg	V
13	B06_C	7.328 kV	98.01 Deg	V
14	B09APQ_A	51.04 uMho	164.8 Deg	V
15	B09BPQ_A	49.70 uMho	165.0 Deg	V
16	B09CPQ_A	52.86 uMho	165.3 Deg	V
17	B09_A	7.295 kV	-23.22 Deg	V
18	B09_B	7.289 kV	-143.2 Deg	V
19	B09_C	7.285 kV	96.70 Deg	V
20	B09_N	2.318 V	88.78 Deg	V
21	B10APQ_A	158.2 uMho	107.6 Deg	V
22	B10BPQ_A	156.3 uMho	105.9 Deg	V
23	B10CPQ_A	155.9 uMho	105.4 Deg	V

Figure 2-16. Estimated State Report, Section 1.

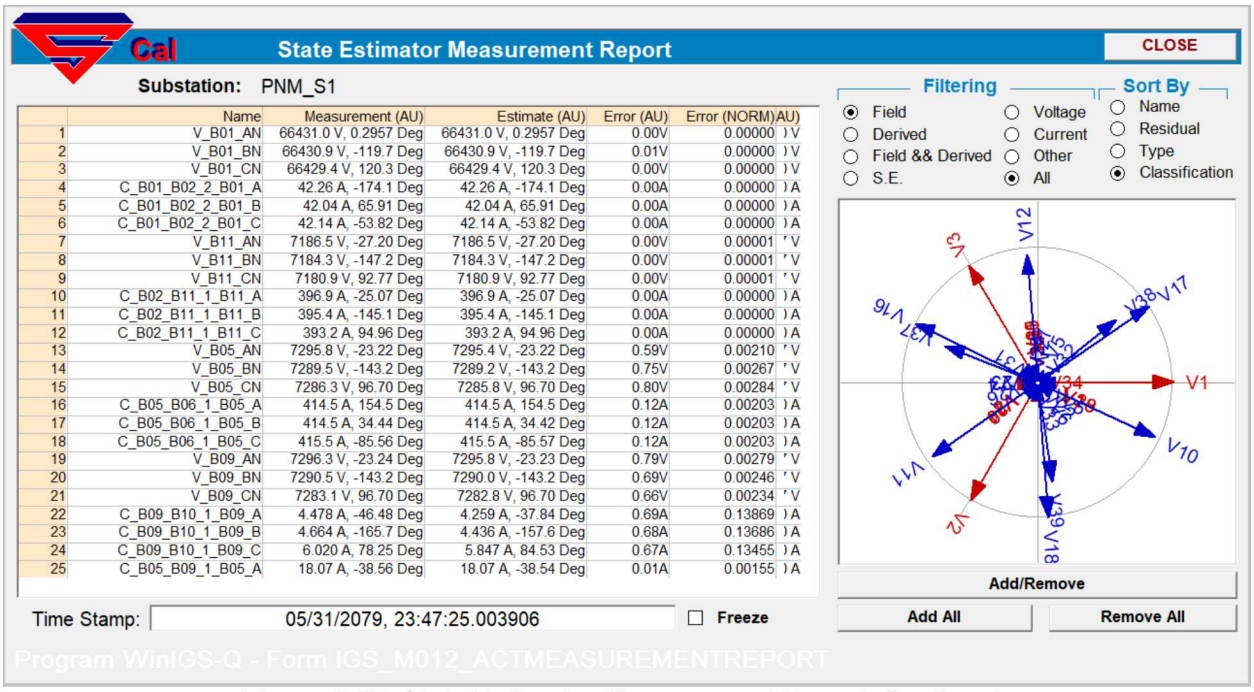

	Name	Measurement (AU)	Estimate (AU)	Error (AU)	Error (NORM)AU)
1	V_B01_AN	66431.0 V, 0.2957 Deg	66431.0 V, 0.2957 Deg	0.00V	0.00000) V
2	V_B01_BN	66430.9 V, -119.7 Deg	66430.9 V, -119.7 Deg	0.01V	0.00000) V
3	V_B01_CN	66429.4 V, 120.3 Deg	66429.4 V, 120.3 Deg	0.00V	0.00000) V
4	C_B01_B02_2_B01_A	42.26 A, -174.1 Deg	42.26 A, -174.1 Deg	0.00A	0.00000) A
5	C_B01_B02_2_B01_B	42.04 A, 65.91 Deg	42.04 A, 65.91 Deg	0.00A	0.00000) A
6	C_B01_B02_2_B01_C	42.14 A, -53.82 Deg	42.14 A, -53.82 Deg	0.00A	0.00000) A
7	V_B11_AN	7186.5 V, -27.20 Deg	7186.5 V, -27.20 Deg	0.00V	0.00001) V
8	V_B11_BN	7184.3 V, -147.2 Deg	7184.3 V, -147.2 Deg	0.00V	0.00001) V
9	V_B11_CN	7180.9 V, 92.77 Deg	7180.9 V, 92.77 Deg	0.00V	0.00001) V
10	C_B02_B11_1_B11_A	396.9 A, -25.07 Deg	396.9 A, -25.07 Deg	0.00A	0.00000) A
11	C_B02_B11_1_B11_B	395.4 A, -145.1 Deg	395.4 A, -145.1 Deg	0.00A	0.00000) A
12	C_B02_B11_1_B11_C	393.2 A, 94.96 Deg	393.2 A, 94.96 Deg	0.00A	0.00000) A
13	V_B05_AN	7295.8 V, -23.22 Deg	7295.4 V, -23.22 Deg	0.59V	0.00210) V
14	V_B05_BN	7289.5 V, -143.2 Deg	7289.2 V, -143.2 Deg	0.75V	0.00267) V
15	V_B05_CN	7286.3 V, 96.70 Deg	7285.8 V, 96.70 Deg	0.80V	0.00284) V
16	C_B05_B06_1_B05_A	414.5 A, 154.5 Deg	414.5 A, 154.5 Deg	0.12A	0.00203) A
17	C_B05_B06_1_B05_B	414.5 A, 34.44 Deg	414.5 A, 34.42 Deg	0.12A	0.00203) A
18	C_B05_B06_1_B05_C	415.5 A, -85.56 Deg	415.5 A, -85.57 Deg	0.12A	0.00203) A
19	V_B09_AN	7296.3 V, -23.24 Deg	7295.8 V, -23.23 Deg	0.79V	0.00279) V
20	V_B09_BN	7290.5 V, -143.2 Deg	7290.0 V, -143.2 Deg	0.69V	0.00246) V
21	V_B09_CN	7283.1 V, 96.70 Deg	7282.8 V, 96.70 Deg	0.66V	0.00234) V
22	C_B09_B10_1_B09_A	4.478 A, -46.48 Deg	4.259 A, -37.84 Deg	0.69A	0.13869) A
23	C_B09_B10_1_B09_B	4.664 A, -165.7 Deg	4.436 A, -157.6 Deg	0.68A	0.13686) A
24	C_B09_B10_1_B09_C	6.020 A, 78.25 Deg	5.847 A, 84.53 Deg	0.67A	0.13455) A
25	C_B05_B09_1_B05_A	18.07 A, -38.56 Deg	18.07 A, -38.54 Deg	0.01A	0.00155) A

Figure 2-17. State Estimator Measurement Report, Section 1.

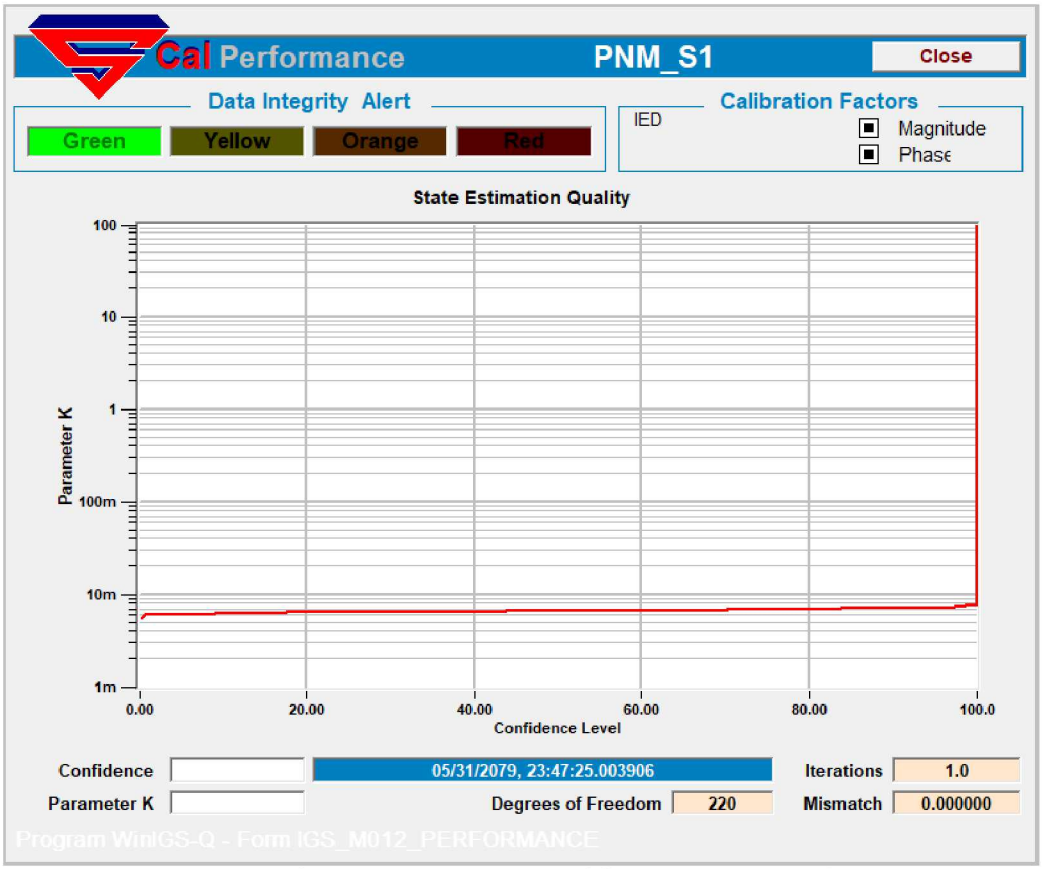

Figure 2-18. Performance Evaluation of State Estimation, Section 1.

In section 2, IEDs collect 24 voltage phasor measurements and 27 current phasor measurements. Since the state estimator divides each phasor measurement into real and imaginary parts, we have 102 actual measurements in total. Furthermore, the state estimator automatically creates type I derived, type II derived, pseudo, and virtual measurements: 1) 66 type I derived measurements, 2) 14 type II derived measurements, 3) 20 virtual measurements, and 4) 16 pseudo measurements. In summary, we have 218 measurements at time *t*. Since section 2 consists of 88 states at time *t*, the redundancy is 218/88 = 247.73%.

The local state estimator at section 2 uses section-wise measurements to estimate the states of the whole section. Since the generated data are very large in size, we depict the state estimation results by some specific data. Figure 2-19 depicts the estimated states (voltage at each bus and internal states of devices) of this section. Figure 2-20 snapshots the actual and estimated measurements and the differences of all the actual measurements (voltage and current phasor measurements from IEDs) in section 2. Figure 2-21 shows the performance evaluation (confidence level) of section 2 at one time stamp. As shown in Figure 2-21, the confidence level is 100% when k equals to 1. As a matter of fact, the confidence level of the whole section remains at 100% during the event, which indicates a strong consistency between the measurements and the system model, i.e., the estimated states of this section are trustworthy, and the system model of this section is validated.

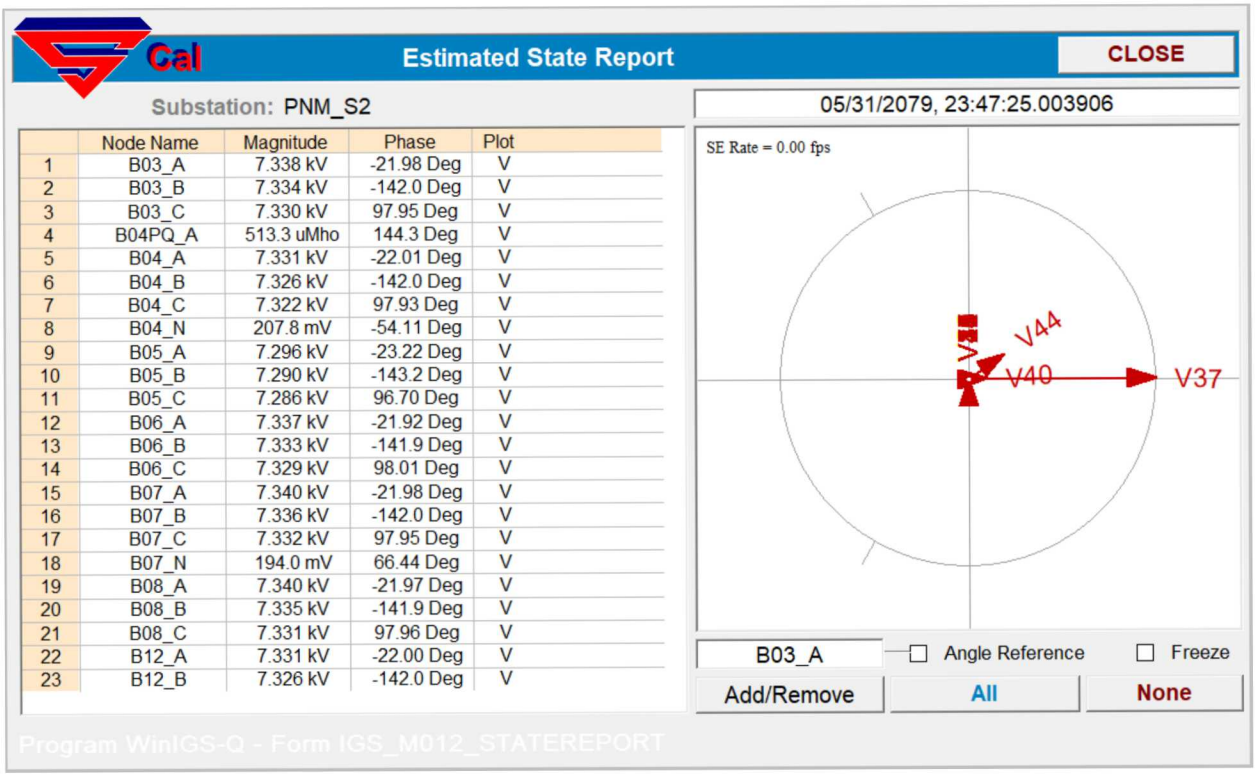

	Node Name	Magnitude	Phase	Plot
1	B03_A	7.338 kV	-21.98 Deg	V
2	B03_B	7.334 kV	-142.0 Deg	V
3	B03_C	7.330 kV	97.95 Deg	V
4	B04PQ_A	513.3 uMho	144.3 Deg	V
5	B04_A	7.331 kV	-22.01 Deg	V
6	B04_B	7.326 kV	-142.0 Deg	V
7	B04_C	7.322 kV	97.93 Deg	V
8	B04_N	207.8 mV	-54.11 Deg	V
9	B05_A	7.296 kV	-23.22 Deg	V
10	B05_B	7.290 kV	-143.2 Deg	V
11	B05_C	7.286 kV	96.70 Deg	V
12	B06_A	7.337 kV	-21.92 Deg	V
13	B06_B	7.333 kV	-141.9 Deg	V
14	B06_C	7.329 kV	98.01 Deg	V
15	B07_A	7.340 kV	-21.98 Deg	V
16	B07_B	7.336 kV	-142.0 Deg	V
17	B07_C	7.332 kV	97.95 Deg	V
18	B07_N	194.0 mV	66.44 Deg	V
19	B08_A	7.340 kV	-21.97 Deg	V
20	B08_B	7.335 kV	-141.9 Deg	V
21	B08_C	7.331 kV	97.96 Deg	V
22	B12_A	7.331 kV	-22.00 Deg	V
23	B12_B	7.326 kV	-142.0 Deg	V

Figure 2-19. Estimated State Report, Section 2.

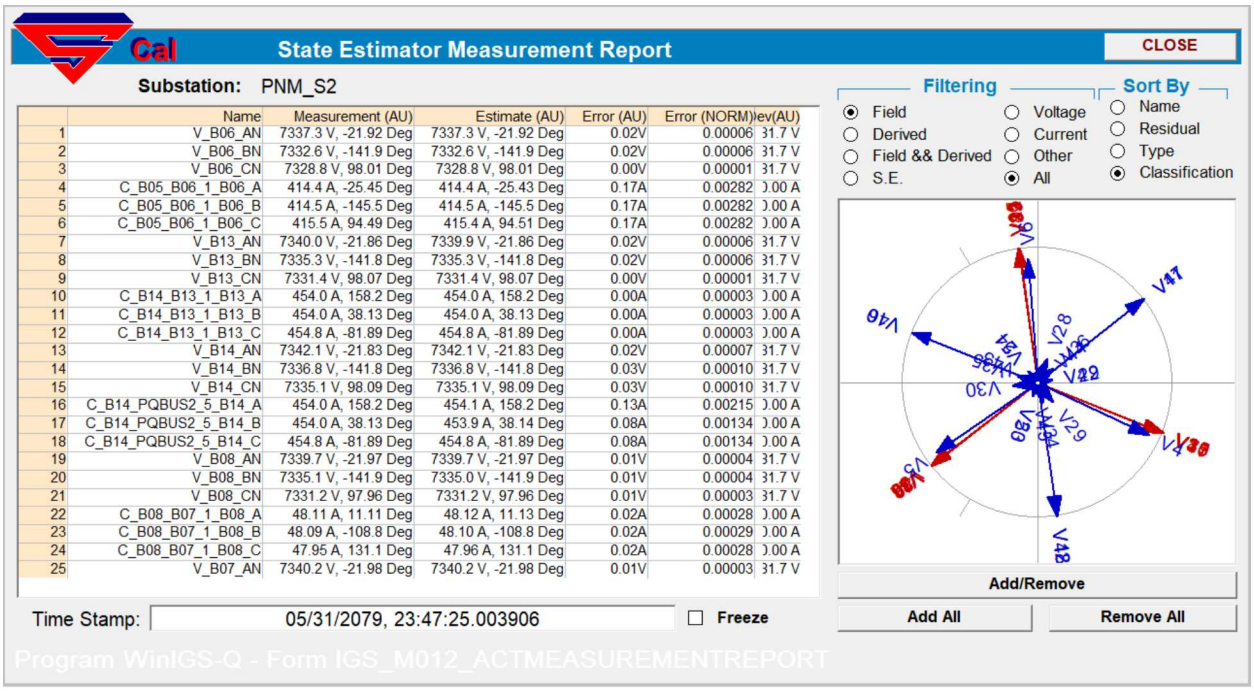

	Name	Measurement (AU)	Estimate (AU)	Error (AU)	Error (NORM)	lev(AU)
1	V_B06_AN	7337.3 V, -21.92 Deg	7337.3 V, -21.92 Deg	0.02V	0.00006	31.7 V
2	V_B06_BN	7332.6 V, -141.9 Deg	7332.6 V, -141.9 Deg	0.02V	0.00006	31.7 V
3	V_B06_CN	7328.8 V, 98.01 Deg	7328.8 V, 98.01 Deg	0.00V	0.00001	31.7 V
4	C_B05_B06_1_B06_A	414.4 A, -25.45 Deg	414.4 A, -25.43 Deg	0.17A	0.00282	0.00 A
5	C_B05_B06_1_B06_B	414.5 A, -145.5 Deg	414.5 A, -145.5 Deg	0.17A	0.00282	0.00 A
6	C_B05_B06_1_B06_C	415.5 A, 94.49 Deg	415.4 A, 94.51 Deg	0.17A	0.00282	0.00 A
7	V_B13_AN	7340.0 V, -21.86 Deg	7339.9 V, -21.86 Deg	0.02V	0.00006	31.7 V
8	V_B13_BN	7335.3 V, -141.8 Deg	7335.3 V, -141.8 Deg	0.02V	0.00006	31.7 V
9	V_B13_CN	7331.4 V, 98.07 Deg	7331.4 V, 98.07 Deg	0.00V	0.00001	31.7 V
10	C_B14_B13_1_B13_A	454.0 A, 158.2 Deg	454.0 A, 158.2 Deg	0.00A	0.00003	0.00 A
11	C_B14_B13_1_B13_B	454.0 A, 38.13 Deg	454.0 A, 38.13 Deg	0.00A	0.00003	0.00 A
12	C_B14_B13_1_B13_C	454.8 A, -81.89 Deg	454.8 A, -81.89 Deg	0.00A	0.00003	0.00 A
13	V_B14_AN	7342.1 V, -21.83 Deg	7342.1 V, -21.83 Deg	0.02V	0.00007	31.7 V
14	V_B14_BN	7336.8 V, -141.8 Deg	7336.8 V, -141.8 Deg	0.03V	0.00010	31.7 V
15	V_B14_CN	7335.1 V, 98.09 Deg	7335.1 V, 98.09 Deg	0.03V	0.00010	31.7 V
16	C_B14_PQBUS2_5_B14_A	454.0 A, 158.2 Deg	454.1 A, 158.2 Deg	0.13A	0.00215	0.00 A
17	C_B14_PQBUS2_5_B14_B	454.0 A, 38.13 Deg	453.9 A, 38.14 Deg	0.08A	0.00134	0.00 A
18	C_B14_PQBUS2_5_B14_C	454.8 A, -81.89 Deg	454.8 A, -81.89 Deg	0.08A	0.00134	0.00 A
19	V_B08_AN	7339.7 V, -21.97 Deg	7339.7 V, -21.97 Deg	0.01V	0.00004	31.7 V
20	V_B08_BN	7335.1 V, -141.9 Deg	7335.0 V, -141.9 Deg	0.01V	0.00004	31.7 V
21	V_B08_CN	7331.2 V, 97.96 Deg	7331.2 V, 97.96 Deg	0.01V	0.00003	31.7 V
22	C_B08_B07_1_B08_A	48.11 A, 11.11 Deg	48.12 A, 11.13 Deg	0.02A	0.00028	0.00 A
23	C_B08_B07_1_B08_B	48.09 A, -108.8 Deg	48.10 A, -108.8 Deg	0.02A	0.00029	0.00 A
24	C_B08_B07_1_B08_C	47.95 A, 131.1 Deg	47.96 A, 131.1 Deg	0.02A	0.00028	0.00 A
25	V_B07_AN	7340.2 V, -21.98 Deg	7340.2 V, -21.98 Deg	0.01V	0.00003	31.7 V

Figure 2-20. State Estimator Measurement Report, Section 2.

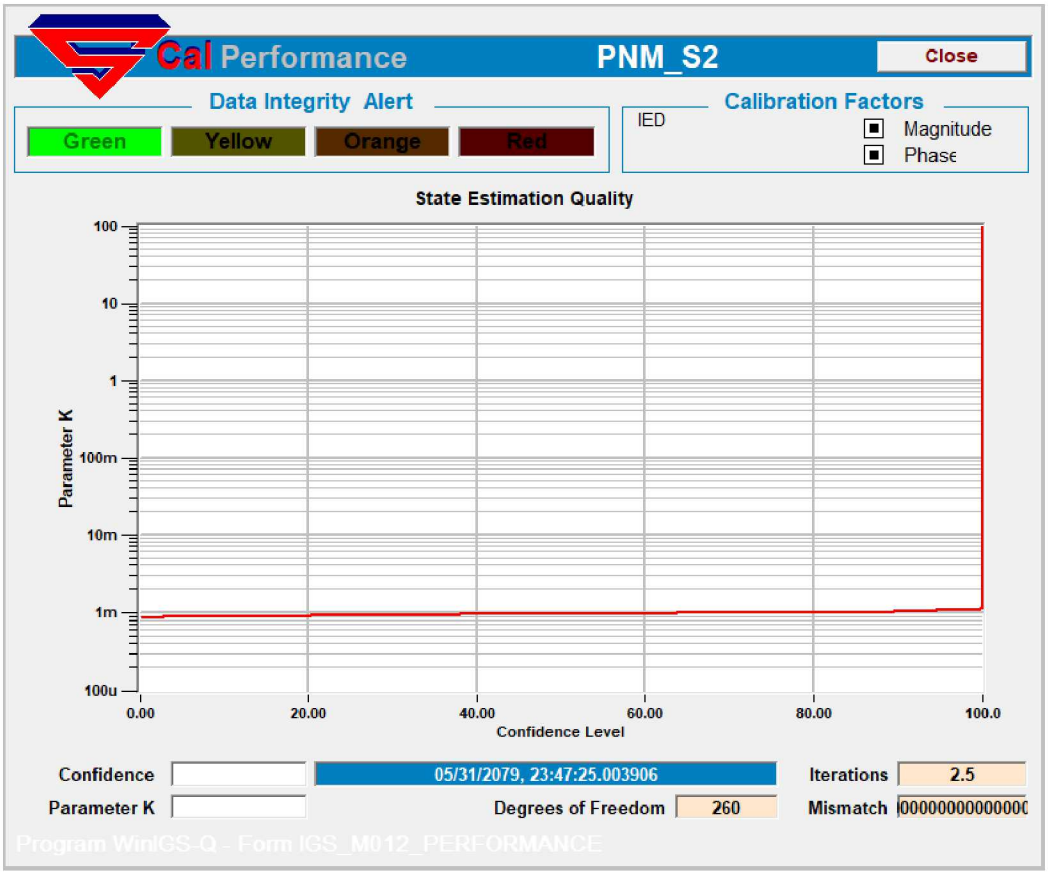

Figure 2-21. Performance Evaluation of State Estimation, Section 2.

2.3.2.5. State Estimation Sensitivity Assessment

For this analysis the accuracy of the state estimator is given by the maximum error of all state estimates relative to measurements that are assumed to be correct. In practice, field measurements could be taken from the feeder and passed to the state estimator to generate state estimates, however, the field measurements were not available for this analysis. The procedure for evaluating the accuracy of the state estimator involves performing a quasi-static time series simulation of the OpenDSS model of the PNM feeder, creating COMTRADE files from the measurements recorded in OpenDSS, using the COMTRADE files to generate state estimates of the PNM feeder, and comparing the state estimates to measurements from the OpenDSS model. EPRI received both the OpenDSS model and WinIGS model of the PNM feeder from the team at Georgia Tech, and did not alter topology or circuit characteristics of either model. Monitor objects were added to the OpenDSS model to record the required measurement values to be used in the state estimator. EPRI also created time-varying load and PV profiles that were used in some tests, however, the underlying model of individual loads or distributed generation were not changed. It was assumed that all calibration and validation of the WinIGS model relative to the OpenDSS model was performed prior to transferring the models to EPRI.

The accuracy of the state estimate is both location and time dependent; the system state is comprised of many individual states from each location or node on the feeder, and it is possible that state estimates at some locations may be more accurate than others. Some initial tests also showed that the accuracy of each state estimate changes with time. The state estimate at each location was examined independently, and the maximum error among the individual estimates is used to describe the accuracy of the entire system state. In order to account for the time varying nature of the state estimates the error was calculated using both root mean square error (RMSE) and mean average error (MAE), given by the following equations:

$$RMSE = \sqrt{\frac{\sum_{i=1}^{N}(p_i - a_i)^2}{N}} \quad (2.5.2.5.1)$$

$$MAE = \frac{\sum_{i=1}^{N}|p_i - a_i|}{N} \quad (2.5.2.5.2)$$

where p_i is the estimate, a_i is the measurement, and N is the number of samples used in the calculation. Both RMSE and MAE report errors in the same units as the estimate and measurement. While it is useful to examine errors in terms of the measurement unit in some cases, electric power distribution systems operate at multiple voltage levels, and it is more useful to compare errors in per-unit values relative to the nominal voltage at the measurement location. In the unique case that the error between the estimate and the measurement does not change with time the RMSE is equal to the MAE. A difference between errors calculated with RMSE and MAE indicates that the error between the estimate and the measurement changes with time. Upon inspection of some test results, it was observed that the error between the estimate and the measurement is quite large when the state estimator starts, and that the error generally diminishes with time. Because of the large initial error produced by the state estimator, the first 50 state estimates were excluded from the error calculation. By excluding the first 50 estimates from the calculation the RMSE and MAE were equal for some locations, indicating that the startup inaccuracies were resolved at those locations.

Several simulations were performed to evaluate the accuracy of the state estimator. The first simulation compared the state estimates (produced from the test case that accompanied the WinIGS model) to

measurements from the OpenDSS model (produced from a simulation of the model without any modifications). The test case accompanying the WinIGS model contained one hour of measurement data at a one second resolution; it was decided to only use the first 300 seconds of data because the input data did not vary with time. The corresponding OpenDSS model was simulated for 300 time-steps at a resolution of one second. In this scenario, the test case used in the state estimator was not created by measurement values recorded from the OpenDSS simulation. Although it was assumed that the WinIGS model was validated against the OpenDSS model there is some small amount of disagreement between the two models. Because of the underlying validation error between the two models, it was expected to see some small amount of error between the state estimate and the measurement data. In this case the maximum RMSE was 0.0088 p.u. and the maximum MAE was 0.0069 p.u.; the maximum error for both calculations was recorded from the IED measuring phase A voltage magnitude at node 15. EPRI created another test case that used measurements from the OpenDSS model as the input to the state estimator. This test case was also 300 seconds of data in which the loads and generation remained constant throughout the entire simulation. It was hypothesized that using measurement data from the OpenDSS simulation as the input data for the state estimator would reduce the error over the simulation period. In this second test case the maximum RMSE was calculated to be 0.0089 pu and the maximum MAE was calculated to be 0.0070 p.u., again at the IED measuring phase A voltage magnitude at bus 15. The tabular results of these analyses is presented in Table 2-10.

Table 2-10: Maximum errors from non-time-varying simulation

Source of data	Max RMSE p.u.	Max MAE p.u.	Max RSME measurement	Max MAE measurement
WinIGS default values	0.0088	0.0069	V_B15_AN_M	V_B15_AN_M
OpenDSS simulated values	0.0089	0.0070	V_B15_AN_M	V_B15_AN_M

The state of an electric power distribution system changes with time, therefore, the state estimate of a system also changes with time. In order to capture the accuracy of the state estimate of a dynamic system it was required to simulate the time-varying condition of the PNM feeder. A load-shape was developed for both loads and PV systems contained within the OpenDSS model. One load-shape was applied to all loads uniformly, and, similarly, the one load-shape was applied to all PV systems uniformly. The two load-shapes were not based on field measurements of the actual PNM feeder and were not meant to be representative of the expected operating conditions, rather they were only intended to create a dynamic scenario with which to test the accuracy of the state estimator. It is important to note that an infinite number of load and generation conditions on the feeder are possible, and it would be impossible to test the accuracy of all conditions. The results of the analysis using the load shapes presented in Figure 2-22 show the accuracy of the state estimator only under the conditions simulated. Using the measurements from the time-varying simulation in OpenDSS as inputs to the state estimator, the maximum RMSE and MAE were calculated to be 0.0093 p.u. and 0.0073 p.u., respectively, both measured on the voltage magnitude of phase at bus 15. These results suggest that the accuracy of the state estimator decreases slightly under dynamic load and generation conditions. The tabular results from the time varying load and generation conditions are presented in Table 2-11.

Table 2-11: Maximum errors from time varying simulation

Source of data	Max RMSE p.u.	Max MAE p.u.	Max RSME measurement	Max MAE measurement
OpenDSS simulated values	0.0093	0.0073	V_B15_AN_M	V_B15_AN_M

The results from the first two test cases used the exact measurements from the OpenDSS model as the inputs to the state estimator, however, state estimation is intended to handle the case that there may be some error in the measurement values used to generate the state estimate. A sensitivity analysis was proposed to determine the accuracy of the state estimator when errors exist in the measurement data. For the sensitivity analysis an error was introduced at each IED independently; two multiplicative white noise signals were created using normal distributions with means of 1 and standard deviations of 0.005 and 0.01. For each IED, the same white noise signal was applied to all three voltage or current magnitudes as well as all three phase angle measurements. The IEDs that measure both voltage and current were treated as two separate IEDs to determine the effect of introducing error to both types of measurements independently. This this method is representative of an IED that has some inherent measurement error that cannot be attributed to calibration alone. The intent of this sensitivity analysis was to determine if certain measurements are more critical to the accuracy of the state estimator than others.

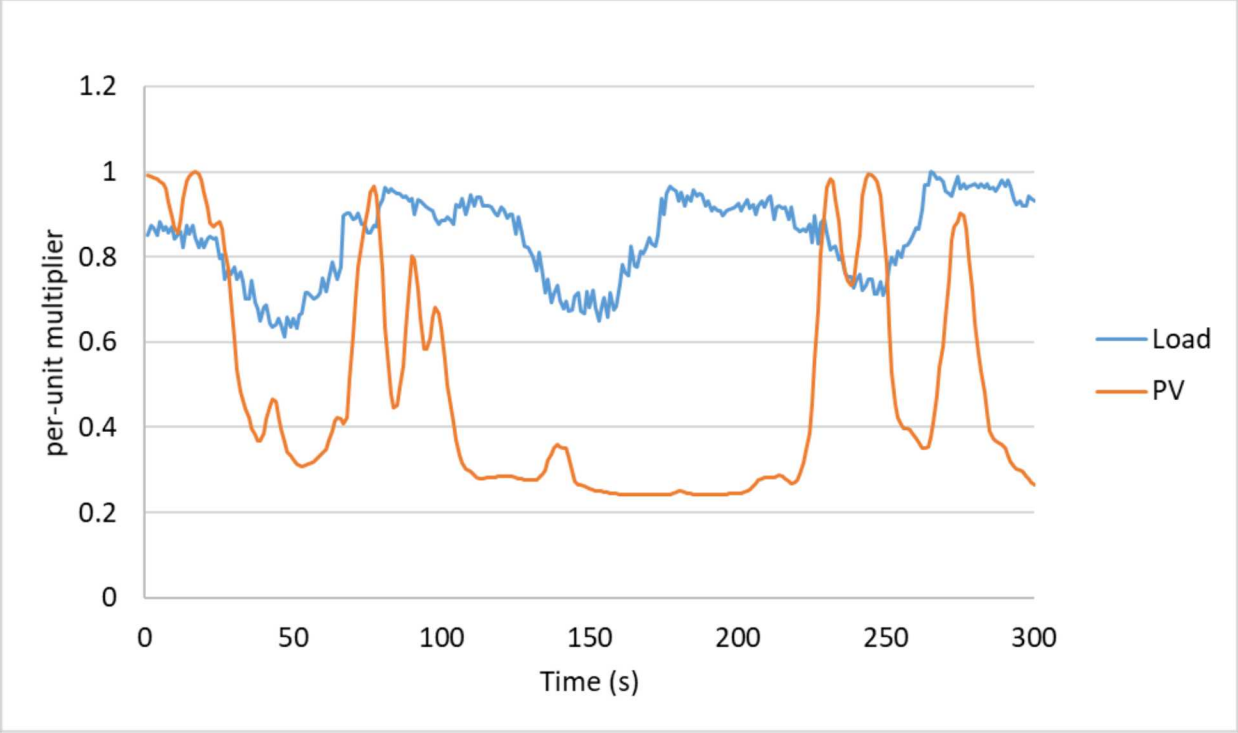

Figure 2-22. Load-Shapes used for state estimator evaluation.

For the case that a white noise with a standard deviation of 0.005 was applied to each IED independently there were nine instances that resulted in a slight increase to both the maximum RMSE and maximum MAE, five instances that resulted in a slight increase to the maximum MAE, two instances that resulted in a slight increase to the maximum RMSE, and one instance the resulted in the significant increase to both maximum RMSE and maximum MAE. Interestingly, the maximum

RMSE and maximum MAE for all cases was at bus 15 voltage magnitude. The maximum increase to RSME and MAE was measured on the phase A voltage magnitude of bus 15 when error was introduced to the voltage measurement on IED6_B15, which is located at bus 15. It is notable that the increase to the maximum RMSE for this instance is less than the standard deviation of the noise introduced to the measurement value. The tabular results from this case are shown in Table 2-12.

For the case that a white noise with a standard deviation of 0.01 was applied to each IED independently there were 12 instances that resulted in a slight increase to both the maximum RMSE and maximum MAE. There were an additional 13 instances that resulted in a significant increase to both the maximum RMSE and maximum MAE. Only four instances of introducing white noise did not affect the maximum RMSE or maximum MAE, and the introduction of white noise at one location resulted in a decrease of maximum RMSE and maximum MAE. By introducing white noise to the current measurement at IED12_B03 the maximum RMSE and maximum MAE were reduced to 0.0087 p.u. and 0.0069 p.u., both measured at bus 15 on the phase A voltage magnitude. It is notable that the increase to the maximum RMSE for this instance is less than the standard deviation of the noise introduced to the measurement value. These errors are similar to the static test case errors. The tabular results from this case are shown in Table 2-13.

Table 2-12. Maximum errors from the introduction of white noise with 0.005 standard deviation.

IED Name	Measurement	Max RMSE p.u.	Max MAE p.u.	Max RSME measurement	MaxMAE measurement
IED1_B01	**Voltage**	0.0093	0.0074	V_B15_AN_M	V_B15_AN_M
IED1_B01	**Current**	0.0093	0.0073	V_B15_AN_M	V_B15_AN_M
IED2_B11	**Voltage**	0.0093	0.0073	V_B15_AN_M	V_B15_AN_M
IED2_B11	**Current**	0.0093	0.0073	V_B15_AN_M	V_B15_AN_M
IED3_B05	**Voltage**	0.0093	0.0074	V_B15_AN_M	V_B15_AN_M
IED3_B05	**Current**	0.0093	0.0073	V_B15_AN_M	V_B15_AN_M
IED4_B09	**Voltage**	0.0094	0.0073	V_B15_AN_M	V_B15_AN_M
IED4_B09	**Current**	0.0093	0.0073	V_B15_AN_M	V_B15_AN_M
IED15_B05	**Current**	0.0093	0.0074	V_B15_AN_M	V_B15_AN_M
IED5_B10	**Voltage**	0.0095	0.0074	V_B15_AN_M	V_B15_AN_M
IED5_B10	**Current**	0.0094	0.0074	V_B15_AN_M	V_B15_AN_M
IED6_B15	**Voltage**	0.0110	0.0084	V_B15_AN_M	V_B15_AN_M
IED6_B15	**Current**	0.0094	0.0073	V_B15_AN_M	V_B15_AN_M
IED7_B06	**Voltage**	0.0094	0.0074	V_B15_AN_M	V_B15_AN_M
IED7_B06	**Current**	0.0094	0.0074	V_B15_AN_M	V_B15_AN_M
IED8_B13	**Voltage**	0.0094	0.0074	V_B15_AN_M	V_B15_AN_M
IED8_B13	**Current**	0.0094	0.0074	V_B15_AN_M	V_B15_AN_M
IED9_B14	**Voltage**	0.0094	0.0074	V_B15_AN_M	V_B15_AN_M

IED Name	Measurement	Max RMSE p.u.	Max MAE p.u.	Max RSME measurement	MaxMAE measurement
IED9_B14	**Current**	0.0094	0.0074	V_B15_AN_M	V_B15_AN_M
IED10_B08	**Voltage**	0.0094	0.0074	V_B15_AN_M	V_B15_AN_M
IED10_B08	**Current**	0.0093	0.0074	V_B15_AN_M	V_B15_AN_M
IED11_B07	**Voltage**	0.0093	0.0073	V_B15_AN_M	V_B15_AN_M
IED11_B07	**Current**	0.0093	0.0073	V_B15_AN_M	V_B15_AN_M
IED12_B03	**Voltage**	0.0093	0.0073	V_B15_AN_M	V_B15_AN_M
IED12_B03	**Current**	0.0093	0.0073	V_B15_AN_M	V_B15_AN_M
IED13_B04	**Voltage**	0.0093	0.0073	V_B15_AN_M	V_B15_AN_M
IED14_B12	**Voltage**	0.0093	0.0073	V_B15_AN_M	V_B15_AN_M
IED14_B12	**Current**	0.0093	0.0073	V_B15_AN_M	V_B15_AN_M
IED16_B06	**Current**	0.0093	0.0073	V_B15_AN_M	V_B15_AN_M
IED17_B06	**Current**	0.0093	0.0074	V_B15_AN_M	V_B15_AN_M

Table 2-13. Maximum errors from the introduction of white noise with 0.01 standard deviation.

IED Name	Measurement	Max RMSE p.u.	Max MAE p.u.	Max RSME measurement	Max MAE measurement
IED1_B01	**Voltage**	0.0093	0.0073	V_B15_AN_M	V_B15_AN_M
IED1_B01	**Current**	0.0093	0.0073	V_B15_AN_M	V_B15_AN_M
IED2_B11	**Voltage**	0.0126	0.0100	V_B11_AN_M	V_B11_AN_M
IED2_B11	**Current**	0.0097	0.0080	V_B15_BN_M	V_B15_BN_M
IED3_B05	**Voltage**	0.0098	0.0081	V_B10_AN_M	V_B10_AN_M
IED3_B05	**Current**	0.0097	0.0080	V_B15_BN_M	V_B15_BN_M
IED4_B09	**Voltage**	0.0098	0.0082	V_B15_BN_M	V_B15_BN_M
IED4_B09	**Current**	0.0097	0.0080	V_B15_BN_M	V_B15_BN_M
IED15_B05	**Current**	0.0097	0.0080	V_B15_BN_M	V_B15_BN_M
IED5_B10	**Voltage**	0.0099	0.0081	V_B15_BN_M	V_B15_BN_M
IED5_B10	**Current**	0.0093	0.0073	V_B15_AN_M	V_B15_AN_M
IED6_B15	**Voltage**	0.0104	0.0076	V_B15_AN_M	V_B15_AN_M
IED6_B15	**Current**	0.0144	0.0133	V_B15_AN_M	V_B15_AN_M
IED7_B06	**Voltage**	0.0168	0.0155	V_B15_AN_M	V_B15_AN_M
IED7_B06	**Current**	0.0142	0.0131	V_B15_AN_M	V_B15_AN_M
IED8_B13	**Voltage**	0.0142	0.0131	V_B15_AN_M	V_B15_AN_M

IED Name	Measurement	Max RMSE p.u.	Max MAE p.u.	Max RSME measurement	Max MAE measurement
IED8_B13	**Current**	0.0142	0.0131	V_B15_AN_M	V_B15_AN_M
IED9_B14	**Voltage**	0.0142	0.0131	V_B15_AN_M	V_B15_AN_M
IED9_B14	**Current**	0.0093	0.0073	V_B15_AN_M	V_B15_AN_M
IED10_B08	**Voltage**	0.0142	0.0131	V_B15_AN_M	V_B15_AN_M
IED10_B08	**Current**	0.0142	0.0131	V_B15_AN_M	V_B15_AN_M
IED11_B07	**Voltage**	0.0142	0.0131	V_B15_AN_M	V_B15_AN_M
IED11_B07	**Current**	0.0142	0.0131	V_B15_AN_M	V_B15_AN_M
IED12_B03	**Voltage**	0.0142	0.0131	V_B15_AN_M	V_B15_AN_M
IED12_B03	**Current**	0.0087	0.0069	V_B15_AN_M	V_B15_AN_M
IED13_B04	**Voltage**	0.0097	0.0081	V_B15_BN_M	V_B15_BN_M
IED14_B12	**Voltage**	0.0097	0.0081	V_B15_BN_M	V_B15_BN_M
IED14_B12	**Current**	0.0097	0.0081	V_B15_BN_M	V_B15_BN_M
IED16_B06	**Current**	0.0097	0.0081	V_B15_BN_M	V_B15_BN_M
IED17_B06	**Current**	0.0097	0.0081	V_B15_BN_M	V_B15_BN_M

The final sensitivity analysis performed on the distribution system state estimator involved introducing an error that is representative of a measurement device either not recording data or loosing communication with the state estimator. In this case, the data for a measurement—either voltage or current magnitudes and angles—at each IED was not updated for the entire simulation. The state estimator will not solve if a measurement value is not included in the input data, but not updating the measurement throughout the simulation could be representative of the case that the measurement device either fails to measure or fails to communicate. In this case there were three instances that resulted in a slight increase to the maximum MAE, one instance that resulted in a slight increase to both the maximum RMSE and maximum MAE, and one instance that resulted in a significant increase to both the maximum RMSE and maximum MAE. When the voltage measurement values at IED6_B15 were not updated the maximum RMSE and maximum MAE were 0.0142 p.u. and 0.0129 p.u., respectively, both measured at bus 15 on the phase A voltage magnitude. There was also one instance that resulted in a slight decrease of the maximum RMSE; when the current measurement at IED4_B09 was not updated the maximum RMSE was measured at 0.092 p.u. at bus 15 on the phase A voltage magnitude. The full tabular results from this sensitivity analysis are shown in Table 2-14.

Table 2-14. Maximum errors from fixed measurement values during simulation.

IED Name	Measurement	Max RMSE p.u.	Max MAE p.u.	Max RSME measurement	MaxMAE measurement
IED1_B01	**Voltage**	0.0093	0.0073	V_B15_AN_M	V_B15_AN_M
IED1_B01	**Current**	0.0093	0.0073	V_B15_AN_M	V_B15_AN_M
IED2_B11	**Voltage**	0.0093	0.0073	V_B15_AN_M	V_B15_AN_M

IED Name	Measurement	Max RMSE p.u.	Max MAE p.u.	Max RSME measurement	MaxMAE measurement
IED2_B11	**Current**	0.0093	0.0073	V_B15_AN_M	V_B15_AN_M
IED3_B05	**Voltage**	0.0093	0.0074	V_B15_AN_M	V_B15_AN_M
IED3_B05	**Current**	0.0093	0.0073	V_B15_AN_M	V_B15_AN_M
IED4_B09	**Voltage**	0.0093	0.0074	V_B15_AN_M	V_B15_AN_M
IED4_B09	**Current**	0.0092	0.0073	V_B15_AN_M	V_B15_AN_M
IED15_B05	**Current**	0.0093	0.0073	V_B15_AN_M	V_B15_AN_M
IED5_B10	**Voltage**	0.0093	0.0073	V_B15_AN_M	V_B15_AN_M
IED5_B10	**Current**	0.0094	0.0074	V_B15_AN_M	V_B15_AN_M
IED6_B15	**Voltage**	0.0142	0.0129	V_B15_BN_M	V_B15_BN_M
IED6_B15	**Current**	0.0093	0.0073	V_B15_AN_M	V_B15_AN_M
IED7_B06	**Voltage**	0.0093	0.0073	V_B15_AN_M	V_B15_AN_M
IED7_B06	**Current**	0.0093	0.0073	V_B15_AN_M	V_B15_AN_M
IED8_B13	**Voltage**	0.0093	0.0074	V_B15_AN_M	V_B15_AN_M
IED8_B13	**Current**	0.0093	0.0073	V_B15_AN_M	V_B15_AN_M
IED9_B14	**Voltage**	0.0093	0.0073	V_B15_AN_M	V_B15_AN_M
IED9_B14	**Current**	0.0093	0.0073	V_B15_AN_M	V_B15_AN_M
IED10_B08	**Voltage**	0.0093	0.0073	V_B15_AN_M	V_B15_AN_M
IED10_B08	**Current**	0.0093	0.0073	V_B15_AN_M	V_B15_AN_M
IED11_B07	**Voltage**	0.0093	0.0073	V_B15_AN_M	V_B15_AN_M
IED11_B07	**Current**	0.0093	0.0073	V_B15_AN_M	V_B15_AN_M
IED12_B03	**Voltage**	0.0093	0.0073	V_B15_AN_M	V_B15_AN_M
IED12_B03	**Current**	0.0093	0.0073	V_B15_AN_M	V_B15_AN_M
IED13_B04	**Voltage**	0.0093	0.0073	V_B15_AN_M	V_B15_AN_M
IED14_B12	**Voltage**	0.0093	0.0073	V_B15_AN_M	V_B15_AN_M
IED14_B12	**Current**	0.0093	0.0073	V_B15_AN_M	V_B15_AN_M
IED16_B06	**Current**	0.0093	0.0073	V_B15_AN_M	V_B15_AN_M
IED17_B06	**Current**	0.0093	0.0073	V_B15_AN_M	V_B15_AN_M

The evaluation of the distribution system state estimator errors between the state estimates and the assumed true values measured in the corresponding OpenDSS model. These errors and their magnitudes are applicable only to the PNM distribution system model that was analyzed; different distribution system models may present errors that are less than, greater than, or similar to the errors determined in this model. The analysis showed that there was some inherent validation error present

between the distribution system as modeled in the state estimator and the distribution system as modeled in OpenDSS. There was a slight increase in the errors when the distribution system was simulated with time varying loads and generation. When random white noise was introduced to various measurements it was determined that the increase in error for the measurement with the maximum error was less than the standard deviation of the error introduced. Although the increase in error was less than the introduced error, there is a positive correlation between the standard deviation of the introduced error and the increase in observed error. In general, when measurements are not updated due to a failure of the measurement devices or a lapse in communication between the device and the state estimator, the error in the estimates does not increase. For the PNM feeder model, the maximum error was most likely to occur on the voltage measurements at bus 15. Bus 15 includes both load and PV generation, however, the PV system is the smallest of the three PV systems modeled on the distribution system. The sensitivity analysis of the state estimator did not include any investigation into modeling improvements that would result in decreased error measurements.

2.4. Estimation Based Protection

Estimation based protection (EBP) has been inspired from—and can be considered an extension and generalization to—the differential protection function as illustrated in Figure 2-23. In current differential protection, the electric currents at all terminals of a protection zone are measured and their weighted sum must be equal to zero (generalized from Kirchhoff's current law). Thus, the current differential protection function consists of measuring the sum of the currents and as long as it is zero or near zero, no action is taken. In EBP, all existing measurements in the protection zone are utilized. These measurements include currents and voltages at the terminals of the protection zone, currents and voltages inside the protection zone, speed and torque (as in rotating machinery), or other internal measurements including thermal measurements. All above measurements should obey the physical laws for the protection zone (physical laws such as KCL, KVL, motion laws, and thermo-dynamic laws). The physical laws of the protection zone are captured in the dynamic model of the protection zone. This means that in absence of an internal fault (a fault within the protection zone), the measurements would satisfy the dynamic model of the protection zone, i.e., all the physical laws of the protection zone are satisfied. When there is an internal fault, the measurements would not satisfy the dynamic model of the protection zone. This distinction is a powerful, secure, and reliable method to identify internal faults and ignore any external faults.

EBP solves the challenges generated for distribution system protection by the introduction of higher penetrations of DER devices. Specifically, the challenges are created by the fact that DER create bidirectional flow of power and fault currents as well as fault current contributions from DER that are comparable to load currents. EBP is independent of power and fault current direction as well as independent of fault current levels. Therefore, it is a method that is well suitable for the new realities in distribution systems with low or high penetration of DERs.

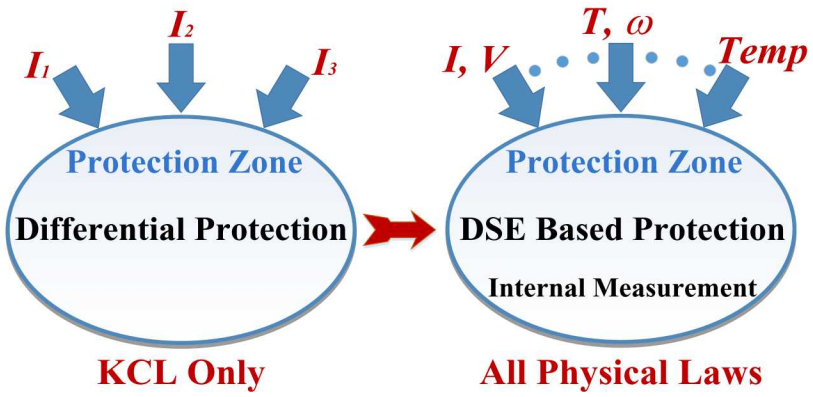

Figure 2-23: Conceptual Illustration of the Estimation Based Protection

An EBP tool, based on one previously created for microgrids[9], was established for the ProDROMOS system. In the original vision of the ProDROMOS system, all control actions would be taken by a centralized controller based on field measurements and forecasts. Unfortunately, it was determined that communication latency between Sandia and Connected Energy was too great to conduct EBP tests with the PNM and NG RT or PHIL test environment because protection systems need to take decisions within a few cycles. This is not possible with a centralized command and control configuration. The team therefore established a new vision for this software being deployed in distribution systems with fiber communications or cellular communications (LTE) that have the capability to transmit data with latencies that are far shorter than the required response of protection systems. To validate the EBP, an experiment was conducted at the Georgia Tech laboratory with a merging unit acting as the hardware-in-the-loop component.

2.4.1. Object-Oriented Device Modeling

EBP requires a high-fidelity mathematical model of all the devices in the protection zone. The model of a device is a set of differential and algebraic equations. In general, the model may include electrical laws, thermal laws, and motion laws, i.e., it is a multi-physics model and many times it is a nonlinear model, which is referred as a compact device model. A quadratization procedure is then applied to the compact model. This procedure consists of introducing additional variables to reduce higher order terms to nonlinear terms of highest order two. The end result is a state and control quadratized device model (SCQDM), which in general is also in terms of states and controls with other device information (connectivity, etc.), described in Section 2.3.2.1. The SCQDM is then integrated for the purpose of converting it into an algebraic model. The quadratic integration method is adopted, and the integration process transforms the SCQDM into a state and control algebraic quadratic companion form (SCAQCF), described in Section 2.3.2.1. The EBP works directly on this SCAQCF syntax.

2.4.2. Construction of the Protection Zone Measurement Model

This subsection presents a seamless procedure of creating the protection zone measurement model based on device SCAQCF models and measurements from merging units in this protection zone as shown in Figure 2-24. Then, the dynamic state estimation works directly on the protection zone measurement model and releases the trip decision without any other interference.

[9] Yu Liu, A. P. Sakis Meliopoulos, Rui Fan and Liangyi Sun, "Dynamic State Estimation based protection of microgrid circuits," 2015 IEEE Power & Energy Society General Meeting, Denver, CO, 2015, pp. 1-5.

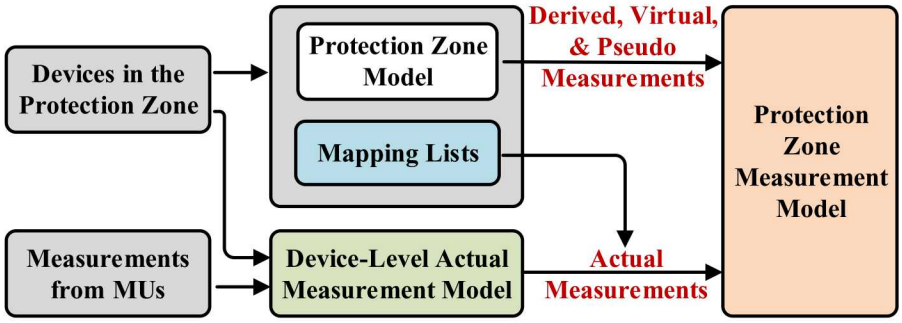

Figure 2-23. Overall Approach of Constructing the Zone Measurement Model.

Given the measurements from merging units and the device SCAQCF models, the device-level actual measurement model can be directly constructed. For an across measurement, its measurement model is simply a linear combination of the states of the measured device plus a measurement error from this merging unit, i.e.,

$$z(t) = A\mathbf{x}(t) + \eta \tag{2.5.1}$$

where $z(t)$ is the measurement, A is the linear coefficient matrix, $\mathbf{x}(t)$ is the device state vector at time t, and η is the noise introduced by this merging unit. For a through measurement, its measurement model is obtained directly from the corresponding equation of the device SCAQCF model, i.e.,

$$z(t) = Y_{zx}\mathbf{x} + Y_{zu}\mathbf{u} + \begin{Bmatrix} \vdots \\ \mathbf{x}^T F_{zx}^i \mathbf{x} \\ \vdots \end{Bmatrix} + \begin{Bmatrix} \vdots \\ \mathbf{u}^T F_{zu}^i \mathbf{u} \\ \vdots \end{Bmatrix} + \begin{Bmatrix} \vdots \\ \mathbf{u}^T F_{zux}^i \mathbf{x} \\ \vdots \end{Bmatrix} - B_z + \eta \tag{2.5.2}$$

$$B_z = -N_{zx}\mathbf{x}(t-h) - N_{zu}\mathbf{u}(t-h) - M_z i(t-h) - K_z$$

where Y, N, M matrices are linear coefficient matrices, F matrices are nonlinear coefficient matrices, and K is the constant term. Once the device-level actual measurement model is formed, the network-level actual measurement model is easily obtained by using the formulated mapping lists that map the states, controls, and equations in the device-level actual measurement model to those in the network-level actual measurement model.

Next, we use the devices in the protection zone with SCAQCF representation to construct the protection zone in the same syntax. With the protection zone SCAQCF model, we create the protection zone level measurement model, which is processed by EBP. To construct the protection zone level measurement model, three tasks are performed:

1. construct the zone-level SCAQCF model and form the mapping lists (states, controls, equations) from devices to the protection zone

2. create the zone-level actual measurement model based on the formulated device-level actual measurement model and the mapping lists
3. create the zone-level derived, virtual, and pseudo measurement model using the zone-level SCAQCF model.

Given *n* device SCAQCF models in the protection zone, the first task is to create the zone model in SCAQCF syntax. In general, a device SCAQCF model consists of three types of equations: a) equations corresponding to the zone interface nodes, b) equations corresponding to the zone common nodes, and c) device internal equations. To formulate zone SCAQCF model, we keep types a and c equations and replace the states and controls in terms of devices by the states and controls in terms of the protection zone. For type b equations from different devices but corresponding to a same common node, we apply Kirchhoff's current law (KCL) at each node which provides one equation for each node and which eliminates the through variables. These equations are in terms of the states and controls of the protection zone. During this task, we first create the mapping lists (states, controls, equations) from devices to the protection zone based on the device connectivity. Then, the zone SCAQCF model is automatically created by the device SCAQCF models in this protection zone and the mapping lists. Note that in the zone SCAQCF model, the equations with the current *i* on the left-hand side denote the currents flowing into the zone through the interface nodes, while all the other equations with zero value on the left-hand side are the device internal equations and the zero sum of equations at the common nodes derived from KCL.

The second task is to form the zone-level actual measurement model by using the formulated mapping lists that map the states, controls, and equations in the device-level actual measurement model to those in the zone-level actual measurement model. To achieve the observability and increase redundancy, the third task is then performed, which creates three other types of measurement model, i.e., derived, virtual, and pseudo measurement models. Derived measurements are created by derivations from actual measurements based on the network topology. For instance, if device *i* and *j* are connected at node *O* with available current measurement i_i, and no other devices are connected at this node. Then, the current flowing into device *j* is simply derived as $z = i_j + \eta = -i_i + \eta$, and this is considered as a derived measurement. Virtual measurement models are provided by the protection zone internal equations reflecting the physical property (e.g., KCL, etc.) of the protection zone with high accuracy. These are directly obtained from the equations with zero value on the left-hand side in the zone-level SCAQCF model with a relatively small measurement error compared to actual measurement models. Pseudo measurement models are not directly measured but are quantities for which we know their approximate values. For example, the voltage at a neutral is around zero during normal operations. This voltage can be introduced as a pseudo measurement. Since we do not know the exact value of pseudo measurements, a relatively higher measurement error compared to the actual measurement model is introduced.

By following all these three tasks and combining zone-level actual, derived, virtual, and pseudo measurement models, the final expression of the protection zone measurement model with a similar syntax as the zone SAQCF model is obtained:

$$\mathbf{z}(t) = h(\mathbf{x}) + \boldsymbol{\eta} = Y_{zx}\mathbf{x} + Y_{zu}\mathbf{u} + \begin{Bmatrix} \vdots \\ \mathbf{x}^T F_{zx}^i \mathbf{x} \\ \vdots \end{Bmatrix} + \begin{Bmatrix} \vdots \\ \mathbf{u}^T F_{zu}^i \mathbf{u} \\ \vdots \end{Bmatrix} + \begin{Bmatrix} \vdots \\ \mathbf{u}^T F_{zux}^i \mathbf{x} \\ \vdots \end{Bmatrix} - B_z + \boldsymbol{\eta} \tag{2.5.3}$$

$$B_z = -N_{zx}\mathbf{x}(t-h) - N_{zu}\mathbf{u}(t-h) - M_z i(t-h) - K_z$$

2.4.3. Dynamic State Estimation and Fault Detection

The dynamic state estimation algorithm is applied on the formulated zone measurement model and provides the best estimate of the states at each time step by applying the weighted least square method:

$$Minimize \quad J = \left(h(\mathbf{x},\mathbf{u}) - \mathbf{z}\right)^T W \left(h(\mathbf{x},\mathbf{u}) - \mathbf{z}\right) \tag{2.5.4}$$

where W is the weight matrix with the weights defined as the inverse of the squared standard deviation δ_i for each measurement: $W = diag\left\{1/\delta_1^2, 1/\delta_2^2, ..., 1/\delta_n^2\right\}$.

Then we substitute the control vector $\mathbf{u}$ in $h(\mathbf{x},\mathbf{u})$ with actual values, yielding $h(\mathbf{x})$. The unknown state vector $\mathbf{x}$ is obtained by the optimal condition:

$$dJ/d\mathbf{x} = 0 \tag{2.5.5}$$

To obtain the solution of the nonlinear optimization problem above, we linearize the nonlinear equations by assuming an initial guess $\mathbf{x}^n$, and the residual between the measurements and the linearized measurement model is:

$$\mathbf{r} = h(\mathbf{x}^n) + H(\mathbf{x}^n)(\mathbf{x} - \mathbf{x}^n) - \mathbf{z} = H(\mathbf{x}^n)\mathbf{x} - \mathbf{z}' \tag{2.5.6}$$

where $\mathbf{z}' = -h(\mathbf{x}^n) + H(\mathbf{x}^n)\mathbf{x}^n + \mathbf{z}$, $H(\mathbf{x}^n)$ is the Jacobian matrix of $h(\mathbf{x})$ at $\mathbf{x}^n$, and it is denoted as H for simplicity in the following paragraphs.

Now the objective function is in a linear form:

$$Minimize \quad J = \left(H\mathbf{x} - \mathbf{z}'\right)^T W \left(H\mathbf{x} - \mathbf{z}'\right) \tag{2.5.7}$$

where the optimal solution is obtained when $dJ/d\mathbf{x} = 0$. Therefore, the solution is achieved by the iterative equation:

$$\mathbf{x}^{n+1} = (H^T W H)^{-1} H^T W \mathbf{z}' = \mathbf{x}^n - (H^T W H)^{-1} H^T W (\mathbf{h}(\mathbf{x}^n) - \mathbf{z}) \tag{2.5.8}$$

After the solution is obtained, the chi-square test is performed. The chi-square test is a mathematical method to check the consistency between the measurements and the zone model. The procedure is expressed as:

$$\xi = \sum_i \left(\left(h_i(\mathbf{x}) - z_i \right) / \delta_i \right)^2 \qquad \mathrm{P} = 1 - \Pr(\xi, \nu) \tag{2.5.9}$$

where ξ is the chi-square value, ν is the difference between the number of measurements and states (degree of freedom), $\Pr(\xi, \nu)$ is the probability function, and P is the confidence level evaluating if the measurements fit the zone model. A high confidence level (e.g., 100%) indicates the measurements match the zone model, concluding that no fault exists in the protection zone. A low confidence level (e.g., 0%) denotes an inconsistency between the measurements and the zone model, which implies the protection zone is not in good health, i.e., the occurrence of an internal fault. The trip decision is issued based on a user-defined delay time and reset time:

$$trip = \begin{cases} 1, \text{ if } \int_{t-t_{reset}}^{t} P(\tau)\, d\tau > t_{delay} \\ 0, \text{ otherwise} \end{cases} \tag{2.5.10}$$

2.4.4. Demonstration Case – Protection of a Distribution Feeder Section

This subsection uses a demonstration case to illustrate the effectiveness of EBP. As shown in Figure 2-24, the demonstration case is to protect a distribution feeder section in a distribution system. The protection zone contains two three-phase distribution lines and two breakers. The diagram also includes two merging units that capture the voltages and currents from distribution lines. The parameters of the two distribution lines are listed in Table 2-15.

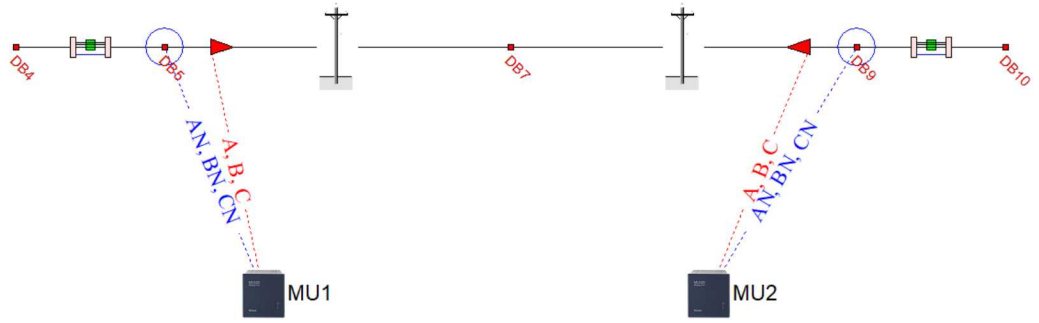

Figure 2-24. Single Line Diagram of the Protection Zone.

Table 2-15. Parameters of Distribution Lines in the Protection Zone.

Three-Phase Distribution Lines						
#	Device Name	Bus Name	Positive/Negative Sequence Impedance (ohm)	Zero Sequence Impedance (ohm)	Length (mile)	Rated Voltage (kV)
1	DL3	DB5, DB7	0.0998+j0.5756	0.5581+j2.8059	1.0	13.8
2	DL4	DB7, DB9	0.1297+0.7483	0.7256+j3.6477	1.3	13.8

Two merging units were installed in this protection zone. Each merging unit collected three-phase voltage and current measurements. The merging units and their measurements are listed in Table 2-16. Notice the measurements from these merging units were GPS-synchronized. The total number of actual measurements is 12. In addition, the EBP automatically created 44 virtual measurements (40 of them are device internal equations and other 4 measurements are derived from KCL at the common node), and 3 pseudo measurements. The total number of measurements is 59, and the total number of states of this protection zone is 52. The redundancy is 59/52 = 113.5%.

Two events are demonstrated to show the effectiveness of EBP. Event A is an internal fault case and event B is an external fault case. The EBP successfully identified the internal fault in event A and sent the trip command but ignored the external fault in event B because it was not within in the zone protected by the EBP. The detailed description of two events and how the EBP responds to these two events are illustrated section 2.5.4.1 and 2.5.4.2.

Table 2-16. Measurements of Merging Units in the Protection Zone.

MU Name	Voltage	Current)	# of Measurements
MU1	AN, BN, CN at DB5	A, B, C from DB5 to DB7, at DB5	6
Mu2	AN, BN, CN at DB9	A, B, C from DB9 to DB7, at DB9	6

2.4.4.1. Event A: Internal Fault Case

Event A is defined with a phase A to neutral fault occurring in the distribution line DL4 with 0.8 miles away from bus DB9. This is a fault inside the protection zone, so it should be cleared by opening the two breakers connected to this zone. The fault is initiated at 0.5 seconds from the start of the simulation. The simulation is executed for a period of one second. The measurements generated during the simulation are stored in COMTRADE files. Note that the time step is selected to match the standard merging unit sampling rate at 80 samples per cycle. For a 60 Hz system, the simulation time step is 208.33 microseconds, and the whole event has 4800 samples. The voltages and currents captured by the two merging units are plotted in Figure 2-25 and Figure 2-26.

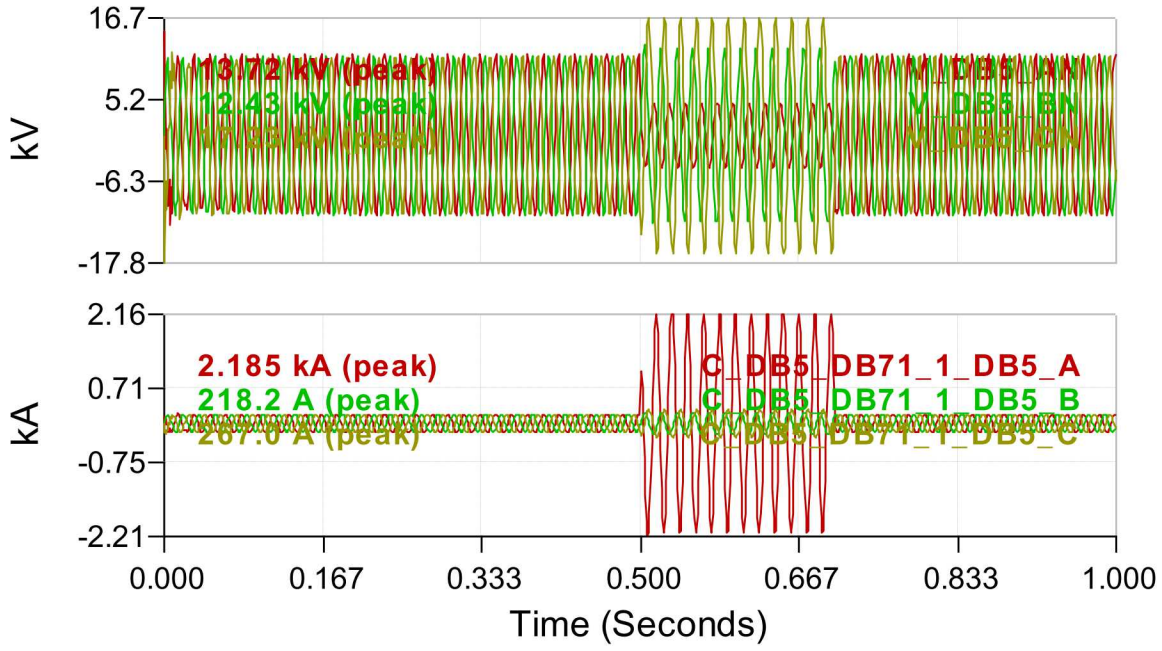

Figure 2-25. Voltage and Current Measurements Obtained from Merging Unit 1 in Event A.

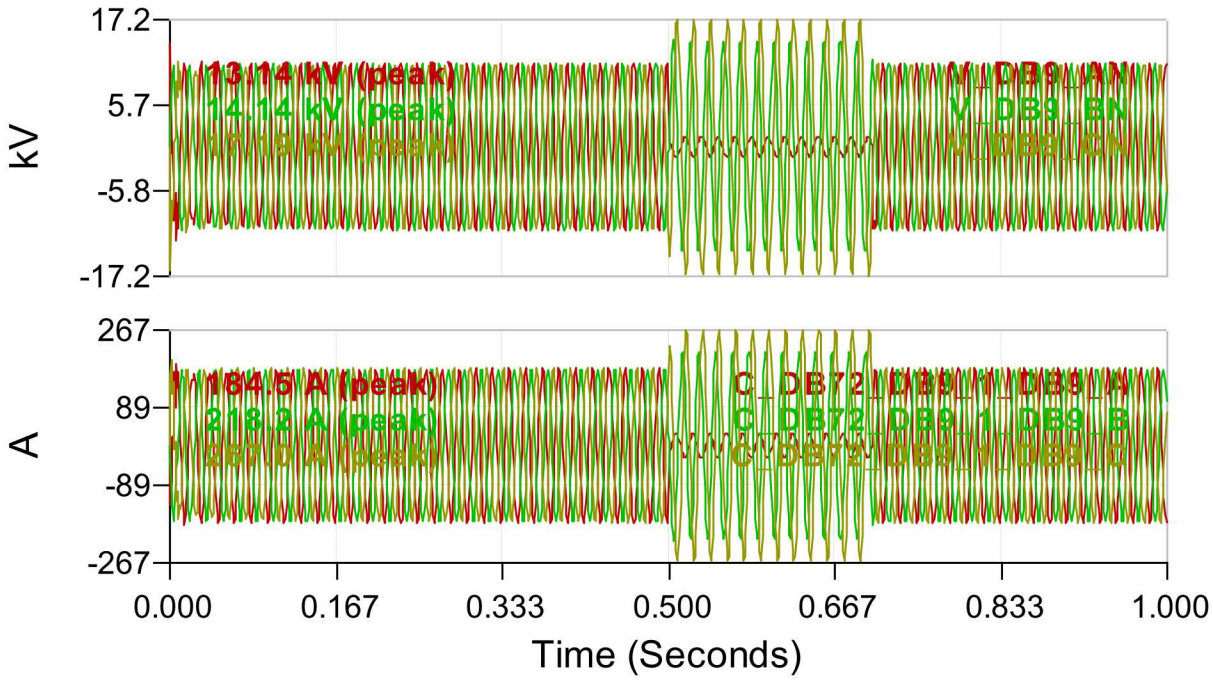

Figure 2-26. Voltage and Current Measurements Obtained from Merging Unit 2 in Event A.

The EBP program reads all the models in SCAQCF syntax in this protection zone and checks the consistency between the protection zone model and the measurements from the merging units by performing dynamic state estimation. Figure 2-27 shows phase A to N voltage, phase A current from merging unit 1, their estimated measurements, and the residuals between these measurements and their estimated measurements. Figure 2-28 depicts the confidence level and trip decision for this event. Note that the confidence level is 100% before the fault and reaches to zero immediately upon the fault initiation. The trip decision is then made within a user-defined delay.

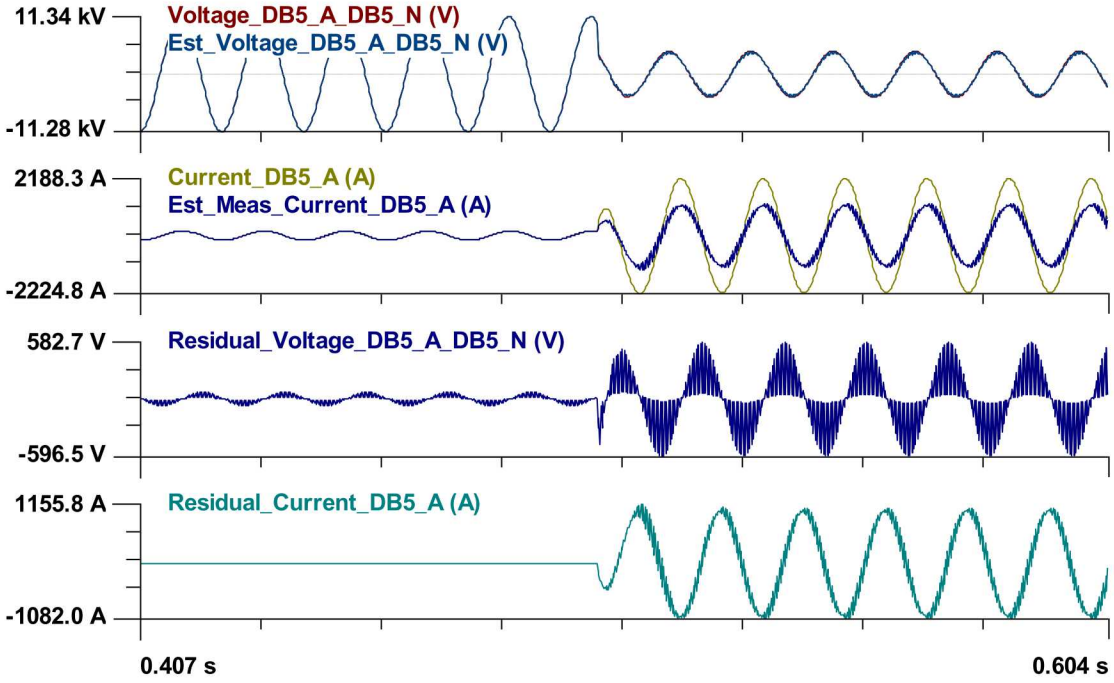

Figure 2-27. Plots of Some Actual/Estimated Measurements and Their Residuals in Event A.

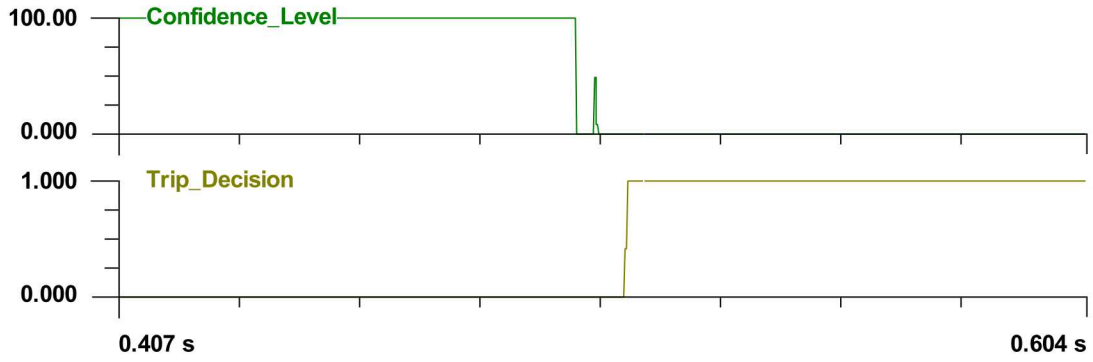

Figure 2-28. Confidence Level and Trip Decision of Event A.

2.4.4.2. Event B: External Fault Case

Event B is defined as a phase A to neutral fault 1.5 miles away from bus DB9 at a distribution line. This is a fault occurring outside of the protection zone and therefore the breakers of the protection zone should not operate. The fault is initiated at 0.5 seconds from the start of the simulation and lasts 0.2 seconds. The simulation is executed for a period of one second. The measurements generated during the simulation are stored in COMTRADE files. Note that the time step is selected to match the standard merging unit sampling rate at 80 samples per cycle. For a 60 Hz system, the simulation time step is 208.33 microseconds, and the whole event has 4800 samples. The voltages and currents captured by the two merging units are plotted in Figure 2-29 and Figure 2-30.

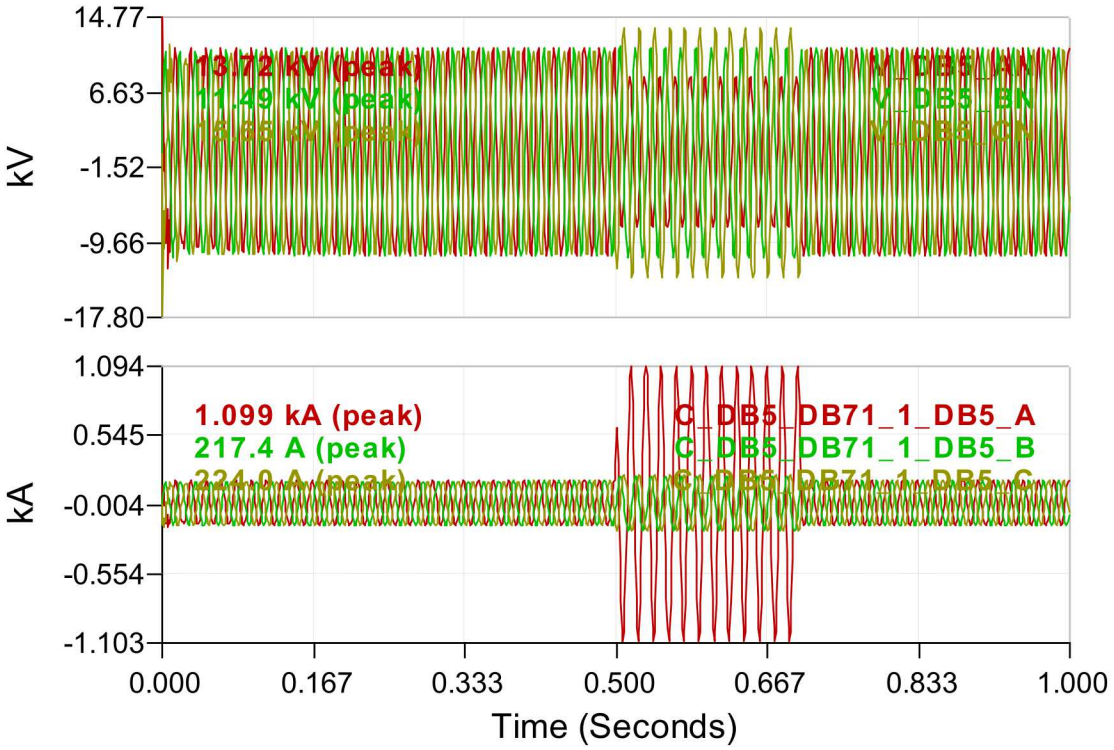

Figure 2-29. Voltage and Current Measurements Obtained from Merging Unit 1 in Event B.

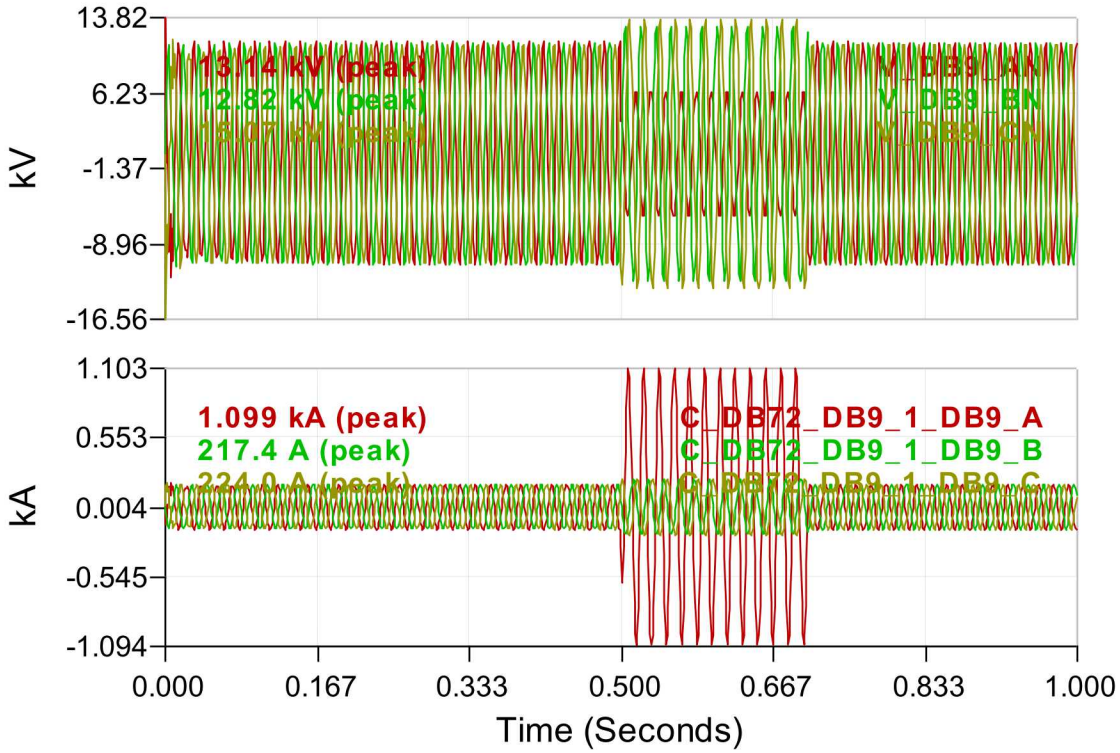

Figure 2-30. Voltage and Current Measurements Obtained from Merging Unit 2 in Event B.

The EBP program reads all the models in SCAQCF syntax in this protection zone and checks the consistency between the protection zone model and the measurements from the merging units by performing dynamic state estimation. Since the generated data are very large, we present part of them. Figure 2-30 shows phase A to neutral voltage, phase A current from merging unit 1, their estimated measurements, residuals between these measurements and their estimated measurements, confidence level, and the trip decision of the breakers in event B. As demonstrated in Figure 2-31, the confidence level keeps 100% through the whole event. Therefore, no trip decision is released, and this external fault is successfully ignored.

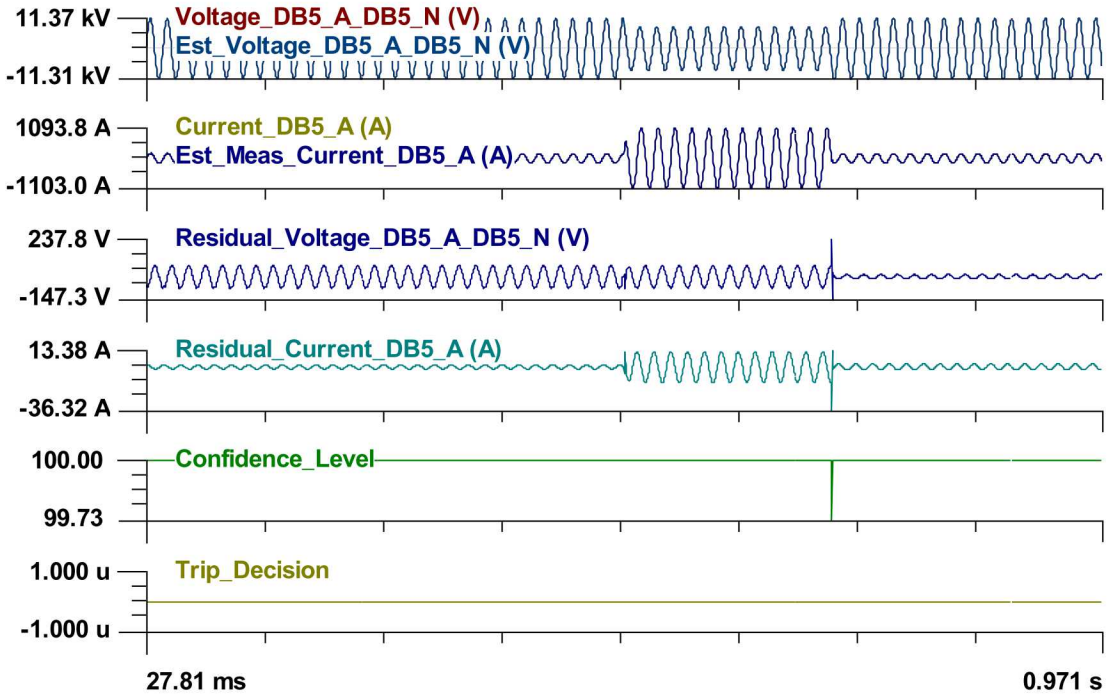

Figure 2-31. Plots of Selected Actual/Estimated Measurements, Residuals, Confidence Level, and Trip Decision in Event B.

2.5. Optimization

Three optimization approaches were analyzed in this project. These were designed to determine the optimal power factors of controllable DER systems. The first optimization technique used a distributed method that operated with sparse feeder data. The other two required results (real time operating conditions and model) from a state estimator.

The first optimization method used Extremum Seeking Control to adjust the reactive power of the DER devices. Each DER device generated a reactive power sinusoid with unique frequencies to determine its impact on an objective function. Based on this gradient, the DER devices move toward the optimal power factor setpoints.

The second optimization method, referred to as the "PSO" or "PSO OPF" approach, determined the PV PF setpoints and associated optimal power flow (OPF) by wrapping an OpenDSS time series simulation of the reduced order feeder model inside a particle swarm optimization (PSO). The active and reactive components of the loads in the OpenDSS model were populated using live state estimation results. PV forecasts for each of the PV systems were inserted into the OpenDSS model to optimize operations over a future time horizon.

The third optimization method, called "multi-stage flexible OPF," was a deterministic optimization based on the RT quadratized model of the distribution system. Object-oriented physically based device models form the basis of system modeling. A sequential linear programming approach incorporating the co-state method was adapted in solving the optimization problem.

In Sections 4-6, the ESC and PSO methods are compared to baseline scenarios where the DER devices were kept at unity power factor and a scenario where the DER devices were programmed with an autonomous Volt-Var grid-support function. The Volt-Var function adjusts the reactive power of the DER based on local grid voltage measurements according to an adjustable curve of (voltage, reactive power) points.

2.5.1. Extremum Seeking Control

Extremum Seeking Control (ESC) is a distributed optimization technique for multi-agent, nonlinear systems that can be configured for voltage regulation[10,11,12] and bulk power system services[13]. The technique operates by adjusting system inputs (e.g., reactive power) to optimize measured outputs (e.g., feeder voltage). The method adjusts system inputs, u, via use of a sinusoidal perturbation, demodulates system outputs, $J(u)$, to extract approximate gradients, and finally performs a gradient descent. A block diagram of the approach is shown in Figure 2-32. The parameters k, l, h, a, and ω were chosen based on prior experience with ESC and a systematically debugging process described in Section 6.2.1. Figure 2-33 depicts how a centralized control center would implement ESC: the ProDROMOS collects data from the circuit (A) necessary to calculate the objective function (B); this objective function is used to extract each DER's frequency-specific effect on the objective function and adjust reactive power output to trend toward the global optimum calculate impact on the objective function (C) by issuing power factor setpoints to each of the DER devices (D).

The sequence for implementing the ESC control follows:

1. The ProDROMOS manager configures the DER with unique parameters (ω's) to avoid controller conflict.
2. The ProDROMOS manager constructs the objective function, J, that represents the objective of the grid support function. For example, this could be the root-mean-square error from nominal voltage.
3. The ProDROMOS monitors the objective function and makes PF changes to each DER to improve the performance of the system. This is done by demodulating the J signal, i.e., determining the gradient of the ω harmonic of J.

[10] D. B. Arnold, M. Negrete-Pincetic, M. D. Sankur, D. M. Auslander and D. S. Callaway, "Model-Free Optimal Control of VAR Resources in Distribution Systems: An Extremum Seeking Approach," IEEE Transactions on Power Systems, vol. 31, no. 5, pp. 3583-3593, Sept. 2016.

[11] J. Johnson, A. Summers, R. Darbali-Zamora, J. Hernandez-Alvidrez, J. Quiroz, D. Arnold, J. Anandan, "Distribution Voltage Regulation using Extremum Seeking Control with Power Hardware-in-the-Loop," IEEE Journal of Photovoltaics, vol. 8, no. 6, pp. 1824-1832, 2018. doi: 10.1109/JPHOTOV.2018.2869758

[12] J. Johnson, S. Gonzalez, and D.B. Arnold, "Experimental Distribution Circuit Voltage Regulation using DER Power Factor, Volt-Var, and Extremum Seeking Control Methods," IEEE PVSC, Washington, DC, 25-30 June, 2017.

[13] D. B. Arnold, M. D. Sankur, M. Negrete-Pincetic and D. Callaway, "Model-Free Optimal Coordination of Distributed Energy Resources for Provisioning Transmission-Level Services," in IEEE Transactions on Power Systems, vol. 33, no. 1, pp. 817-828, 2017.

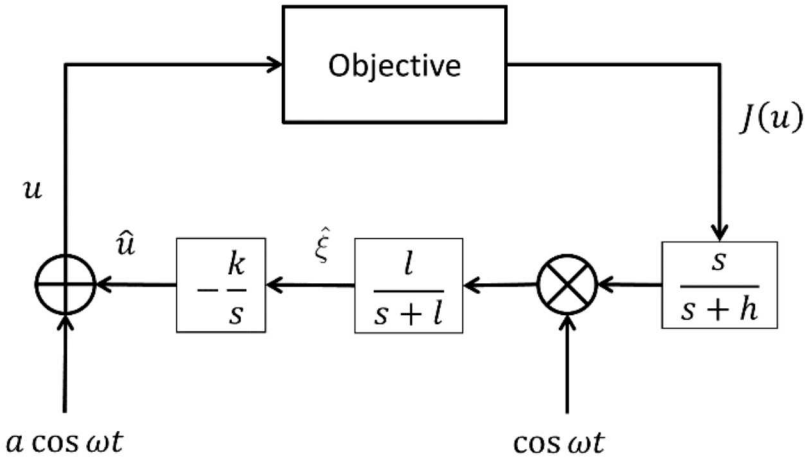

Figure 2-32. Block diagram of ESC.

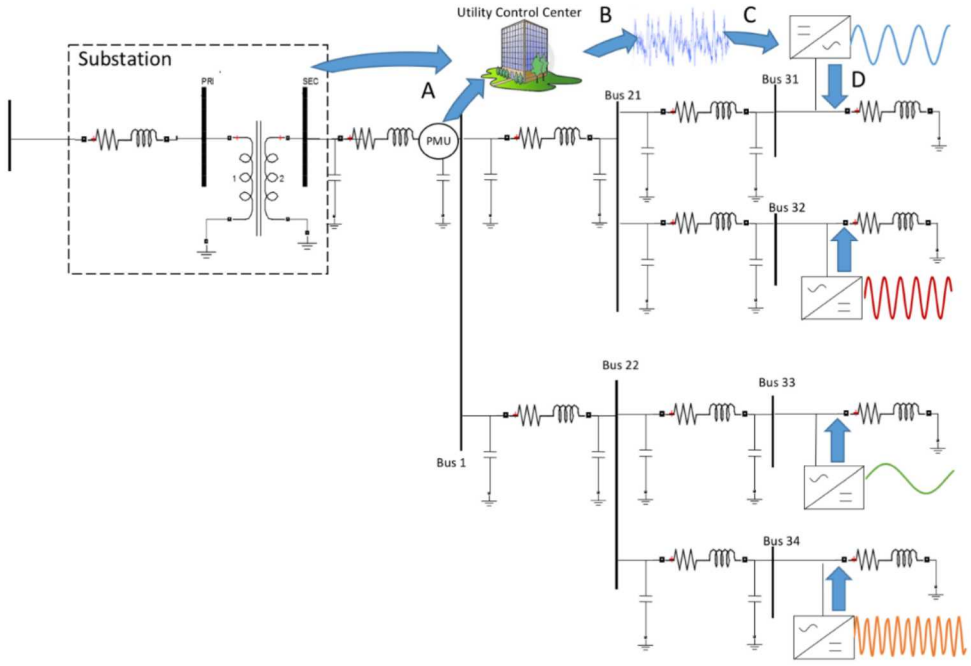

Figure 2-33. Distribution circuit with multiple PV inverters running ESC.

2.5.2. Particle Swarm Optimization (PSO)

In the PSO OPF method, time-series OpenDSS simulations were wrapped in an PSO loop to calculate the best PF values. The OpenDSS load data is populated by the WinIGS state estimation solution and the PV production was populated by the PV forecasts. A simplified representation of the PSO approach is shown in Figure 2-34 and the code is located on GitHub. A Python interface was created to capture the state estimation IEEE C37.118 data streams from WinIGS. These phasor data for each of the buses and PV systems were used to calculate the active and reactive power levels for the dynamic loads in the OpenDSS model. Then using the communication interface to OpenDSS, the active and

reactive multipliers, p_mult and q_mult, were updated in the OpenDSS environment. The optimization was completed every minute over a 15-min horizon using 3 periods with a 5-minute step size. The forecast PV production for each of the epochs is calculated using the forecasting code. In cases where there was no PV production data available, scaled surrogate PV system forecasts could be used. The p_mult and q_mult values persisted for the entire time simulation. The PSO was used to locate the optimal DER PF settings because the fitness landscape was nonconvex because of the voltage regulators and other binary components. Early experiments mapped the voltage root-mean-square error (RMSE) fitness landscape of the PNM model for the two largest PV systems, shown in Figure 2-35. PSO was selected based on its ability to overcome challenges associated with solution space nonconvexities.

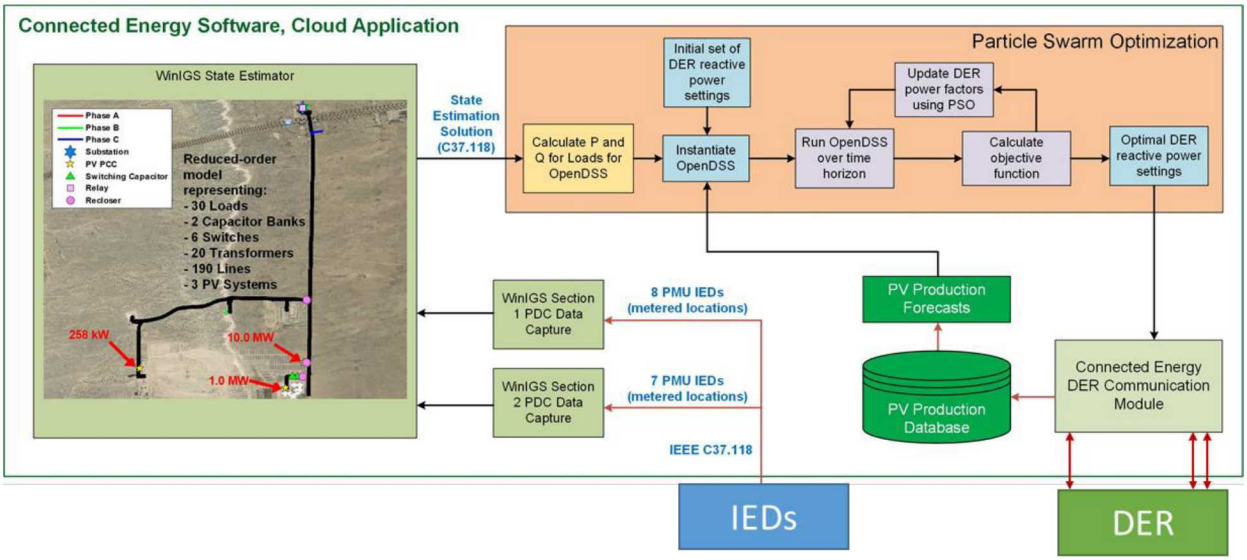

Figure 2-34: Information flows in the PSO optimization method.

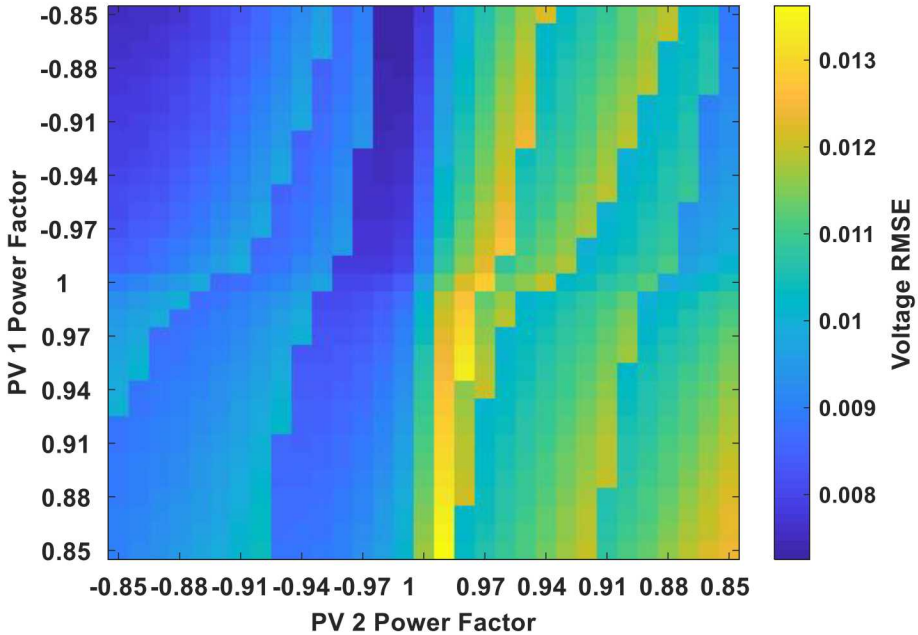

Figure 2-35: Fitness landscape for the PSO optimization when considering 2 PV devices.

The optimization formulation was designed to capture the voltage regulation components and economics considerations of operating PV systems off unity PF:

$$\underset{PF}{\text{Minimize}} \left[w_0 \delta_{violation}(\boldsymbol{V}) + w_1 \sigma(\boldsymbol{V} - \boldsymbol{V}_{base}) + w_2 C(\boldsymbol{PF})\right] \quad (2.6.2.1)$$

where

$$\delta_{violation}(\boldsymbol{V}) = 1 \text{ if any } |\boldsymbol{V}| > V_{lim} \quad (2.6.2.2)$$

$$\sigma(\boldsymbol{V} - \boldsymbol{V}_{base}) \text{ is the standard deviation of } \boldsymbol{V} - \boldsymbol{V}_{base} \quad (2.6.2.3)$$

$$C(PF) = \sum 1 - |\boldsymbol{PF}| \quad (2.6.2.4)$$

$\boldsymbol{V}$ is a vector of bus voltages, $\boldsymbol{V}_{base}$ is a vector the nominal voltages for each bus, and $\boldsymbol{PF}$ is a vector of the DER PFs. The objective function is minimized when the bus voltages are at $\boldsymbol{V}_{base}$ and PF = 1. V_{lim} was selected to be the ANSI C84.1 Range A limits of ±0.05 pu, so any solutions outside the limits would be highly penalized. The third term was a simplified method to discourage solution that moved away from unity power factor, because these solutions would curtail active power (and expense the PV owner through net metering, power purchase agreements, etc.) at high irradiance times. More sophisticated methods for determining the curtailment magnitude accounting were considered, but the simple approach shown here was implemented. For the experiments conducted in this project w_0 = 1.0, w_1 = 2.0, and w_2 = 0.05.

There was also logic wrapped around when the PSO would run and if the new solution would be issued to the DER devices. The optimization was configured so that if all the bus voltages were within an acceptance threshold (set to 0.2% of nominal voltage) the PSO would not run. If any of the voltages were outside ANSI Range A the PSO would run. Furthermore, if the new PF values did not change the objective function by an objective threshold (set to 1e-7), the new PFs would not be sent to the DER devices to minimize communications and DER memory writes.

2.5.3. Multi-Stage Flexible Optimal Power Flow for Voltage Control

This section presents a voltage control scheme for multi-period voltage control of distribution systems using the RT model and operating conditions from the state estimator. Specifically, a quasi-dynamic state estimator performs state estimation and provides the estimated system operating conditions and RT network model. The network model is used with a user-defined objective function, which is levelizing (i.e., normalizes) the voltage magnitudes at selected buses across the system, to form a multi-stage quadratic flexible OPF (F-OPF) problem. A sequential linear programming (SLP) method is utilized to solve the F-OPF problem iteratively. In each iteration, the F-OPF is linearized at the current operating point with respect to the control variables using the co-state method. Then, the linearized problem is solved, and the operating point is updated. When the SLP algorithm converges, the optimal control actions are found and implemented to drive the system towards the optimal operating point, which achieves the desired voltage control. Note this voltage control process is done autonomously.

Considering various devices, including DER, in the system that can be used to fine-tune the voltage profile, a generic formulation is given by (2.6.3).

$$\min \quad \sum_{i \in S_{bus}} \left(V_i - 1.0\right)^2 \tag{2.6.3a}$$

$$\text{s.t.} \quad g\left(x,u\right) = 0 \tag{2.6.3b}$$

$$h\left(x,u\right) \le 0 \tag{2.6.3c}$$

$$\underline{u} \le u \le \overline{u} \tag{2.6.3d}$$

where V_i is the bus i voltage in per unit, x is the state vector, and u is the control vector. The objective is to levelize bus voltages, i.e. control them to near 1.0 pu. The variables are node voltages, device internal states, and control signals. At each node i we have $\sum I_{ij} = 0$ that is part of (2.6.3b), where j is in the set of nodes connected to i. Another part of (2.6.3b) is given by device internal states or physical laws. (2.6.3c) are some operational constraints like line thermal limits, while (2.6.3d) are bounds on the system control variables, respectively. The control variables can be transformer taps in substations, energy storage power outputs, voltage setpoints of generators, etc. The optimization problem is quadratic and non-convex so linearization techniques are applied to solve the problem.

The voltage control problem is formed and solved as a multi-stage F-OPF problem following the procedures illustrated in Figure 2-36.

The formulated multi-stage quadratic F-OPF model (QFOPFM) is quadratic, so sequential linear programming (SLP) is used to solve the problem. At the beginning of each iteration, the inequality constraints are checked for violations. The violated constraints are marked as model constraints, which are considered in the following linear program. The co-state method is used to linearize the objective function and model constraints with respect to the control variables. Then the linearized F-OPF model (LFOPFM) is solved by a linear programming solver. Transforming the LFOPFM into a linear program in standard form (LPSF) and solving it using the simplex method is one way. The solution is the control variation, which is used to compute the controls, and thus update the states, yielding the new operating point. The objective function value is computed and compared with that in the previous iteration. The control excursion limits for non-binary controls are halved if no improvement is observed for the objective function value. The algorithm then proceeds to the next iteration.

The following characteristics exist during the iterative process.

1. FOPFSolution is true: this means that the optimal solution has been reached and all relaxation variables are zero for the linearized problem.
2. SolutionModelConstraints is true: this means all solution model constraints are satisfied.
3. NonSolutionModelConstraints is true: this means that all constraints that are not included in the linearized model are satisfied.

The SLP algorithm is said to converge only when all three characteristics are satisfied. Otherwise, the algorithm continues.

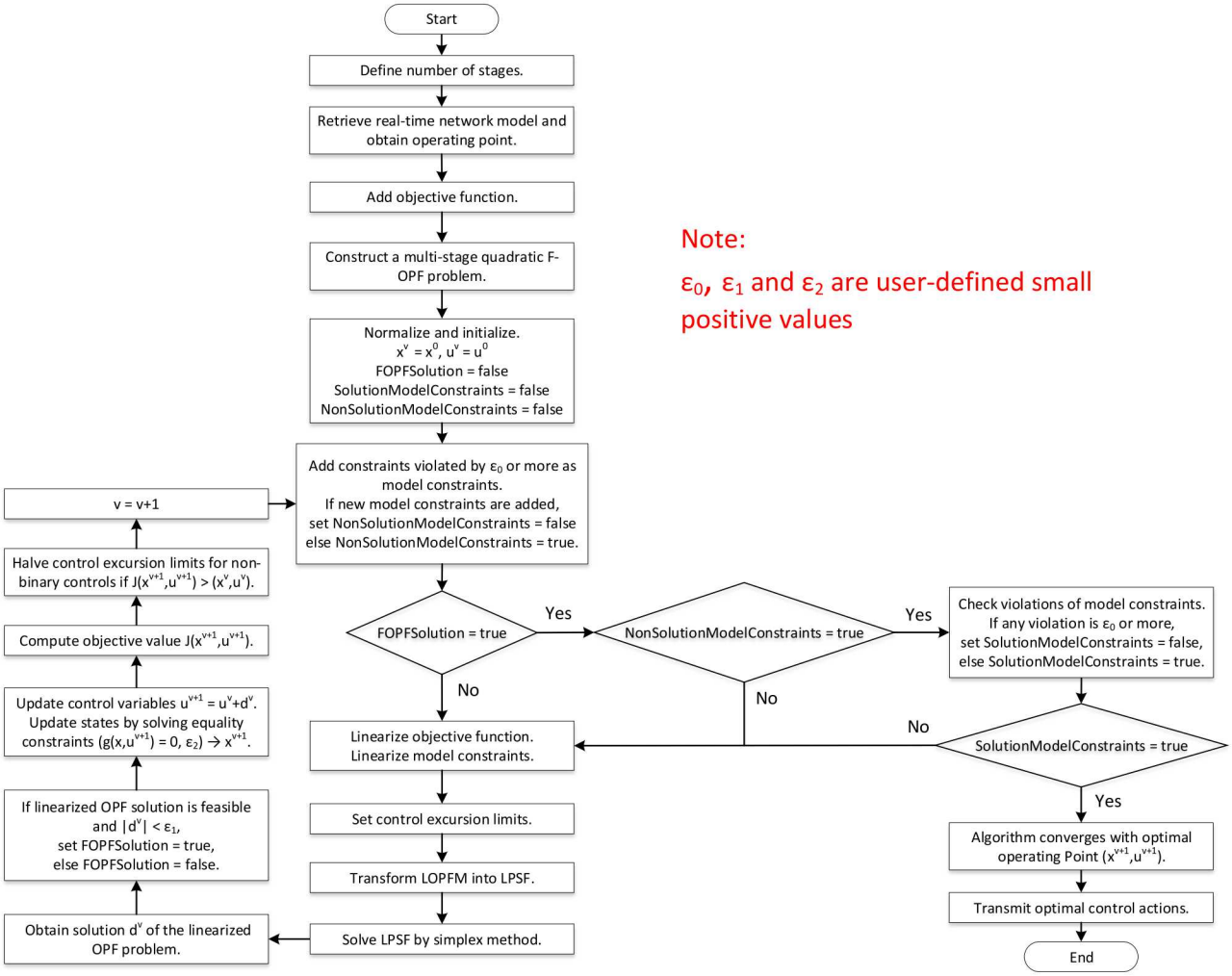

Figure 2-36. Multi-Stage Flexible OPF Algorithm.

2.5.3.1. Physically Based Device Modeling

The formation of the F-OPF starts from device modeling, which models the devices as standardized mathematical objects based on their physical circuits. The state and control algebraic quadratic companion form (SCAQCF) is the standard syntax for modeling the devices. The syntax is given by:

Model Description: *Type*, *Code*, *ID*, *Title*

$$\begin{Bmatrix} i(t) \\ 0 \\ 0 \\ i(t_m) \\ 0 \\ 0 \end{Bmatrix} = \mathbf{e_{lhs}} = Y_{eqx}\mathbf{x} + \begin{Bmatrix} \vdots \\ \mathbf{x}^T \left\langle F^i_{eqxx} \right\rangle \mathbf{x} \\ \vdots \end{Bmatrix} + Y_{equ}\mathbf{u} + \begin{Bmatrix} \vdots \\ \mathbf{u}^T \left\langle F^i_{equu} \right\rangle \mathbf{u} \\ \vdots \end{Bmatrix} + \begin{Bmatrix} \vdots \\ \mathbf{u}^T \left\langle F^i_{equx} \right\rangle \mathbf{x} \\ \vdots \end{Bmatrix} - B_{eq}$$

$$B_{eq} = -N_{eqx}\mathbf{x}(t-h) - N_{equ}\mathbf{u}(t-h) - M_{eq}I(t-h) - K_{eq}$$

$$\mathbf{h}(\mathbf{x},\mathbf{u}) = Y_{feqx}\mathbf{x} + Y_{fequ}\mathbf{u} + \begin{Bmatrix} \vdots \\ \mathbf{x}^T \left\langle F^i_{feqxx} \right\rangle \mathbf{x} \\ \vdots \end{Bmatrix} + \begin{Bmatrix} \vdots \\ \mathbf{u}^T \left\langle F^i_{fequu} \right\rangle \mathbf{u} \\ \vdots \end{Bmatrix} + \begin{Bmatrix} \vdots \\ \mathbf{u}^T \left\langle F^i_{fequx} \right\rangle \mathbf{x} \\ \vdots \end{Bmatrix} + C_{feqc}$$

Constraints : $\mathbf{h}(\mathbf{x},\mathbf{u}) \le \mathbf{0}, \mathbf{u_{min}} \le \mathbf{u} \le \mathbf{u_{max}}, \ |\mathbf{d}| \le \mathbf{u_{llim}}$

Model Dimensions: n_{equ}, n_{state}, $n_{control}$, n_{Feqxx}, n_{Fequu}, n_{Fequx}, n_{fconst}, n_{Ffeqxx}, n_{Ffequu}, n_{Ffequx}

Connectivity: nn_t, *ivn*, *inn*, *onn*, S_{st}

Normalization Factor: x_{NF}, e_{NF}, u_{NF}, h_{NF}

Units: *xUnit*, *eUnit*, *uUnit*, *hUnit*

where i, $\mathbf{x}$ and $\mathbf{u}$ are the terminal currents, states and controls of the device respectively, including both time t and t_m values, where $t_m = t - h/2$. The functional constraints are expressed by $h \le 0$, while the lower and upper control bounds correspond to vectors $\mathbf{u_{min}}$ and $\mathbf{u_{max}}$. In addition, $\mathbf{d}$ and $\mathbf{u_{llim}}$ contain the differences of the control values and the maximum permissible control excursions between two consecutive iterations in the SLP process, respectively. Matrices Y and F respectively contain the coefficients of the linear and quadratic terms. Past history vector B_{eq} is used to store the model information from the previous simulation time step. The linear coefficients of the variables at the previous step are contained in matrices N_{eq} and M_{eq}, while the constant terms are stored in vectors K_{eq}. Note that subscripts $\mathbf{x}$ and $\mathbf{u}$ represent the state and control variables, while f represents the functional constraints.

2.5.3.2. Network Formulation

Given the device models in a system, the model of the entire system (network) is generated autonomously. The equations, constraints, states and controls are mapped from the device level to the network level. KCL is applied to every node in the network at both time t and t_m. Given n device models in the SCAQCF syntax, Figure 2-37 illustrates the construction of the network model, which is also represented in the SCAQCF syntax.

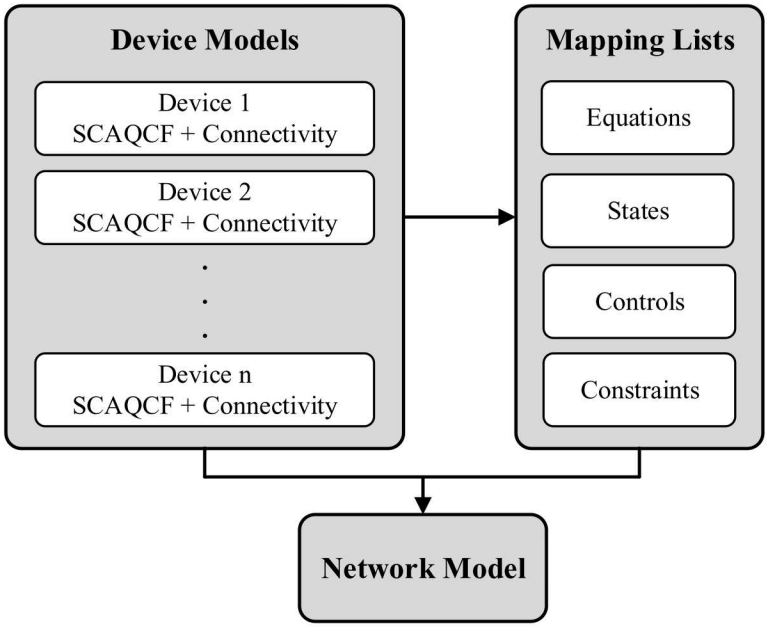

Figure 2-37. Network Model Construction Process.

The network SCAQCF is given by

$$\begin{Bmatrix} \mathbf{i}_{\mathbf{net}}(t) \\ 0 \\ 0 \\ \mathbf{i}_{\mathbf{net}}(t_m) \\ 0 \\ 0 \end{Bmatrix} = Y_{eqx}\mathbf{x} + \begin{Bmatrix} \vdots \\ \mathbf{x}^T \left\langle F^i_{eqxx} \right\rangle \mathbf{x} \\ \vdots \end{Bmatrix} + Y_{equ}\mathbf{u} + \begin{Bmatrix} \vdots \\ \mathbf{u}^T \left\langle F^i_{equu} \right\rangle \mathbf{u} \\ \vdots \end{Bmatrix} + \begin{Bmatrix} \vdots \\ \mathbf{u}^T \left\langle F^i_{equx} \right\rangle \mathbf{x} \\ \vdots \end{Bmatrix} - B_{eq}$$

$$B_{eq} = -N_{eqx}\mathbf{x}(t-h) - N_{equ}\mathbf{u}(t-h) - M_{eq}\mathbf{i}(t-h) - K_{eq}$$

$$\mathbf{i}(t) = Y_{ieqx}\mathbf{x} + \begin{Bmatrix} \vdots \\ \mathbf{x}^T \left\langle F^i_{ieqxx} \right\rangle \mathbf{x} \\ \vdots \end{Bmatrix} + Y_{iequ}\mathbf{u} + \begin{Bmatrix} \vdots \\ \mathbf{u}^T \left\langle F^i_{iequu} \right\rangle \mathbf{u} \\ \vdots \end{Bmatrix} + \begin{Bmatrix} \vdots \\ \mathbf{u}^T \left\langle F^i_{iequx} \right\rangle \mathbf{x} \\ \vdots \end{Bmatrix} - B_{ieq}$$

$$B_{ieq} = -N_{ieqx}\mathbf{x}(t-h) - N_{iequ}\mathbf{u}(t-h) - M_{ieq}\mathbf{i}(t-h) - K_{ieq}$$

$$\mathbf{h}(\mathbf{x},\mathbf{u}) = Y_{feqx}\mathbf{x} + Y_{fequ}\mathbf{u} + \begin{Bmatrix} \vdots \\ \mathbf{x}^T \left\langle F^i_{feqxx} \right\rangle \mathbf{x} \\ \vdots \end{Bmatrix} + \begin{Bmatrix} \vdots \\ \mathbf{u}^T \left\langle F^i_{fequu} \right\rangle \mathbf{u} \\ \vdots \end{Bmatrix} + \begin{Bmatrix} \vdots \\ \mathbf{u}^T \left\langle F^i_{fequx} \right\rangle \mathbf{x} \\ \vdots \end{Bmatrix} + C_{feqc} \le 0$$

$$\mathbf{u}_{min} \le \mathbf{u} \le \mathbf{u}_{max}$$

$$|\mathbf{d}| \le \mathbf{u}_{llim}$$

where $\mathbf{i}_{\mathbf{net}}$ denotes the network through variables at the interface nodes. Subscript i represents the rows corresponding to the vector of all device through variables i. The device equations corresponding to each node are combined into one network internal equation using KCL by eliminating the through variables of the devices connected to that node and expressed in terms of the states. The internal equations, functional constraints and control limits of the network model directly come from those of the individual device models.

2.5.3.3. Multi-Stage Quadratic F-OPF Model

Voltage control of the hybrid system is achieved by forming a multi-stage QFOPFM. The first step is to create the objective function, which is levelizing the voltage profile across the network. We define the objective function to be minimizing the sum of squared voltage magnitude mismatches (differences between voltage magnitude and desired voltage value) at selected buses. The mathematical expression of this objective function is:

$$\min \quad J = \sum_{i \in S_{bus}} \left(\frac{V_{i,mag} - V_{i,des}}{\alpha_i V_{i,des}} \right)^2 \tag{2.6.2}$$

where S_{bus} is the set of selected buses. $V_{i,mag}$ and $V_{i,des}$ are the voltage magnitude and desired voltage value at bus i, respectively, while α_i is a pre-defined tolerance value (e.g., 4%) at that bus. The objective function in (2.6.1) is converted to a standard quandratized form:

$$J = Y_{objx}^T \mathbf{x} + Y_{obju}^T \mathbf{u} + \mathbf{x}^T F_{objx} \mathbf{x} + \mathbf{u}^T F_{obju} \mathbf{u} + \mathbf{u}^T F_{objux} \mathbf{x} + C_{objc} \tag{2.6.3}$$

where subscript obj is used to denote the coefficients corresponding to the objective function.

Note that any discrete control variables in the system are converted into continuous variables at the device level. Discrete control variable u is constrained by additional equations in terms of additional variables that make the system continuous. The final solution of these equations will yield the correct value for the variable u. Specifically, the additional variable y is introduced so that the equation $0 = y - u(1-u)$ is appended to the device model before forming the network SCAQCF. The objective function in (2.6.2) becomes

$$\min \quad J = \sum_{i \in S_{bus}} \left(\frac{V_{i,mag} - V_{i,des}}{\alpha_i V_{i,des}} \right)^2 + \sum_{i \in S_{bc}} w_i y_i \tag{2.6.4}$$

where w_i corresponds to the weight of state y_i related to binary control u_i. The weights are large numbers to make sure that variables y are driven to 0, thereby making binary controls u equal to 0 or 1.

The multi-stage F-OPF problem is assumed to be constructed over n stages (time intervals). The timeline is given in Figure 2-38. Note that $t_{n+1} = t_n + h$.

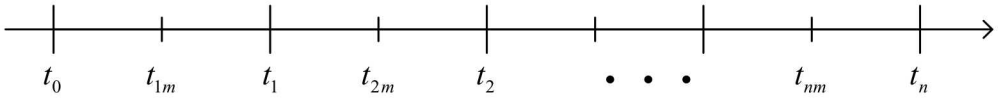

Figure 2-38. Timeline of Stages.

Given a network model and a user-defined objective function, a single-stage quadratic F-OPF model is defined. The objective function, equations and constraints of each single-stage model from stage 1 to stage n are listed below.

Stage 1:

$$\min \quad J(t_1) = Y_{objx}^T \mathbf{x}(t_1,t_{1m}) + Y_{obju}^T \mathbf{u}(t_1,t_{1m}) + \mathbf{x}(t_1,t_{1m})^T F_{objxx} \mathbf{x}(t_1,t_{1m}) + \mathbf{u}(t_1,t_{1m})^T F_{objuu} \mathbf{u}(t_1,t_{1m}) + \mathbf{u}(t_1,t_{1m})^T F_{objux} \mathbf{x}(t_1,t_{1m}) + C_{objc}$$

$$\text{s.t.} \quad 0 = Y_{eqx} \mathbf{x}(t_1,t_{1m}) + Y_{equ} \mathbf{u}(t_1,t_{1m}) + \left\{ \begin{matrix} \vdots \\ \mathbf{x}(t_1,t_{1m})^T \left\langle F_{eqxx}^i \right\rangle \mathbf{x}(t_1,t_{1m}) \\ \vdots \end{matrix} \right\} + \left\{ \begin{matrix} \vdots \\ \mathbf{u}(t_1,t_{1m})^T \left\langle F_{equu}^i \right\rangle \mathbf{u}(t_1,t_{1m}) \\ \vdots \end{matrix} \right\} + \left\{ \begin{matrix} \vdots \\ \mathbf{u}(t_1,t_{1m})^T \left\langle F_{equx}^i \right\rangle \mathbf{x}(t_1,t_{1m}) \\ \vdots \end{matrix} \right\} - B_{eq}(t_0) - \mathbf{e}_{lhs}(t_1,t_{1m})$$

$$B_{eq}(t_0) = -N_{eqx} \mathbf{x}(t_0) - N_{equ} \mathbf{u}(t_0) - M_{eq} \mathbf{i}(t_0) - K_{eq}$$

$$0 = Y_{ieqx} \mathbf{x}(t_1,t_{1m}) + Y_{iequ} \mathbf{u}(t_1,t_{1m}) + \left\{ \begin{matrix} \vdots \\ \mathbf{x}(t_1,t_{1m})^T \left\langle F_{ieqxx}^i \right\rangle \mathbf{x}(t_1,t_{1m}) \\ \vdots \end{matrix} \right\} + \left\{ \begin{matrix} \vdots \\ \mathbf{u}(t_1,t_{1m})^T \left\langle F_{iequu}^i \right\rangle \mathbf{u}(t_1,t_{1m}) \\ \vdots \end{matrix} \right\} + \left\{ \begin{matrix} \vdots \\ \mathbf{u}(t_1,t_{1m})^T \left\langle F_{iequx}^i \right\rangle \mathbf{x}(t_1,t_{1m}) \\ \vdots \end{matrix} \right\} - B_{ieq}(t_0) - \mathbf{i}(t_1)$$

$$B_{ieq}(t_0) = -N_{ieqx} \mathbf{x}(t_0) - N_{iequ} \mathbf{u}(t_0) - M_{ieq} \mathbf{i}(t_0) - K_{ieq}$$

$$\mathbf{h}(t_1) = Y_{feqx} \mathbf{x}(t_1,t_{1m}) + Y_{fequ} \mathbf{u}(t_1,t_{1m}) + \left\{ \begin{matrix} \vdots \\ \mathbf{x}(t_1,t_{1m})^T \left\langle F_{feqxx}^i \right\rangle \mathbf{x}(t_1,t_{1m}) \\ \vdots \end{matrix} \right\} + \left\{ \begin{matrix} \vdots \\ \mathbf{u}(t_1,t_{1m})^T \left\langle F_{fequu}^i \right\rangle \mathbf{u}(t_1,t_{1m}) \\ \vdots \end{matrix} \right\} + \left\{ \begin{matrix} \vdots \\ \mathbf{u}(t_1,t_{1m})^T \left\langle F_{fequx}^i \right\rangle \mathbf{x}(t_1,t_{1m}) \\ \vdots \end{matrix} \right\} + C_{feqc} \le 0$$

$$\mathbf{u}_{min} \le \mathbf{u}(t_1,t_{1m}) \le \mathbf{u}_{max}$$

$$\left| \mathbf{d}(t_1,t_{1m}) \right| \le \mathbf{u}_{llim}$$

Stage 2:

$$\min \quad J(t_2) = Y_{objx}^T \mathbf{x}(t_2,t_{2m}) + Y_{obju}^T \mathbf{u}(t_2,t_{2m}) + \mathbf{x}(t_2,t_{2m})^T F_{objxx} \mathbf{x}(t_2,t_{2m}) + \mathbf{u}(t_2,t_{2m})^T F_{objuu} \mathbf{u}(t_2,t_{2m}) + \mathbf{u}(t_2,t_{2m})^T F_{objux} \mathbf{x}(t_2,t_{2m}) + C_{objc}$$

$$\text{s.t.} \quad 0 = Y_{eqx} \mathbf{x}(t_2,t_{2m}) + Y_{equ} \mathbf{u}(t_2,t_{2m}) + \left\{ \begin{matrix} \vdots \\ \mathbf{x}(t_2,t_{2m})^T \left\langle F_{eqxx}^i \right\rangle \mathbf{x}(t_2,t_{2m}) \\ \vdots \end{matrix} \right\} + \left\{ \begin{matrix} \vdots \\ \mathbf{u}(t_2,t_{2m})^T \left\langle F_{equu}^i \right\rangle \mathbf{u}(t_2,t_{2m}) \\ \vdots \end{matrix} \right\} + \left\{ \begin{matrix} \vdots \\ \mathbf{u}(t_2,t_{2m})^T \left\langle F_{equx}^i \right\rangle \mathbf{x}(t_2,t_{2m}) \\ \vdots \end{matrix} \right\} - B_{eq}(t_1) - \mathbf{e}_{lhs}(t_2,t_{2m})$$

$$B_{eq}(t_1) = -N_{eqx} \mathbf{x}(t_1) - N_{equ} \mathbf{u}(t_1) - M_{eq} \mathbf{i}(t_1) - K_{eq}$$

$$0 = Y_{ieqx} \mathbf{x}(t_2,t_{2m}) + Y_{iequ} \mathbf{u}(t_2,t_{2m}) + \left\{ \begin{matrix} \vdots \\ \mathbf{x}(t_2,t_{2m})^T \left\langle F_{ieqxx}^i \right\rangle \mathbf{x}(t_2,t_{2m}) \\ \vdots \end{matrix} \right\} + \left\{ \begin{matrix} \vdots \\ \mathbf{u}(t_2,t_{2m})^T \left\langle F_{iequu}^i \right\rangle \mathbf{u}(t_2,t_{2m}) \\ \vdots \end{matrix} \right\} + \left\{ \begin{matrix} \vdots \\ \mathbf{u}(t_2,t_{2m})^T \left\langle F_{iequx}^i \right\rangle \mathbf{x}(t_2,t_{2m}) \\ \vdots \end{matrix} \right\} - B_{ieq}(t_1) - \mathbf{i}(t_2)$$

$$B_{ieq}(t_1) = -N_{ieqx} \mathbf{x}(t_1) - N_{iequ} \mathbf{u}(t_1) - M_{ieq} \mathbf{i}(t_1) - K_{ieq}$$

$$\mathbf{h}(t_2) = Y_{feqx} \mathbf{x}(t_2,t_{2m}) + Y_{fequ} \mathbf{u}(t_2,t_{2m}) + \left\{ \begin{matrix} \vdots \\ \mathbf{x}(t_2,t_{2m})^T \left\langle F_{feqxx}^i \right\rangle \mathbf{x}(t_2,t_{2m}) \\ \vdots \end{matrix} \right\} + \left\{ \begin{matrix} \vdots \\ \mathbf{u}(t_2,t_{2m})^T \left\langle F_{fequu}^i \right\rangle \mathbf{u}(t_2,t_{2m}) \\ \vdots \end{matrix} \right\} + \left\{ \begin{matrix} \vdots \\ \mathbf{u}(t_2,t_{2m})^T \left\langle F_{fequx}^i \right\rangle \mathbf{x}(t_2,t_{2m}) \\ \vdots \end{matrix} \right\} + C_{feqc} \le 0$$

$$\mathbf{u}_{min} \le \mathbf{u}(t_2,t_{2m}) \le \mathbf{u}_{max}$$

$$\left| \mathbf{d}(t_2,t_{2m}) \right| \le \mathbf{u}_{llim}$$

Stage n :

$$\min \quad J(t_n) = Y_{objx}^T \mathbf{x}(t_n, t_{nm}) + Y_{obju}^T \mathbf{u}(t_n, t_{nm}) + \mathbf{x}(t_n, t_{nm})^T F_{objxx} \mathbf{x}(t_n, t_{nm}) + \mathbf{u}(t_n, t_{nm})^T F_{objuu} \mathbf{u}(t_n, t_{nm}) + \mathbf{u}(t_n, t_{nm})^T F_{objux} \mathbf{x}(t_n, t_{nm}) + C_{objc}$$

$$\text{s.t.} \quad 0 = Y_{eqx} \mathbf{x}(t_n, t_{nm}) + Y_{equ} \mathbf{u}(t_n, t_{nm}) + \left\{ \begin{matrix} \vdots \\ \mathbf{x}(t_n, t_{nm})^T \left\langle F_{eqxx}^i \right\rangle \mathbf{x}(t_n, t_{nm}) \\ \vdots \end{matrix} \right\} + \left\{ \begin{matrix} \vdots \\ \mathbf{u}(t_n, t_{nm})^T \left\langle F_{equu}^i \right\rangle \mathbf{u}(t_n, t_{nm}) \\ \vdots \end{matrix} \right\} + \left\{ \begin{matrix} \vdots \\ \mathbf{u}(t_n, t_{nm})^T \left\langle F_{equx}^i \right\rangle \mathbf{x}(t_n, t_{nm}) \\ \vdots \end{matrix} \right\} - B_{eq}(t_{n-1}) - \mathbf{e}_{lhs}(t_n, t_{nm})$$

$$B_{eq}(t_{n-1}) = -N_{eqx} \mathbf{x}(t_{n-1}) - N_{equ} \mathbf{u}(t_{n-1}) - M_{eq} \mathbf{i}(t_{n-1}) - K_{eq}$$

$$0 = Y_{ieqx} \mathbf{x}(t_n, t_{nm}) + Y_{iequ} \mathbf{u}(t_n, t_{nm}) + \left\{ \begin{matrix} \vdots \\ \mathbf{x}(t_n, t_{nm})^T \left\langle F_{ieqxx}^i \right\rangle \mathbf{x}(t_n, t_{nm}) \\ \vdots \end{matrix} \right\} + \left\{ \begin{matrix} \vdots \\ \mathbf{u}(t_n, t_{nm})^T \left\langle F_{iequu}^i \right\rangle \mathbf{u}(t_n, t_{nm}) \\ \vdots \end{matrix} \right\} + \left\{ \begin{matrix} \vdots \\ \mathbf{u}(t_n, t_{nm})^T \left\langle F_{iequx}^i \right\rangle \mathbf{x}(t_n, t_{nm}) \\ \vdots \end{matrix} \right\} - B_{ieq}(t_{n-1}) - \mathbf{i}(t_n)$$

$$B_{ieq}(t_{n-1}) = -N_{ieqx} \mathbf{x}(t_{n-1}) - N_{iequ} \mathbf{u}(t_{n-1}) - M_{ieq} \mathbf{i}(t_{n-1}) - K_{ieq}$$

$$\mathbf{h}(t_n) = Y_{feqx} \mathbf{x}(t_n, t_{nm}) + Y_{fequ} \mathbf{u}(t_n, t_{nm}) + \left\{ \begin{matrix} \vdots \\ \mathbf{x}(t_n, t_{nm})^T \left\langle F_{feqxx}^i \right\rangle \mathbf{x}(t_n, t_{nm}) \\ \vdots \end{matrix} \right\} + \left\{ \begin{matrix} \vdots \\ \mathbf{u}(t_n, t_{nm})^T \left\langle F_{fequu}^i \right\rangle \mathbf{u}(t_n, t_{nm}) \\ \vdots \end{matrix} \right\} + \left\{ \begin{matrix} \vdots \\ \mathbf{u}(t_n, t_{nm})^T \left\langle F_{fequx}^i \right\rangle \mathbf{x}(t_n, t_{nm}) \\ \vdots \end{matrix} \right\} + C_{feqc} \le 0$$

$$\mathbf{u}_{min} \le \mathbf{u}(t_n, t_{nm}) \le \mathbf{u}_{max}$$

$$\left| \mathbf{d}(t_n, t_{nm}) \right| \le \mathbf{u}_{llim}$$

The general form of the multi-stage F-OPF is

$$\begin{aligned}
&\min \quad J(\mathbf{x}, \mathbf{u}) = Y_{Mobjx}^T \mathbf{x} + Y_{Mobju}^T \mathbf{u} + \mathbf{x}^T F_{Mobjxx} \mathbf{x} + \mathbf{u}^T F_{Mobjuu} \mathbf{u} + \mathbf{u}^T F_{Mobjux} \mathbf{x} + C_{Mobjc} \\
&\text{s.t.} \quad 0 = \mathbf{g}(\mathbf{x}, \mathbf{u}) = Y_{Meqx} \mathbf{x} + Y_{Mequ} \mathbf{u} + \left\{ \begin{matrix} \vdots \\ \mathbf{x}^T \left\langle F_{Meqxx}^i \right\rangle \mathbf{x} \\ \vdots \end{matrix} \right\} + \left\{ \begin{matrix} \vdots \\ \mathbf{u}^T \left\langle F_{Mequu}^i \right\rangle \mathbf{u} \\ \vdots \end{matrix} \right\} + \left\{ \begin{matrix} \vdots \\ \mathbf{u}^T \left\langle F_{Mequx}^i \right\rangle \mathbf{x} \\ \vdots \end{matrix} \right\} + K_{Meq} - \mathbf{e}_{lhs} \\
&\qquad \mathbf{h}(\mathbf{x}, \mathbf{u}) = Y_{Mfeqx} \mathbf{x} + Y_{Mfequ} \mathbf{u} + \left\{ \begin{matrix} \vdots \\ \mathbf{x}^T \left\langle F_{Mfeqxx}^i \right\rangle \mathbf{x} \\ \vdots \end{matrix} \right\} + \left\{ \begin{matrix} \vdots \\ \mathbf{u}^T \left\langle F_{Mfequu}^i \right\rangle \mathbf{u} \\ \vdots \end{matrix} \right\} + \left\{ \begin{matrix} \vdots \\ \mathbf{u}^T \left\langle F_{Mfequx}^i \right\rangle \mathbf{x} \\ \vdots \end{matrix} \right\} + C_{Mfeqc} \le 0 \\
&\qquad \mathbf{u}_{Mmin} \le \mathbf{u} \le \mathbf{u}_{Mmax} \\
&\qquad \left| \mathbf{d} \right| \le \mathbf{u}_{Mllim}
\end{aligned} \tag{2.6.5}$$

where M in the subscript denotes the multi-stage QFOPFM. Note that the device through variables also become part of the states in the F-OPF problem. The states and controls are

$$\mathbf{x} = \left[\mathbf{x}(t_1) \quad \mathbf{x}(t_{1m}) \quad \mathbf{i}(t_1) \quad \mathbf{x}(t_2) \quad \mathbf{x}(t_{2m}) \quad \mathbf{i}(t_2) \quad \cdots \quad \mathbf{x}(t_n) \quad \mathbf{x}(t_{nm}) \quad \mathbf{i}(t_n) \right]^T$$

$$\mathbf{u} = \left[\mathbf{u}(t_1) \quad \mathbf{u}(t_{1m}) \quad \mathbf{u}(t_2) \quad \mathbf{u}(t_{2m}) \quad \cdots \quad \mathbf{u}(t_n) \quad \mathbf{u}(t_{nm}) \right]^T$$

The objective function of the multi-stage QFOPFM is given by

$$Y_{Mobjx} = \begin{bmatrix} Y_{objx} \\ 0 \\ Y_{objx} \\ 0 \\ \vdots \\ Y_{objx} \\ 0 \end{bmatrix} \qquad Y_{Mobju} = \begin{bmatrix} Y_{obju} \\ Y_{obju} \\ \vdots \\ Y_{obju} \end{bmatrix} \qquad F_{Mobjxx} = \begin{bmatrix} F_{objxx} & & & & & & \\ & 0 & & & & & \\ & & F_{objxx} & & & & \\ & & & 0 & & & \\ & & & & \ddots & & \\ & & & & & F_{objxx} & \\ & & & & & & 0 \end{bmatrix}$$

$$F_{Mobjuu} = \begin{bmatrix} F_{objuu} & & & \\ & F_{objuu} & & \\ & & \ddots & \\ & & & F_{objuu} \end{bmatrix} \qquad F_{Mobjux} = \begin{bmatrix} F_{objux} & 0 & & \\ & F_{objux} & 0 & \\ & & \ddots & \\ & & & F_{objux} \quad 0 \end{bmatrix}$$

$$C_{Mobjc} = nC_{objc}$$

Note that the past history vectors B_{eq} link variables among different stages. As long there are past history vectors, the various stages are coupled. In absence of coupling, the problem collapses to the problem of n independent OPF problems. Hence, with $B_{eq}(t_0)$ known, the corresponding matrices and vectors in the equality constraints of the multi-stage QFOPFM are given by

$$Y_{Meqx} = \begin{bmatrix} Y_{eqx} & 0 & & & & & & \\ Y_{ieqx} & -I & & & & & & \\ N_{eqx} & M_{eq} & Y_{eqx} & 0 & & & & \\ N_{ieqx} & M_{ieq} & Y_{ieqx} & -I & & & & \\ & & N_{eqx} & M_{eq} & Y_{eqx} & 0 & & \\ & & N_{ieqx} & M_{ieq} & Y_{ieqx} & -I & & \\ & & & & & & \ddots & \\ & & & & & & N_{eqx} \quad M_{eq} & Y_{eqx} \quad 0 \\ & & & & & & N_{ieqx} \quad M_{ieq} & Y_{ieqx} \quad -I \end{bmatrix}$$

$$Y_{Mequ} = \begin{bmatrix} Y_{equ} & 0 & & & & \\ Y_{equ} & 0 & & & & \\ N_{equ} & Y_{equ} & & & & \\ N_{iequ} & Y_{iequ} & & & & \\ & N_{equ} & Y_{equ} & & & \\ & N_{iequ} & Y_{iequ} & & & \\ & & & \ddots & & \\ & & & & N_{equ} & Y_{equ} \\ & & & & N_{iequ} & Y_{iequ} \end{bmatrix} \qquad F_{Meqxx} = \begin{bmatrix} F_{eqxx} & & & & & \\ F_{ieqxx} & & & & & \\ & F_{eqxx} & & & & \\ & F_{ieqxx} & & & & \\ & & F_{eqxx} & & & \\ & & F_{ieqxx} & & & \\ & & & \ddots & & \\ & & & & & F_{eqxx} \\ & & & & & F_{ieqxx} \end{bmatrix}$$

$$F_{Mequu}=\begin{bmatrix} F_{equu} & & & & & \\ F_{iequu} & & & & & \\ & F_{equu} & & & & \\ & F_{iequu} & & & & \\ & & F_{equu} & & & \\ & & F_{iequu} & & & \\ & & & \ddots & & \\ & & & & F_{equu} & \\ & & & & F_{iequu} & \end{bmatrix} \qquad F_{Mequx}=\begin{bmatrix} F_{equx} & & & & & \\ F_{iequx} & & & & & \\ & F_{equx} & & & & \\ & F_{iequx} & & & & \\ & & F_{equx} & & & \\ & & F_{iequx} & & & \\ & & & \ddots & & \\ & & & & F_{equx} & \\ & & & & F_{iequx} & \end{bmatrix}$$

$$K_{Meq}=\begin{bmatrix} -B_{eq}(t_0) & -B_{ieq}(t_0) & K_{eq} & K_{ieq} & K_{eq} & K_{ieq} & \cdots & K_{eq} & K_{ieq} \end{bmatrix}^T$$

$$\mathbf{e}_{lhs}=\begin{bmatrix} \mathbf{e}_{lhs}(t_1) & \mathbf{e}_{lhs}(t_{1m}) & 0 & \mathbf{e}_{lhs}(t_2) & \mathbf{e}_{lhs}(t_{2m}) & 0 & \cdots & \mathbf{e}_{lhs}(t_n) & \mathbf{e}_{lhs}(t_{nm}) & 0 \end{bmatrix}^T$$

As for the inequality constraints and control limits, the corresponding matrices and vectors in the multi-stage QFOPFM are

$$Y_{Mfeqx}=\begin{bmatrix} Y_{feqx} & 0 & & & \\ & Y_{feqx} & 0 & & \\ & & \ddots & & \\ & & & Y_{feqx} & 0 \end{bmatrix} \qquad Y_{Mfequ}=\begin{bmatrix} Y_{fequ} & & & \\ & Y_{fequ} & & \\ & & \ddots & \\ & & & Y_{fequ} \end{bmatrix}$$

$$F_{Mfeqxx}=\begin{bmatrix} F_{feqxx} & & & \\ & F_{feqxx} & & \\ & & \ddots & \\ & & & F_{feqxx} \end{bmatrix} \qquad F_{Mfequu}=\begin{bmatrix} F_{fequu} & & & \\ & F_{fequu} & & \\ & & \ddots & \\ & & & F_{fequu} \end{bmatrix}$$

$$F_{Mfequx}=\begin{bmatrix} F_{fequx} & & & \\ & F_{fequx} & & \\ & & \ddots & \\ & & & F_{fequx} \end{bmatrix} \qquad C_{Mfeqc}=\begin{bmatrix} C_{feqc} \\ C_{feqc} \\ \vdots \\ C_{feqc} \end{bmatrix}$$

$$\mathbf{u_{Mmax}}=\begin{bmatrix} \mathbf{u_{max}} & \mathbf{u_{max}} & \cdots & \mathbf{u_{max}} \end{bmatrix}^T,\ \mathbf{u_{Mmin}}=\begin{bmatrix} \mathbf{u_{min}} & \mathbf{u_{min}} & \cdots & \mathbf{u_{min}} \end{bmatrix}^T,$$

$$\mathbf{u_{Mllim}}=\begin{bmatrix} \mathbf{u_{llim}} & \mathbf{u_{llim}} & \cdots & \mathbf{u_{llim}} \end{bmatrix}^T,\ \mathbf{d}=\begin{bmatrix} \mathbf{d}(t_1) & \mathbf{d}(t_{1m}) & \mathbf{d}(t_2) & \mathbf{d}(t_{2m}) & \cdots & \mathbf{d}(t_n) & \mathbf{d}(t_{nm}) \end{bmatrix}^T$$

With the QFOPFM in (2.6.5) successfully formed, the problem is first normalized before the solution method proceeds to the SLP algorithm.

2.5.3.4. Linearized F-OPF Model

Once the multi-stage QFOPFM is obtained together with initial operating point $\left(\mathbf{x}^0, \mathbf{u}^0\right)$, the SLP solution process begins. The linearized F-OPF model (LFOPFM) is used to represent the linearized optimal power flow problem derived from the QFOPFM using linearization techniques. The reasons for linearization are:

1. The QFOPFM consists of both state variables and control variables. To simplify the problem, we apply the co-state method so that the F-OPF problem becomes a linearized problem represented by only control variables.
2. After the linearization, with the help of the standard linear programming solver, we can easily solve the OPF problem.

The expression of the LFOPFM is:

$$\begin{aligned} &\textit{Minimize}: \quad J\left(\mathbf{d}\right) = c^T\mathbf{d} + e \\ &\textit{subject to}: \quad a\mathbf{d} + b \le 0 \\ &\qquad\qquad\quad \mathbf{d}_{\min} \le \mathbf{d} \le \mathbf{d}_{\max} \end{aligned} \tag{2.6.6}$$

where $\mathbf{d}_{\min}$ and $\mathbf{d}_{\max}$ are the lower and upper bounds. Vector c contains the linear coefficients of the objective function and e is the constant term. Matrix a and vector b correspond to the linear coefficients and constant terms in the inequality constraints, respectively.

Before the linearization of inequalities, the set of inequalities that are considered need to be defined. Hence, the current operating state and control variables $\left(\mathbf{x}^\nu, \mathbf{u}^\nu\right)$ are substituted into the QFOPFM inequality constraints to check for violations. Violated constraints are marked as model constraints. For instance, if constraint $h_i\left(\mathbf{x}^\nu, \mathbf{u}^\nu\right) \ge \varepsilon_0$, $h_i\left(\mathbf{x}^\nu, \mathbf{u}^\nu\right) \le 0$ is considered as a model constraint.

Linearization of the objective function $J\left(\mathbf{x}, \mathbf{u}\right)$ around the present operating point yields:

$$J\left(\mathbf{x}, \mathbf{u}\right) \cong J\left(\mathbf{x}^\nu, \mathbf{u}^\nu\right) + \frac{dJ\left(\mathbf{x}^\nu, \mathbf{u}^\nu\right)}{d\mathbf{u}}\mathbf{d} \tag{2.6.7}$$

where

$$\frac{dJ\left(\mathbf{x}^\nu, \mathbf{u}^\nu\right)}{d\mathbf{u}} = \frac{\partial J\left(\mathbf{x}^\nu, \mathbf{u}^\nu\right)}{\partial \mathbf{u}} + \frac{\partial J\left(\mathbf{x}^\nu, \mathbf{u}^\nu\right)}{\partial \mathbf{x}}\frac{d\mathbf{x}}{d\mathbf{u}} \tag{2.6.8}$$

Since the objective function is quadratic and all the coefficient matrices have been defined and formed, the partial derivatives $\dfrac{\partial J\left(\mathbf{x}^\nu, \mathbf{u}^\nu\right)}{\partial \mathbf{u}}$ and $\dfrac{\partial J\left(\mathbf{x}^\nu, \mathbf{u}^\nu\right)}{\partial \mathbf{x}}$ can be computed directly:

$$\frac{\partial J\left(\mathbf{x}^\nu, \mathbf{u}^\nu\right)}{\partial \mathbf{u}} = Y_{obju} + \left\{\mathbf{u}^{\nu T} F^i_{objuu}\right\} + \left\{F^i_{objuu}\mathbf{u}^\nu\right\}^T + \left\{F^i_{objux}\mathbf{x}^\nu\right\}^T \tag{2.6.9}$$

$$\frac{\partial J\left(\mathbf{x}^{\nu},\mathbf{u}^{\nu}\right)}{\partial \mathbf{x}} = Y_{objx} + \left\{\mathbf{x}^{\nu T} F^{i}_{objxx}\right\} + \left\{F^{i}_{objxx}\mathbf{x}^{\nu}\right\}^{T} + \left\{\mathbf{u}^{\nu T} F^{i}_{objux}\right\} \tag{2.6.10}$$

The derivative $\frac{d\mathbf{x}}{d\mathbf{u}}$ is obtained from the equality constraints $g\left(\mathbf{x},\mathbf{u}\right)$. Upon differentiation of the equality constraints, with respect to control variable **u**, we have

$$\frac{\partial \mathbf{g}\left(\mathbf{x}^{\nu},\mathbf{u}^{\nu}\right)}{\partial \mathbf{u}} + \frac{\partial \mathbf{g}\left(\mathbf{x}^{\nu},\mathbf{u}^{\nu}\right)}{\partial \mathbf{x}}\frac{d\mathbf{x}}{d\mathbf{u}} = 0 \tag{2.6.11}$$

The solution of $\frac{d\mathbf{x}}{d\mathbf{u}}$ is:

$$\frac{d\mathbf{x}}{d\mathbf{u}} = -\left(\frac{\partial \mathbf{g}\left(\mathbf{x}^{\nu},\mathbf{u}^{\nu}\right)}{\partial \mathbf{x}}\right)^{-1}\frac{\partial \mathbf{g}\left(\mathbf{x}^{\nu},\mathbf{u}^{\nu}\right)}{\partial \mathbf{u}} \tag{2.6.12}$$

Since the equality constraints are also quadratic and all the coefficient matrices have been defined and formed, the partial derivatives $\frac{\partial \mathbf{g}\left(\mathbf{x}^{\nu},\mathbf{u}^{\nu}\right)}{\partial \mathbf{x}}$ and $\frac{\partial \mathbf{g}\left(\mathbf{x}^{\nu},\mathbf{u}^{\nu}\right)}{\partial \mathbf{u}}$ are automatically computed as

$$\frac{\partial \mathbf{g}\left(\mathbf{x}^{\nu},\mathbf{u}^{\nu}\right)}{\partial \mathbf{u}} = Y_{equ} + \left\{\mathbf{u}^{\nu T} F^{i}_{equu}\right\} + \left\{F^{i}_{equu}\mathbf{u}^{\nu}\right\}^{T} + \left\{F^{i}_{equx}\mathbf{x}^{\nu}\right\}^{T} \tag{2.6.13}$$

$$\frac{\partial \mathbf{g}\left(\mathbf{x}^{\nu},\mathbf{u}^{\nu}\right)}{\partial \mathbf{x}} = Y_{eqx} + \left\{\mathbf{x}^{\nu T} F^{i}_{eqxx}\right\} + \left\{F^{i}_{eqxx}\mathbf{x}^{\nu}\right\}^{T} + \left\{\mathbf{u}^{\nu T} F^{i}_{equx}\right\} \tag{2.6.14}$$

By back substitution in $\frac{dJ\left(\mathbf{x}^{\nu},\mathbf{u}^{\nu}\right)}{d\mathbf{u}}$ yields

$$\frac{dJ\left(\mathbf{x}^{\nu},\mathbf{u}^{\nu}\right)}{d\mathbf{u}} = \frac{\partial J\left(\mathbf{x}^{\nu},\mathbf{u}^{\nu}\right)}{\partial \mathbf{u}} - \frac{\partial J\left(\mathbf{x}^{\nu},\mathbf{u}^{\nu}\right)}{\partial \mathbf{x}}\left(\frac{\partial \mathbf{g}\left(\mathbf{x}^{\nu},\mathbf{u}^{\nu}\right)}{\partial \mathbf{x}}\right)^{-1}\frac{\partial \mathbf{g}\left(\mathbf{x}^{\nu},\mathbf{u}^{\nu}\right)}{\partial \mathbf{u}} \tag{2.6.15}$$

Note that $\frac{\partial J\left(\mathbf{x}^{\nu},\mathbf{u}^{\nu}\right)}{\partial \mathbf{x}}\left(\frac{\partial \mathbf{g}\left(\mathbf{x}^{\nu},\mathbf{u}^{\nu}\right)}{\partial \mathbf{x}}\right)^{-1}$ is the co-state vector that is independent of the control variables, and it is pre-computed at the present operating point. The vector is represented by $\hat{\mathbf{x}}$, and we have:

$$\hat{\mathbf{x}} = \frac{\partial J\left(\mathbf{x}^{\nu},\mathbf{u}^{\nu}\right)}{\partial \mathbf{x}}\left(\frac{\partial \mathbf{g}\left(\mathbf{x}^{\nu},\mathbf{u}^{\nu}\right)}{\partial \mathbf{x}}\right)^{-1} \tag{2.6.16}$$

As a result, the linearization of the objective function around the present operating point is:

$$J(\mathbf{x},\mathbf{u}) \cong J(\mathbf{x}^{\nu},\mathbf{u}^{\nu}) + \left(\frac{\partial J(\mathbf{x}^{\nu},\mathbf{u}^{\nu})}{\partial \mathbf{u}} - \hat{\mathbf{x}} \frac{\partial \mathbf{g}(\mathbf{x}^{\nu},\mathbf{u}^{\nu})}{\partial \mathbf{u}} \right) \mathbf{d} \tag{2.6.17}$$

Therefore, linear coefficient vector c and constant term e in the objective function are given by:

$$c^T = \frac{dJ(\mathbf{x}^{\nu},\mathbf{u}^{\nu})}{d\mathbf{u}} = \frac{\partial J(\mathbf{x}^{\nu},\mathbf{u}^{\nu})}{\partial \mathbf{u}} - \hat{\mathbf{x}} \frac{\partial \mathbf{g}(\mathbf{x}^{\nu},\mathbf{u}^{\nu})}{\partial \mathbf{u}} \tag{2.6.18}$$

$$e = J(\mathbf{x}^{\nu},\mathbf{u}^{\nu}) \tag{2.6.19}$$

The inequality constraints are linearized in a similar way as the objective function. Linearization of model constraint functions $\mathbf{h}_m(\mathbf{x}^{\nu},\mathbf{u}^{\nu})$ around the present operating point yields:

$$\mathbf{h}_m(\mathbf{x},\mathbf{u}) \cong \mathbf{h}_m(\mathbf{x}^{\nu},\mathbf{u}^{\nu}) + \frac{d\mathbf{h}_m(\mathbf{x}^{\nu},\mathbf{u}^{\nu})}{d\mathbf{u}} \mathbf{d} \tag{2.6.20}$$

where

$$\frac{d\mathbf{h}_m(\mathbf{x}^{\nu},\mathbf{u}^{\nu})}{d\mathbf{u}} = \frac{\partial \mathbf{h}_m(\mathbf{x}^{\nu},\mathbf{u}^{\nu})}{\partial \mathbf{u}} + \frac{\partial \mathbf{h}_m(\mathbf{x}^{\nu},\mathbf{u}^{\nu})}{\partial \mathbf{x}} \frac{d\mathbf{x}}{d\mathbf{u}} \tag{2.6.21}$$

Since the inequality constraints are also quadratic and all the coefficient matrices have been defined and formed, the partial derivatives $\frac{\partial \mathbf{h}_m(\mathbf{x}^{\nu},\mathbf{u}^{\nu})}{\partial \mathbf{u}}$ and $\frac{\partial \mathbf{h}_m(\mathbf{x}^{\nu},\mathbf{u}^{\nu})}{\partial \mathbf{x}}$ are computed directly:

$$\frac{\partial \mathbf{h}_m(\mathbf{x}^{\nu},\mathbf{u}^{\nu})}{\partial \mathbf{u}} = Y_{fequ} + \left\{ \mathbf{u}^{\nu T} F^i_{fequu} \right\} + \left\{ F^i_{fequu} \mathbf{u}^{\nu} \right\}^T + \left\{ F^i_{fequx} \mathbf{x}^{\nu} \right\}^T \tag{2.6.22}$$

$$\frac{\partial \mathbf{h}_m(\mathbf{x}^{\nu},\mathbf{u}^{\nu})}{\partial \mathbf{x}} = Y_{feqx} + \left\{ \mathbf{x}^{\nu T} F^i_{feqxx} \right\} + \left\{ F^i_{feqxx} \mathbf{x}^{\nu} \right\}^T + \left\{ \mathbf{u}^{\nu T} F^i_{fequx} \right\} \tag{2.6.23}$$

With $\frac{d\mathbf{x}}{d\mathbf{u}}$ already computed, back substitution of $\frac{d\mathbf{x}}{d\mathbf{u}}$ into $\frac{d\mathbf{h}_m(\mathbf{x}^{\nu},\mathbf{u}^{\nu})}{d\mathbf{u}}$ yields:

$$\frac{d\mathbf{h}_m(\mathbf{x}^{\nu},\mathbf{u}^{\nu})}{d\mathbf{u}} = \frac{\partial \mathbf{h}_m(\mathbf{x}^{\nu},\mathbf{u}^{\nu})}{\partial \mathbf{u}} - \frac{\partial \mathbf{h}_m(\mathbf{x}^{\nu},\mathbf{u}^{\nu})}{\partial \mathbf{x}} \left(\frac{\partial \mathbf{g}(\mathbf{x}^{\nu},\mathbf{u}^{\nu})}{\partial \mathbf{x}} \right)^{-1} \frac{\partial \mathbf{g}(\mathbf{x}^{\nu},\mathbf{u}^{\nu})}{\partial \mathbf{u}} \tag{2.6.24}$$

Note that $\frac{\partial \mathbf{h}_m(\mathbf{x}^{\nu},\mathbf{u}^{\nu})}{\partial \mathbf{x}} \left(\frac{\partial \mathbf{g}(\mathbf{x}^{\nu},\mathbf{u}^{\nu})}{\partial \mathbf{x}} \right)^{-1}$ is the co-state matrix that is independent of the control variables, and it is pre-computed at the present operating point. The vector is represented by $\hat{\mathbf{y}}$, and we have:

$$\hat{\mathbf{y}} = \frac{\partial \mathbf{h}_m\left(\mathbf{x}^\nu, \mathbf{u}^\nu\right)}{\partial \mathbf{x}} \left(\frac{\partial \mathbf{g}\left(\mathbf{x}^\nu, \mathbf{u}^\nu\right)}{\partial \mathbf{x}} \right)^{-1} \tag{2.6.25}$$

As a result, the linearization of the inequality constraints around the present operating point is:

$$\mathbf{h}_m\left(\mathbf{x}, \mathbf{u}\right) \cong \mathbf{h}_m\left(\mathbf{x}^\nu, \mathbf{u}^\nu\right) + \left(\frac{\partial \mathbf{h}_m\left(\mathbf{x}^\nu, \mathbf{u}^\nu\right)}{\partial \mathbf{u}} - \hat{\mathbf{y}} \frac{\partial \mathbf{g}\left(\mathbf{x}^\nu, \mathbf{u}^\nu\right)}{\partial \mathbf{u}} \right) \mathbf{d} \tag{2.6.26}$$

Therefore, linear coefficient matrix *a* and constant vector *b* in the objective function are given by

$$a = \frac{d\mathbf{h}_m\left(\mathbf{x}^\nu, \mathbf{u}^\nu\right)}{d\mathbf{u}} = \frac{\partial \mathbf{h}_m\left(\mathbf{x}^\nu, \mathbf{u}^\nu\right)}{\partial \mathbf{u}} - \hat{\mathbf{y}} \frac{\partial \mathbf{g}\left(\mathbf{x}^\nu, \mathbf{u}^\nu\right)}{\partial \mathbf{u}} \tag{2.6.27}$$

$$b = \mathbf{h}_m\left(\mathbf{x}^\nu, \mathbf{u}^\nu\right) \tag{2.6.28}$$

To reduce linearization errors, maximum permissible control excursions $\mathbf{u}_{\mathbf{llim}}$ are utilized expressed with $\mathbf{d}_{\mathbf{min}} \le \mathbf{d} \le \mathbf{d}_{\mathbf{max}}$. These values are imposed as bounds on the control variations between two consecutive iterations. Every entry *i* in $\mathbf{d}_{\mathbf{min}}$ and $\mathbf{d}_{\mathbf{max}}$ are given by

$$\begin{aligned} d_{min,i} &= \max\left(u_{min,i} - u_i^\nu, -u_{llim,i}\right) \\ d_{max,i} &= \min\left(u_{max,i} - u_i^\nu, u_{llim,i}\right) \end{aligned} \tag{2.6.29}$$

2.5.3.5. Solution to F-OPF Problem

To find the optimal operating point of the hybrid system and implement the corresponding control actions, the F-OPF problem is solved iteratively. Once the linear program LFOPFM is solved in iteration ν and the solution is $\mathbf{d}^\nu$, control variables $\mathbf{u}^{\nu+1} = \mathbf{u}^\nu + \mathbf{d}^\nu$ are updated. As the state and control variables obey the equality constraints $g\left(\mathbf{x}, \mathbf{u}\right) = 0$, these equations are used to solve for the updated states $\mathbf{x}^{\nu+1}$ by the Newton-Raphson method. The steps are listed as follows:

1. Let $\kappa = 0$ and $\mathbf{x}^\kappa = \mathbf{x}^\nu$, where κ is the iteration number in the Newton-Raphson method used to obtain the state variables $\mathbf{x}^{\nu+1}$ in iteration $\nu+1$.
2. Substitute $\mathbf{x}^\kappa$ and $\mathbf{u}^{\nu+1}$ into the power flow equations and compute $g\left(\mathbf{x}^\kappa, \mathbf{u}^{\nu+1}\right)$. If $\left\| g\left(\mathbf{x}^\kappa, \mathbf{u}^{\nu+1}\right) \right\| \le \varepsilon_2$, in which case $\mathbf{x}^\kappa$ is the solution $\mathbf{x}^{\nu+1}$ and the procedure is terminated. Otherwise, go to the next step.
3. Compute the Jacobian matrix $\frac{\partial \mathbf{g}\left(\mathbf{x}^\kappa, \mathbf{u}^{\nu+1}\right)}{\partial \mathbf{x}}$.
4. Compute:

$$\mathbf{x}^{\kappa+1} = \mathbf{x}^{\kappa} - \left(\frac{\partial \mathbf{g}\left(\mathbf{x}^{\kappa}, \mathbf{u}^{\nu+1}\right)}{\partial \mathbf{x}} \right)^{-1} \mathbf{g}\left(\mathbf{x}^{\kappa}, \mathbf{u}^{\nu+1}\right)$$

5. Make $\kappa = \kappa + 1$. If $\kappa \le \kappa_{\max}$, go to step (2); otherwise, return nonconvergence. $\kappa_{\max}$ is the user-defined maximum number of iterations allowed to compute states $\mathbf{x}^{\nu+1}$.

The new operating point $\left(\mathbf{x}^{\nu+1}, \mathbf{u}^{\nu+1}\right)$ is thereby formed from the above computed state vector $\mathbf{x}^{\nu+1}$ and control vector $\mathbf{u}^{\nu+1}$. It is used to compute the objective function value $J\left(\mathbf{x}^{\nu+1}, \mathbf{u}^{\nu+1}\right)$. If $J\left(\mathbf{x}^{\nu+1}, \mathbf{u}^{\nu+1}\right) \ge J\left(\mathbf{x}^{\nu}, \mathbf{u}^{\nu}\right)$, the control excursion limits of the non-binary variables are halved.

Three binary convergence indicators are used to determine the SLP convergence. Once the operating point is updated in iteration ν, the first indicator FOPFSolution is set true if the LFOPFM solution is feasible and $\left|\mathbf{d}^{\nu}\right| < \varepsilon_1$, where ε_1 is a user-defined small positive number. Otherwise, FOPFSolution is set to false. After the control excursion limits are adjusted, the SLP algorithm goes into iteration $\nu+1$ and checks for violations in the QFOPFM inequality constraints that are not in the model constraint set. Since the linearized problem does not include all the inequality constraints in the QFOPFM, the new operating point may not satisfy some of them.

The newly violated constraints are added to the set of model constraints. If no such constraint exists, the second indicator NonSolutionModelConstraint is set to true, meaning all constraints that are not included in the set of model constraints are satisfied, or else NonSolutionModelConstraint is set to false. When FOPFSolution = true and NonSolutionModelConstraint = true, violations in the model constraints are checked. The third indicator SolutionModelConstraint is set to false when model constraint violations are found. Otherwise, SolutionModelConstraint is set to true. The SLP algorithm converges only when all three indicators are true. In this case, $\left(\mathbf{x}^{\nu+1}, \mathbf{u}^{\nu+1}\right)$ is the optimal operating point, containing the normalized operating conditions in all stages. The optimal control actions are computed from the $\mathbf{u}^{\nu+1}$ extracted using the control normalization factors and implemented back into the selected optimized system. The SLP algorithm proceeds to the next step, which is the F-OPF linearization process, if any of the indicators has a different Boolean value.

2.5.3.6. Demonstration Case – Voltage Control of an Example Feeder Model

The modified PNM reduced-order feeder model shown in Figure 2-39 is used as an example to demonstrate the voltage control method via multi-stage flexible optimal power flow. The buses circled are the buses selected for voltage optimization. The performance of a 3-stage F-OPF with the objective function being levelizing the voltages at selected buses is shown in this section.

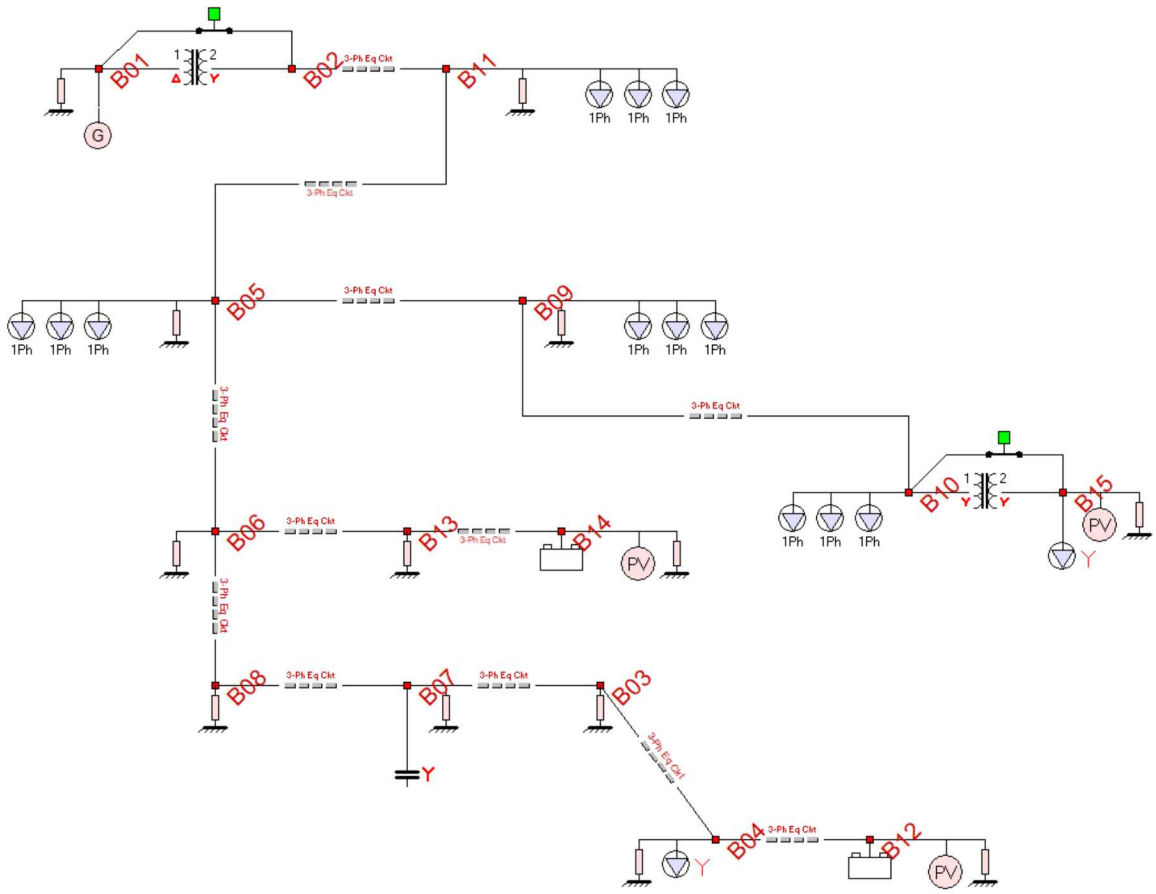

Figure 2-39. Modified PNM Reduced-Order Feeder Model with Energy Storage System.

The example feeder model has 15 three-phase buses and 12 distribution lines. Every bus in the network is grounded through a 1 Ω resistor. The 115 kV transmission system is represented by a 115.01 kV equivalent source at B01, which supplies the 12.47 kV distribution feeder through a delta-wye transformer T1. Another transformer T2 is wye-wye connected at B10 to convert the voltage to 480 V at B15. Both transformers are assumed to have continuous tap-changing capabilities on the secondary windings. A 1.8 MVar capacitor bank is connected at B07. Three PVs are located at B12, B14, and B15 in the network, but only the first two are equipped with an energy storage system (ESS), whose state of charge (SOC) is constrained between 0.1 and 0.9 pu. The reactive power outputs of all PV systems are controllable, while the real power outputs of PV1 at B12, PV2 at B14 and PV3 at B15 are assumed fixed at 1 MW, 10 MW and 258 kW, respectively. The control variables of an ESS are the real power output and the line-to-line voltage at the connected bus. ESS1 at B12 and ESS2 at B14 can store up to 1 and 2 MWh of energy, respectively. The power ratings of their charging/discharging converters are 10 and 20 MVA. Their initial SOC values at time t_0 are 0.13 and 0.8 pu, respectively. The loads are provided in

Table 2-17.

Table 2-17. List of Loads.

Type	Location	Phase	Power Consumption
Single-Phase	B05	A	28.1822 W, -8.95 Var
Single-Phase	B05	B	2.2883 kW, 0.4137 kVar
Single-Phase	B05	C	393.9987 W, 154.4010 Var
Single-Phase	B09	A	97.1185 kW, 22.0604 kVar
Single-Phase	B09	B	100.5786 kW, 22.4071 kVar
Single-Phase	B09	C	116.3177 kW, 25.6155 kVar
Single-Phase	B10	A	107.3842 kW, 11.5588 kVar
Single-Phase	B10	B	108.5619 kW, 11.9113 kVar
Single-Phase	B10	C	118.9302 kW, 12.6054 kVar
Single-Phase	B11	A	0.01 W, 3.4387 Var
Single-Phase	B11	B	3.8603 kW, 0.4895 kVar
Single-Phase	B11	C	2.6704 kW, 0.3025 kVar
Three-Phase	B04	A/B/C	1885 kW, 1292 kVar
Three-Phase	B15	A/B/C	25.5 kW, 19.2 kVar

The time step h is equal to 5 minutes and the pre-defined small positive numbers are defined as $\varepsilon_0 = \varepsilon_1 = \varepsilon_2 = 0.0001$. Three-phase voltages at B04, B05, B07, B09, B11 and B15 are selected for voltage profile optimization, all with tolerance $\mu = 5\%$. The target phase voltage V_{tar} is 277.13 V for B15, while for the other 5 buses $V_{tar} = 7.2$ kV. The algorithm converges in 10 iterations.

Table 2-18 summarizes the controls available in the feeder model, including their initial values and optimal values in all stages. We use P and Q to denote the real and reactive power outputs correspondingly, while V is the line voltage. The voltage profile of the PNM feeder model after optimization is shown in

Table 2-19. Let V_{an}, V_{bn} and V_{cn} denote the voltages for phase A, B and C, respectively. The target value and initial value of the selected bus voltages are also presented for references. With the multi-stage F-OPF applied, all voltages are successfully driven towards their target values in all 3 stages. Therefore, controlling the PVs and ESSs through the proposed method can optimize the voltage profile for the PNM feeder.

Table 2-18. Available Control Variables.

Device	Location	Control	Initial Value	Optimal Value		
				Stage 1 Value	Stage 2 Value	Stage 3 Value
T1	B01-B02	Tap	1	1.0142	1.0139	1.0139
T2	B10-B15	Tap	1	1.0036	1.0035	1.0035
PV1	B12	Q	0 kVar	-150.0784 kVar	-135.9942 kVar	-112.3263 kVar
PV2	B14	Q	0 kVar	472.1766 kVar	24.0824 kVar	-54.3522 kVar
PV3	B15	Q	0 kVar	3.6621 kVar	3.5645 kVar	3.8574 kVar
ESS1	B12	P	-500 kW	20.5925 kW	-38.4587 kW	-102.5390 kW
		V	12.47 kV	12.4639 kV	12.4639 kV	12.4639 kV
ESS2	B14	P	1 MW	0.2832 MW	0.2793 MW	0. 2949 MW
		V	12.47 kV	12.4873 kV	12.4878 kV	12.4873 kV

Table 2-19. Example Feeder Model Voltage Profile.

Location	Selected Voltage	Target Value	Initial Value	Optimal Value		
				Stage 1 Value	Stage 2 Value	Stage 3 Value
B04	V_{an}	7.2 kV	7.1998 kV	7.1966 kV	7.1966 kV	7.1966 kV
	V_{bn}	7.2 kV	7.1997 kV	7.1963 kV	7.1963 kV	7.1963 kV
	V_{cn}	7.2 kV	7.1975 kV	7.1944 kV	7.1944 kV	7.1944 kV
B05	V_{an}	7.2 kV	7.1751 kV	7.2000 kV	7.1999 kV	7.2001 kV
	V_{bn}	7.2 kV	7.1719 kV	7.1968 kV	7.1966 kV	7.1968 kV
	V_{cn}	7.2 kV	7.1703 kV	7.1958 kV	7.1956 kV	7.1958 kV
B07	V_{an}	7.2 kV	7.2048 kV	7.2078 kV	7.2078 kV	7.2078 kV
	V_{bn}	7.2 kV	7.2045 kV	7.2072 kV	7.2072 kV	7.2073 kV
	V_{cn}	7.2 kV	7.2021 kV	7.2052 kV	7.2052 kV	7.2052 kV
B09	V_{an}	7.2 kV	7.1756 kV	7.2005 kV	7.2003 kV	7.2005 kV
	V_{bn}	7.2 kV	7.1729 kV	7.1978 kV	7.1976 kV	7.1978 kV
	V_{cn}	7.2 kV	7.1670 kV	7.1925 kV	7.1924 kV	7.1926 kV
B11	V_{an}	7.2 kV	7.1316 kV	7.2040 kV	7.2031 kV	7.2036 kV
	V_{bn}	7.2 kV	7.1300 kV	7.1988 kV	7.1979 kV	7.1984 kV
	V_{cn}	7.2 kV	7.1285 kV	7.2000 kV	7.1991 kV	7.1996 kV
B15	V_{an}	277.13 V	275.3034 V	281.2365 V	281.1798 V	281.2032 V
	V_{bn}	277.13 V	275.0719 V	275.2665 V	275.2099 V	275.2330 V
	V_{cn}	277.13 V	274.8051 V	275.0172 V	274.9598 V	274.9830 V

Figure 2-40 shows the SOC of ESS1 and ESS2 from t_0 to t_3 upon convergence. Both SOC values are constrained within limits over all 3 stages. The objective function value is plotted against the number of SLP iterations in Figure 2-41. Results for additional iterations after algorithm convergence are shown.

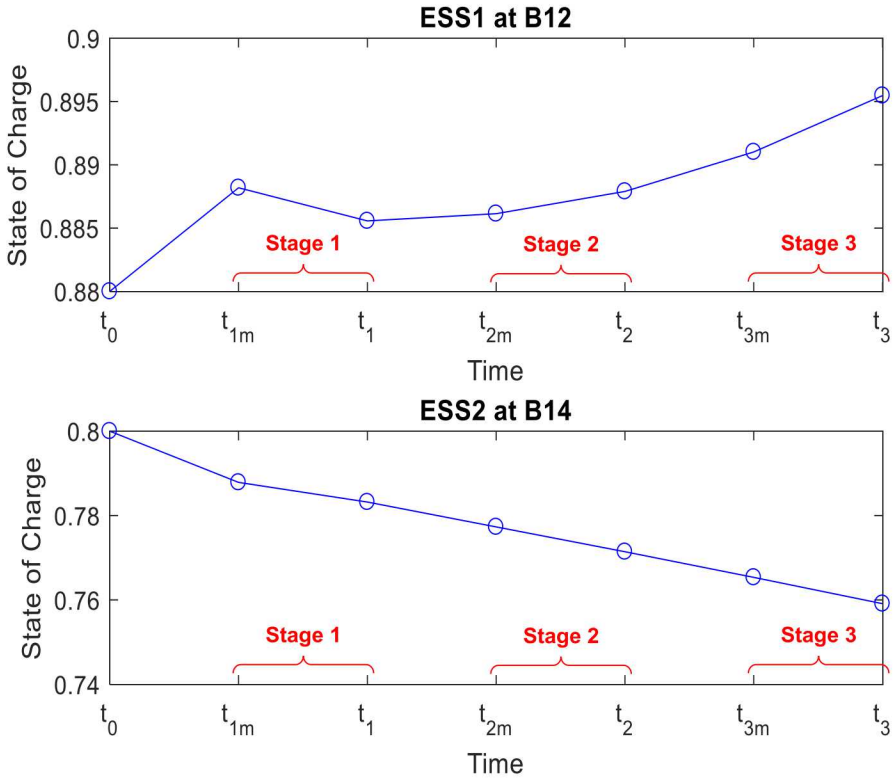

Figure 2-40. SOC of ESS1 and ESS2 over All Three Stages.

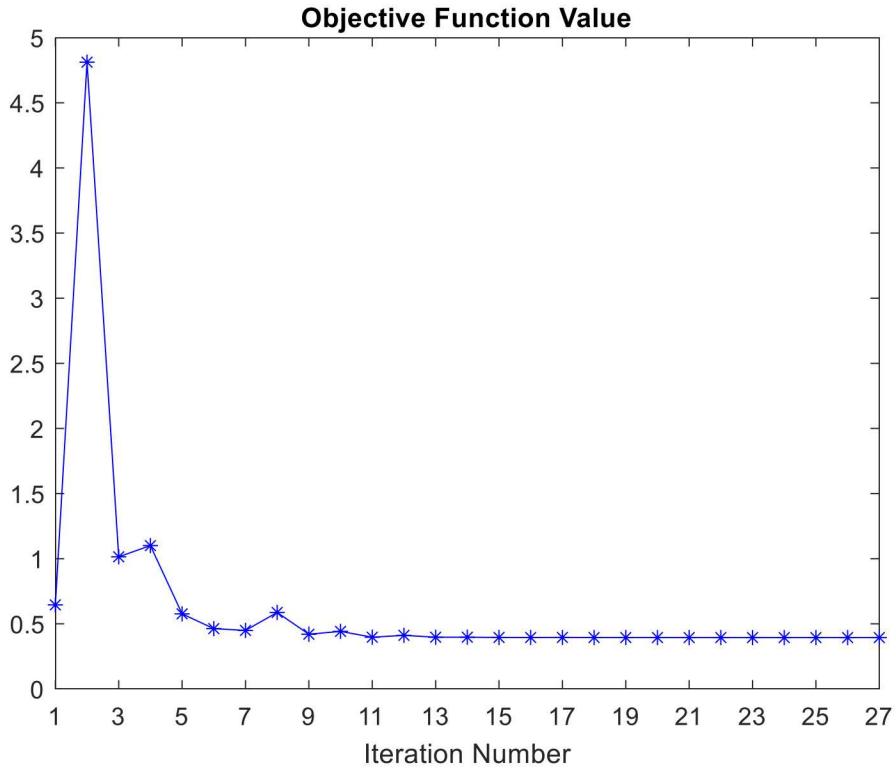

Figure 2-41. Objective Function Value.

The optimization results show that the voltage control method successfully forms and solves the 3-stage F-OPF problem for the modified PNM feeder model that levelizes the voltages at the selected buses. The process starts from the device level, using physically based device models constructed in the standard SCAQCF syntax to achieve object orientation. Then, network formulation is performed to incorporate all devices in the system to form the network SCAQCF, leading to the multi-stage QFOPFM after an objective function is defined. Finally, the F-OPF problem is solved through an SLP algorithm, generating the optimal control actions to be implemented to drive the system to the optimal operating point.

2.6. Cybersecurity

As part of this project, on August 24, 2017 the SunSpec/Sandia DER Cybersecurity Workgroup[14] was established to discuss methods of better securing DER/DERMS communications. This team has been convening international stakeholders across the industry to talk about DER cyber requirements, protocols, test requirements, audits, etc. The structure of the working group and statuses of the subgroups is shown in Figure 2-42. At this point, multiple subgroups have been formed to address DER certification protocols, secure DER network architectures, and data-in-flight requirements. The certification protocol is being transitioned to a UL standards technical panel and the networking requirements have been drafted and are currently undergoing a review. The newly initiated data-in-flight subgroup is investigating encryption, authentication, and trust requirements for DER networks. The products of this group are likely directly support DER vendors, DER aggregators, and utilities security construct and operate DER networks.

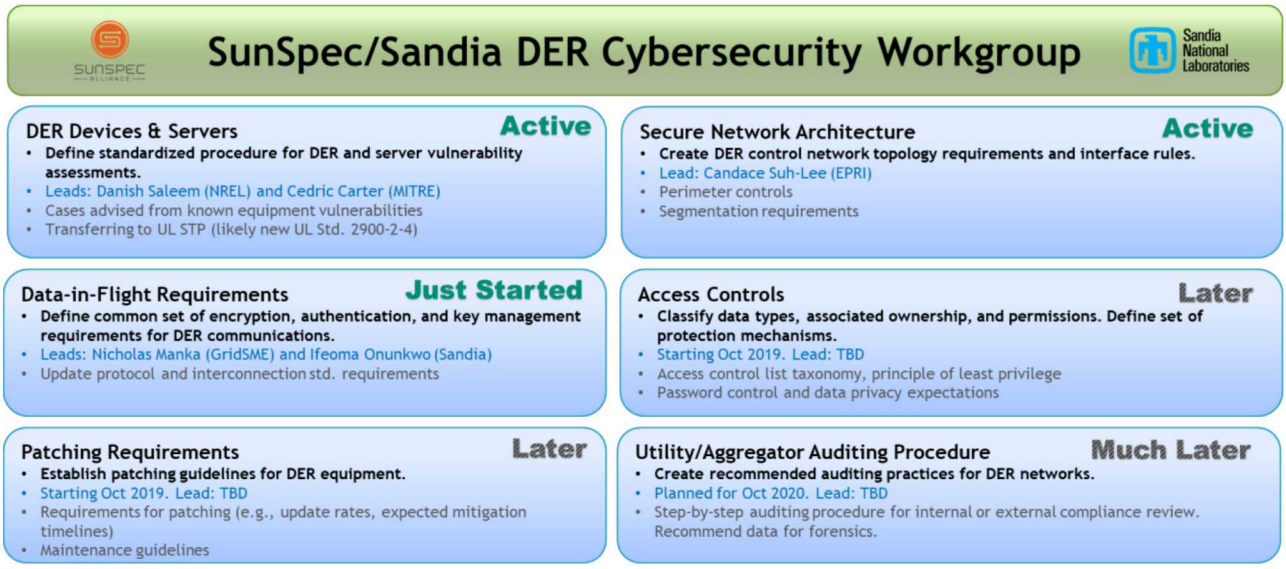

Figure 2-42. DER Cyber Security Working Group structure.

[14] SunSpec/Sandia DER Cybersecurity Workgroup. URL: http://sunspec.org/sunspec-cybersecurity-workgroup/

3. SYSTEMS OF STUDY

3.1. Distribution Systems

The team acquired three PNM feeders (Synergi) and four National Grid Feeders (CYME). These were converted into reduced-order Simulink models for RT simulations and WinIGS model for state estimation through the process indicated in Figure 3-1. Ultimately, only one PNM model and one NG model were used for the analysis because of time and funding constraints, but the others were reduced and available for future analysis.

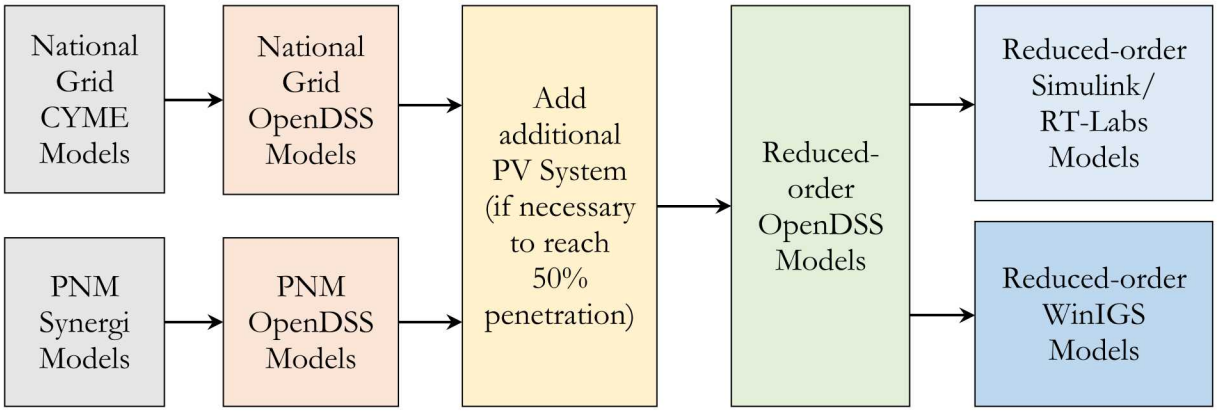

Figure 3-1. Distribution system model conversions required to create the state estimation tool and RT PHIL simulation environment.

To run the power hardware-in-the-loop experiments, a series of conversions took place to convert the models to RT-Lab-compliant formats (MATLAB/Simulink). The CYME and Synergi models were first converted to OpenDSS to provide a common open-source modelling environment for all project participants. The OpenDSS models were validated to be equivalent to the original utility models, and then the OpenDSS models were used as the base case for all simulations and comparisons going forward. In additional to the full OpenDSS models, circuit reduction was performed to save reduced -order models of the seven utility feeders. At that point, two reduced-order OpenDSS models (1 from PNM and 1 from NG) were built as Simulink models to be run in RT with the Opal-RT 5600 and WinIGS format to complete the state estimation. The reduced-order OpenDSS models were used for the PSO optimization.

3.1.1. OpenDSS Circuit Reduction

OpenDSS is a Distribution System Simulator developed by Electric Power Research Institute (EPRI) primarily used for the modelling of distribution systems. Circuit reduction algorithms can reduce the number of buses in model while maintaining an equivalent model at locations of interest on the feeder[15]. This approach is necessary due to bus limitations when implementing the RT simulations. The full distribution system models were reduced to smaller equivalent distribution systems using by

[15] M. J. Reno, K. Coogan, R. J. Broderick, and S. Grijalva, "Reduction of Distribution Feeders for Simplified PV Impact Studies," in IEEE PVSC, Tampa, FL, 2013.

selecting critical buses.[16, 17] For this reduction, buses with protective devices and controllable DER devices were specifically included in the reduced-order model. Figure 3-2 shows the actual PNM feeder layout and device locations. Figure 3-3 shows the reduction process for the PNM feeder with the feeder layout for the full and reduced distribution system and the voltage profile during the reduction process.

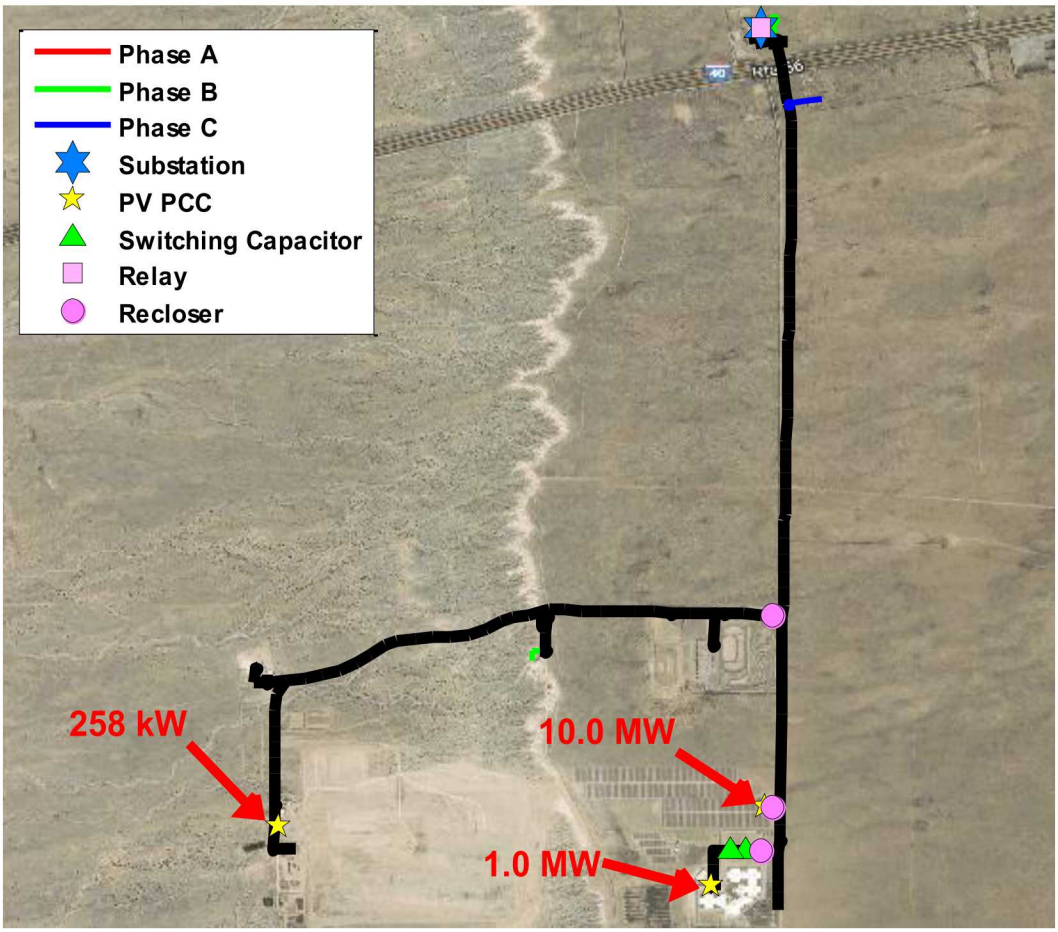

Figure 3-2: PNM feeder Circuit Diagram.

[16] Z. K. Pecenak, V. R. Disfani, M. J. Reno, and J. Kleissl, "Multiphase Distribution Feeder Reduction," IEEE Transactions on Power Systems, 2017.

[17] Z. K. Pecenak, V. R. Disfani, M. J. Reno, and J. Kleissl, "Comprehensive Reduction of Multiphase Distribution Feeder Models," IEEE Transactions on Power Systems, 2018.

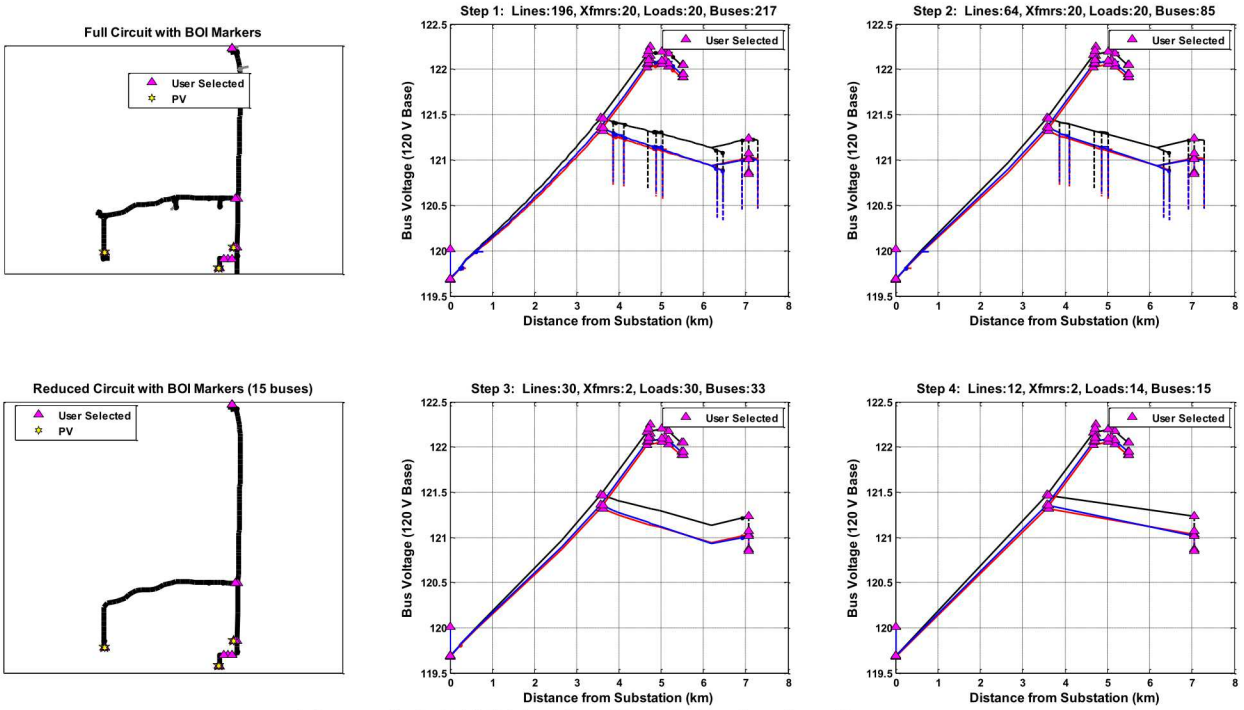

Figure 3-3: PNM Feeder Circuit Reduction Process.

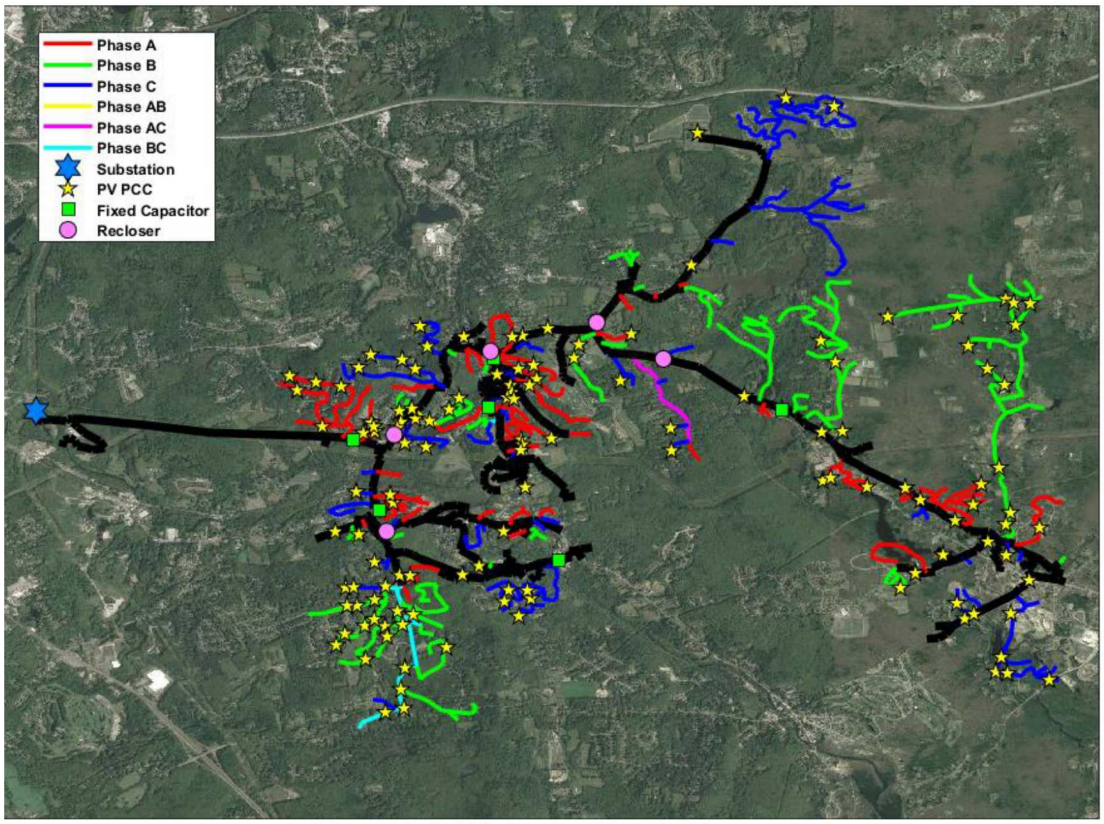

Figure 3-4: NG feeder Circuit Diagram.

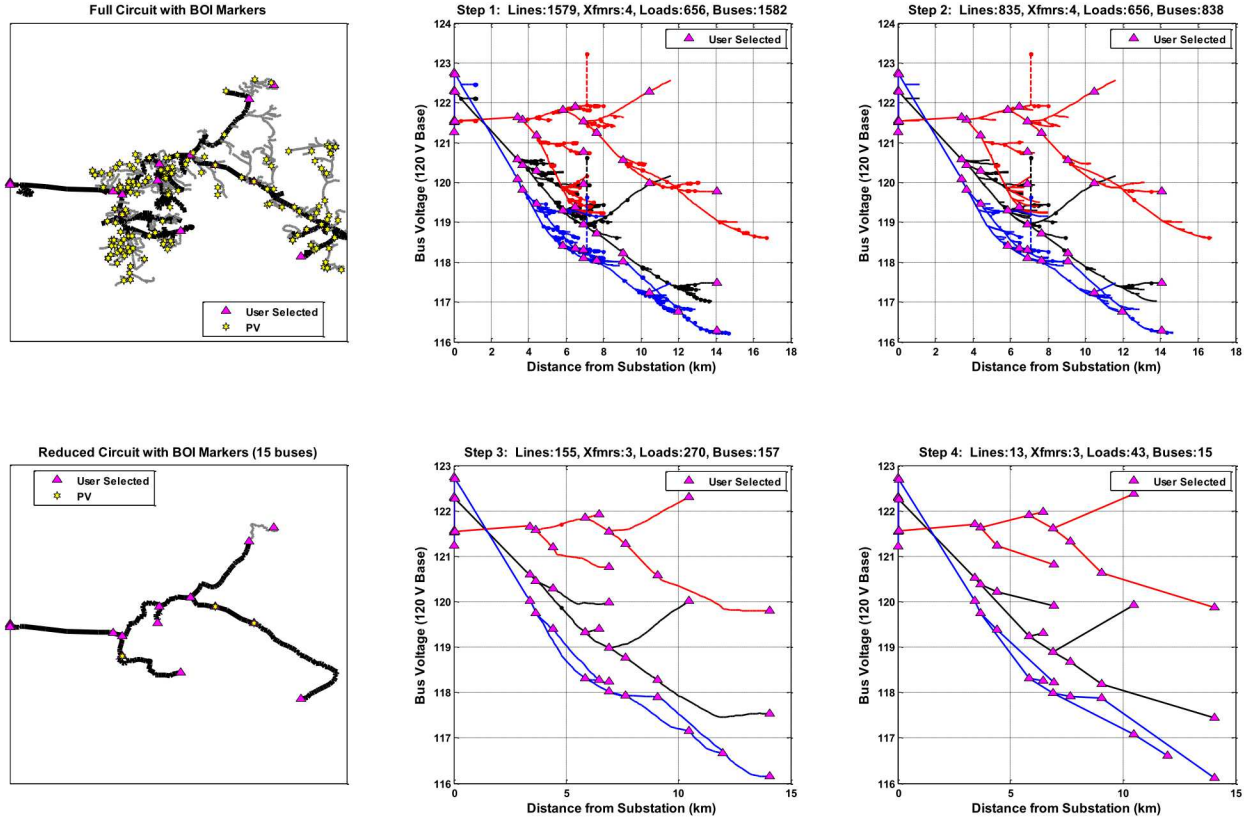

Figure 3-5: NG Feeder Circuit Reduction Process.

3.1.2. WinIGS Models

This subsection introduces the PNM and NG reduced feeder model in WinIGS. The detailed conversion procedure from OpenDSS feeder model to WinIGS feeder model is described previously. The PNM feeder model in WinIGS is shown in Figure 3-7. This reduced feeder model has 15 three-phase buses. The GPS coordinates of the buses are available. This allows the visualization of the feeder topology. The feeder model has been debugged in the WinIGS software. The case is solvable, and the convergence is achieved in 6 iterations to an accuracy of 0.00000001.

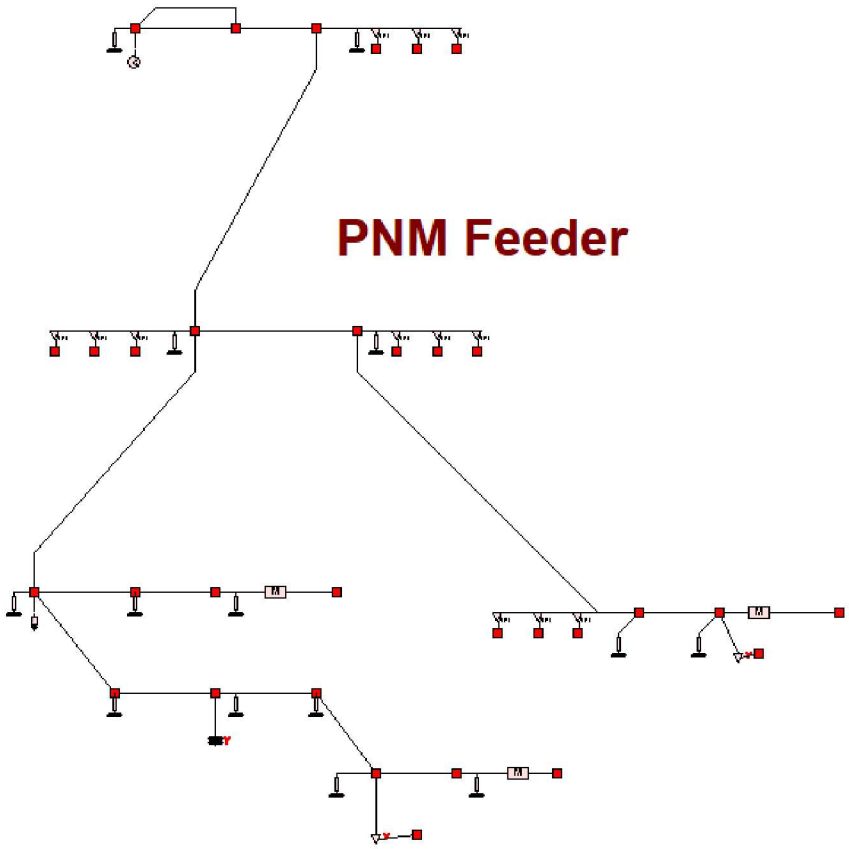

Figure 3-6. Single-Phase Diagram of PNM Feeder Model.

PNM feeder model consists of loads (three-phase, single-phase), capacitor banks, three-phase two-winding transformers, three-phase distribution lines, equivalent sources, PV sources, etc. Table 3-1 shows these devices in this feeder. The detailed parameters of each type of device are listed from Table 3-2 - Table 3-6, respectively.

Table 3-1. Devices in PNM Feeder Model.

Device Type		Number
Constant Power Load	Three-Phase Load	2
	Single-Phase Load	12
Capacitor Bank	Three-Phase	2
Transformer	Three-Phase Two-Winding	2
Distribution Line	Three-Phase	12
Equivalent Source	Three-Phase	1
PV Source	Three-Phase	3

Table 3-2. Parameters of Load Models in PNM Feeder Model.

Three-Phase Load						
#	Device Name	Bus Name	Phase Number	Rated Voltage (L-L, kV)	Real Power (kW)	Reactive Power (kVar)
1	Load19	B15	3	0.48	25.5	19.2
2	Load20	B04	3	12.47	1885	1292
Single-Phase Load						
1	Load136	B11_A	1	7.19956	-0.03183	0.003439
2	Load137	B11_B	1	7.19956	3.86034	0.489472
3	Load138	B11_C	1	7.19956	2.67042	0.302451
4	Load139	B05_A	1	7.19956	0.028182	-0.00895
5	Load140	B05_B	1	7.19956	2.28829	0.413719
6	Load141	B05_C	1	7.19956	0.393999	0.15441
7	Load142	B09_A	1	7.19956	97.1185	22.0604
8	Load143	B09_B	1	7.19956	100.58	22.4071
9	Load144	B09_C	1	7.19956	116.318	25.6155
10	Load133	B10_A	1	7.19956	107.384	11.5588
11	Load134	B10_B	1	7.19956	108.562	11.9113
12	Load135	B10_C	1	7.19956	118.93	12.6054

Table 3-3. Parameters of Capacitor Bank Models in PNM Feeder Model.

Capacitor Bank					
#	Device Name	Bus Name	Rated Reactive Power (kVar)	Rated Voltage (L-L, kV)	Connection Type
1	Capa1	B07	1800	12.47	WYE

Table 3-4. Parameters of Three-Phase Two-Winding Transformers in PNM Feeder Model.

Three-Phase Two-Winding Transformer					
#	Device Name	Bus Name	Rated Power (MVA)	Rated Voltage (kV)	Connection Type
1	Tran1	B01, B02	30	115/12.47	DELTA/WYE
2	Tran20	B10, B15	0.5	12.47/0.48	WYE/WYE

Table 3-5. Parameters of Three-Phase Equivalent Source in PNM Feeder Model.

Three-Phase Equivalent Source				
#	Device Name	Bus Name	Rated Voltage (kV)	Rated Power (MVA)
1	feeder	B01	115	100

Table 3-6. Parameters of Three-Phase PV Sources in PNM Feeder Model.

Three-Phase PV Source					
#	Device Name	Bus Name	Rated Voltage (kV)	Rated Power (MVA)	Power factor
1	PVSy1	B12	12.47	1	1.0
2	PVSy2	B14	12.47	10	1.0
3	PVSy3	B15	0.48	0.258	1.0

The simulation data (line-to-neutral voltages at each bus) are compared between WinIGS and OpenDSS to validate the converted feeder model is correct. Table 3-7 depicts the line-to-neutral voltage magnitude differences at all 15 buses between the simulation result from OpenDSS and WinIGS. Notice that all the errors are within 0.001 p.u., which is acceptable due to slightly different configuration/parameters of the models between WinIGS and OpenDSS.

Table 3-7. PNM Feeder Line-to-Neutral Bus Voltage Mismatch List Between WinIGS and OpenDSS.

		V_{AN}			V_{BN}			V_{CN}		
Bus Name (OpenDSS)	Bus Name (WinIGS)	Mag (V)	Angle (degree)	Mag in p.u.	Mag (V)	Angle (degree)	Mag in p.u.	Mag (V)	Angle (degree)	Mag in p.u.
b_1	B01	0	0.00219813	0	0	-0.002	0	-0.1	0	0
b_10	B10	0.83	-0.0101	8E-05	3.07	0.04	0.0004	-4.53	-0.0203	-0.00059
b_11	B11	0.43	0.0107	5.5E-05	-1.71	0.033	-0.00024	-5.3	-0.0138	-0.000737
b_12	B12	-0.17	0.0208	-5E-05	3.41	0.04	0.00048	-2.45	0.0496	-0.00031
b_13	B13	-0.51	-0.04	-1E-04	3.06	-0.02	0.00043	-3.05	-0.01	-0.00038
b_14	B14	-0.76	-0.0101	-1E-04	2.08	-0.007	0.00034	-1.73	0.0072	-0.00026
b_15	B15	0.042	0.0319	0.00015	0.133	-0.024	0.00049	-0.189	0.0319	-0.00071
b_2	B02	-2.24	0.0238	-0.00031	-1.75	0.008	-0.00024	-2.6	-0.0016	-0.000367
b_3	B03	-0.26	0.04	-4E-05	3.34	-0.04	0.0005	-2.73	0.07	-0.00042
b_4	B04	-0.33	0.0209	-9E-05	3.5	0.038	0.00048	-2.45	0.0507	-0.00032
b_5	B05	-0.1	0.0016	0	1.69	0.021	0.0002	-3.47	0.0177	-0.00051
b_6	B06	-0.48	0	-6E-05	3.09	0.02	0.00047	-3.01	0.04	-0.00044
b_7	B07	-0.29	-0.0516	-6E-05	3.5	-0.029	0.0005	-2.92	0.0808	-0.00036
b_8	B08	-0.38	-0.04	-4E-05	3.22	-0.02	0.00049	-2.86	-0.01	-0.00042
b_9	B09	0.82	-0.0166	0.00016	3.3	0.036	0.00043	-5.99	0.0205	-0.00086

The NG reduced feeder model is shown in Figure 3-7. This reduced feeder model has 15 three-phase buses. The GPS coordinates of the buses are available. This allows the visualization of the feeder topology. The feeder model has been debugged in the WinIGS software. The case is solvable, and the convergence is achieved in 4 iterations to an accuracy of 0.00000088.

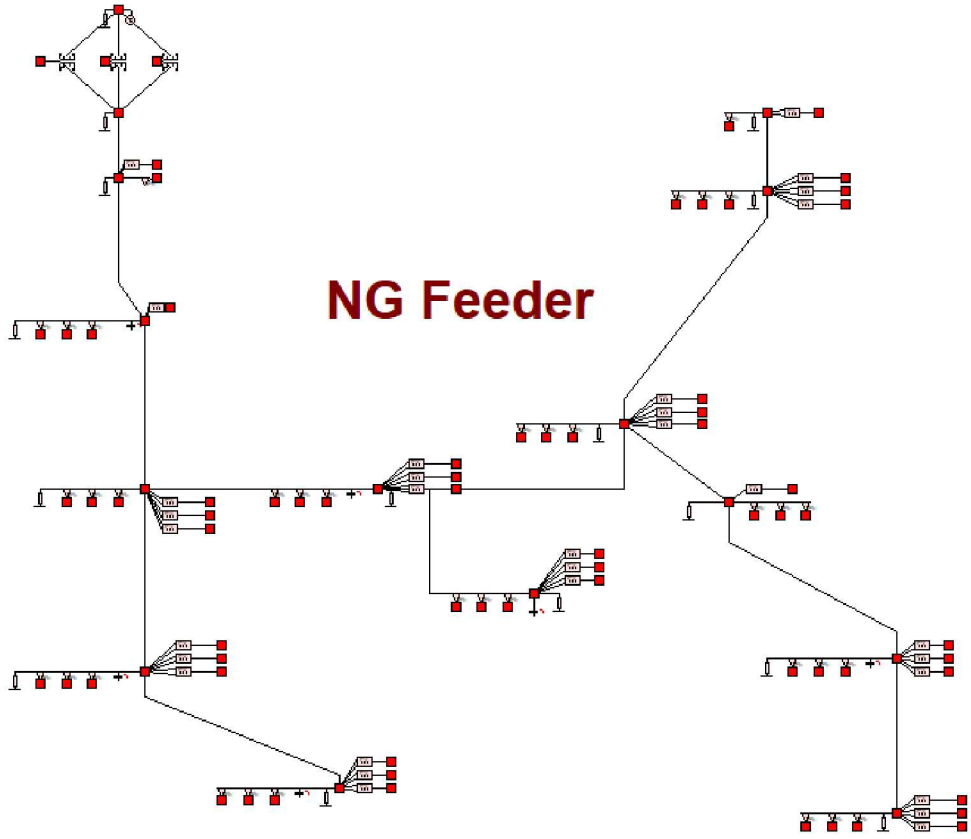

Figure 3-7. Single-Phase Diagram of NG Feeder Model.

NG feeder model consists of single-phase loads, capacitor banks, single-phase two-winding transformers, distribution lines (three-phase, single-phase), equivalent sources, PV sources, etc. Table 3-8 shows these devices in this feeder. The detailed parameters of each type of device are listed from Table 3-9 – Table 3-13.

Table 3-8. Devices in NG Feeder Model.

Device Type		Number
Load	Single-Phase	35
Capacitor Bank	Three-Phase	6
Transformer	Single-Phase Two-Winding	3
Distribution Line	Three-Phase	12
	Single-Phase	1
Equivalent Source	Three-Phase	1
PV Source	Three-Phase	1
	Single-Phase	30

Table 3-9. Parameters of Load Models in NG Feeder Model.

Single-Phase Load						
#	Device Name	Bus Name	Phase Number	Rated Voltage (L-N, kV)	Real Power (kW)	Reactive Power (kVar)
1	Load1633	B14_A	1	7.967	4.551	2.264
2	Load1615	B07_A	1	7.967	208.216	105.579
3	Load1616	B07_B	1	7.967	10.752	5.035
4	Load1617	B07_C	1	7.967	4.8142	3.014
5	Load1612	B04_A	1	7.967	108.323	62.208
6	Load1613	B04_B	1	7.967	91.474	41.477
7	Load1614	B04_C	1	7.967	191.185	115.040
8	Load1609	B06_A	1	7.967	421.138	259.530
9	Load1610	B06_B	1	7.967	122.800	58.367
10	Load1611	B06_C	1	7.967	282.694	180.806
11	Load1624	B12_A	1	7.967	241.844	147.122
12	Load1625	B12_B	1	7.967	195.883	92.467
13	Load1626	B12_C	1	7.967	331.148	210.430
14	Load1618	B08_A	1	7.967	330.456	202.114
15	Load1619	B08_B	1	7.967	359.273	164.258
16	Load1620	B08_C	1	7.967	167.826	104.737
17	Load1603	B11_A	1	7.967	81.396	49.693
18	Load1604	B11_B	1	7.967	22.321	10.623
19	Load1605	B11_C	1	7.967	118.772	74.481
20	Load1621	B02_A	1	7.967	324.233	230.913
21	Load1622	B02_B	1	7.967	664.828	359.143
22	Load1623	B02_C	1	7.967	192.621	153.292
23	Load1636	B03_A	1	7.967	249.018	118.318
24	Load1637	B03_B	1	7.967	315.752	102.715
25	Load1638	B03_C	1	7.967	333.510	179.550
26	Load1606	B09_A	1	7.967	181.390	112.840
27	Load1607	B09_B	1	7.967	95.731	45.808
28	Load1608	B09_C	1	7.967	276.896	217.638
29	Load1602	B10_C	1	7.967	132.739	44.255
30	Load1627	B05_A	1	7.967	473.341	336.359
31	Load1628	B05_B	1	7.967	934.247	467.238
32	Load1629	B05_C	1	7.967	586.765	402.165
33	Load1630	B13_A	1	7.967	406.959	209.693
34	Load1631	B13_B	1	7.967	419.138	167.037
35	Load1632	B13_C	1	7.967	612.731	318.098

Table 3-10. Parameters of Capacitor Bank Models in NG Feeder Model.

Capacitor Bank					
#	Device Name	Bus Name	Rated Reactive Power (kVar)	Rated Voltage (L-L, kV)	Connection Type
1	Capa1	B06	600	13.80	WYE
2	Capa2	B02	600	13.80	WYE
3	Capa3	B05	900	13.80	WYE
4	Capa4	B07	1200	13.80	WYE
5	Capa5	B12	600	13.80	WYE
6	Capa6	B13	600	13.80	WYE

Table 3-11. Parameters of Single-Phase Two-Winding Transformers in NG Feeder Model.

Three-Phase Two-Winding Transformer					
#	Device Name	Bus Name	Rated Power (MVA)	Rated Voltage (kV)	Phase
1	Tran1	B01, B15	3.33	7.967/7.967	A
2	Tran2	B01, B15	3.33	7.967/7.967	B
3	Tran3	B01, B15	3.33	7.967/7.967	C

Table 3-12. Parameters of Three-Phase Equivalent Source in NG Feeder Model.

Three-Phase Equivalent Source				
#	Device Name	Bus Name	Rated Voltage (kV)	Rated Power (MVA)
1	NGfeeder1	B01	13.80	100

Table 3-13. Parameters of Three-Phase PV Sources in NG Feeder Model.

Three-Phase PV Source					
#	Device Name	Bus Name	Rated Voltage (kV)	Rated Power (kVA)	Power factor
1	PVSy1	B11	13.80	684	1.0000
Single-Phase PV Source					
1	PVSy838	B15_C	7.967	4.738	-0.8872
2	PVSy842	B09_A	7.967	1001.99	-0.9998
3	PVSy843	B09_B	7.967	1018.49	1.0000
4	PVSy844	B09_C	7.967	983.68	1.0000
5	PVSy845	B06_A	7.967	57.62	1.0000
6	PVSy846	B06_B	7.967	13.03	1.0000
7	PVSy847	B06_C	7.967	51.87	0.9999
8	PVSy848	B04_A	7.967	27.22	-0.9999
9	PVSy849	B04_B	7.967	29.64	1.0000
10	PVSy850	B04_C	7.967	59.00	-0.9999
11	PVSy851	B07_A	7.967	92.43	1.0000
12	PVSy854	B08_A	7.967	34.51	1.0000
13	PVSy855	B08_B	7.967	22.45	1.0000
14	PVSy856	B08_C	7.967	9.07	1.0000
15	PVSy857	B02_A	7.967	44.03	0.9982

16	PVSy858	B02_B	7.967	150.42	0.9969
17	PVSy859	B02_C	7.967	21.24	0.9671
18	PVSy860	B12_A	7.967	368.95	-0.9984
19	PVSy861	B12_B	7.967	331.06	-0.9985
20	PVSy862	B12_C	7.967	340.23	-0.9988
21	PVSy863	B05_A	7.967	57.08	-0.9994
22	PVSy864	B05_B	7.967	277.87	0.9995
23	PVSy865	B05_C	7.967	127.78	1.0000
24	PVSy866	B13_A	7.967	26.87	-0.9999
25	PVSy867	B13_B	7.967	22.41	-0.9602
26	PVSy868	B13_C	7.967	67.72	1.0000
27	PVSy869	B14_A	7.967	2.22	0.9997
28	PVSy872	B03_A	7.967	18.22	0.9995
29	PVSy873	B03_B	7.967	119.38	-0.9939
30	PVSy874	B03_C	7.967	53.87	-0.9905

The simulation data (line-to-neutral voltages at each bus) are compared between WinIGS and OpenDSS to validate the converted feeder model is correct. Table 3-14 depicts the line-to-neutral voltage magnitude differences at all 15 buses between the simulation result from OpenDSS and WinIGS. Notice that all the errors are within 0.009 p.u., which is acceptable due to slightly different configuration/parameters of the models between WinIGS and OpenDSS.

Table 3-14. NG Feeder Model Line-to-Neutral Bus Voltage Mismatch List Between WinIGS and OpenDSS.

		V_{AN}			V_{BN}			V_{CN}		
Bus Name (OpenDSS)	Bus Name (WinIGS)	Mag (V)	Angle (degree)	Mag in p.u.	Mag (V)	Angle (degree)	Mag in p.u.	Mag (V)	Angle (degree)	Mag in p.u.
b_1	B01	4.9	0.06	0.00066	-4.06	-0.02	-0.00047	8.55	0.01	0.00102
b_10	B10	0	0	0	0	0	0	65.39	-0.096	0.008208
b_11	B11	10.84	0.27264	0.00136	-34.68	-0.2	-0.00431	60.85	0.058	0.007637
b_12	B12	8.7	0.31213	0.00109	-30.92	-0.119	-0.00392	55.57	0.077	0.006975
b_13	B13	3.52	0.21657	0.00045	-24.24	-0.126	-0.00302	46.96	0.05	0.005895
b_14	B14	1.56	0.03	0.00021	-3.05	-0.07	-0.00036	11.25	0.12	0.0014
b_15	B15	4.98	0.037873	0.00061	-4.12	-0.037	-0.00052	8.72	0.089	0.00113
b_2	B02	15.62	0.35611	0.00196	-41.86	-0.154	-0.00527	65.34	0.037	0.008198
b_3	B03	12.69	0.32135	0.00160	-36.92	-0.199	-0.00463	69.3	0.088	0.008701
b_4	B04	4.02	0.22327	0.0005	-22.39	-0.18	-0.00283	41.56	0.117	0.005212
b_5	B05	6.96	0.25906	0.00088	-27.14	-0.129	-0.0034	43.99	0.01	0.005516
b_6	B06	5.53	0.31404	0.00069	-30.45	-0.174	-0.00385	58.08	0.081	0.007289
b_7	B07	2.99	0.20002	0.00038	-22.57	-0.144	-0.00285	41.89	0.064	0.005255
b_8	B08	10.67	0.31117	0.00134	-37.12	-0.189	-0.0047	62.03	-0.002	0.007785
b_9	B09	7.11	0.33701	0.00090	-32.08	-0.195	-0.00402	61.9	0.068	0.007769

3.1.3. RT-Lab Models

The reduced-order PNM and NG models were converted from OpenDSS to MATLAB/Simulink to accommodate the PHIL setup. For the validation of the Opal-RT distribution system, a comparison between OpenDSS and MATLAB/Simulink was conducted[18]. OpenDSS and MATLAB/Simulink use different parameters to represent the same distribution system parameters, so careful migration was required to move the model from OpenDSS to MATLAB/Simulink. A power flow comparison was made to guarantee the accuracy between models. Due to some MATLAB/Simulink limitations, minor adjustments were made to the OpenDSS models to compare them Simulink. For instance, line inductance is represented in Ω/length in OpenDSS and H/km in Simulink. Load settings in OpenDSS were set to Constant Current Magnitude (model=5) but are changed to Constant impedance load (model=2) to behave like the linear load models in MATLAB/Simulink. When specifying loads in OpenDSS, allocation settings can be placed to vary the load value by specifying an allocation factor that will modify the load parameters (kW, PF, and kVar). For this reason, allocation setting was replaced with constant impedance load (model=2) setting.

OpenDSS allows capacitor bank control that varies capacitance values. The MATLAB/Simulink model did not have this functionality, so the OpenDSS model was modified to disable this functionality. The transformer parameters were not easily converted from OpenDSS to MATLAB/Simulink because of differences in the magnetization parameters. The reduction of the PNM models yields equivalent shunt reactances for the lines. The inclusion of the shunt reactances had a minimum effect on the simulation results, but they were not included in the MATLAB/Simulink model. For the validation of the models, bus voltages, as well as line active and reactive power were compared.[19]

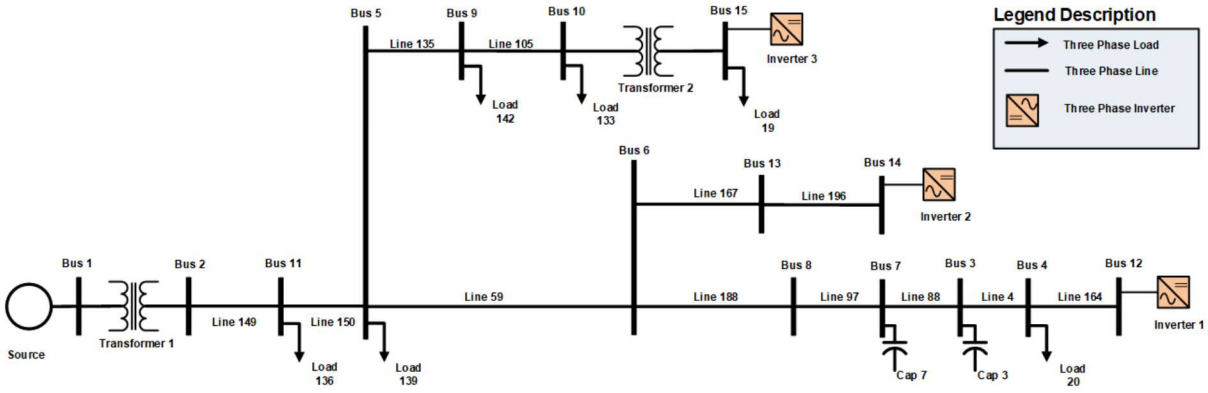

Figure 3-8. PNM Feeder Circuit Diagram.

[18] R. Darbali-Zamora, J. Hernandez-Alvidrez, A. Summers, N. S. Gurule, M. J. Reno and J. Johnson, "Fault Validation Utilizing a Real-Time Power Hardware-in-the-Loop Approach for Distribution Feeders with Photovoltaic Systems", 46th IEEE Photovoltaic Specialists Conference (PVSC), Chicago, Illinois, June 16-21, 2019.

[19] R. Darbali-Zamora, "PV Inverter Voltage Regulation Performance Comparison Using a Power Hardware-in-the-Loop on Distribution Circuit Feeders" University of Puerto Rico – Mayaguez, PhD Dissertation. (Forthcoming)

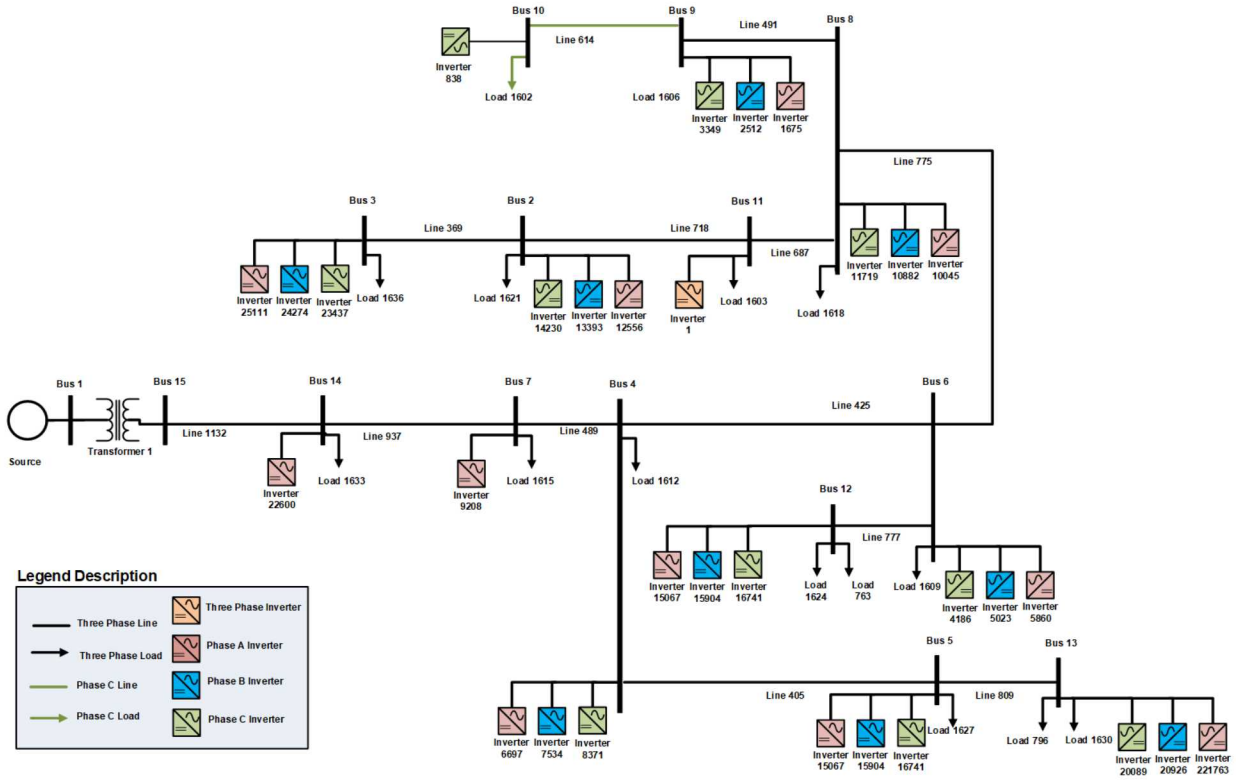

Figure 3-9. NG Feeder Circuit Diagram.

3.2. PV Systems

There were four PV systems used in the ProDROMOS project:

- An installation of 100 SunPower microinverters with 10 communication gateways at DETL.
- A residential 3 kW inverter at DETL.
- The 684 kW Old Upton Rd PV system in MA, owned by National Grid.
- Simulated PV systems created with the EPRI DER/PV simulator.

The first two systems were used for the PHIL simulations. Initially the 100-microinverter installation was intended to be used for all the PHIL simulations, but in the latter stages of the project, communications with the system became intermittent and unreliable. It is believed that high frequency noise produced by the Ametek grid simulator during the PHIL integration steps could have damaged some of the power line carrier filters or communication equipment, but this was never verified. Ultimately, those PHIL devices were replaced by a 3 kW residential system for the experiments, with the advantage that it could be connected to the PV simulator and feed a controlled irradiance profile for all the experiments. The Old Upton Rd site was used for the field demonstration. The EPRI PV simulator was used for all the RT simulations and additional equipment in the PHIL experiments.

3.2.1. SunPower Microinverters

The first experiments verified the SunPower microinverter interoperability and P/Q response by connecting the PVS, PLC filter, and 10 microinverters to 10 independent PV simulator power supplies. An encrypted, proprietary method was used to communicate to the SunPower PV

Supervisors (PVSs) over TCP/IP using secure shell (SSH) locally. The P/Q commands to the PVSs were transmitted to the microinverters using power line carrier (PLC) to each of the 10 microinverters connected to the PVS. The results of these experiments are shown in Table 3-15 and Table 3-16. The power values were averaged over each test taken between 75 and 320 Watts. The output powers were averaged for 45 seconds. As shown in the results, the P/Q characteristics can be changed through communications to the devices.

Table 3-15. Curtailment results with 100% DC Input.

Power Target (W)	1 Microinverter, No Filter (W)	10 Microinverters, No Filter (W)
320	302.2	3122.5
300	284.2	2956.4
250	233.6	2478.9
200	182.9	1995.6
150	131.7	1461.2
100	72.7	895.6
75	39.3	550.1

Table 3-16. Fixed power factor results at 100% DC Input.

PF Target	1 Microinverter, No Filter	10 Microinverters, No Filter
1.0	0.906	0.966
0.85	0.766	0.843
0.90	0.811	0.888
0.95	0.847	0.933
-0.85	-0.772	-0.844
-0.90	-0.825	-0.895
-0.95	-0.881	-0.942

To conduct the PHIL experiments, Sandia's Distributed Energy Technologies Laboratory (DETL) East Array was upgraded, as shown in Figure 3-10, to include 100 320-kVA SunPower microinverters connected to 200 W monocrystalline PV modules. Each microinverter could be controlled to an independent power factor setting between ±0.85 by issuing the command to one of the 10 SunPower PV Supervisors (PVSs). PF commands were sent to the PVSs via SSH commands and then issued the microinverters using PLC. Sandia firewall SSH rules were established to allow Connected Energy to measure the performance of the PV systems and issue curtailment and power factor commands to the equipment. An example of the data measured from one of the systems is shown in Figure 3-11.

Figure 3-10: DETL East Array with 100 microinverters and 10 PVS5s.

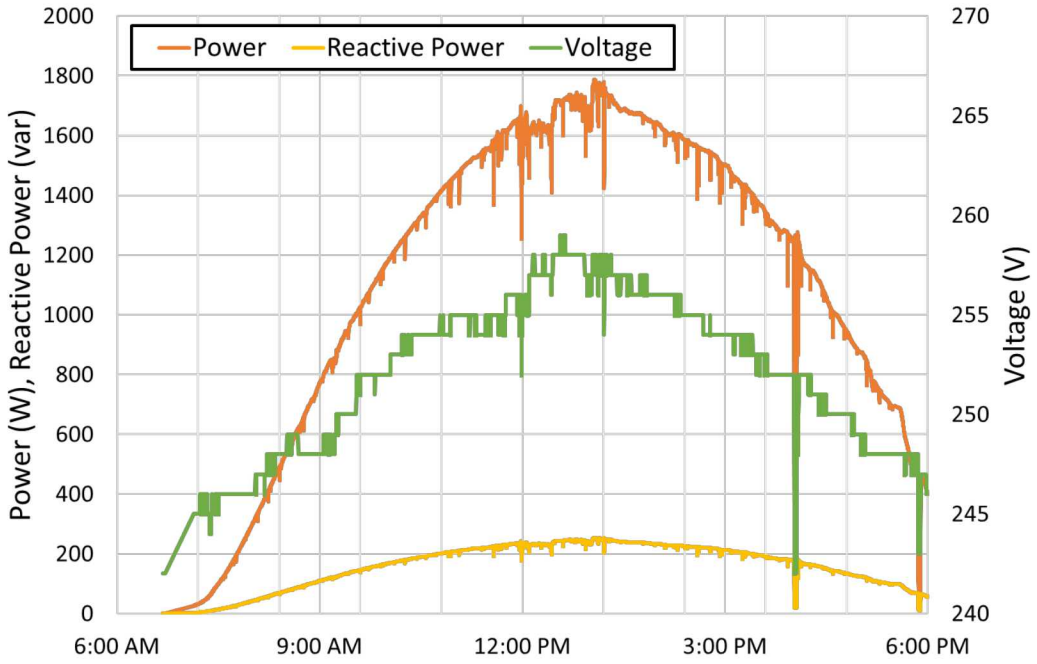

Figure 3-11: SunPower data as measured by Connected Energy.

3.2.2. EPRI PV Simulator

The EPRI-developed DER Simulator[20] software, shown in Figure 3-12, emulates solar smart inverter and energy storage systems that includes several grid-support functionalities and communication interfaces. Any number of DER devices, with different nameplate capacities and phasing configurations, can be instantiated with independent irradiance profiles. DER Simulator supports seven smart inverter functions, shown in Table 3-17.

Table 3-17. Supported smart functions.

Function Name	Description
Connect/Disconnect	This function is used to command the device to connect or disconnect from the grid.
Adjust Maximum Generation Level Up/Down	This function is used to set the maximum generation limit of the device as a percentage of its nominal capacity.
Adjust Power Factor	This function is used to set the power factor of the smart inverter. The DER follows the IEEE sign convention in which a leading (capacitive) power factor is positive and a lagging (inductive) power factor is negative. Note that this function and the Volt-VAR functions are mutually exclusive and it is not possible for both to be active simultaneously.
Charge/Discharge *(Energy Storage only)*	This function is used to set the charging and discharging set points for the storage systems.
Volt-VAR Curves	This function is used to send Volt-VAR curves to the device to produce or absorb reactive power as a function of locally-observed voltage.
Frequency-Watt Mode	This function is used to alter the active power output in response to the measured deviation from a specified nominal frequency.
Volt-Watt Mode	This function is used to filter the active power output in proportion to the measured deviation from the grid nominal voltage.

[20] Overview of EPRI's simulation tool for emulating smart solar inverters on communication networks: An introduction to EPRI's smart solar inverter simulator," EPRI, Palo Alto, CA, USA, EPRI Report 3002009851, 2017

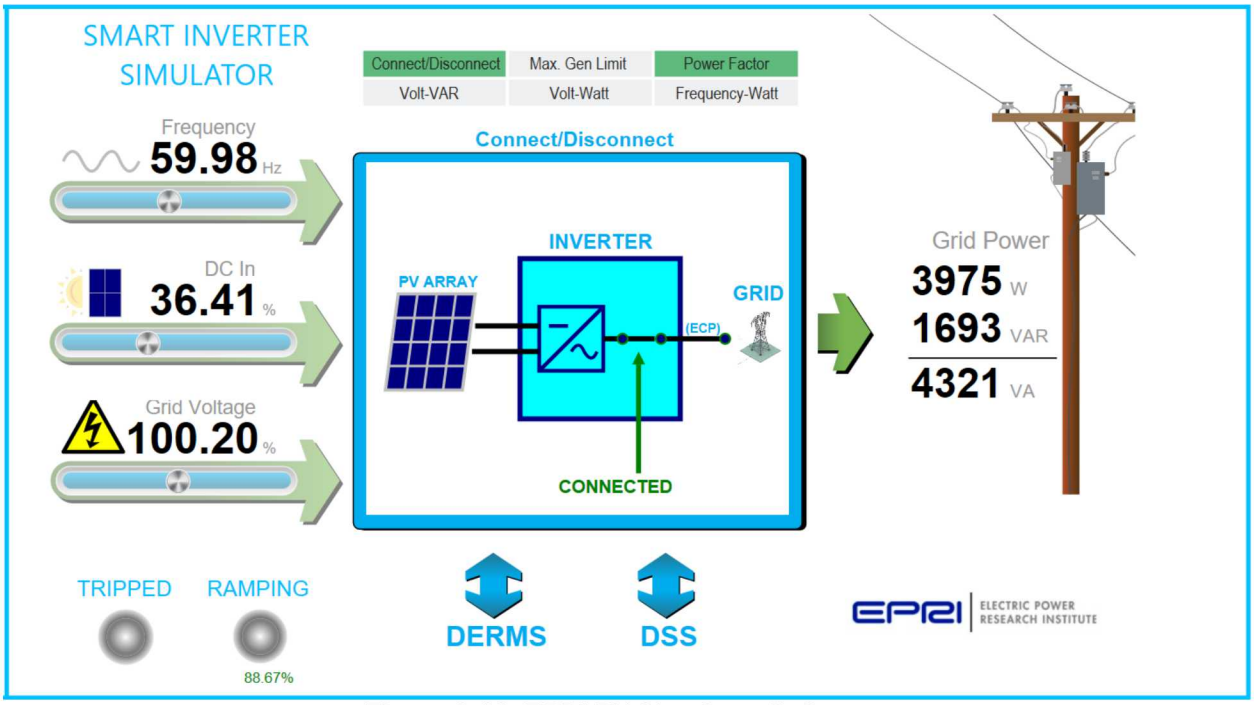

Figure 3-12: EPRI PV Simulator Software.

3.2.2.1. DNP3 Interface

Communications to/from the Connected Energy system used the DNP3 Application Note[21] information model to change the grid-support functions. Volt-Var (VV), Adjust Maximum Generation Level Up/Down (INV2), and Adjust Power Factor (INV3) functions were used to change the active and reactive power behaviors of the PV systems.

3.2.2.2. DBus interface

The communications between the simulated EPRI - DER Simulator and the power simulation used the EPRI-developed TCP/IP protocol called Data Bus (DBus). DBus is a co-simulation interface that facilitates communication between co-simulation components running in different threads enabling them exchange data in an asynchronous or synchronous interaction depending on the use case of the simulation.
This interface allows the components of the Co-Simulation to:

- To register as a Master/Slave Component
- To describe the variables of the component to be shared
- To request information about the registered components and its variables
- To dynamically publish data about component's local variables
- To download variables data from other registered components
- To subscribe to a set of data from other registered components
- To verify the Co-Simulation flags to determine the simulation's dynamic (asynchronous/synchronous)

[21] DNP Application Note AN2013-001, "DNP3 Profile for Advanced Photovoltaic Generation and Storage" 2013-01-14.

- To control the simulation progress in the case of being necessary from a Master component
- To be able to check the Co-Simulation flags to allow a Master component to control the simulation progress for a Slave component

The Opal-RT system exchanged V, and f data points from various nodes through DBus interface with the EPRI PV simulator. PV Simulator determines the output powers of the devices based on the irradiance, Voltage, frequency and DER settings and exchanges the data with the Opal-RT system every simulation cycle.

3.3. Intelligent Electronic Devices (IEDs)

Intelligent Electronic Devices (IEDs) make voltage and current measurements of the power system to perform RT state estimation. In theory, these measurements can be calculated from smart meters, advanced interoperable DER devices, μPMUs, and other field equipment—but this project only used simulated PMUs in the Opal-RT/RT-Lab simulations as inputs to the state estimation. The PMUs/μPMUs communicated via IEEE C37.118. This data stream was issued at 30 Hz and contained cycle-level resolution.

In the future, it could be possible in incorporate more data streams, though many are too slow to provide much RT information. AMI field data has low temporal resolution and transmitted to the utility once/day, so it has limited value for voltage regulation or protection. However, this data is useful for calibrating and feeder load information, so it has been included here. Substation SCADA data (voltage and current measurements) communicated via DNP3 across the SCADA network are transmitted at a variable rate. In the case of PNM, the utility scans through all the devices on their network every 15 minutes and then restarts at the beginning of the sequence. Depending on how many instruments are being recorded the maximum data rate would change, but could be as low at 8-10 seconds. DER devices themselves can be used to measure the voltage on the feeder at whatever polling rate is selected. For the 100 microinverters, they could all be pulled at ~30 second interval. The 3 kW inverter could be polled every 5 seconds. Typically, DER have low (1%) voltage accuracies, but in cases of high penetrations of PV, this data can provide an accurate representation of the state of the distribution system. A comparison of these options is shown in Table 3-18.

Table 3-18. End-device interoperability information.

Data	Protocol	Resolution	Update Rate	Network
Phasor measurement unit (PMU)/ microPMU	IEEE C37.118	512+ samples/cycle	30-60 Hz	SCADA
Advanced Metering Infrastructure (AMI) (fielded)	Zigbee SEP 1.0, ANSI C12.18/ ANSI C12.22/IEEE Std 1703	15 min	Once per day	AMI network
Utility DER measurements (field demonstration)	DNP3	~15 min	~15 min	SCADA
Physical DER (PHIL)	Proprietary, Modbus	1 min	1 min	Public Internet
Emulated DER (PHIL)	DNP3	10 sec	10 sec	Public Internet

4. REAL-TIME EXPERIMENTS

RT experiments were conducted with the PNM and NG feeder models to see a head-to-head comparison of the voltage regulation approaches. The EPRI PV simulators were used with identical irradiance profiles so the operating conditions of the scenarios were identical. 4-hour baseline experiments were completed with the EPRI devices fixed at unity power factor. The other voltage regulation methods were compared against these simulations.

4.1. Simulations with the PNM Model

The PNM model included three EPRI PV inverters on the rural feeder. The reactive power contributions from each DER was adjusted to provide voltage regulation. EPRI provided three correlated, highly variable irradiance measurements from a PV site on the US east coast to feed to the simulated inverters. These profiles were generated from a single Global Horizontal Irradiance (GHI) measurement and then shifted and scaled to account for geographical separation of the PV sites. The PV irradiance profiles were then smoothed based on the plant sizes using the Wavelet Variability Model[22] to account for spatial averaging with large PV systems. The final PV profiles are shown in Figure 4-1. To understand the impact of spatial averaging on the irradiance profiles, the smoothing algorithm was run on the same GHI profile in Figure 4-2. As seen in the image, the larger PV systems act to smooth the sharper irradiance peaks and toughs like a low pass filter. Physically, this occurs because clouds do not instantaneously shade larger PV systems and it takes time for them to pass over the entire array. Additionally, variable load profiles were used on loads connected to bus 6 and bus 13 to create transient voltage variability.

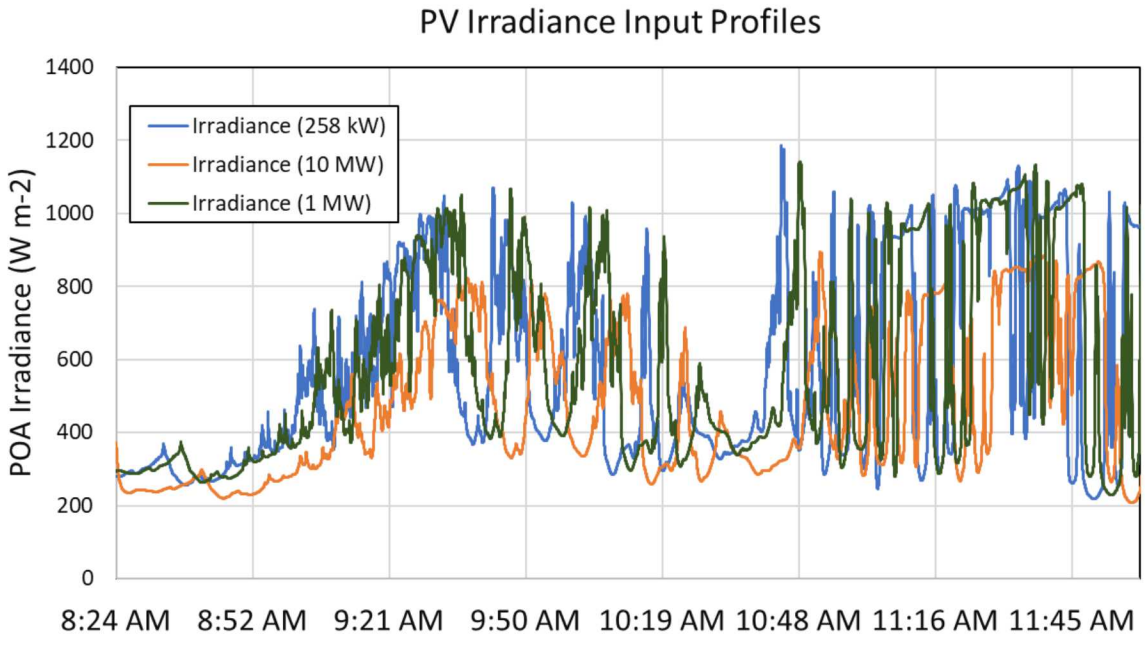

Figure 4-1. PV irradiance profiles for the three DER in the PNM model.

[22] https://pvpmc.sandia.gov/applications/wavelet-variability-model/

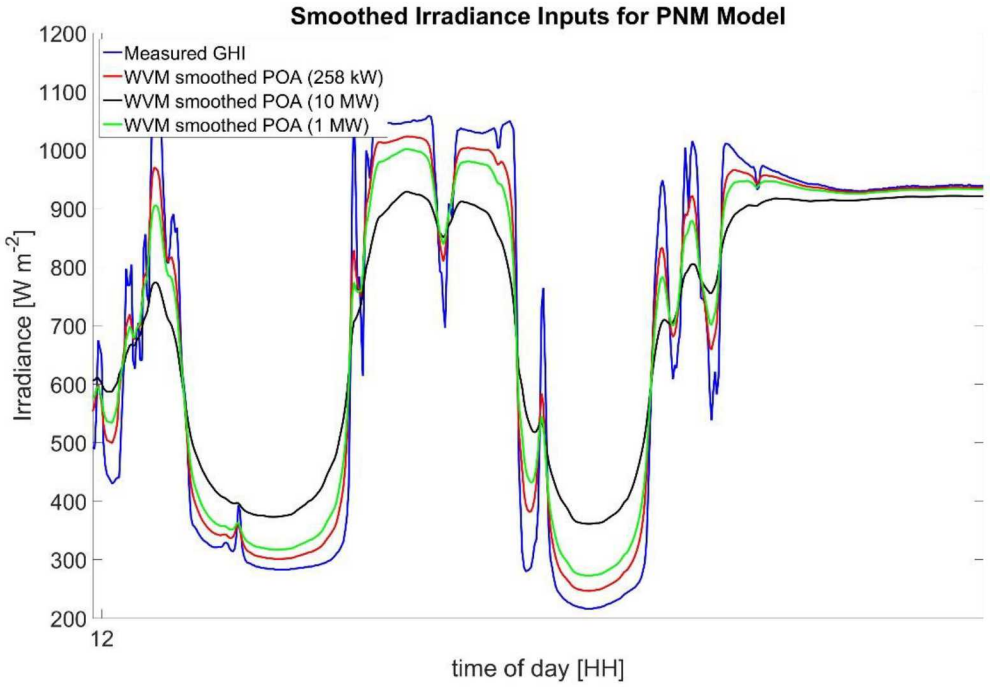

Figure 4-2. The effect of spatial averaging on the irradiance profiles.

4.1.1. Baseline Simulations

The PNM model was simulated using P/Q data passed from the EPRI DER simulator to the RT power simulation using the Data Bus (DBus) exchange. The hardware PV inverter was modeled scaled to represent the 258kVA PV inverter connected to bus 15. The simulated PV inverters connected to bus 12 and bus 14 were simulated using a P/Q controlled PV inverter model[23]. In this feeder model, controllable capacitor banks were removed. The power in the power simulation is shown in Figure 4-3. The voltage profile for each of the 15 buses is shown in Figure 4-4. As can be seen from these results, there is relatively little voltage rise when the PV systems inject power at their points of common coupling (PCCs). Overall, the feeder maximum voltage is driven by the 10 MW PV system on this feeder. For the validation of the distribution system, a comparison between OpenDSS and MATLAB/Simulink is used. Both OpenDSS and MATLAB/Simulink each use different settings to represent the same distribution system parameters. For this reason, power system equations are used to help migrate the model from OpenDSS to MATLAB/Simulink. Line parameters are given by OpenDSS is a Distribution System Simulator developed by Electric Power Research Institute (EPRI) primarily used for the modelling of distribution systems. The reduced PNM models were converted from OpenDSS to MATLAB/Simulink to accommodate the PHIL setup. A power flow comparison is made to guarantee the accuracy between models. Due to some MATLAB/Simulink limitations, minor changes are made to the OpenDSS reduced PNM models to equally compare them Simulink. OpenDSS represents line parameters such as line resistance in Ω/length, line inductance in Ω/length and line capacitance is represented in nf/length. Although the length can be specified in OpenDSS, it

[23]J. Hernandez-Alvidrez *et al.*, "PV-Inverter Dynamic Model Validation and Comparison Under Fault Scenarios Using a Power Hardware-in-the-Loop Testbed," *2018 IEEE 7th World Conference on Photovoltaic Energy Conversion (WCPEC) (A Joint Conference of 45th IEEE PVSC, 28th PVSEC & 34th EU PVSEC)*, Waikoloa Village, HI, 2018, pp. 1412-1417.

is typically expressed in ft. Alternatively to these OpenDSS parameter representations, MATLAB/Simulink, line resistance is given in Ω/km, line inductance is represented in H/km, while line capacitance is given in F/km. Notice that to properly measure power in the line it is important to select the direction and measurement point of the line. In a similar manner, load parameters of the system also must be converter from OpenDSS to MATLAB/Simulink. Voltage, active power and reactive power of the loads are represented in kV, kW and kVAR. To comply with MATLAB/Simulink, these parameters must be converted to V, W and VAR. In addition, Load settings in OpenDSS are set to Constant Current Magnitude (model=5) but are changed to Constant impedance load (model=2) to behave like the linear load models in MATLAB/Simulink. Also, when specifying loads in OpenDSS, allocation settings can be placed to vary the load value by specifying an allocation factor that will modify the load parameters (kW, PF, and kVAR). For this reason, allocation setting was replaced with constant impedance load (model=2) setting. The voltage and reactive power parameters of the capacitor banks are given in kV and kVAR. To comply with MATLAB/Simulink, these parameters must be converted to V and VAR. OpenDSS allows capacitor bank control that will vary capacitance values. Since MATLAB/Simulink does not have these control settings, this will play an important role in the accuracy of the lines and is disabled. The transformer parameters are not easily converted from OpenDSS to MATLAB/Simulink. Some of the magnetization parameters of the transformer in MATLAB/Simulink affects the results. I noticed that when specifying a three-phase load, the selected power values are distributed evenly throughout the three phases. Please let me know what you think. Control options for the transformers have also been disabled. The reduction of the PNM models yields equivalent shunt reactance's for the lines. The inclusion of these shunt reactance's has a minimum effect on the simulation results and are not included in the MATLAB/Simulink model.

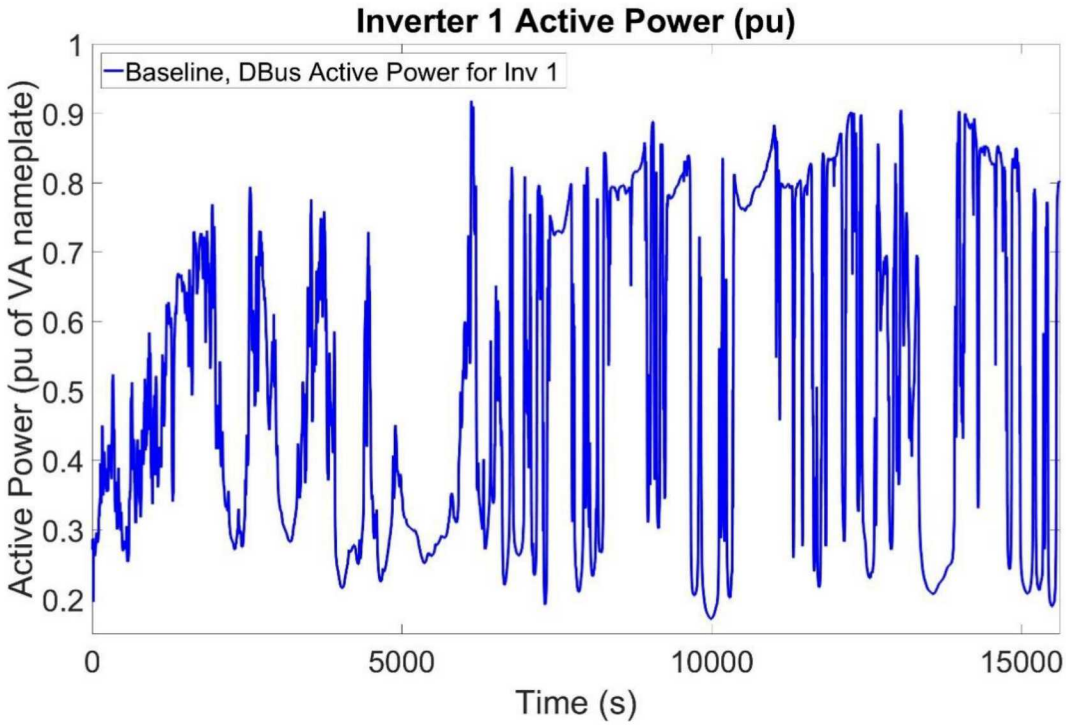

Figure 4-3. PV power levels for the 4-hour simulations.

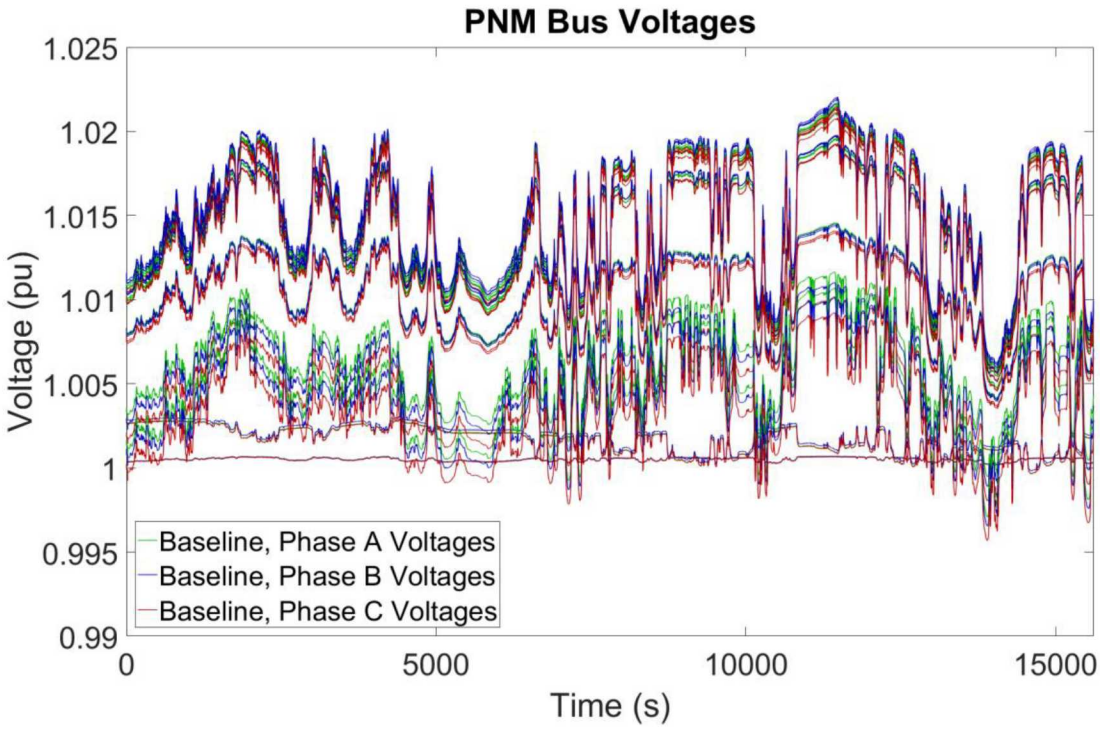

Figure 4-4. Bus voltages for the baseline simulations.

4.1.2. Volt-Var

The volt-var function was implemented in two ways. In the first, Connected Energy programmed the VV function in the EPRI DER devices using a DNP3 command. In the second, Connected Energy read the voltage from the DER device and issued a PF command according to the VV profile. The second method was studied to understand if this functionality could be implemented on DER equipment without the autonomous function (e.g., on the SunPower microinverters) and to better understand the how communication latencies would affect voltage regulation.

Initially, the default IEEE 1547-2018 curve parameters, in (% $V_{nominal}$, % nameplate apparent power rating), were used for the assessment but the voltage rarely exited the deadband, so the deadband was adjusted to ±0.01 pu:

P1 = (92, 44)
P2 = (99, 0)
P3 = (101, 0)
P4 = (108, -44)

Surprisingly, these VV parameters produced reactive power oscillations because the EPRI simulator update round trip time. The inverters in the power simulation updated their reactive power contributions at the 80-100 μs sampling rate of the RT simulation, but DBus read the DER bus voltage once a second and then DBus updated the Opal-RT DER reactive power set point on the next DBus write. So, the EPRI devices were hopping up and down the VV curve because they updated their Q contributions were based on a voltage measurement from 1 second ago. This was seen in both VV implementations, as shown in Figure 4-5. This behavior is often seen in power system simulations,

but not realistic of physical PV systems because they measure the grid voltage much quicker and ramp reactive power between setpoints.

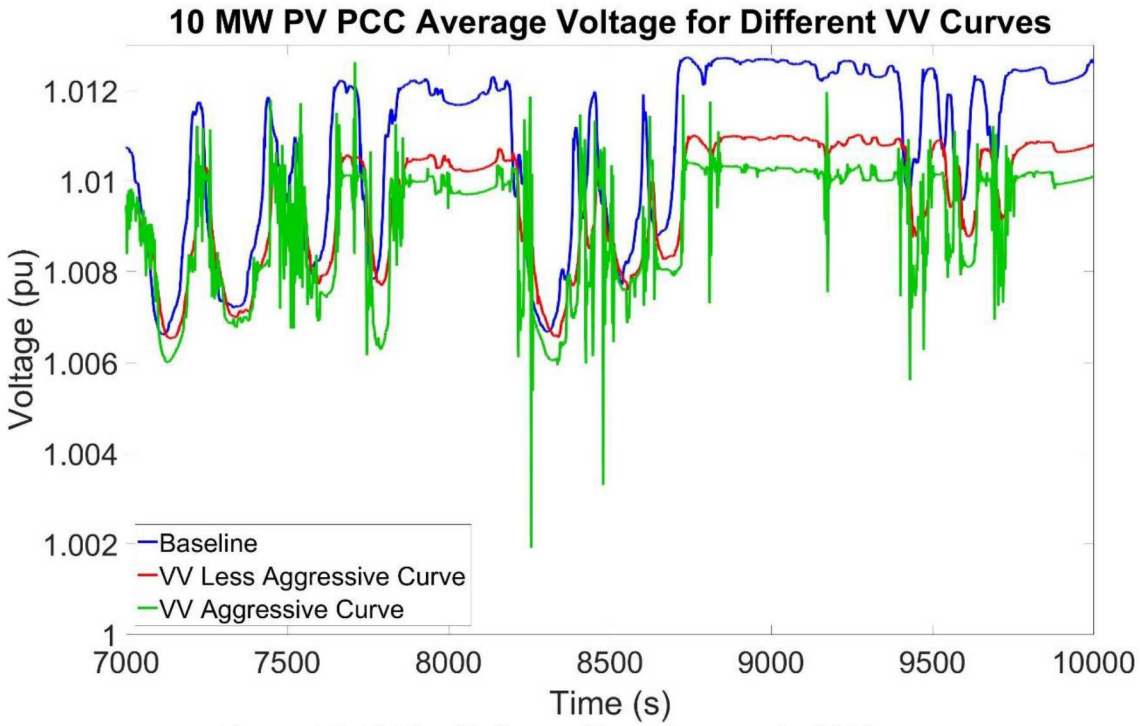

Figure 4-5. VV Oscillations with an "aggressive" VV curve.

To reduce the magnitude of the oscillation, a less aggressive slope was selected for the volt-var curve:

P1 = (92, 25)
P2 = (99, 0)
P3 = (101, 0)
P4 = (108, -25)

A comparison of the reactive power produced by the 10 MW DER device with and without the VV function enabled is shown in Figure 4-6. As shown in the figure, the reactive power contribution from the device is modest, but it reduces the maximum and average voltage as shown in Figure 4-7, where the minimum, maximum, and average voltages were plotted using for all buses and all phases. The line represents the average voltage for all the buses and the colored patch represents the range of voltages over time for the feeder.

Notice from the simulation results that the VV function can bring the average bus voltage closer to the desired nominal value. These effects can also be observed from the maximum voltage, reducing the voltage band created from the maximum and minimum values.

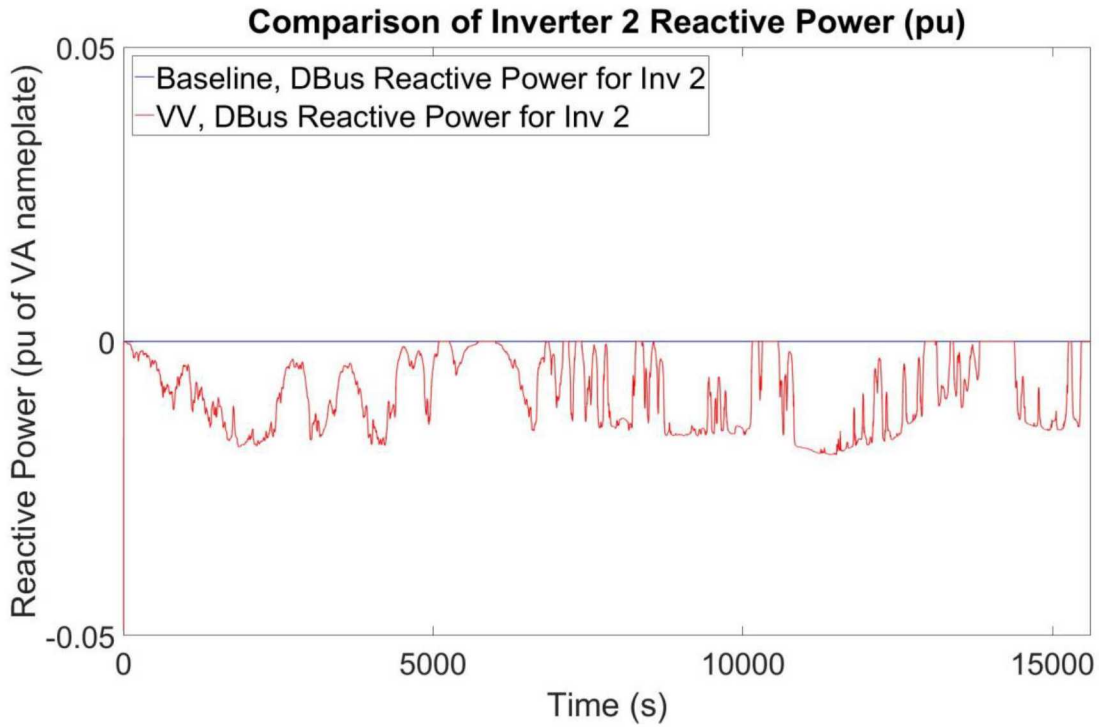

Figure 4-6. Reactive power from the DER devices with and without VV enabled.

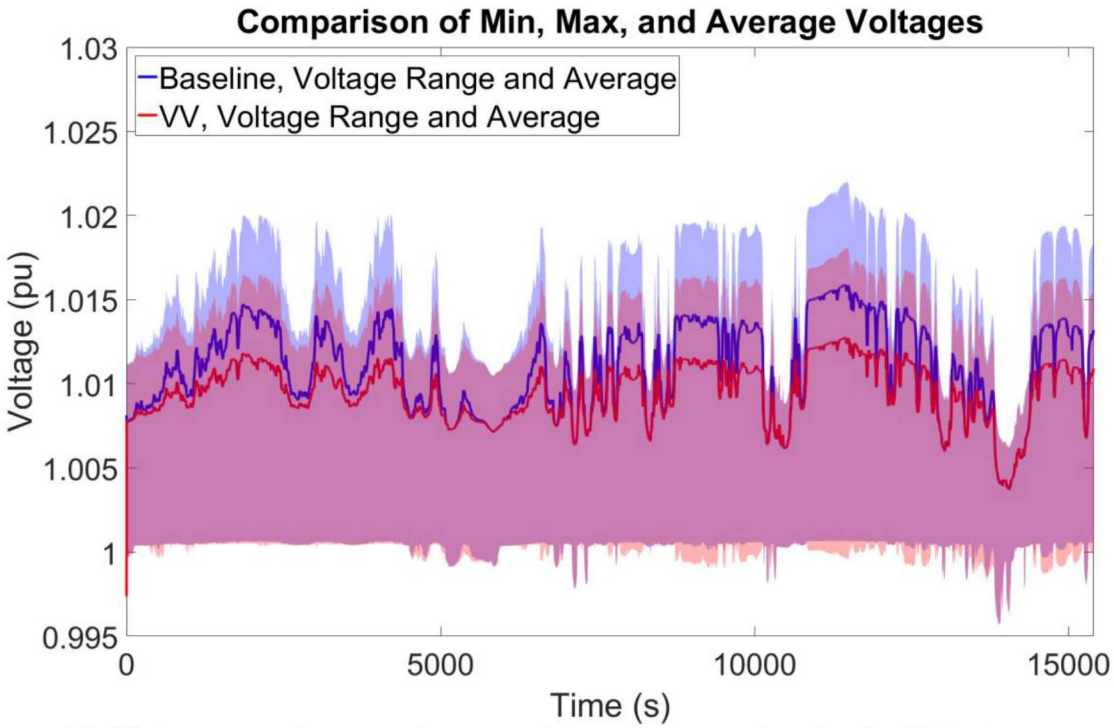

Figure 4-7. Minimum, maximum, and average bus voltages vs time for the VV test compared to the baseline data.

4.1.3. Extremum Seeking Control

ESC was implemented with a RT model of the PNM feeder as shown in Figure 4-8. Two parameter sets for the ESC approach were used, as shown in

Table 4-1. The simulation results for parameter set 1 are shown in Figure 4-9. In that run the ESC adjusted the reactive power from the DER devices to move the average bus voltage toward the nominal set point, i.e., 1 pu. Furthermore, the maximum and minimum bus voltage values are adjusted closer to nominal as well. The reactive power probing signal's impact on the feeder voltage is clearly seen in the results. Although effective, the probing signal magnitudes are large, and the ESC produces an undesirable voltage deviation around the optimal set points. Therefore, the ESC probing amplitudes, *a*, were adjusted in parameter set 2. As seen in Figure 4-10, this reduced the magnitude of the voltage variation from the probing signals. Figure 4-11 illustrates the average voltage compared to the baseline simulation for the 4 hour simulation.

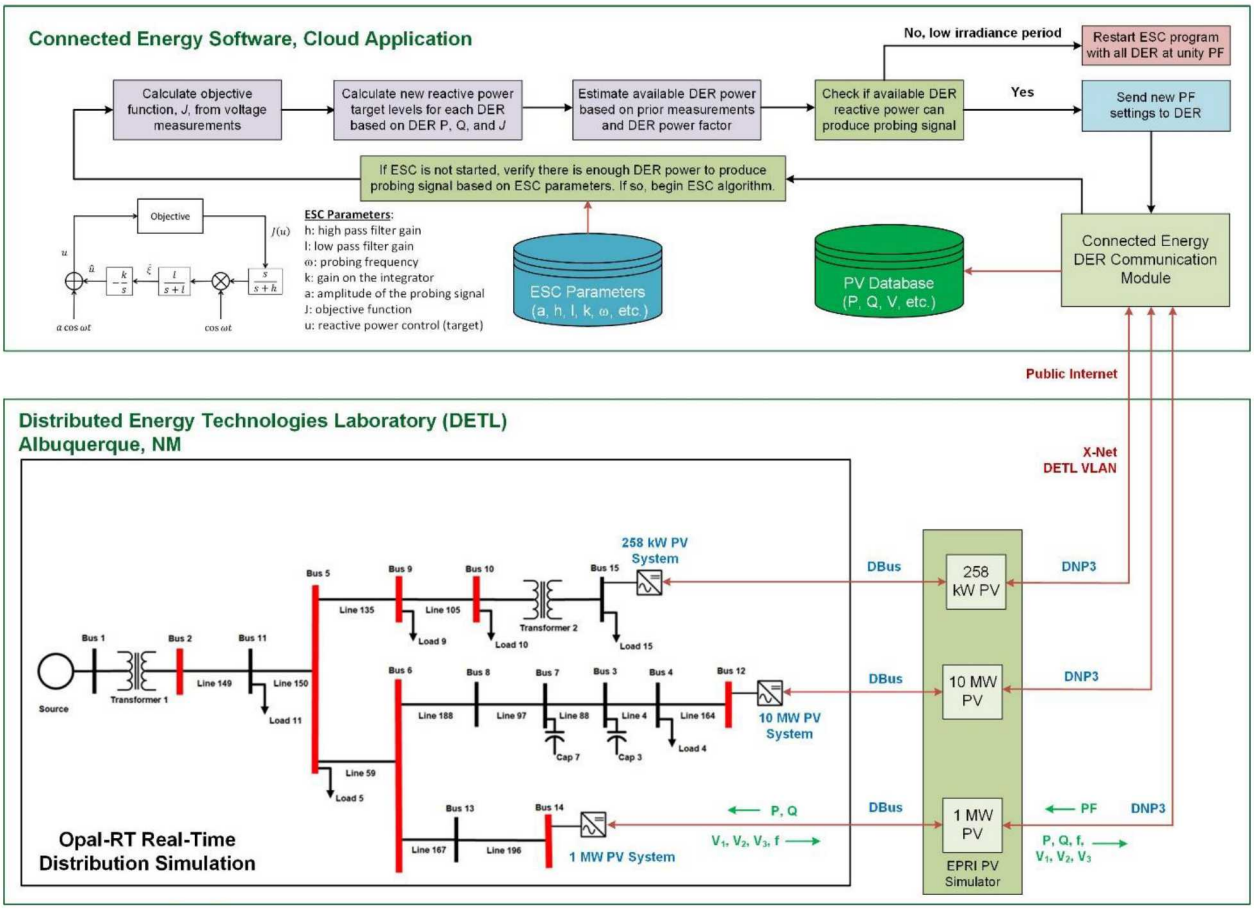

Figure 4-8. ESC implementation with the PNM feeder model.

Table 4-1. ESC Parameters

#	Model	J function	l	h	r_{comm}	Inverter 1 (258 kW)				Inverter 2 (10 MW)				Inverter 3 (1 MW)			
						P	f	a	k	P	f	a	k	P	f	a	k
1	PNM	$\sum_{i=1}^{n}(V_i - V_n)^2$	$\frac{\sqrt{5}}{800}$	$\frac{\sqrt{5}}{800}$	2 s	258 kW	$\frac{\sqrt{2}}{40}$	25.8 kVar	-25.8	10 MW	$\frac{\sqrt{3}}{40}$	1 MVar	-1000	1 MW	$\frac{\sqrt{5}}{40}$	100 kVar	-100
2	PNM	$\frac{1}{n}\sum_{i=1}^{n}\left(\frac{V_i - V_n}{V_n}\right)^2$	$\frac{\sqrt{5}}{800}$	$\frac{\sqrt{5}}{800}$	2 s	258 kW	$\frac{\sqrt{2}}{40}$	51.6 kVar	-2.58e7	10 MW	$\frac{\sqrt{3}}{40}$	50 kVar	-1e9	1 MW	$\frac{\sqrt{5}}{40}$	50 kVar	-1e8

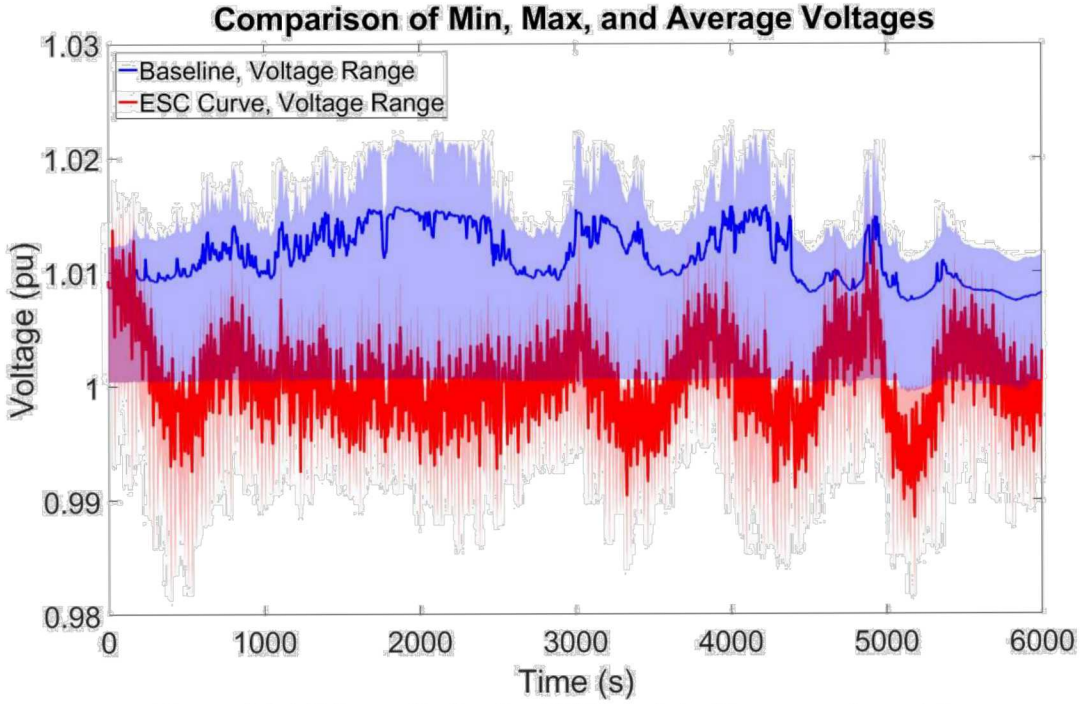

Figure 4-9. ESC results for the PNM model with parameter set 1.

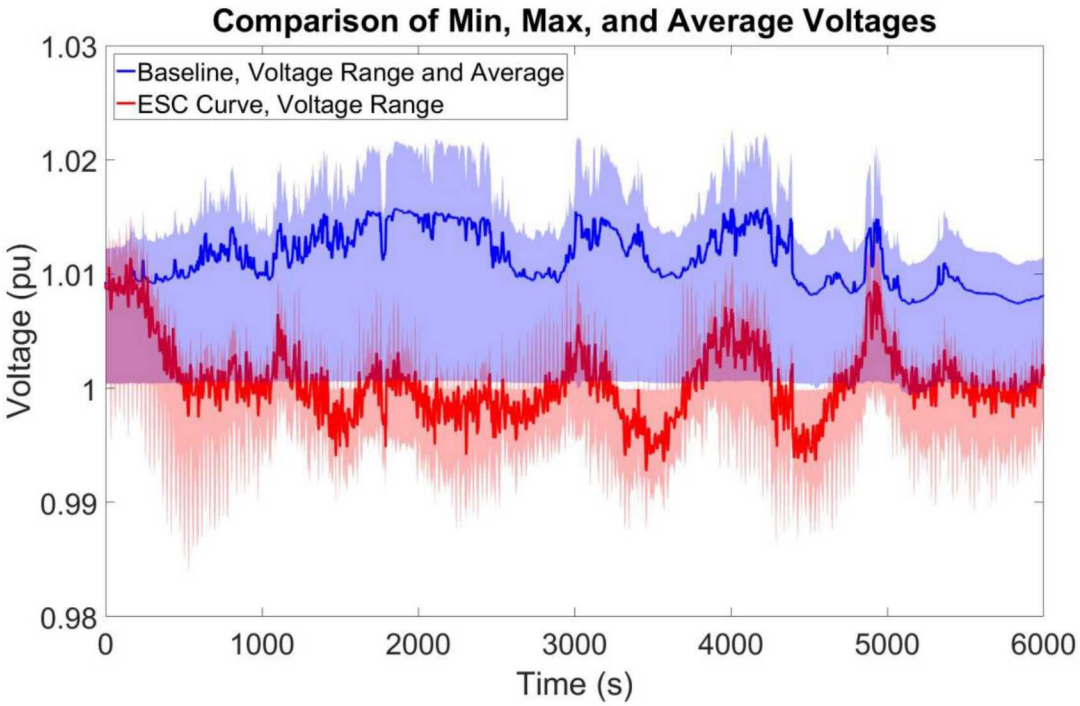

Figure 4-10. ESC results for the PNM model with parameter set 2.

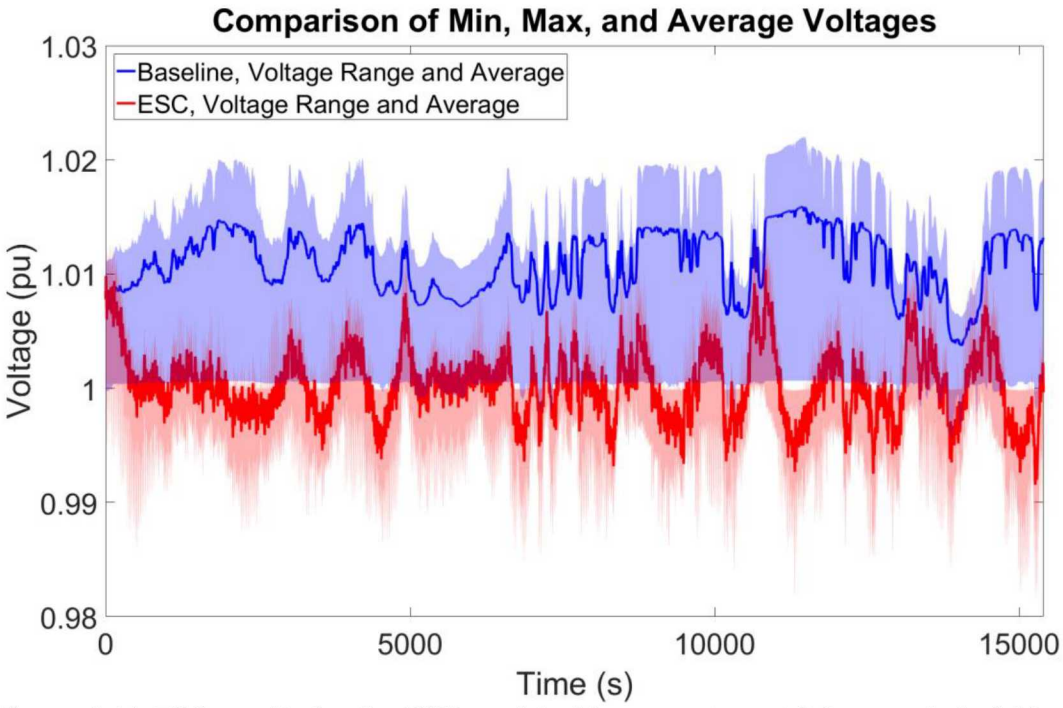

Figure 4-11. ESC results for the PNM model with parameter set 2 for a period of 4 hours.

4.1.4. State-Estimation-Based Particle Swarm Optimization

The setup for the PSO simulations are shown in Figure 4-12. In this case, the state estimation was used to update the load data in the OpenDSS time series simulation and the DER power forecasts were used to update the OpenDSS power levels. An example of the forecasts is shown in Figure 4-13. There is a lag in the energy profile from the PV, but it tracks the DER energy reasonably. Notice it takes 1 hour for the forecast to begin because it uses prior production data and the clear sky index to generate the power prediction. To accelerate the debugging process, the first hour of production data was prerecorded by Connected Energy, and when the simulation was started, this data was prepended to the production data. This way many simulations could be run sequentially to debug the PSO implementation.

The OpenDSS time series simulation was run multiple times using PSO to determine the optimal PF set points for each of the DER devices. However, it was found that absolute care must be taken to use the same component and settings for the Simulink/RT-Lab and OpenDSS models; otherwise erroneous solutions will be found. Binary variables (e.g., capacitor banks) and discrete variables (e.g., tap changes) must also be re-initialized (i.e. reset) with each new run of the OpenDSS time series simulation to prevent updated initial conditions from the prior simulation—an unfortunate byproduct of using the OpenDSS communication interface implementation. One example of a mismatch in the Simulink/RT-Lab and OpenDSS simulations is shown in Figure 4-14. A capacitor bank with a programmed relay existed in the OpenDSS model but not in the RT simulation. As a result, OpenDSS PSO solutions included PF settings that actuated the capacitor bank relay, but without the relay in the RT simulation, those solutions produce nonoptimal solutions (the spikes in Figure 4-14). By removing the capacitor bank relay from the OpenDSS model, much better solutions were determined, shown in Figure 4-15. Interestingly, with the constraints placed on updating a new PF level (e.g., the solution must be a certain amount better than the previous one), there are only 3 times that the DER devices have their PF setting updated. This threshold can be tuned, but it is actually desirable because it reduces the number of PF write commands and shows the solution is robust to changing PV irradiance.

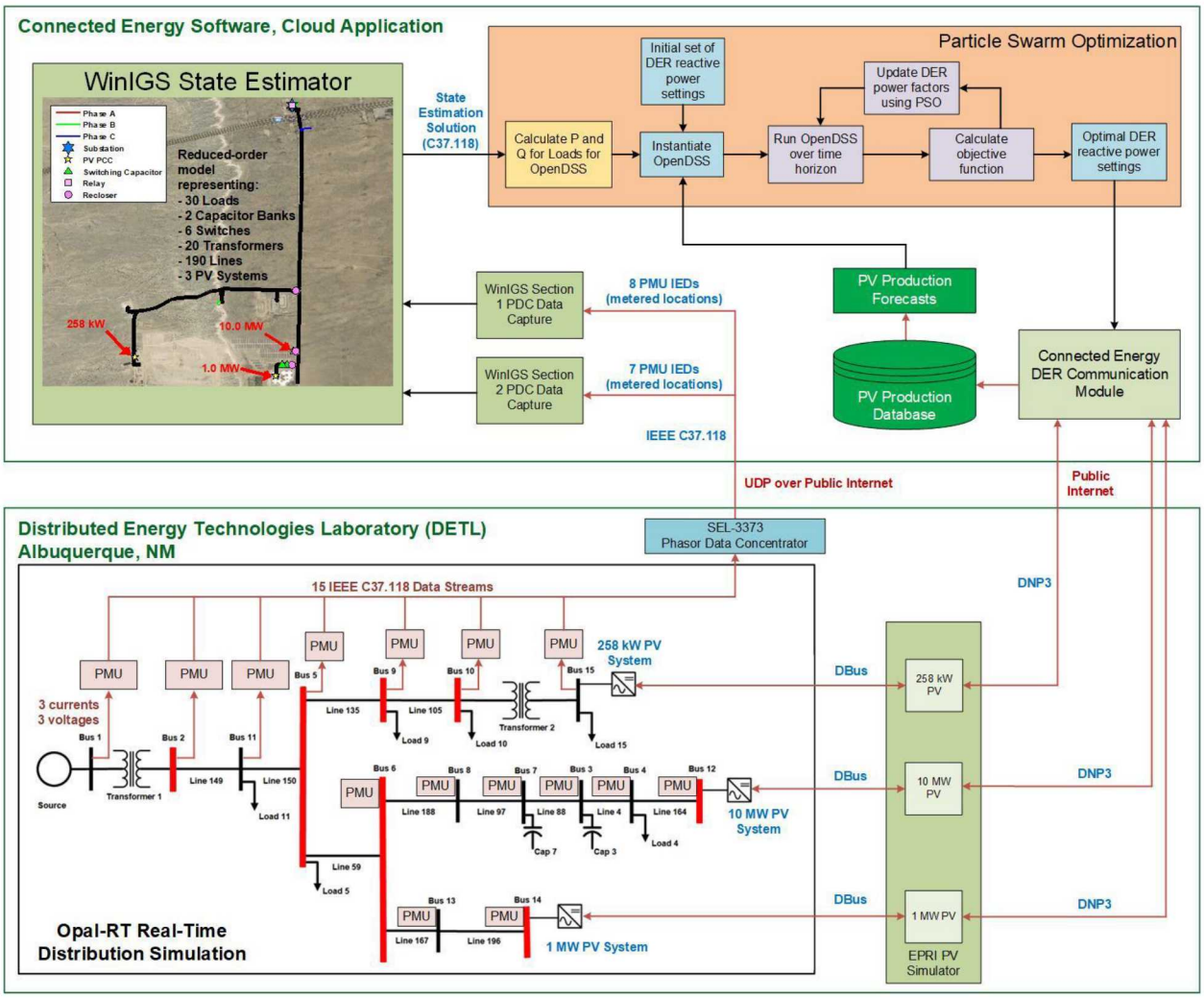

Figure 4-12. State-Estimation Based PSO implementation with the PNM feeder model.

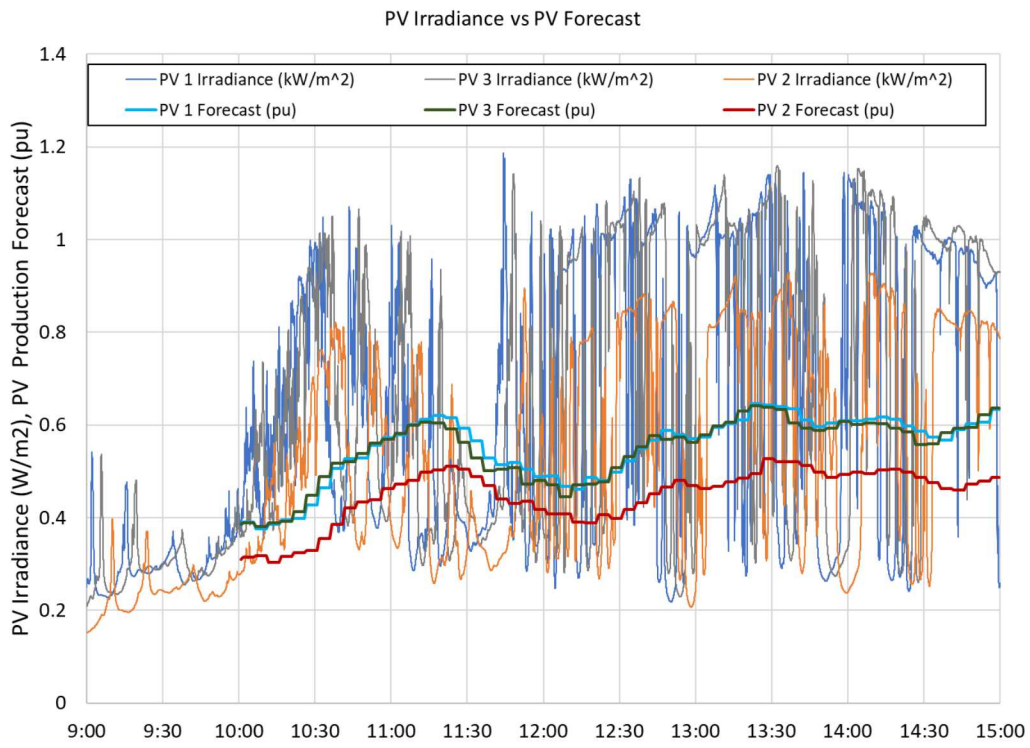

Figure 4-13. PV Irradiance and PV Forecast Profiles. 1000 W/m^2 will produce 1 pu of Power.

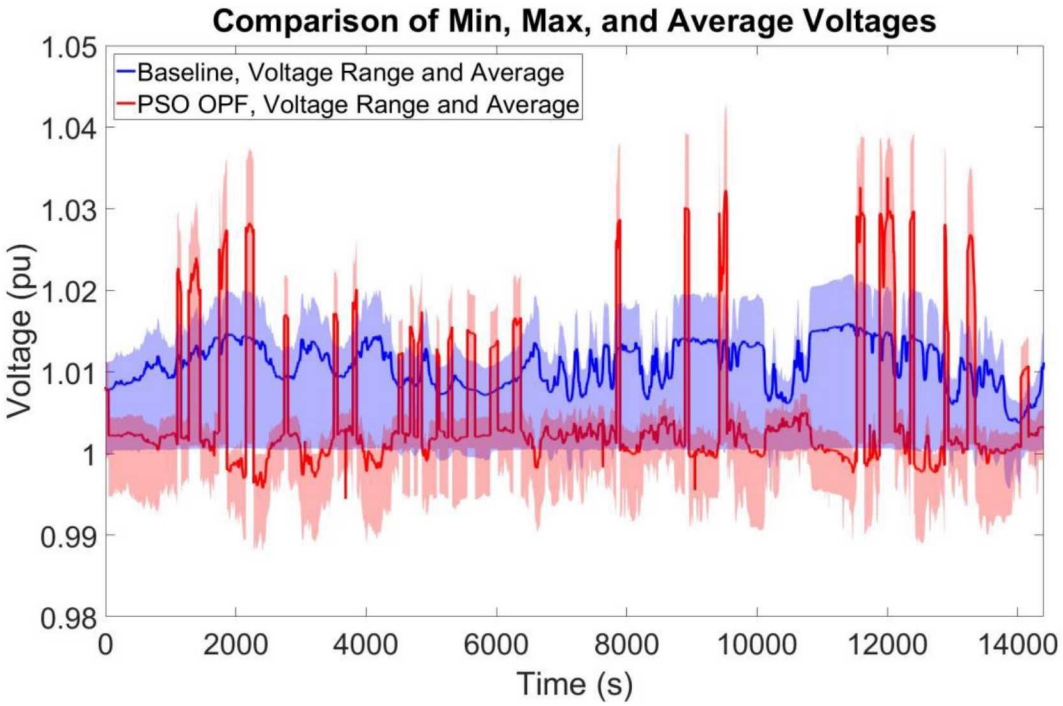

Figure 4-14. PSO results for the OpenDSS PNM model with Switching Capacitor Banks.

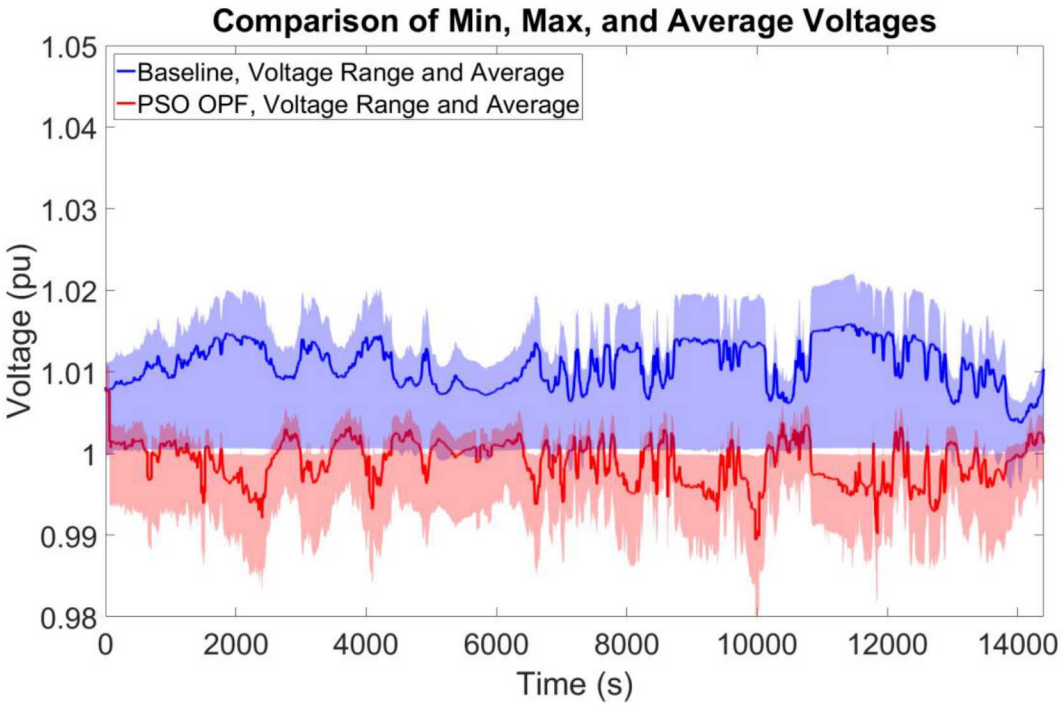

Figure 4-15. PSO results for the OpenDSS PNM model without Switching Capacitor Banks.

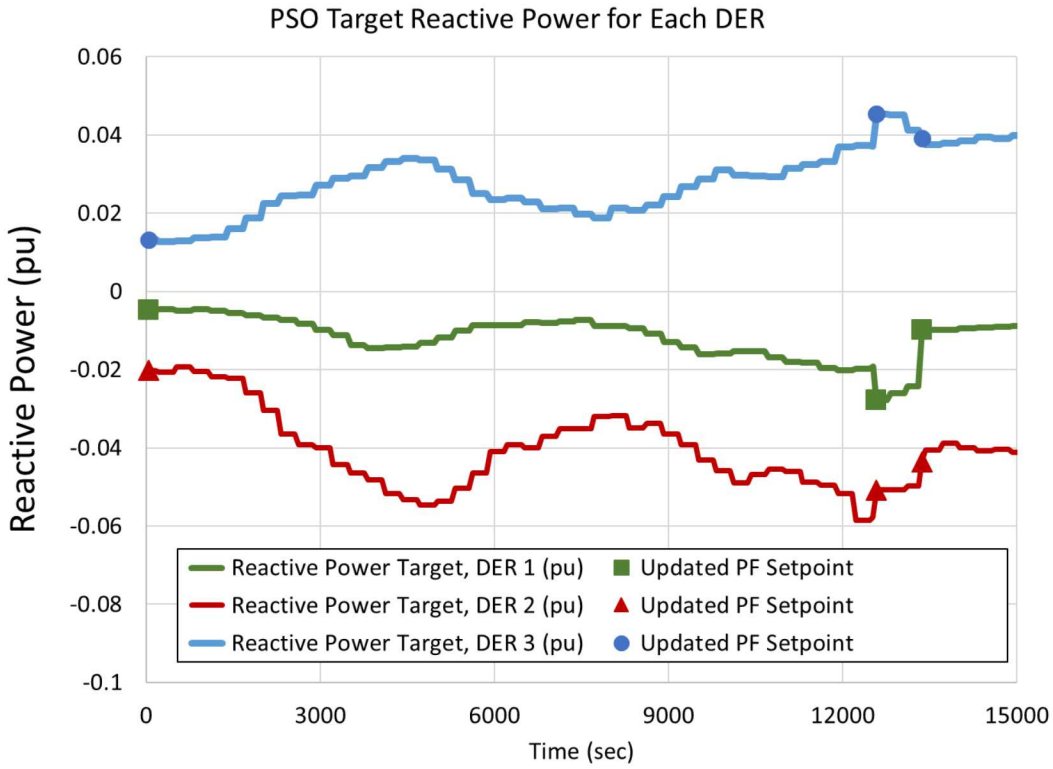

Figure 4-16. PSO PNM target reactive power levels for each DER. The target reactive power is calculated from the PSO PF set point and the PV forecast at that time.

4.1.5. Comparison and Discussion

Each of the voltage regulation methods have their advantages and disadvantages in terms of communications and computational overhead, implementation complexity, and availability in DER equipment. Overall, each of them can reduce the voltage deviation from nominal and maintaining the PNM feeder well within ANSI Range A voltage limits. The reactive power from the 10 MW DER device is shown in Figure 4-17. The VV method barely escapes the deadband so the DER does not absorb much reactive power. The ESC method produces a DER reactive power probing signal that causes a voltage ripple on the feeder, but it allows the DER to track the optimal reactive power setpoint well. The PSO method is the most complicated to implement, but issues optimal set points to each DER every 1 minute. A comparison of each of the voltage regulation methods is shown in Figure 4-18. This figure depicts the minimum, maximum and average bus voltages for each of the methods. The simulation results indicate ESC and PSO can regulate the voltage closer to nominal, compared to VV.

To better understand the differences in these approaches, an analytical score was developed to summarize the effectiveness of each voltage regulation method, and a best score was calculated where the voltage regulation approach drove the solution to 1 pu:

$$score = \frac{1}{T}\int_{t=0}^{t_{end}} \frac{1}{N}\sum_{b=1}^{N}\left(|v_{bl}(t) - v_{nom}| - |v_{reg}(t) - v_{nom}|\right) dt$$

$$best\ score = \frac{1}{T}\int_{t=0}^{t_{end}} \frac{1}{N}\sum_{b=1}^{N}\left(|v_{bl}(t) - v_{nom}|\right) dt$$

where v_{bl} is the baseline voltage, v_{nom} is the nominal voltage (1 pu), v_{reg} is the voltage from the voltage regulation method, T is the time period of the simulation, b is the bus, and t is the simulation time. The scores representing the average voltage improvement for all buses averaged over a four-hour simulation period in units of pu. Table 4-2 summarizes the effectiveness for the PNM model of each approach per phase as well as the average of each phase, calculated with:

$$Impact = \frac{score}{best\ score}$$

VV slightly improved the average bus voltage, with an impact percentage of 12.3%. Moreover, implementing ESC and PSO demonstrated a larger impact on the feeder, with an average impact percentage of 74.5% and 73.7% respectively. A more detailed look at the impact of this regulation approaches per phase, shows that, since the system is relatively balanced, each phase is affected equally.

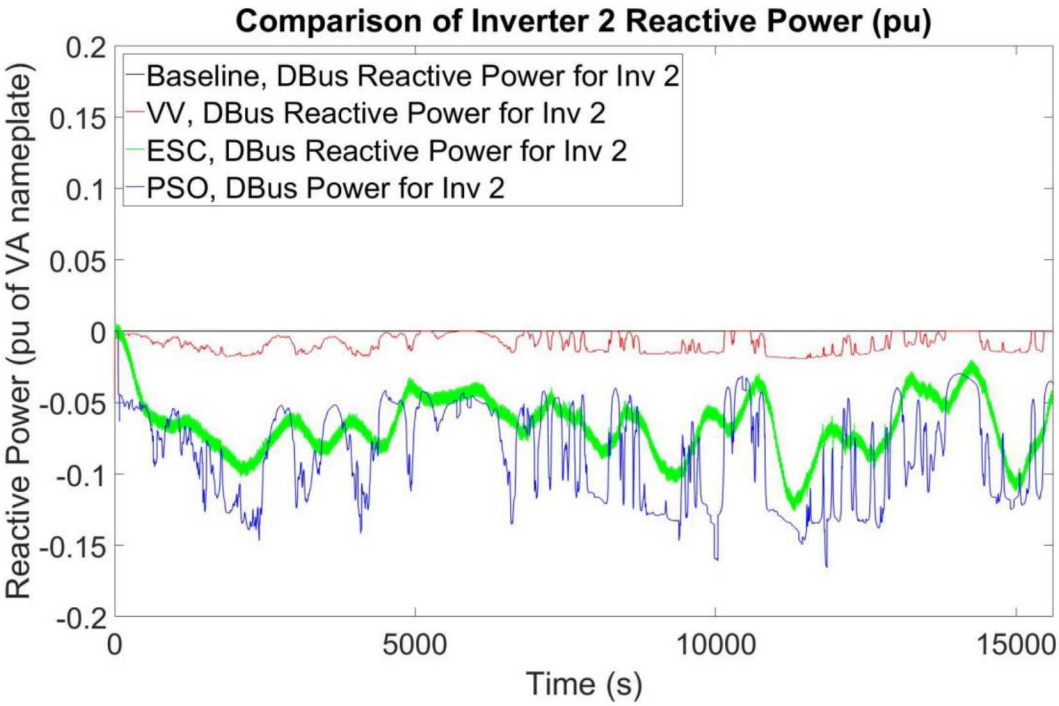

Figure 4-17. Comparison of Reactive Power at PV Inverter 2 the PNM Feeder.

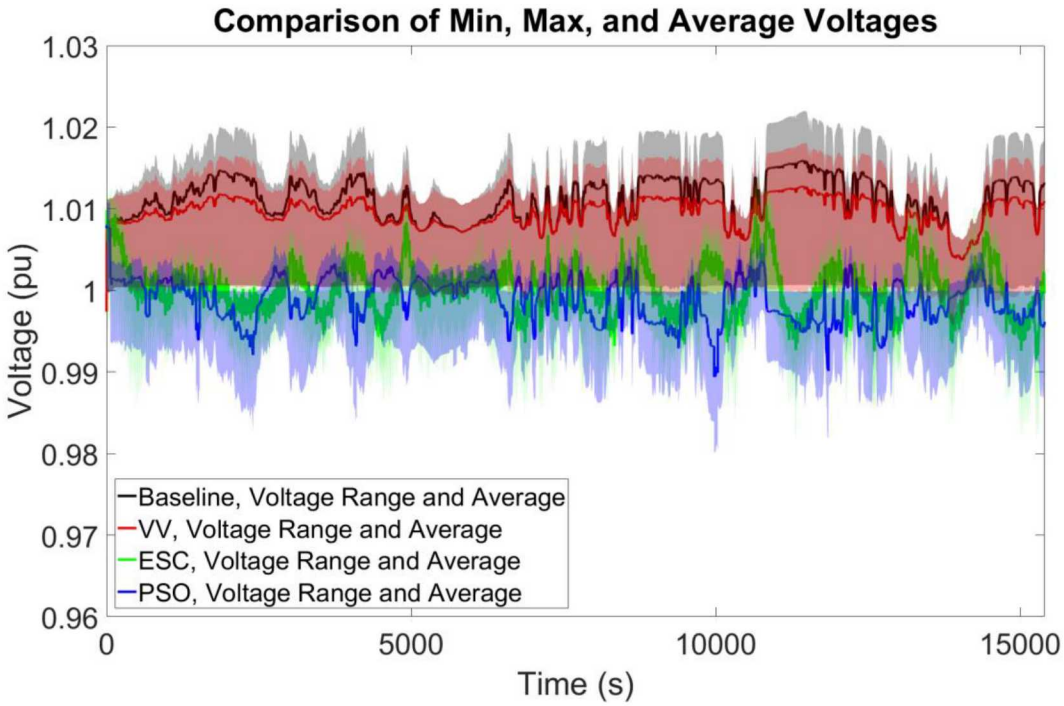

Figure 4-18. Comparison of Voltage Regulation Approaches for the PNM Feeder.

Table 4-2. PNM Voltage Regulation Scores.

PNM Feeder Score					
	Phase A (x1000)	Phase B (x1000)	Phase C (x1000)	Average (x1000)	Average Impact (%)
VV	0.467	0.468	0.466	1.401	**12.9%**
ESC	2.745	2.748	2.591	8.084	**74.5%**
PSO	2.727	2.731	2.541	7.999	**73.7%**
Best Score	**3.650**	**3.681**	**3.519**	**10.850**	

4.2. Simulations with the National Grid Model

In a comparable manner, voltage regulation approaches are compared on a NG feeder model. One of the most significant differences in the NG feeder model in comparison with the PNM feeder is that only the Old Upton Rd 684 kW PV system could be controlled in the field demonstration. For this reason, two test cases are presented: one where only the controllable PV system is used for the voltage regulation methods and one where all the DER devices are used. The NG system is significantly unbalanced, with phase B above nominal voltage, phase C below nominal voltage, and phase A operating approximately at nominal voltage. This prevented many of the voltage regulation methods from making significant improvements to the feeder voltage profile.

4.2.1. Baseline Simulation

Four-hour irradiance profiles were created for the 31 DER devices in this model (1 three-phase and 30 single phase). Figure 4-19 illustrates the baseline active power profile for the 684 kW PV system. Figure 4-20 shows the voltage profiles for each of the phases.

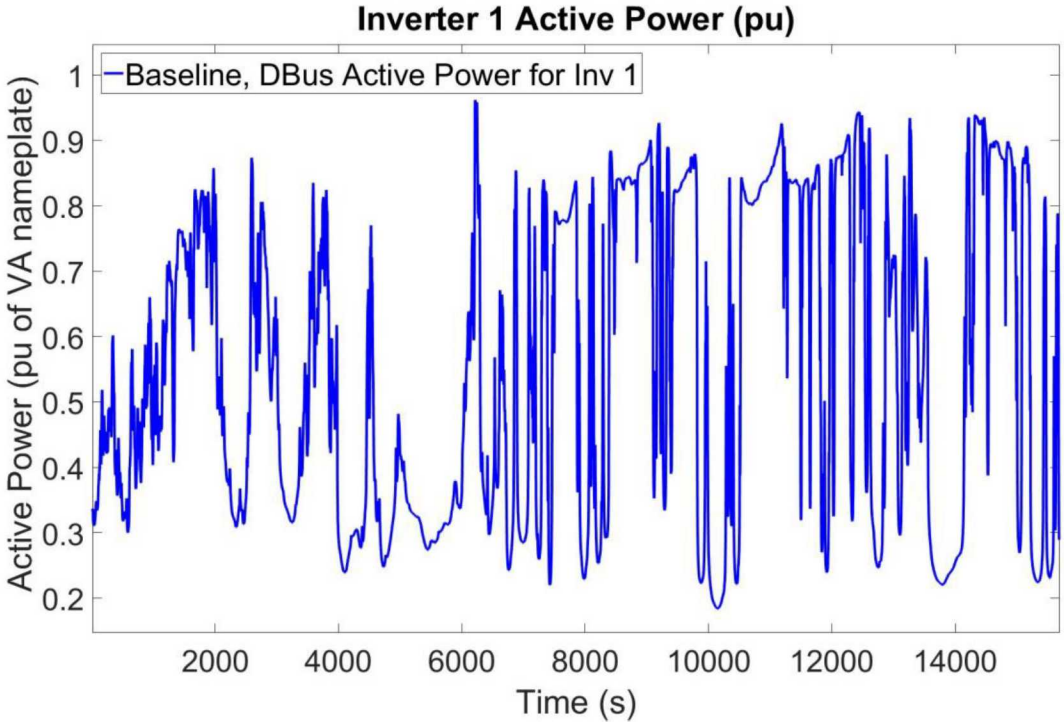

Figure 4-19. PV power levels for the 4-hour simulations.

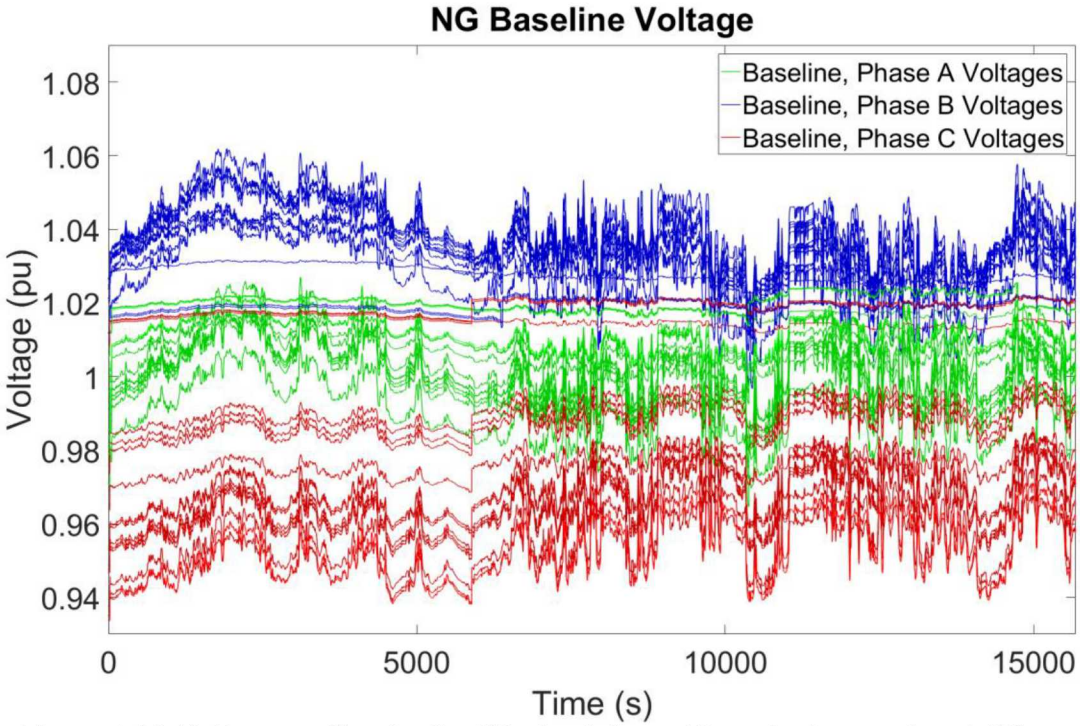

Figure 4-20. Voltage profiles for the NG simulation with each phase colored differently.

4.2.2. Volt-Var

There was is little, to no voltage regulation when using the VV profile as shown in Figure 4-21 because the average voltage at the PCC is within the VV deadband of the PV inverters. However, when all the single-phase inverters are added to the control approach, it is possible to improve the average bus voltage and reduce the maximum and minimum bus voltage band, shown in Figure 4-22.

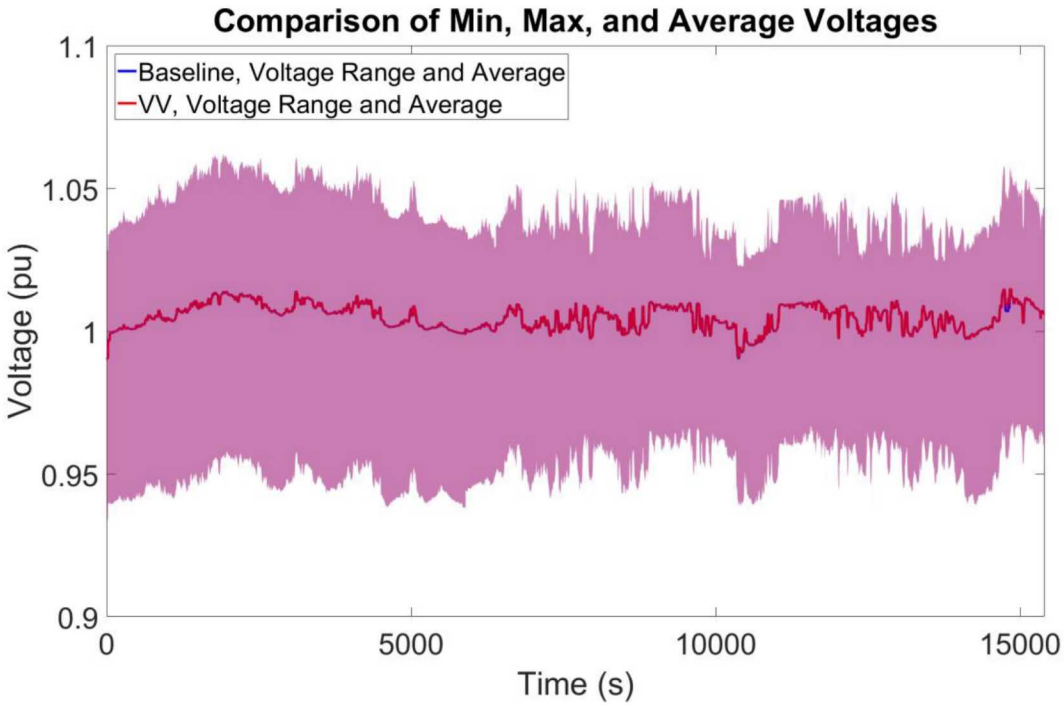

Figure 4-21. Minimum, maximum, and average bus voltages vs time for the VV test compared to the baseline data controlling a single three-phase PV system.

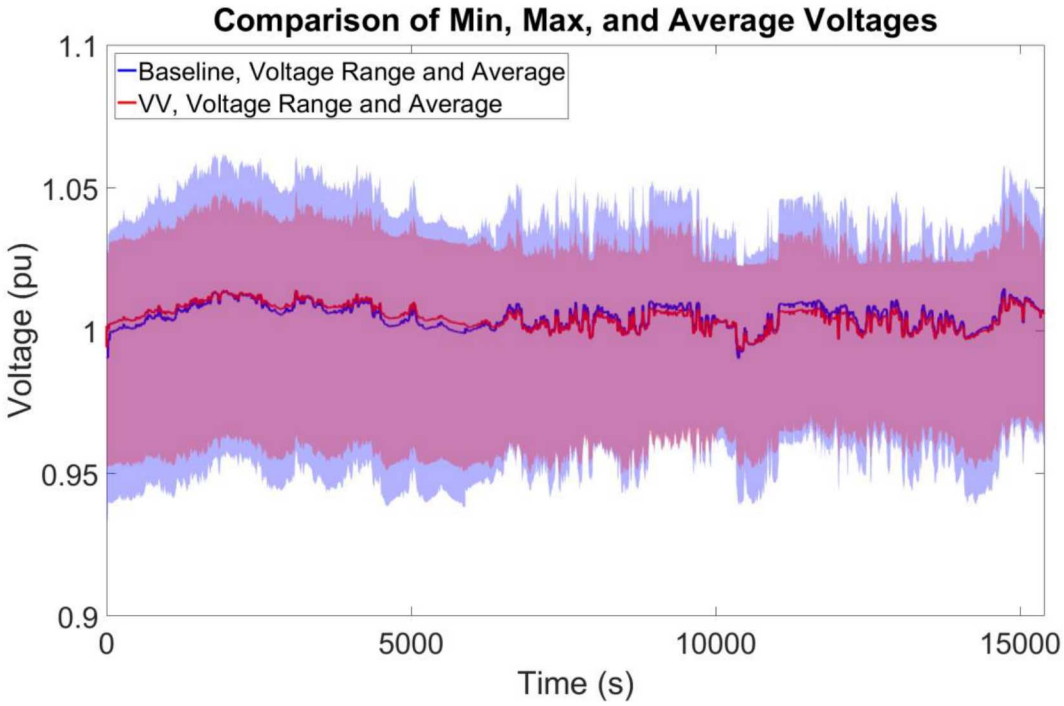

Figure 4-22. Minimum, maximum, and average bus voltages vs time for the VV test compared to the baseline data controlling all PV inverters.

4.2.3. Extremum Seeking Control

Extremum seeking control was conducted on the NG feeder model to reasonably replicate the environment that the controller would be deployed in the field demonstration. The reactive power setpoints were issued to the 684 kW PV system at 30 seconds (based on the read/write times for the fielded SMA system) and voltage measurements were taken only from the PV site. In the first ESC experiment using parameter set 1 in Table 4-3, only the voltage on phase A, V^A, was used to calculate the objective function. In this feeder, there was significant phase imbalance and at the PV system: phase A voltages are close to nominal (~0.99-1.01 pu), phase B voltages are significantly above nominal (at times >1.05 pu), and phase C voltages are <0.95 pu—as shown in Figure 4-23. This presented a challenge for the ESC approach (like all the other voltage regulation methods) because the DER can only inject symmetric (positive sequence) reactive power. This means all the phase voltages are shifted in the same direction with a change in the DER power factor.[24]

As shown in Figure 4-24, the reactive power ripple from the 45.6 kVar probe did not significantly change the voltage on the feeder. Compared to the variability of the voltage variability created from the irradiance changes, the probing signal is hard to see. For this reason, the magnitude of the probing signal was increased in the 2nd test. The objective function was also doubled to drive the DER reactive power changes toward the objective function minimum more aggressively. The results from this simulation are shown in Figure 4-25.

Table 4-3. ESC Parameters for the RT simulations with the NG Feeder model.

#	Model	J function	l	h	r_{comm}	Inverter 1 (684 kWdc)			
						P	f	a	k
1	NG	$\frac{1}{n}\sum_{i=1}^{n}\left(\frac{V_i^A - V_n}{V_n}\right)^2$	$\frac{1}{3000}$	$\frac{1}{3000}$	30 s	684 kW	$\frac{1}{300}$	45.6 kVar	-6.84x10^7
2	NG	$\frac{2}{n}\sum_{i=1}^{n}\left(\frac{\overline{V_i} - V_n}{V_n}\right)^2$	$\frac{1}{3000}$	$\frac{1}{3000}$	30 s	684 kW	$\frac{1}{300}$	85.5 kVar	-6.84x10^7

[24] Note: while not present in most commercial DER currently, there is some research in the area of creating negative sequence DER systems that would be able to inject different levels of reactive power on each phase.

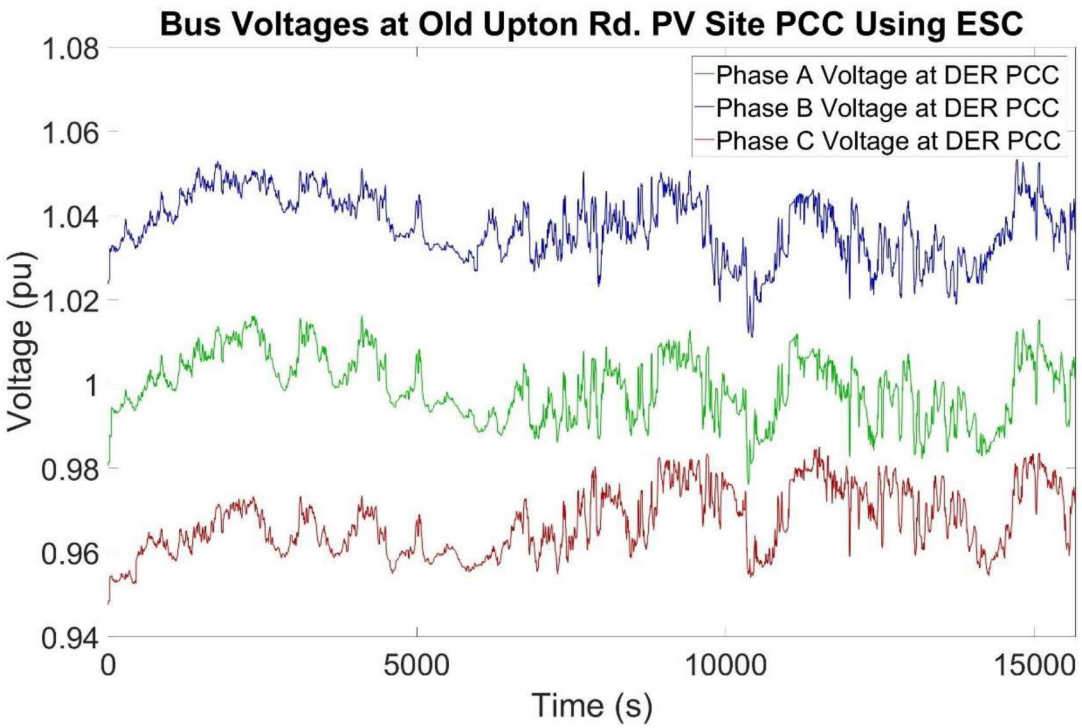

Figure 4-23. Imbalanced phase voltages at the DER device during the ESC simulation using parameter set 1.

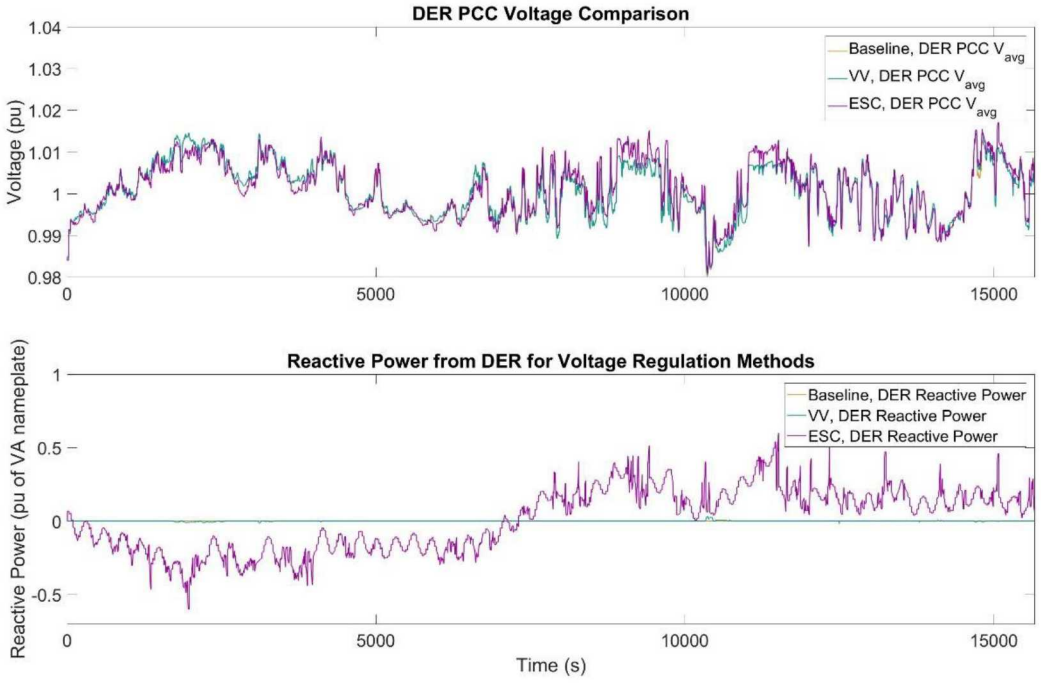

Figure 4-24. Stacked plot showing the average voltage on Bus 15 (top) and the DER reactive power contribution (bottom) compared to the baseline and VV cases.

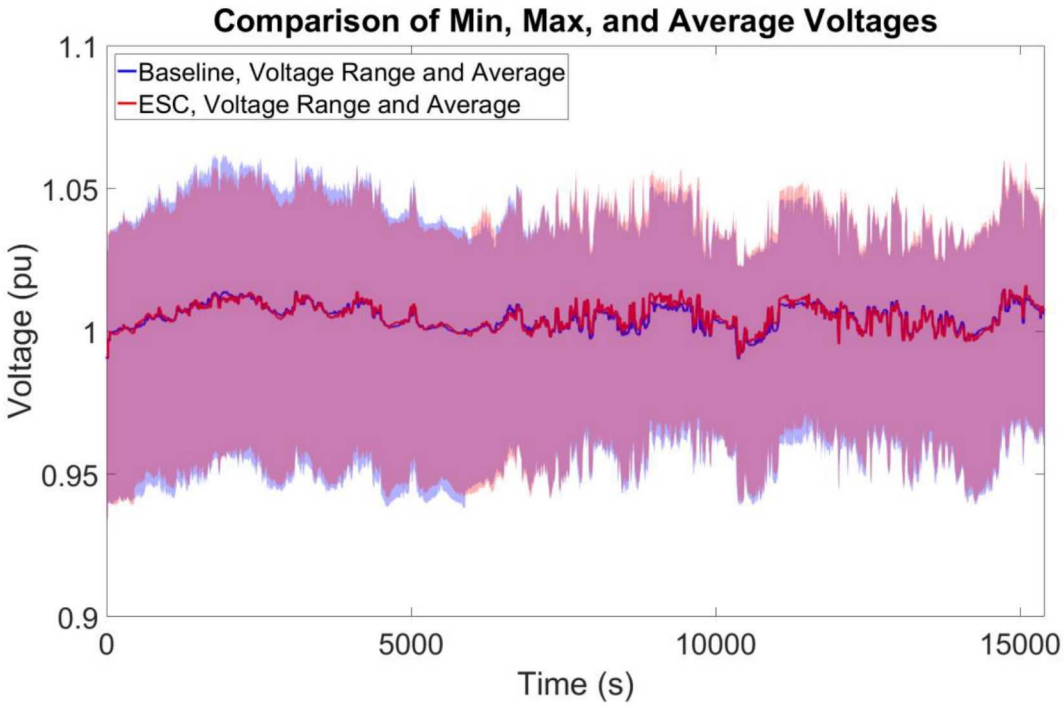

Figure 4-25. Minimum, maximum, and average bus voltages vs time for the ESC test with Parameter Set 2, compared to the baseline results controlling a single PV inverter.

When implementing ESC with the three-phase PV inverter, only a slight improvement on the average bus voltage was possible. However, when controlling all the PV inverters with ESC parameters in Table 4-4, the maximum and minimum voltage band is significantly reduced, shown in Figure 4-27. Grouping the DER based on what phase they were connected to was a good method of limiting the number of probing frequencies , but allowed each of the phases to adjust their reactive power contributions independently. An example of this deployment technique is shown in Figure 4-26. Unfortunately, this also produced a sizable voltage ripple on the power system because all the inverters on each phase had the same probing frequency.

Table 4-4. ESC Parameters for the RT simulations with all inverters on the NG Feeder model.

#	Model	J function	l	h	r_{comm}	Three-Phase Inverters			Inverters on Phase A			Inverters on Phase B			Inverters on Phase C		
						f	a	k	f	a	k	f	a	k	f	a	k
1	NG	$\frac{2}{n}\sum_{i=1}^{n}\left(\frac{\overline{V_i}-V_n}{V_n}\right)^2$	$\frac{\sqrt{5}}{800}$	$\frac{\sqrt{5}}{800}$	2 s	$\frac{1}{40}$	$\frac{S}{15}$	$\frac{-S}{100}$	$\frac{\sqrt{2}}{40}$	$\frac{S}{10}$	$\frac{-S}{100}$	$\frac{\sqrt{3}}{40}$	$\frac{S}{10}$	$\frac{-S}{100}$	$\frac{\sqrt{5}}{40}$	$\frac{S}{10}$	$\frac{-S}{100}$

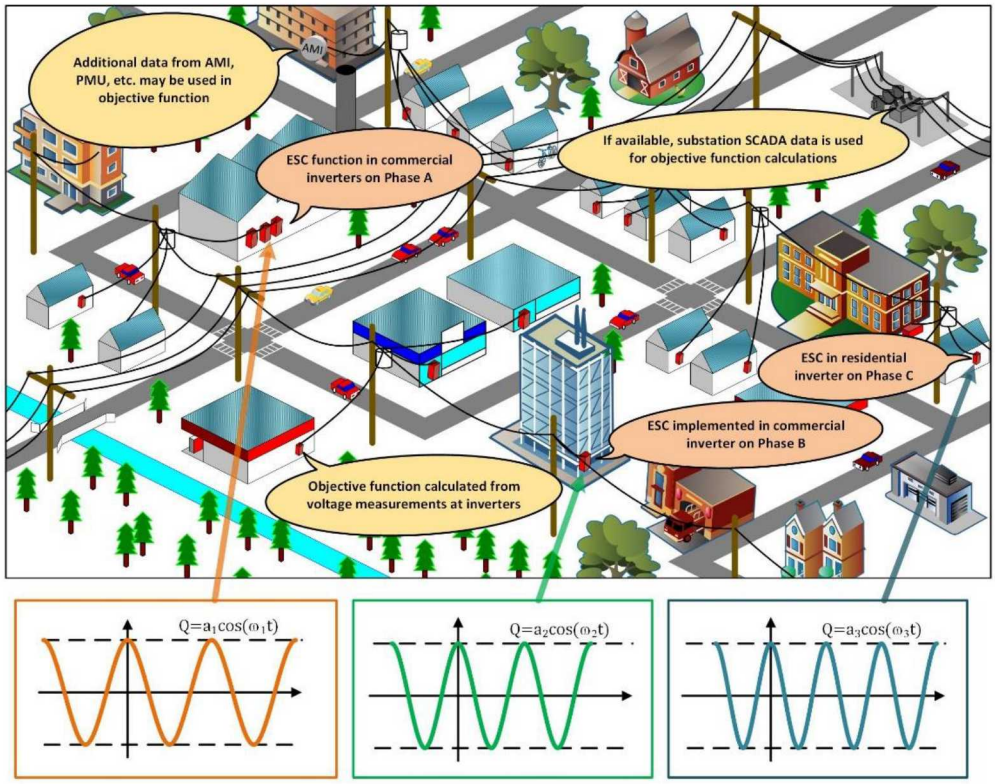

Figure 4-26. Cartoon of the ESC control deployed for inverters on each phase with different probing frequencies.

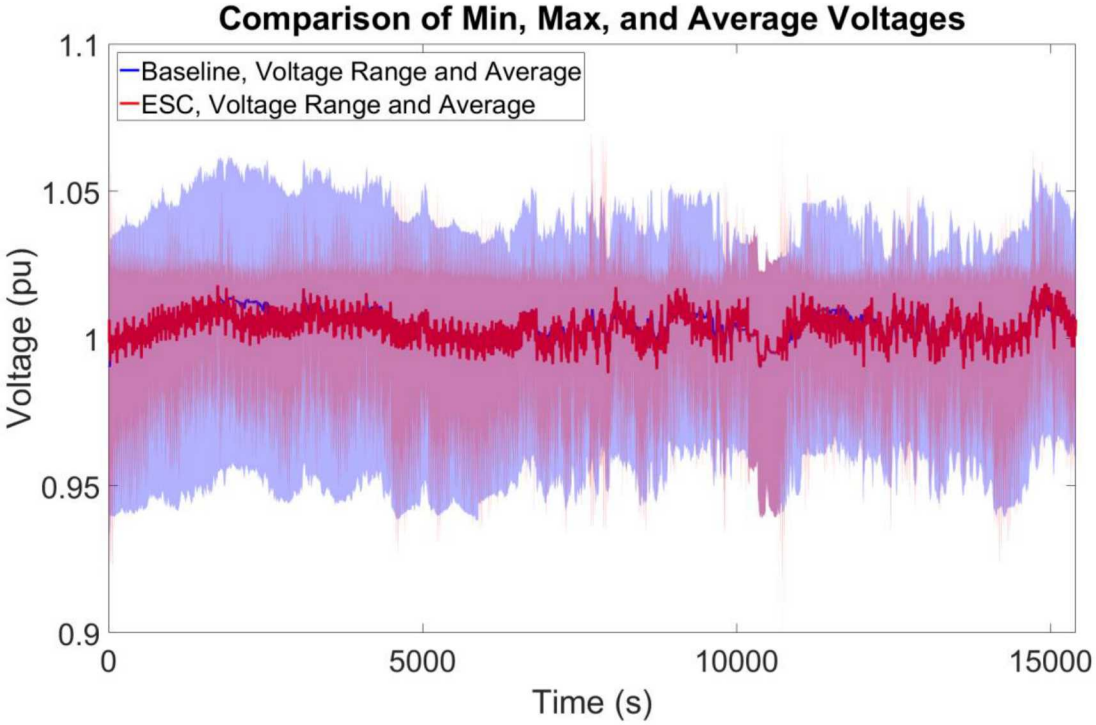

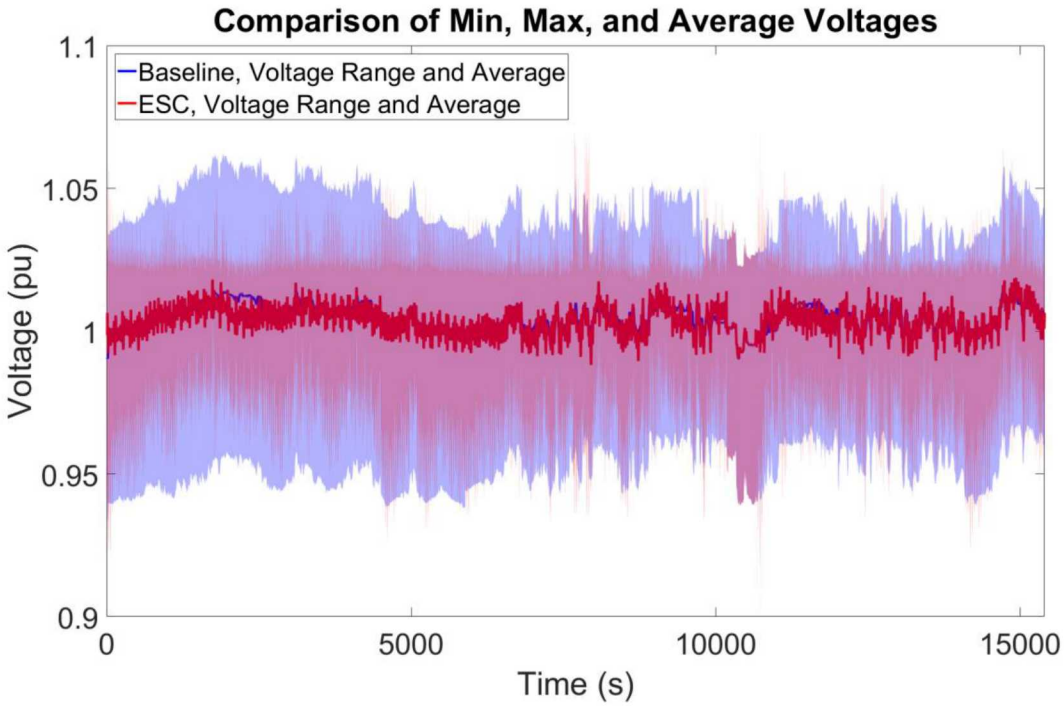

Figure 4-27. Minimum, maximum, and average bus voltages vs time for the ESC test with Parameter Set 2, compared to the baseline results controlling all PV inverters.

4.2.4. State-Estimation-Based Particle Swarm Optimization

The PSO optimization technique was deployed using the NG WinIGS state estimation code and the NG OpenDSS time-series simulations. Some of the differences in these models included voltage regulation equipment at the substation and differences in handling noncontrollable DER devices in the PSO code. When using only one controllable DER in the PSO, the solutions were determined much quicker than with the three DER devices in the PNM model. The code was configured to execute every 1 minute to determine the optimal set point for the Old Upton Rd PV site. The bus voltage results for the PSO OPF on the NG feeder are shown in Figure 4-28. Predictably, the solutions to the PSO were close to unity PF and the voltage did not change significantly in the simulation.

Next, all the DER devices were controlled by the PSO. Using the same swarm size of 60, the solution time was much longer. If the optimization took the full 10 iterations, it would often take longer than 60 seconds and roll into the next period, so solutions would appear after 2 minutes. As shown in Figure 4-29, optimizing 31 DER devices was difficult with a swarm size of 60 because the first two solutions produced results that pushed the minimum or maximum voltages outside the baseline envelope. However, after a few more solutions, the PSO significantly improved the voltage profile of the feeder for the remainder of the simulation.

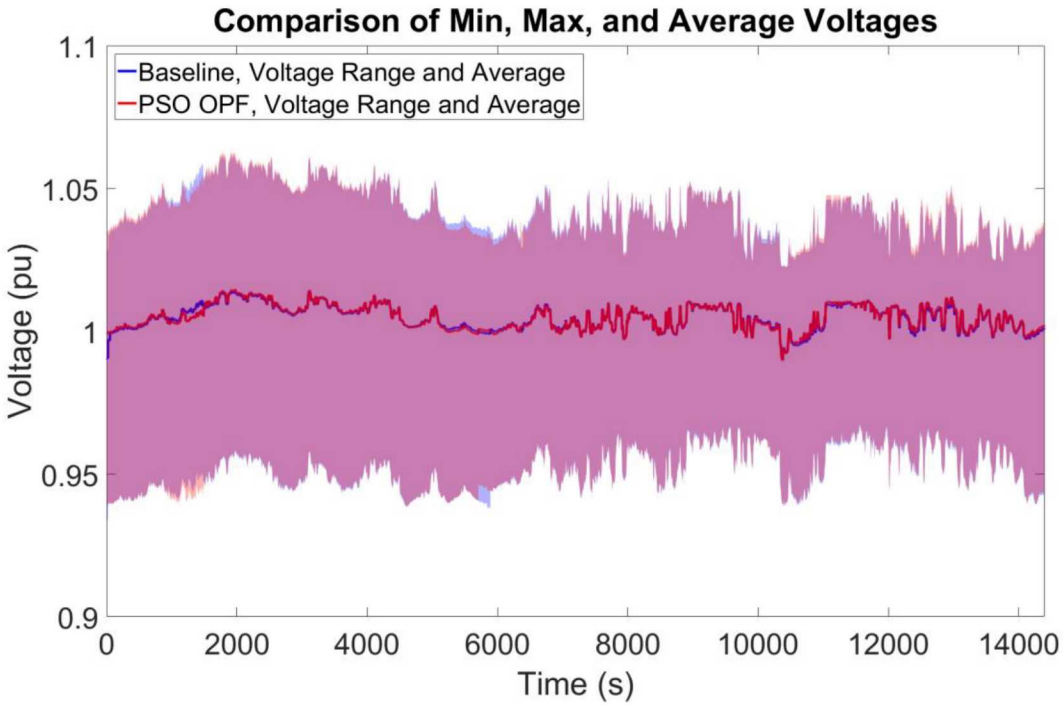

Figure 4-28. Minimum, maximum, and average bus voltages vs time for the PSO test compared to the baseline results controlling a single PV inverter.

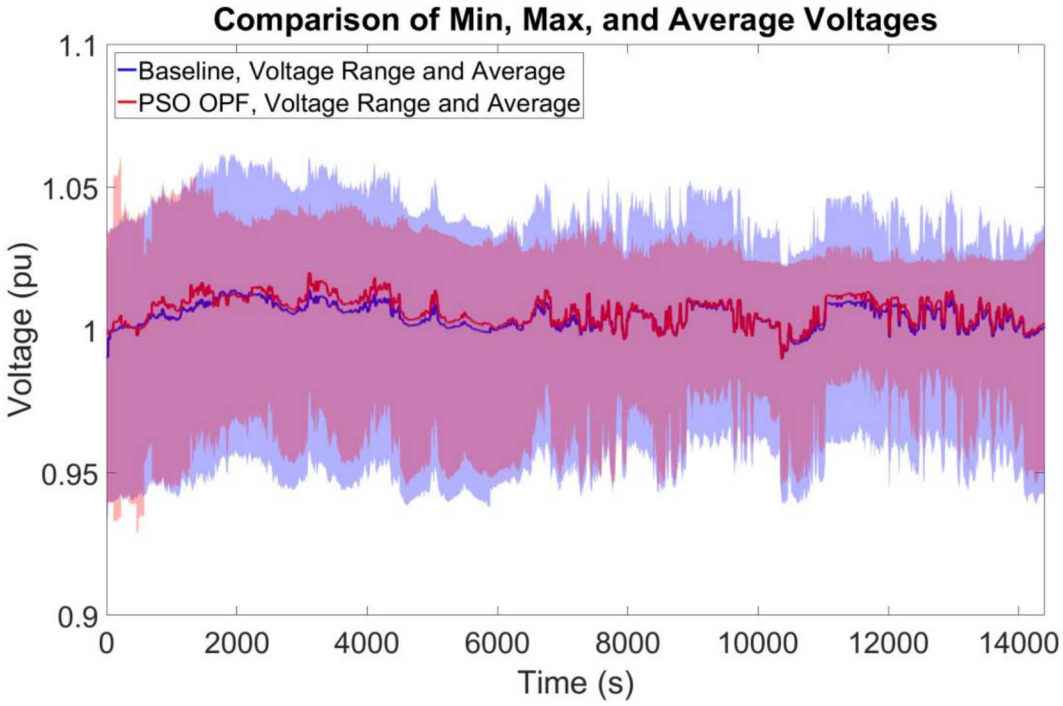

Figure 4-29. Minimum, maximum, and average bus voltages vs time for the PSO test compared to the baseline results controlling all PV inverters.

4.2.5. Comparison and Discussion

A comparison of the bus voltages is illustrated in Figure 4-30 for each of the control methods where only the 684 kW PV site was controlled. Notice from this simulation results, that there is negligible improvement in the voltage profile. This result is further confirmed when observing the NG feeder score results in Table 4-5. The VV control has no effect on the average voltage profile. And while PSO and ESC significantly improved the voltage for the PNM model, they were far less effective when implemented on the NG feeder because of the phase imbalance.

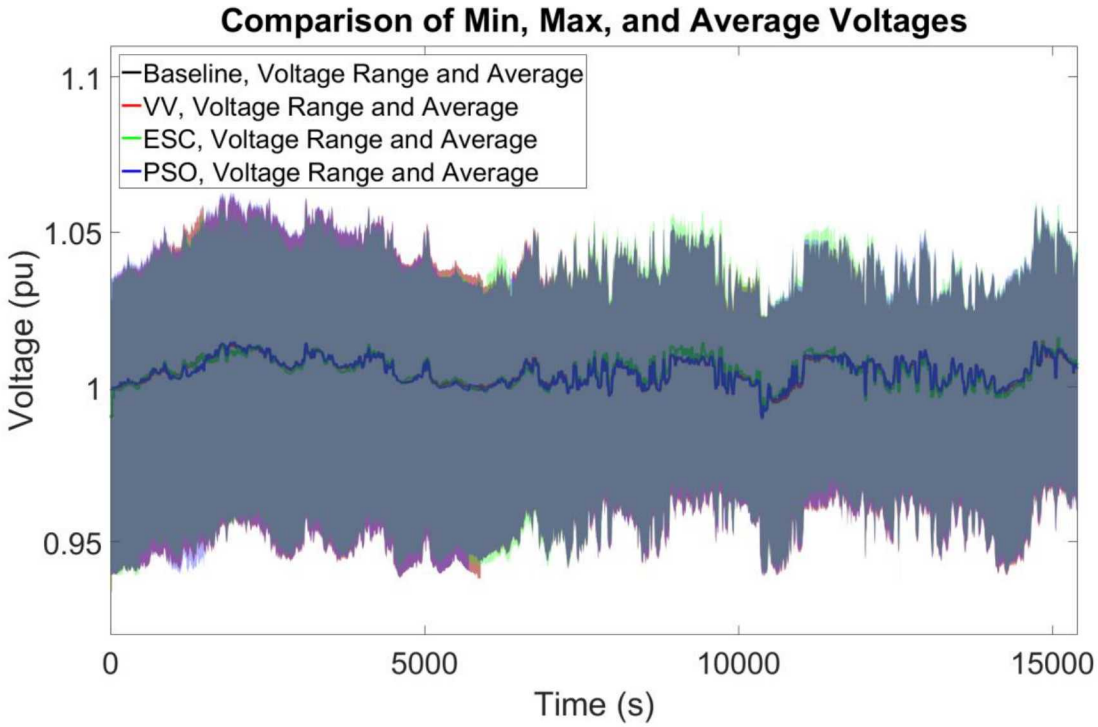

Figure 4-30. Comparison of Minimum, Maximum and Average Voltage Regulation Approaches for the NG Feeder Controlling a Single PV Inverter.

Table 4-5. NG Feeder Score Results Controlling a Single PV inverter.

NG Feeder Score Controlling All PV					
	Phase A (x1000)	**Phase B (x1000)**	**Phase C (x1000)**	**Average (x1000)**	**Average Impact (%)**
VV	-3.822	122.445	84.536	203.159	**15.2%**
ESC	-22.754	328.060	202.493	507.799	**38.0%**
PSO	-22.751	123.941	137.215	238.405	**17.8%**
Best Score	**193.831**	**635.157**	**506.737**	**1335.724**	

Table 4-6. Normalized NG Feeder Scores Results Controlling a Single PV inverter Based on System Buses

NG Feeder Score Controlling a Single PV					
	Phase A (x1000)	Phase B (x1000)	Phase C (x1000)	Average (x1000)	Average Impact (%)
VV	0.128	-0.109	-0.072	-0.530	**0.0%**
ESC	11.986	-0.179	31.328	43.135	**3.2%**
PSO	-1.311	-0.432	4.055	2.312	**0.2%**
Best Score	**193.831**	**635.157**	**506.737**	**1335.724**	

When implementing these strategies with all the DER devices, there was far better performance. VV, ESC, and PSO all collapse the voltage envelope toward nominal voltage. In this case, ESC slightly outperforms the other two methods, shown in Table 4-7. Interestingly, all the methods caused phase A (that was close to nominal to start) to deviate from the nominal voltage.

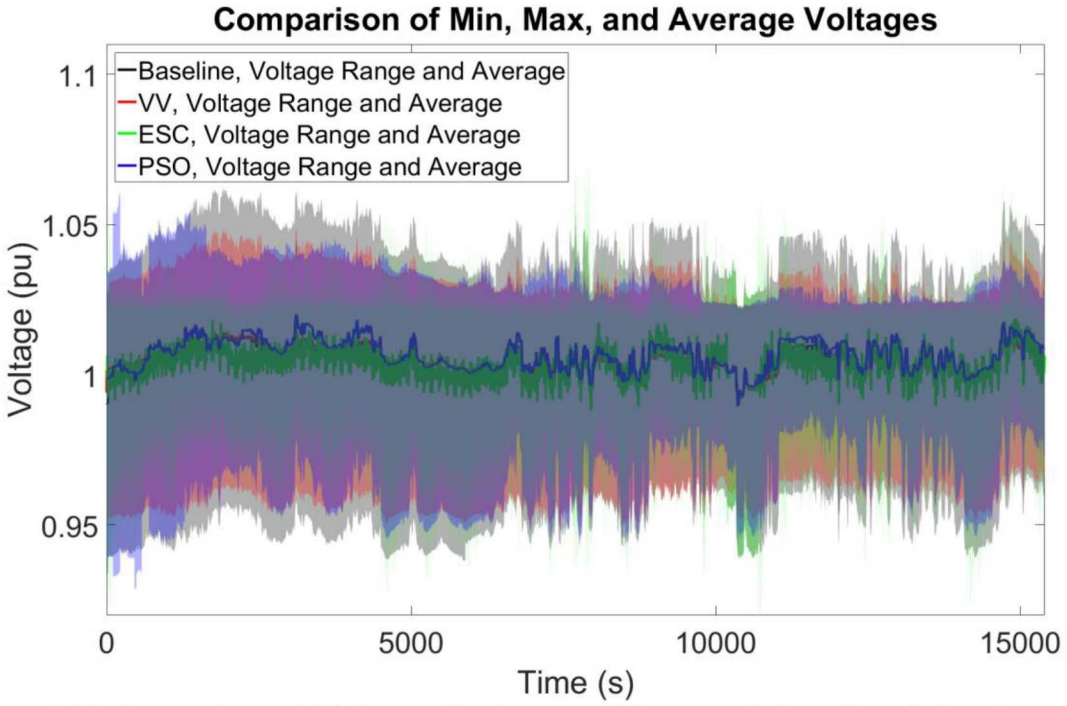

Figure 4-31. Comparison of Minimum, Maximum and Average Voltage Regulation Approaches for the NG Feeder Controlling All PV Inverters.

Table 4-7. NG Feeder Score Results Controlling All PV Inverters.

NG Feeder Score Controlling All PV					
	Phase A (x1000)	Phase B (x1000)	Phase C (x1000)	Average (x1000)	Average Impact (%)
VV	-0.058	1.855	1.281	3.078	**15.2%**
ESC	-0.345	4.971	3.068	7.694	**38.0%**
PSO	-0.345	1.878	2.079	3.612	**17.8%**
Best Score	**2.937**	**9.624**	**7.678**	**20.238**	

Table 4-8. Normalized NG Feeder Scores Results Controlling All Single PV inverter Based on System Buses.

NG Feeder Score Controlling a Single PV					
	Phase A (x1000)	Phase B (x1000)	Phase C (x1000)	Average (x1000)	Average Impact (%)
VV	0.002	-0.002	-0.001	-0.008	**0.0%**
ESC	0.182	-0.003	0.475	0.654	**3.2%**
PSO	-0.020	-0.007	0.061	0.035	**0.2%**
Best Score	**2.937**	**9.624**	**7.678**	**20.238**	

5. PHIL EXPERIMENTS

To further validate the operational effectiveness of the voltage regulation methods, realistic DER power hardware-in-the-loop (PHIL) simulations were conducted with both the PNM and NG feeder models. These simulations provide better fidelity because they show ProDROMOS can work with real PV communications systems and ramp rates, not represented in the EPRI simulator. Originally, the 100 microinverters were going to be used for the PHIL experiments, but (a) it was not possible to create reproducible irradiance profiles with them because they were connected to PV modules in the field and (b) in the latter stages of the project the devices stopped communicating consistently through power line carrier. Instead, a 3-kW residential-scale PV inverter was used that could be connected to a 200 kW Ametek PV simulator. Connected Energy communicated to it using the Modbus interface.

5.1. PNM Baseline

To validate the PHIL setup for the PNM feeder model, a comparison was made between active power, reactive power, and bus voltage for the RT and PHIL simulations. Figure 5-1 shows the reactive power comparison between the PHIL and RT simulation for Inverter 1. The positive and negative reactive power changes around 1000 seconds were due to Connected Energy changing the PF settings of the DER equipment. Figure 5-2 shows the voltage profiles for the RT and PHIL simulations. The impact of a +0.85 and a -0.85 PF setpoint on the voltage profile are indicated at ~1000 seconds. Overall the RT and PHIL simulations are closely matched.

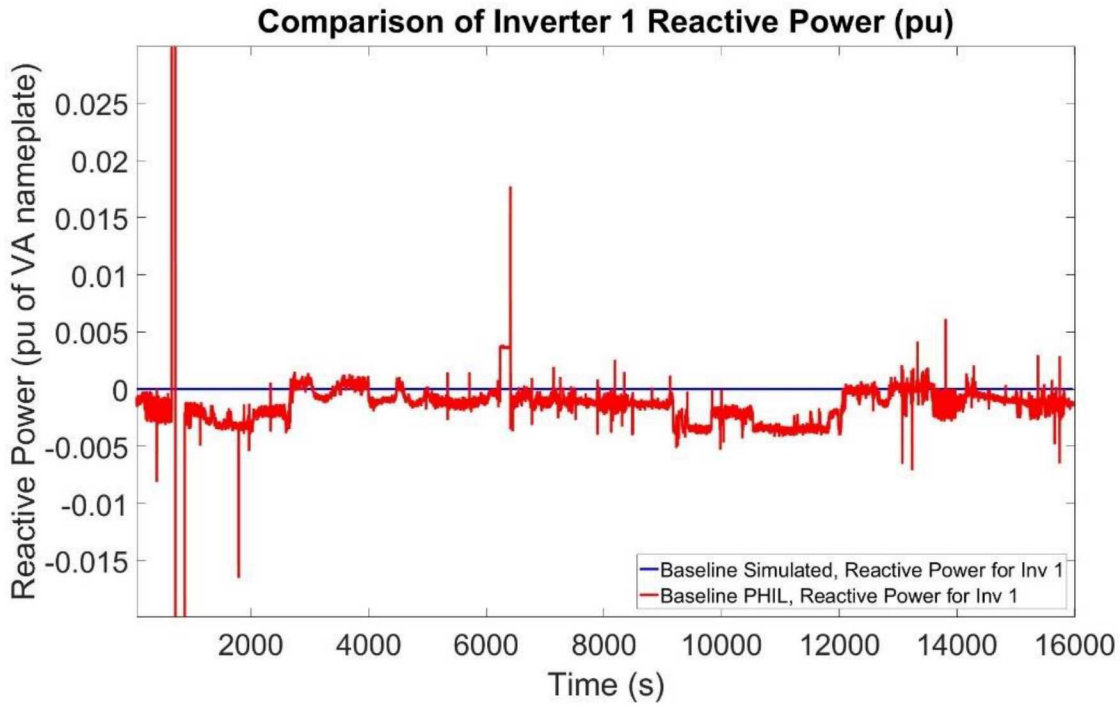

Figure 5-1. Comparison Between Simulated and PHIL Baseline Reactive Power for Inverter 1.

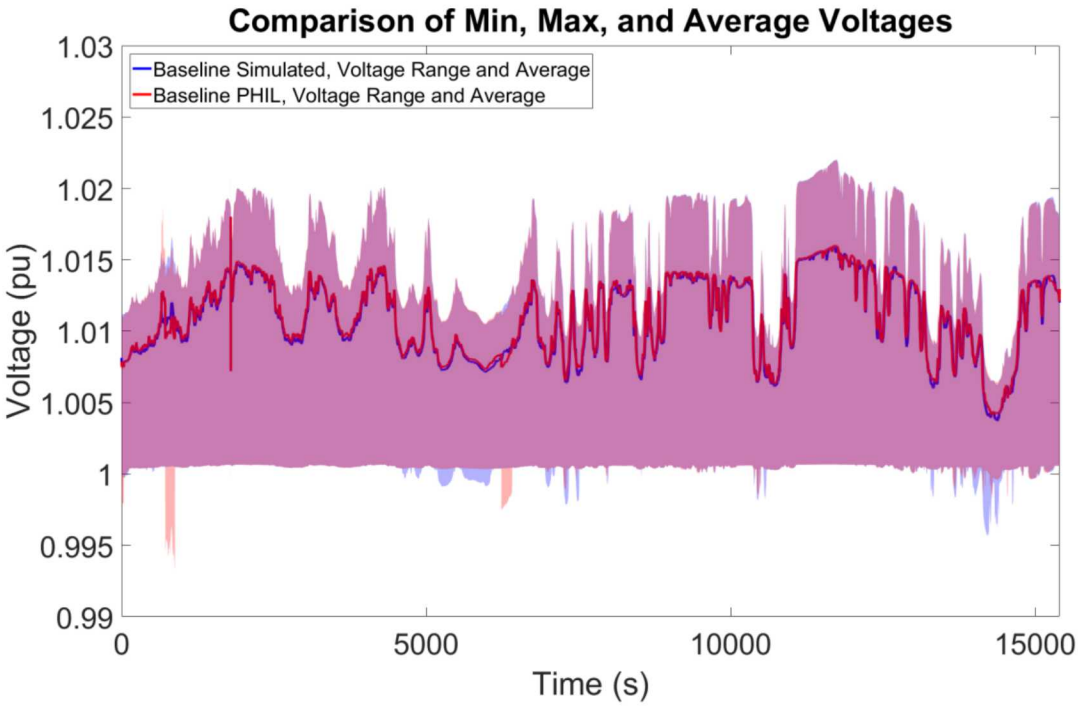

Figure 5-2. Comparison Between Simulated and PHIL Baseline Minimum, Maximum and Average Bus Voltage for the PNM Feeder Model.

5.2. PNM Particle Swarm Optimization PHIL

The test configuration for the PSO PHIL experiments is shown in Figure 5-3. The only change from the RT simulations was that Connected Energy communicated with a physical device to change the power factor and this DER was connected to the power simulation using a PHIL interface, as opposed to DBus. A comparison of the active power (Figure 5-4) and reactive power (Figure 5-5) from the EPRI DER device and the scaled 3 kW DER device when conducting the PSO voltage regulation shows:

1. The physical equipment recreates the power profile reasonably well. Slight differences in the active power are due to efficiencies of the devices and slightly oversizing the simulated PV system in the Ametek PV simulator.
2. The PSO solutions are repeatable for multiple runs. There were some deviations in the reactive power contributions from the PSO solutions, but overall, they matched well.

Comparing the voltage profiles from the RT simulation and the PHIL simulation in Figure 5-6, provided confidence that the PSO method would work well in a field demonstration. Note, the

PHIL PSO simulation was not started for approximately 10 minutes at the beginning of the RT-Lab simulation, which is why it takes some time for the reactive power on the physical DER to change.

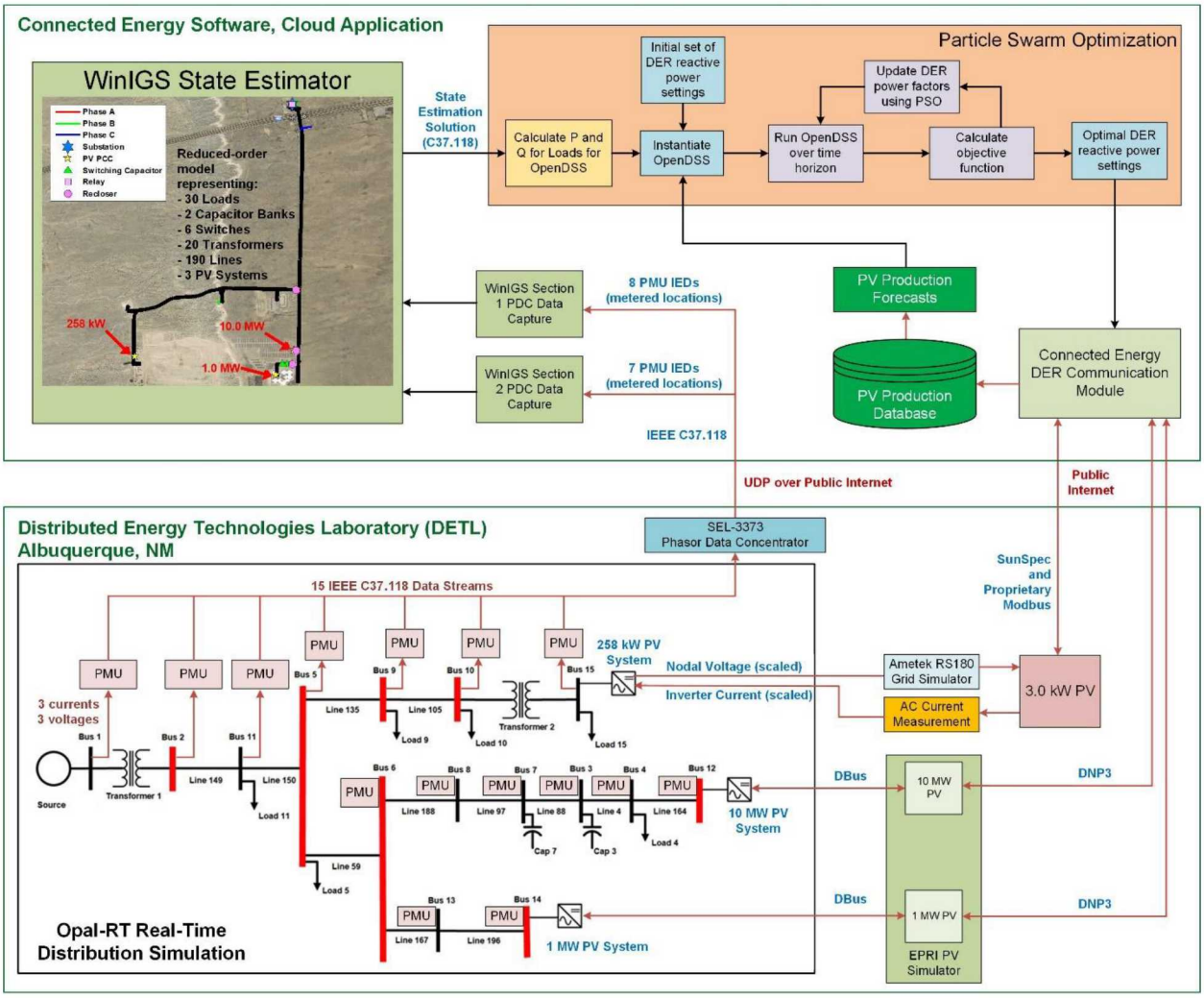

Figure 5-3. PNM PSO PHIL configuration with associated data flows.

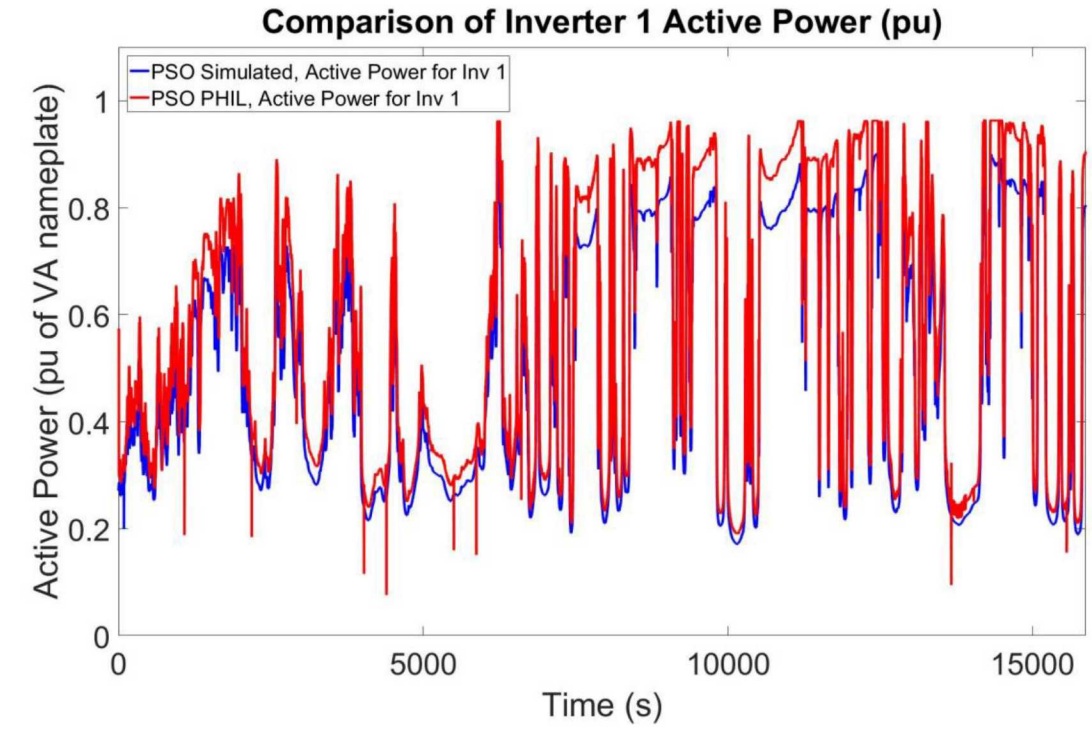

Figure 5-4. Comparison Between Simulated and PHIL Baseline Active Power for Inverter 1.

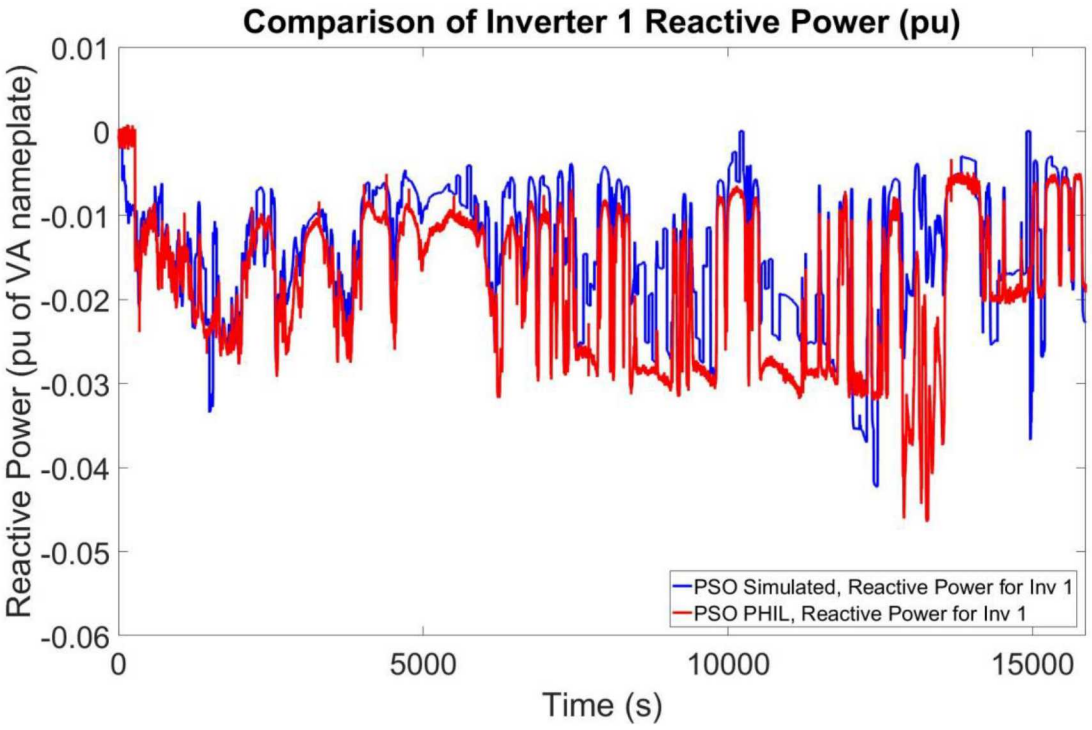

Figure 5-5. Comparison Between Simulated and PHIL Baseline Reactive Power for Inverter 1.

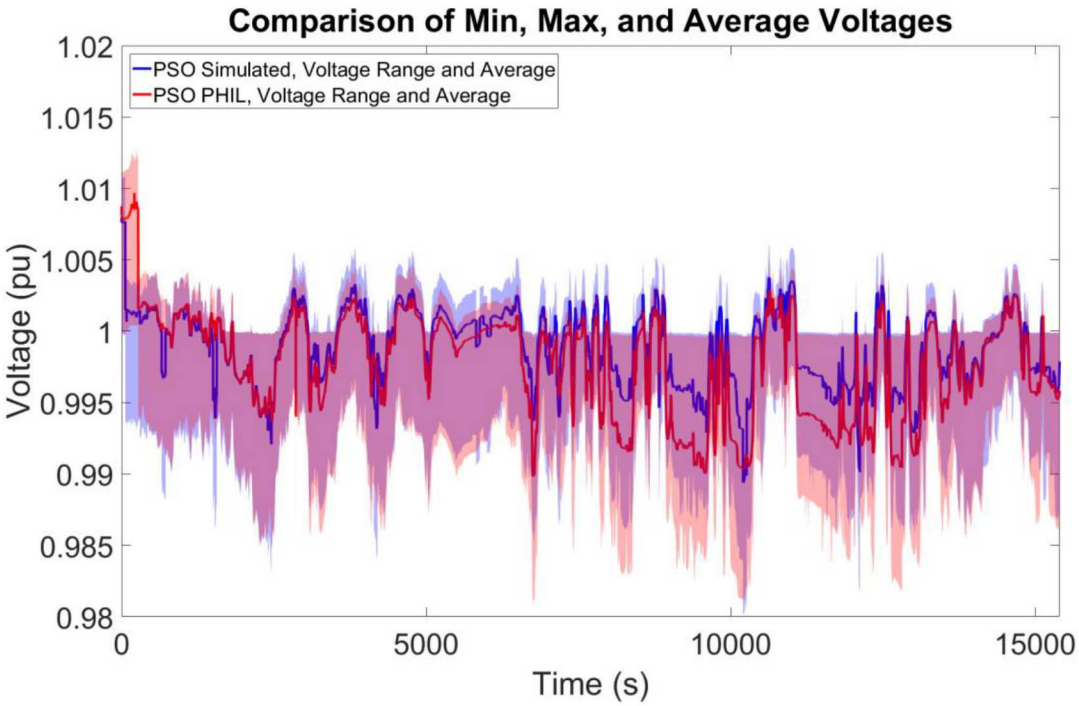

Figure 5-6. Comparison Between Simulated and PHIL Baseline Minimum, Maximum and Average Bus Voltage for the PNM Feeder Model.

5.3. NG Baseline

The same technique was used to validate the PHIL setup for the NG feeder model. First, the baseline methods were compared, where the 3 kW PV system represented the Old Upton Rd PV system. The phase-shifted DER current from the single-phase device was injected on each of the phases to represent the three phase inverters at the Old Upton Rd PV site. A comparison between bus voltages for the RT and PHIL simulations is shown in Figure 5-7. There is close alignment between the two simulations when the DER devices are a unity PF.

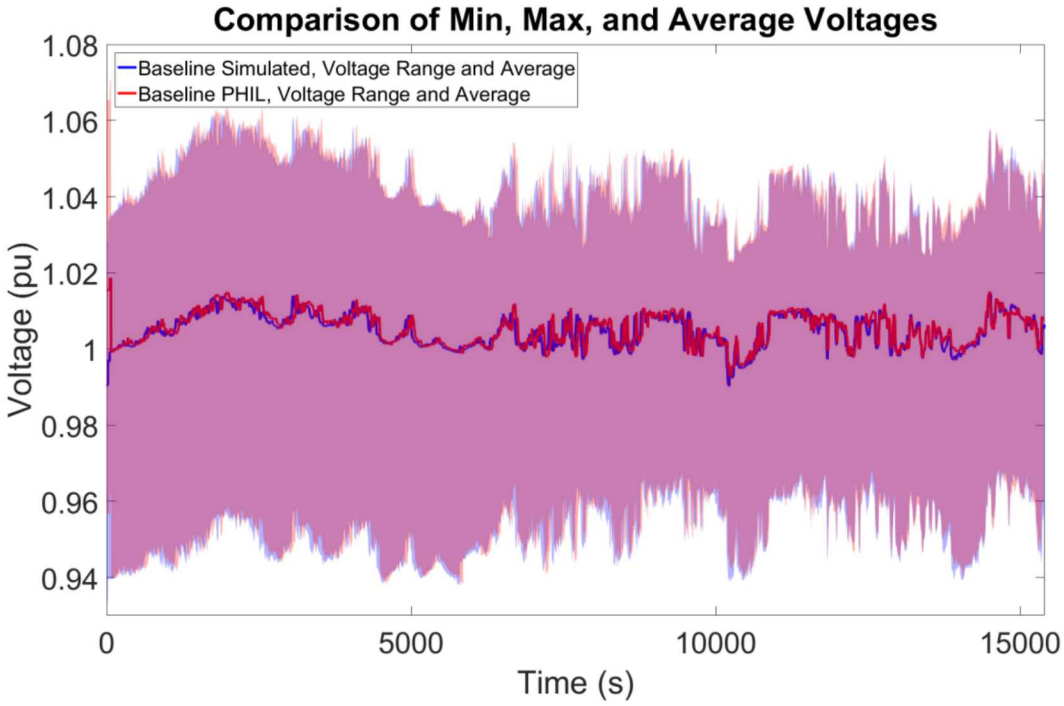

Figure 5-7. Comparison Between Simulated and PHIL Baseline Minimum, Maximum and Average Bus Voltage for the NG Feeder Model.

5.4. NG Particle Swarm Optimization PHIL

The PSO code was operated on the PHIL environment with only the Old Upton Rd PV site being controlled, as shown in Figure 5-8. In this case, toward the end of the PHIL simulation, the PSO found a solution that produced lower reactive power values for the DER and the voltage average was less than in the RT simulation, shown in Figure 5-9. These results indicated the PSO would provide stable results when implemented on the fielded system.

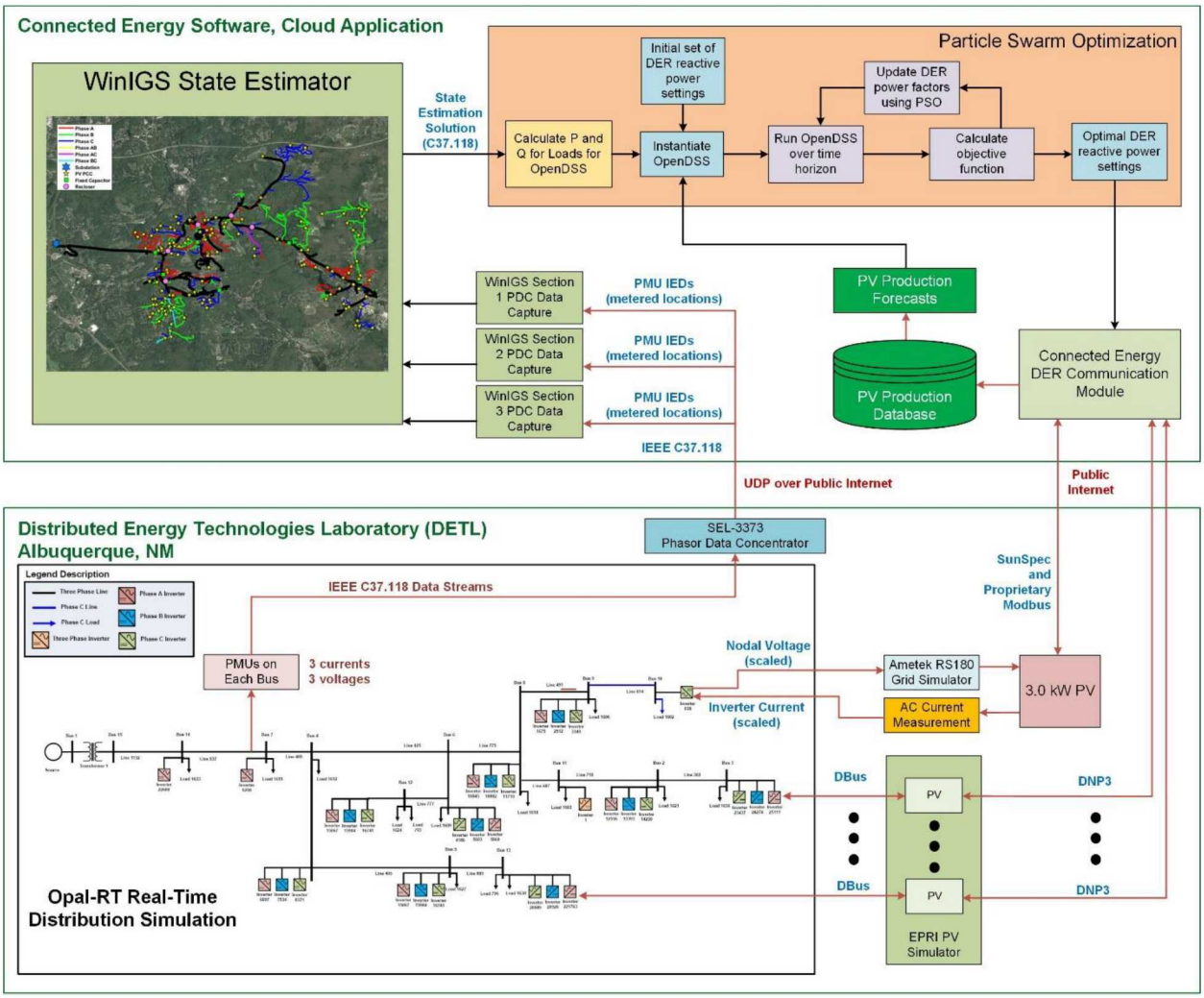

Figure 5-8. NG PSO PHIL configuration with associated data flows.

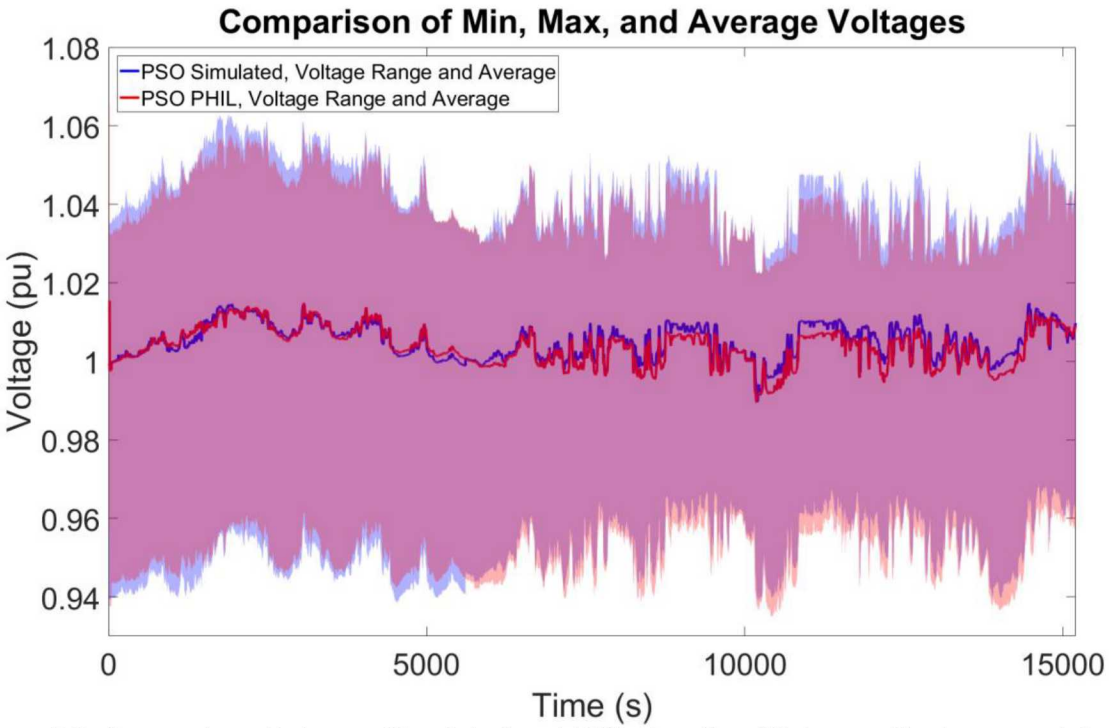

Figure 5-9. Comparison Between Simulated and PHIL Baseline Minimum, Maximum and Average Bus Voltage for the NG Feeder Model.

6. FIELD DEMONSTRATION

The ProDROMOS system was implemented on a live distribution power system in Grafton, MA that contained three utility-scale PV sites. Inverters at the National Grid-owned Old Upton Rd PV Site (Figure 6-1) were controlled for the field demonstrations. Since the PV irradiance and other voltage regulation equipment operations were not the same for each of the experiments, no attempt was made to do a direct comparison of the techniques in the field. Generally, none of the approaches were able to help the phase imbalance on the feeder because the three-phase inverter contributed reactive powers on all phases. Any attempt to correct the overvoltage on Phase B, resulted in lowering the undervoltage on Phase C, and vice versa.

Figure 6-1. 684 kW_{dc}/672 kW_{ac} Old Upton Rd PV Site.

6.1. Communications in the Field Demonstration

Trimark Associates had previously installed a monitoring and control system, which communicated to the SMA Cluster Controller at the Old Upton Rd Site. For the purposes of this project, Trimark provided a simple DNP3 API to Connected Energy to read average bus voltage, power factor, and active and reactive power. The API also included the ability to enable the PF command and set the power factor to three decimal places. Writing the DNP3 point to the Trimark system, issued commands to the SMA Cluster Controller which wrote Modbus registers in the 28 24-kW SMA Tripower PV inverters at the site, five of which are shown in Figure 6-3.

Figure 6-2. PV Inverters at the Old Upton Rd PV Site.

To better determine the impact of the voltage regulation approaches on National Grid feeder, a 3-phase SEL-734 feeder monitor was installed on the feeder of study. It was pole mounted near the substation on a branch with the 684 kW Old Upton Rd system and another 1 MW PV site. Unfortunately, a damaged sensor on Phase B only allowed measurements on phases A and C.

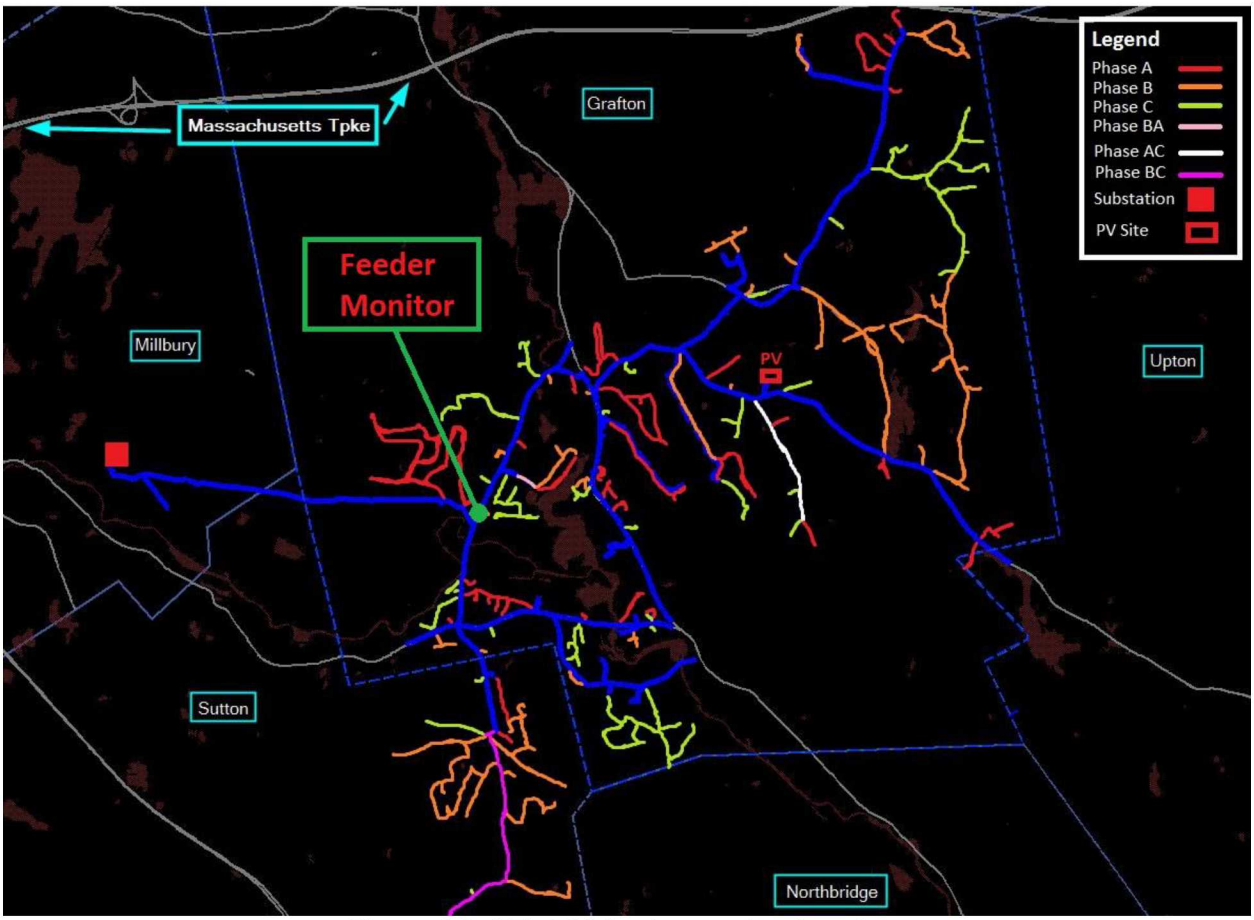

Figure 6-3. SEL-734 feeder monitor location.

6.2. Baseline Data

Baseline PV production and voltage data was collected from the PV site and the feeder monitor—once it was installed in mid-March 2019. There was a correlation between the PV Point of Common Coupling (PCC) voltage and the PV production shown in Figure 6-4. The influence of the other voltage regulation equipment on the PCC voltage is shown by the step on Feb 16. This could be the actuation of a capacitor bank, adjustments by the voltage regulators on each phase at the substation, or some other equipment.

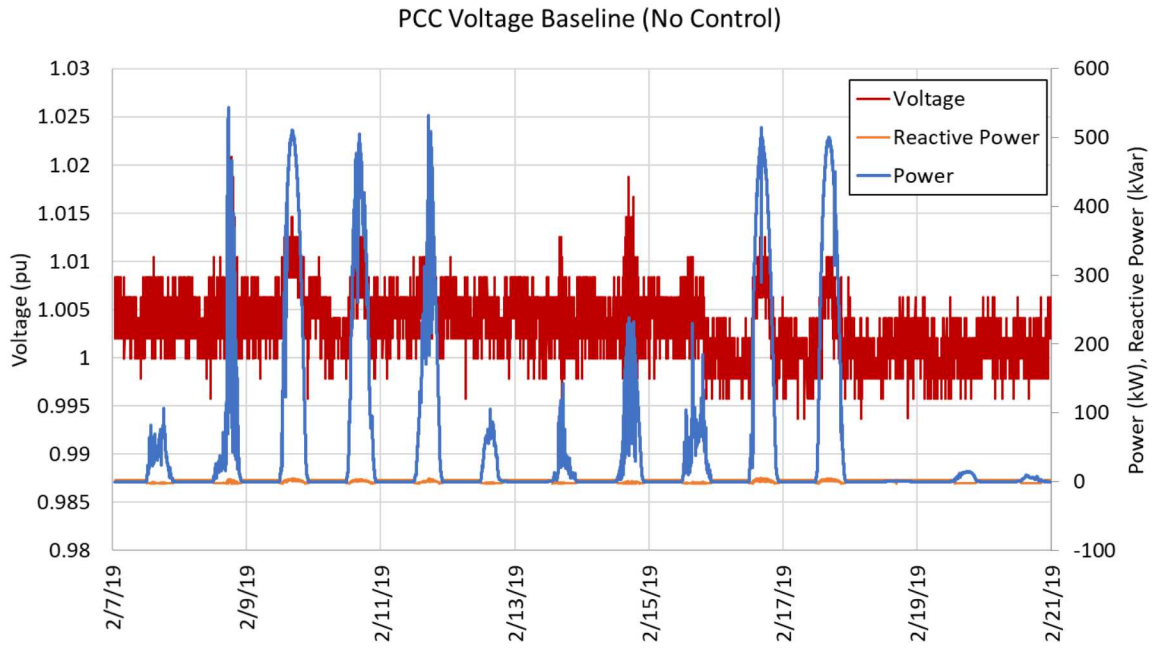

Figure 6-4. Baseline voltage data, averaged from all phases, from the Old Upton Rd PCC. Times are shown as Coordinated Universal Time (UTC).

The feeder monitor showed that during sunny days the 1.684 MW of utility-scale PV and an unknown quantity of residential-scale PV would produce approximately a power flow swing from 1000-1200 kW to ~–1000 kW on phases A and C—shown in Figure 6-5. Note the reverse power flow periods appear to be positive because the current sensor is incapable of determining the current direction. Surprisingly, the feeder monitor voltage during these high PV production periods decreases while the PV site PCC voltage increases. This trend is shown in Figure 6-6. The cause of the voltage reduction is from the substation voltage regulator's line drop compensation (sometimes called load drop compensation) that changes the voltage based on a preprogrammed voltage vs amperage/power ratio. As the load increases, the voltage regulator increases the voltage because there will be a larger line drop. The operations of the regulators are shown in Figure 6-7. These devices were programmed to change the voltage 6 V (per 120 V base) for each 400 amps/phase, meaning there would be a 0.05 pu voltage change per 9561 kW or a 5.23×10^{-6} pu/kW ratio when there were small magnitudes of reactive power. While the feeder monitor was not located at the substation, it reasonably approximates power and voltage that the voltage regulators saw and can be used to determine if the feeder model parameters match the field equipment. The voltage vs power curve was plotted for 5 days in Figure 6-8. The fit line parameters indicate the voltage regulation curve was 5.5×10^{-6} pu/kW—closely

matching the NG regulator settings. The vertical band represents the regulator bandwidth of 1.5 V (on a 120 V base) or 0.0125 pu, and NG feeder model had a voltage regulation setpoint of 1.0 pu, which is well approximated by the 0.995 y-intercept. Based on this feeder data analysis, it appears the voltage regulator settings in the NG model are accurate.

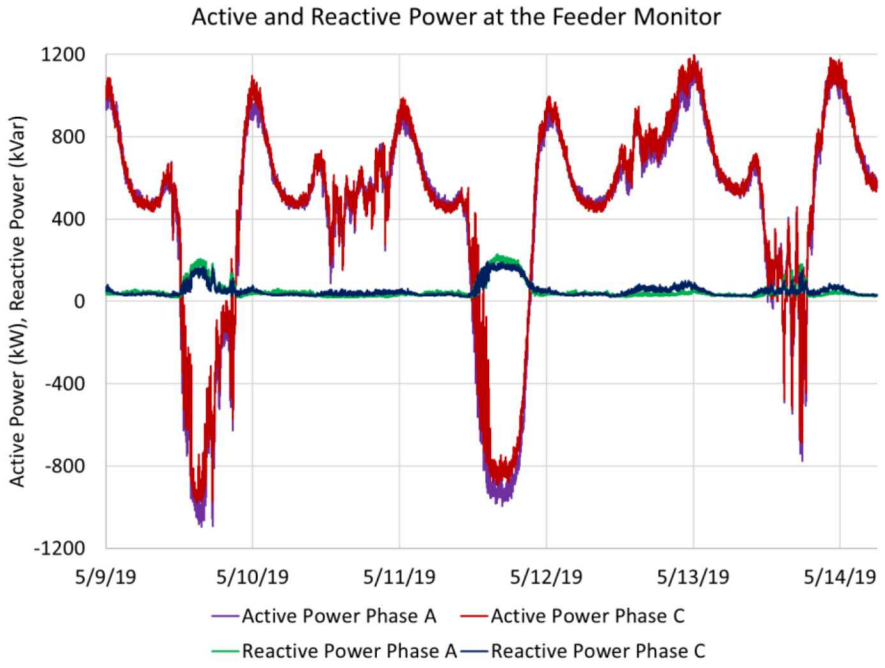

Figure 6-5. Baseline feeder monitor active and reactive power data for 5 days.

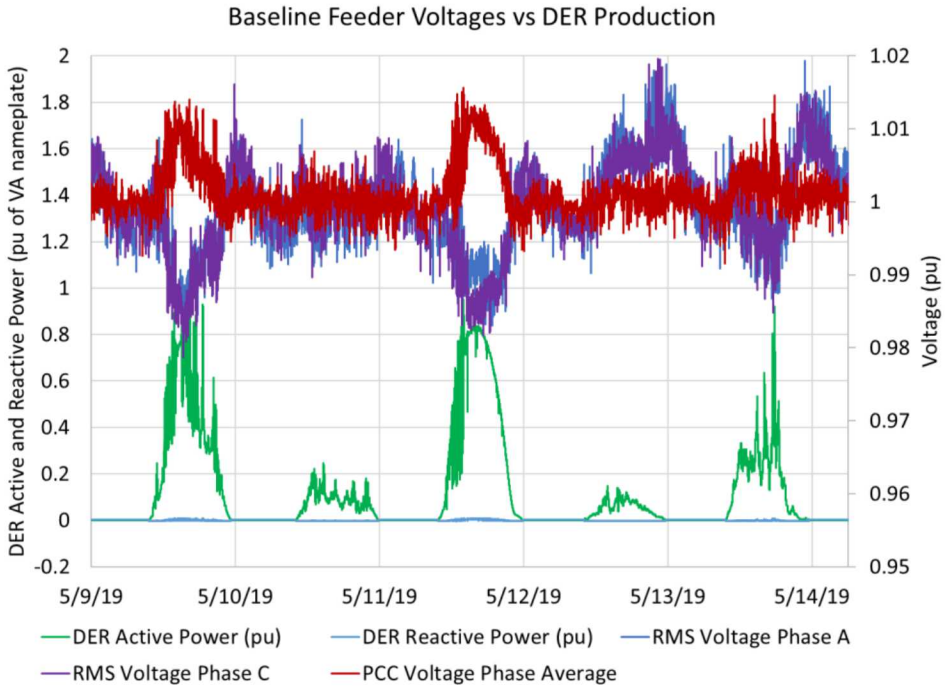

Figure 6-6. Baseline feeder monitor and PCC voltage data for 5 days.

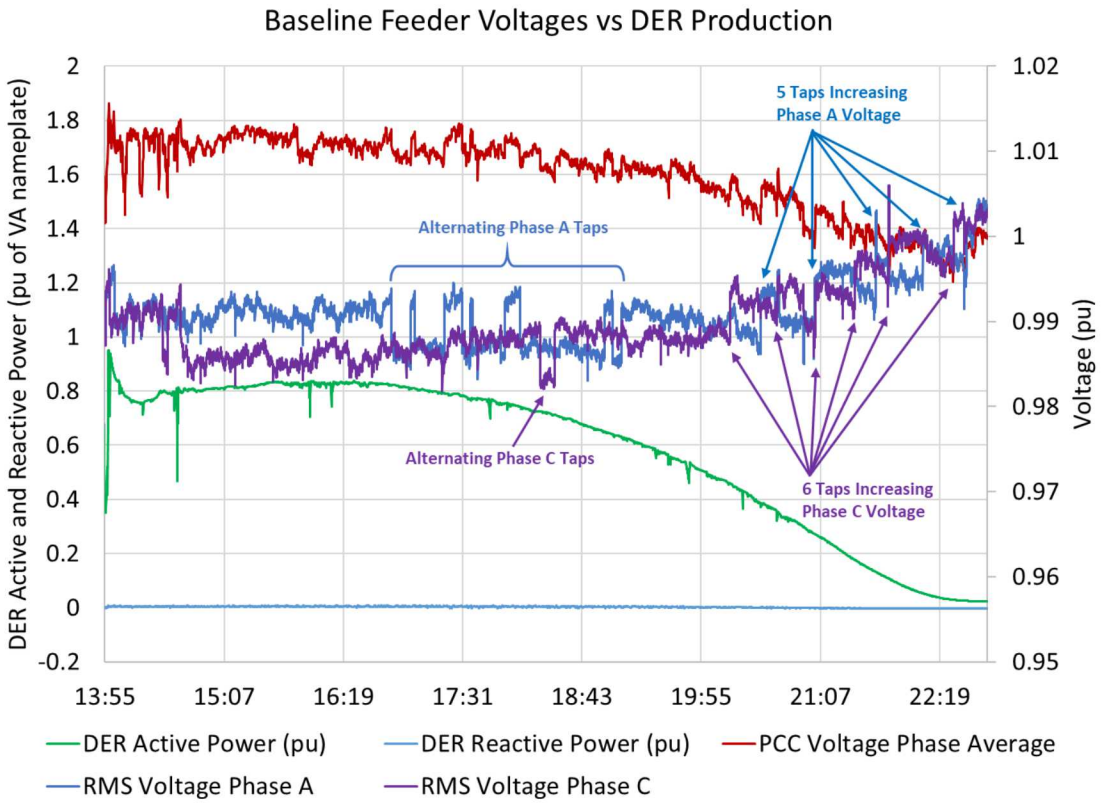

Figure 6-7. Influence of voltage regulator line drop compensation on feeder monitor voltage.

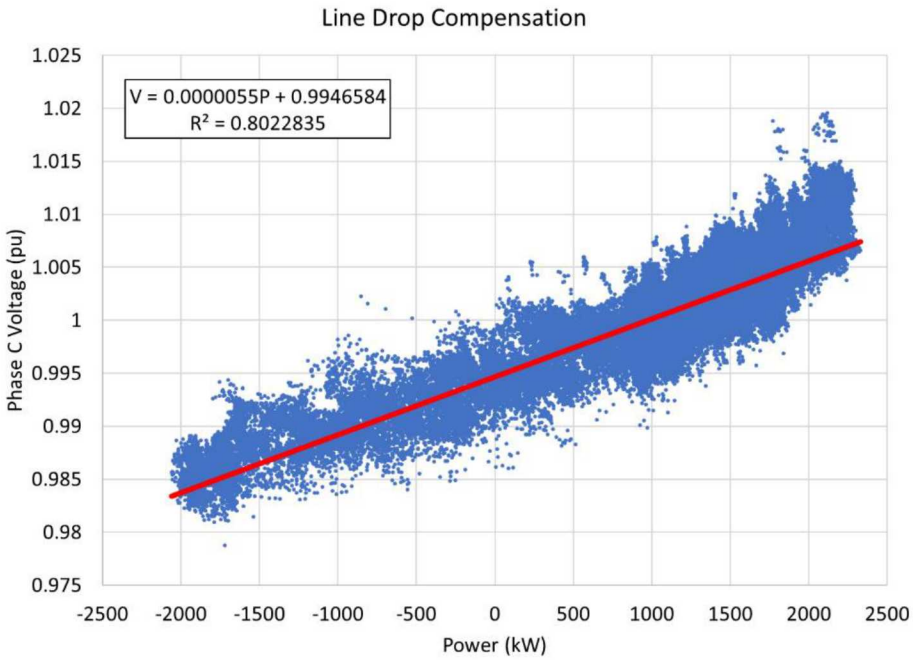

Figure 6-8. Phase C Voltage vs Feeder Power fit.

6.3. PF Adjustment Experiments

To better understand the influence of the Old Upton Rd reactive power setpoints on the feeder voltage, two sweeps from PF = -0.85 to 0.85 were taken at 0.01 PF steps. The changes in the reactive power at the PCC and feeder monitor for each sweep are shown in Figure 6-9. While the reactive power changes are clear at the PCC, the changes in reactive power at the feeder monitor are noisier because of the influence of feeder loads. The influence of the PF setpoints on PCC and feeder monitor voltages are shown in Figure 6-10. Injecting reactive power increases the PCC voltage; absorbing reactive power decreases the PCC voltage. The power factor settings were capable of swinging the local bus voltage by ~0.05 pu, but the average voltage stayed within the ±0.05 pu ANSI Range A limits. However, based on the simulation data, it is likely the phases were imbalanced and could have exceeded these limits. At the feeder monitor, the voltage change from the ~400 kVar was small (~0.01 pu) and poorly correlated to the PV reactive power. In this case, the load/line drop compensation was unlikely to have played a role because the active power at the substation would not have changed significantly. The reactive power from Old Upton Rd had little impact to the feeder voltages close to the substation.

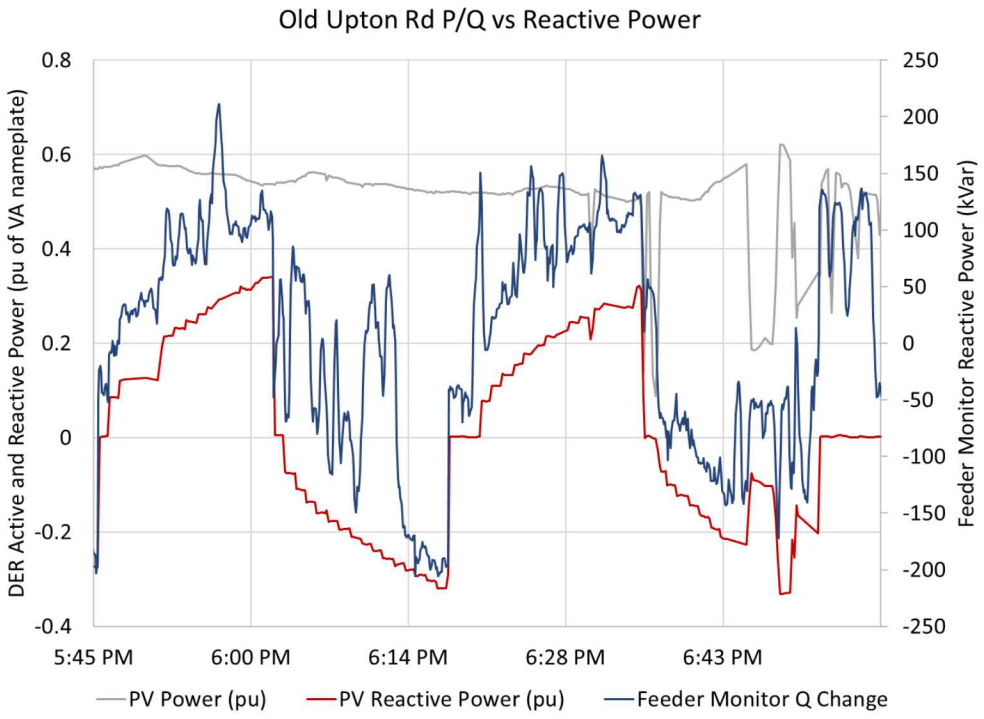

Figure 6-9. DER reactive power is reflected by changes at the feeder monitor.

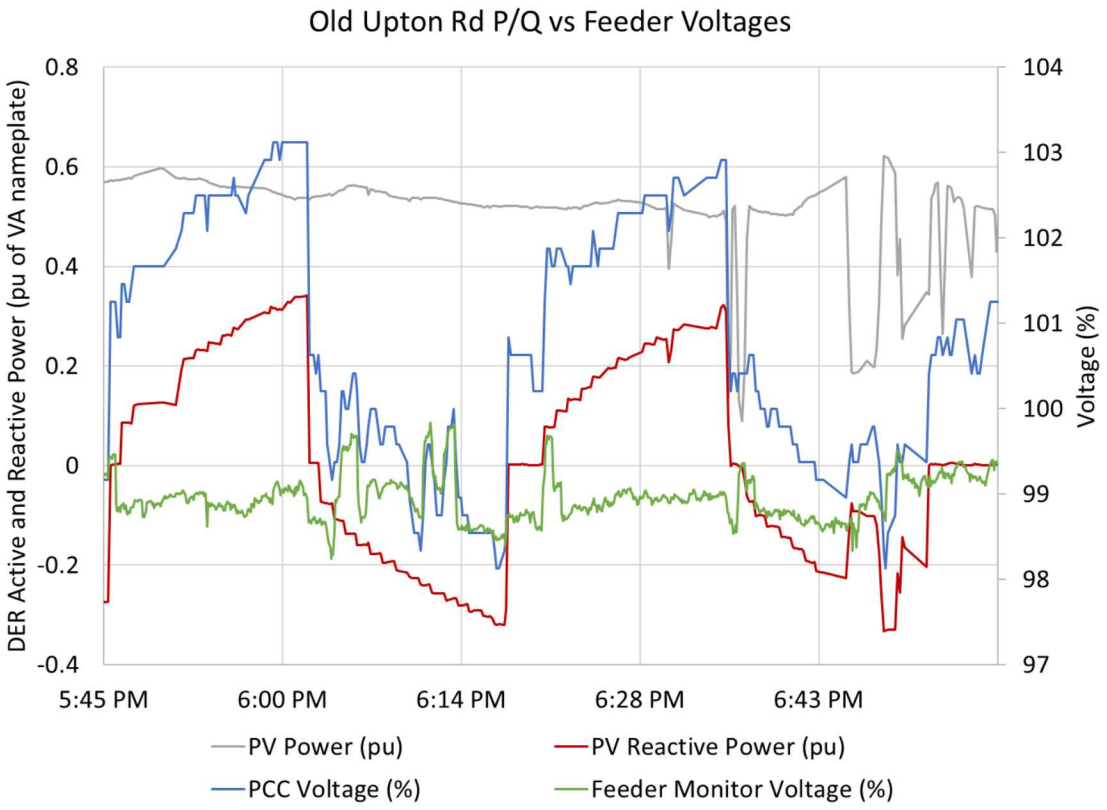

Figure 6-10. DER reactive power changed PCC voltage, but had little influence on the voltage of the feeder monitor.

6.4. Volt-Var Experiments

The autonomous volt-var (VV) function is a well-known function that has been included in many national and international standards. It is included in many fielded DER devices currently—though the functionality is rarely enabled. To generate a baseline dataset for the voltage optimization studies, the 28 PV inverters at Old Upton Rd were programmed remotely using the SMA Cluster Controller web interface. The following VV curve was programmed into the PV inverters for five days:

P1 = (95, 100)
P2 = (99, 0)
P3 = (101, 0)
P4 = (105, -100)

where the points are in units of ($\%V_{nom}$, $\%Q_{available}$). The inverters did not reduce their active power to provide the reactive power support. The active and reactive power from the PV site and the voltage at the PCC and the feeder monitor are shown for the experiment in Figure 6-11. The voltage did not significantly leave the VV deadband so only a small amount of reactive power was absorbed in the high voltage cases. It is worth noting that the PCC voltage was likely slightly lower than the electrical connection point (EPC) voltages measured by each of the inverters. This explains why reactive power is provided when the PCC voltage has not left the deadband. Also note that the Trimark DNP3 voltage

measurement points were changed on March 22 from integer values to float values (red spike on 3/22 in Figure 6-11), so the fidelity of the measurements became much better after that point.

While there is no way to draw direct or conclusive comparisons between this VV field demonstration period and the baseline data, it appears the higher baseline PCC voltages were reduced slightly when the VV function was enabled. It also appears that the range of feeder monitor voltages were reduced.

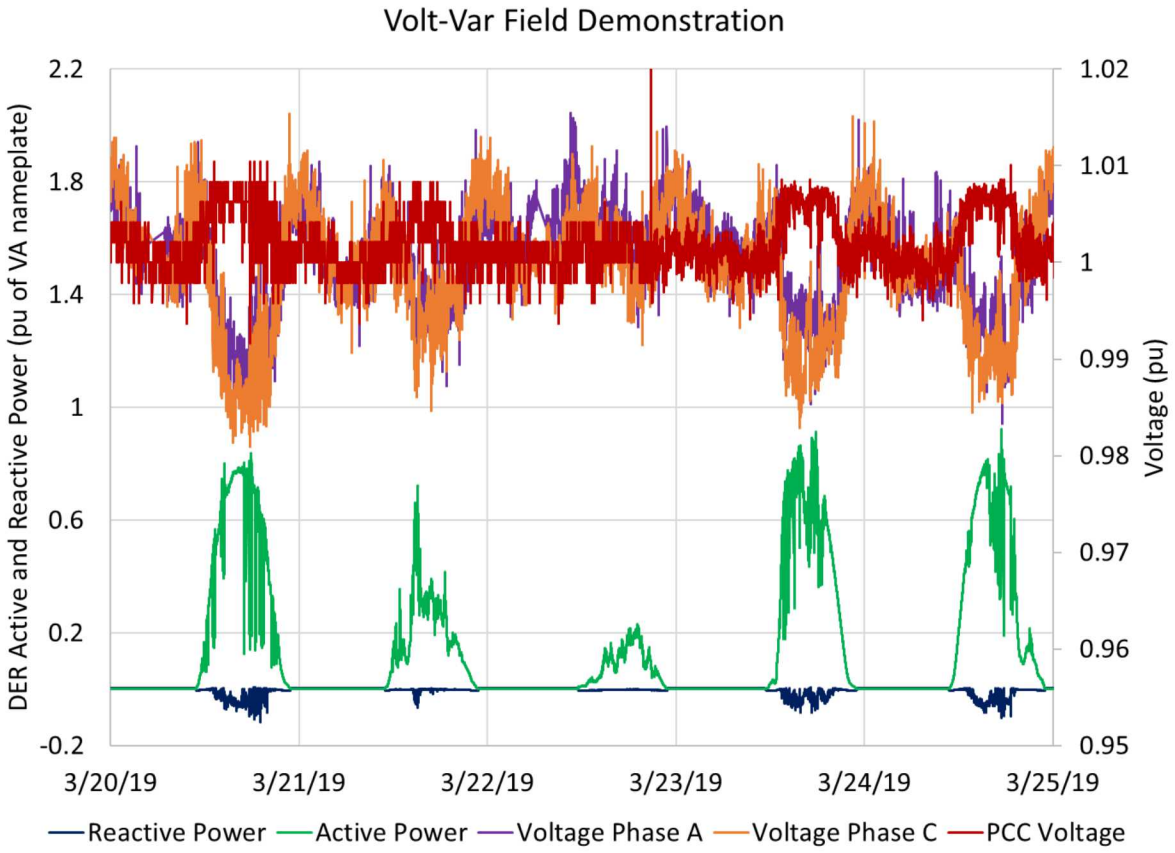

Figure 6-11. Field data from VV experiments with NG Site.

6.5. ESC Experiments

Extremum Seeking Control experiments were conducted at DETL using the 100 SunPower microinverters to estimate the parameters to use with the Old Upton Rd PV system. These experiments helped the team understand appropriate ESC parameters and the challenges of DER communications latencies from a cloud-based ProDROMOS platforms.

6.5.1. ESC Parameter Selection using 100 Microinverters

Prior to conducting the Extremum Seeking Control field demonstrations with the Old Upton Rd PV Site, several experiments were conducted with physical and simulated PV systems to estimate the

correct ESC parameters. Prior ESC tests with a simplified circuit at DETL[25] and using a simple PHIL setup with a 7-bus distribution circuit[26] allowed the probing signal to become saturated. Those experiments were conducted for less than an hour to demonstrate the ability of the algorithm to trend in the correct direction. In this work, the ESC algorithm ran for longer periods of time (days), communication errors were possible, and the load and PV irradiance changes changed the optimal PF setpoints of the DER devices.

For this reason, additional logic was added to the ESC algorithm:

1. The probing signal was always present, so the algorithm could continuously monitor the objective function gradient for any changes. To do this, the maximum reactive power was calculated for every control loop and the reactive power setpoint limitation was applied.
2. The ESC system was reset when the available reactive power was insufficient to generate the probing signal for any of the DER devices.

Connected energy implemented the open-source ESC code[27] in their DERMS environment to communicate to 10 SunPower PVS Gateways which monitored and controlled 100 microinverters at DETL. To estimate the available (uncontrolled) power for the fleet of DER devices, 1 of the PVS systems was not controlled and only monitored for active power production—through the DC/AC ratio for all the systems was so small it was not necessary. The remaining 90 microinverters, connected to 9 PVSs, independently measured the local voltage. These measurements were averaged and used to calculate the objective function for the ESC algorithm. Each microinverter had a PF range of ±0.85. Collecting voltage data from each of the devices and issuing PF commands to the 90 devices took ~30 seconds (depending on the number of re-transmissions) because of a slow power line communications (PLC) with the associated confirmation steps. Multiple day-long experiments were conducted to investigate algorithm stability and failure cases. A simple objective function, *J*, was created shown in parameter set 1 in Table 6-1.

Table 6-1. ESC parameters for the DETL microinverter experiments.

#	Model	J function	l	h	DETL Microinverters (18 kW_{dc}, 28.8 $kVA_{namplate}$)			
					P	f	a	k
1	SunPower Demo	$\sum_{i=1}^{n}(V_i - V_n)^2$	$\frac{\sqrt{5}}{800}$	$\frac{\sqrt{5}}{800}$	20 kW	$\frac{\sqrt{2}}{40}$	2.13 kVar	−0.00288

The ESC was run for multiple days in January 2019. The microinverters were installed at the end of a long, high impedance line so the local voltages were high (~1.08 pu). As shown in Figure 6-12, the ESC controller quickly determined the gradient because of the high voltages. It was able to respond within a single probing signal cycle to reach the maximum reactive power absorption. In this case, since the voltage is always above nominal for this location, it is advantageous to set a high gain (k) to drive the reactive power to the limit very quickly, but in other cases, especially when multiple DER have different probing frequencies, that would not be ideal. The controller is reset when DER Q_{avail}

[25] J. Johnson, S. Gonzalez, and D.B. Arnold, "Experimental Distribution Circuit Voltage Regulation using DER Power Factor, Volt-Var, and Extremum Seeking Control Methods," IEEE PVSC, Washington, DC, 25-30 Jun 2017.
[26] J. Johnson, A. Summers, R. Darbali-Zamora, J. Hernandez-Alvidrez, J. Quiroz, D. Arnold, J. Anandan, "Distribution Voltage Regulation using Extremum Seeking Control with Power Hardware-in-the-Loop," IEEE Journal of Photovoltaics, vol. 8, no. 6, pp. 1824-1832, 2018. doi: 10.1109/JPHOTOV.2018.2869758
[27] URL: https://github.com/sunspec/prodromos/blob/master/optimization/extemum_seeking_control.py

drops to a point where the probing signal can't be produced (shown at the right of the figure). Very similar behavior was seen on another clear sky day, Jan 28, 2019 in Figure 6-13. Again, the parameters work well. Q_{avail} is dynamically tracked such that there is always a probing signal present. Unfortunately, the large probing signal results in voltage swings of almost 0.01 pu, so it may be advantageous to reducing the *a* parameter, but since these devices only had PF setpoints to 2 decimal places, it is difficult to produce the signal near unity at full output with smaller *a* parameters.

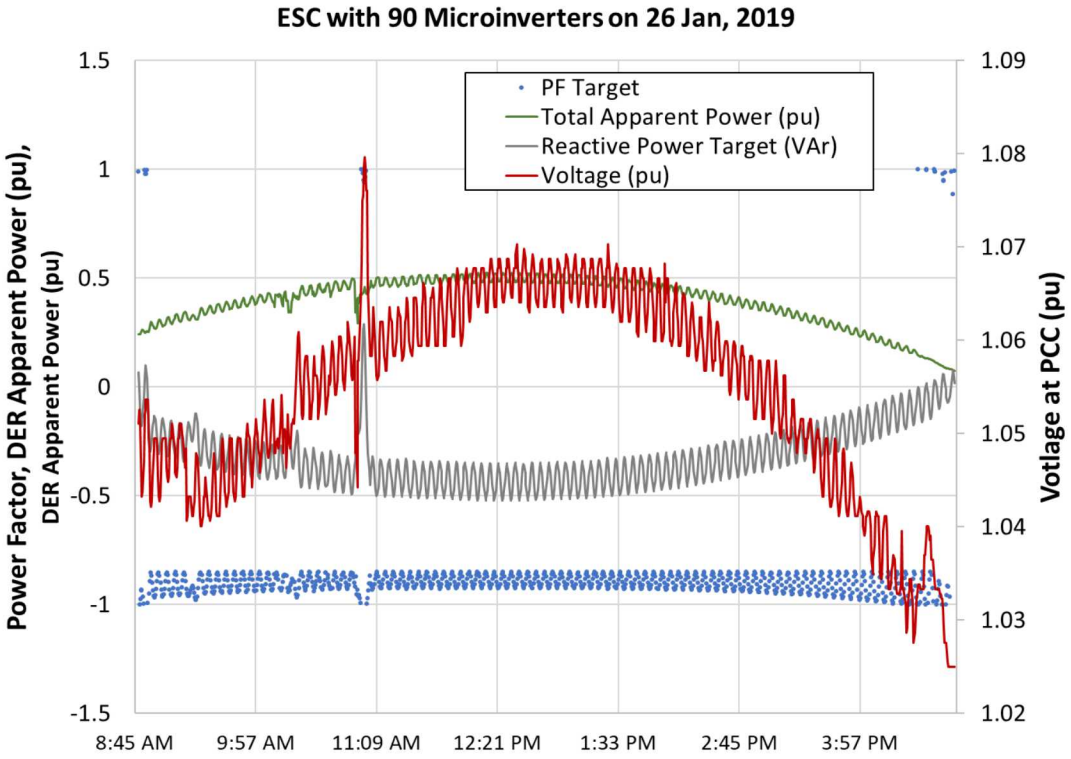

Figure 6-12: ESC with 90 microinverters. Controller was reset at ~10:30 AM.

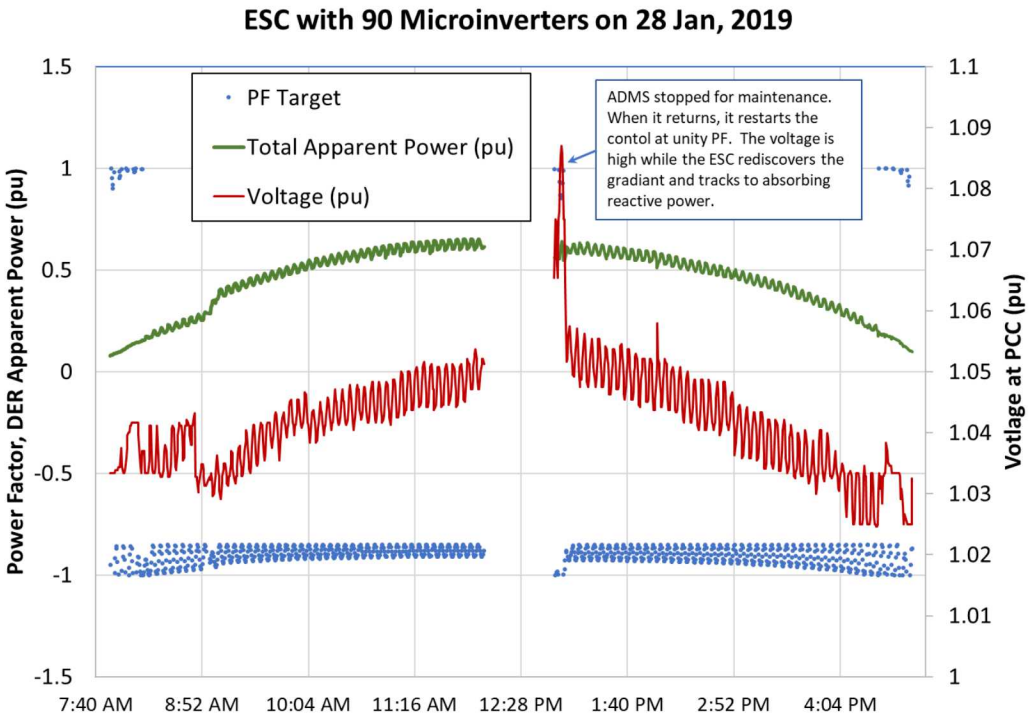

Figure 6-13: ESC results for a day running on the SunPower Microinverters at DETL.

The ESC operations for a cloudy day are shown in Figure 6-14 and Figure 6-15. Because the irradiance is low in the morning and evening, the algorithm resets multiple times. It also struggles to determine the gradient as quickly as in the clear sky case. From 9:17 to 14:05, the controller does a good job of absorbing reactive power and pulling down the voltage, except for a period of time around 12:20, where a drop in power from a cloud occurred at the same time that the probing signal was decreasing. This resulted in the ESC thinking that absorbing reactive power would decrease the voltage and for a full cycle the reactive power moves the voltage away from nominal (up to 1.09 pu). The controller corrects this issue on the next cycle. To minimize the effects, it is possible to adjust the filters and the integrator gain so that a longer history of the control action is considered to determine the ESC gradient.

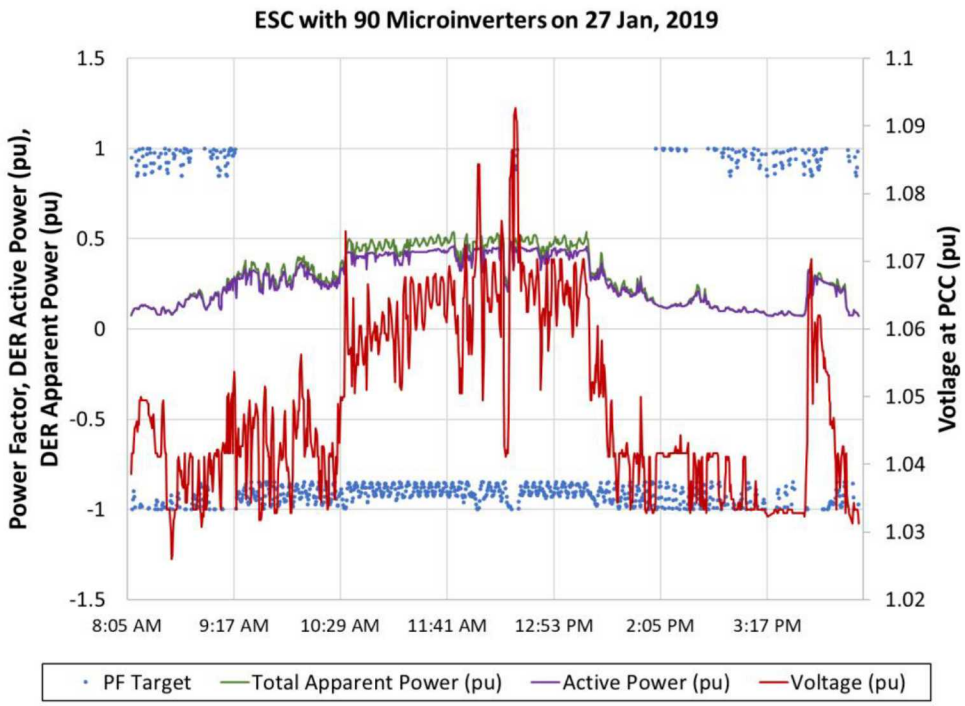

Figure 6-14: ESC results for a partly cloudy day on Jan 27th.

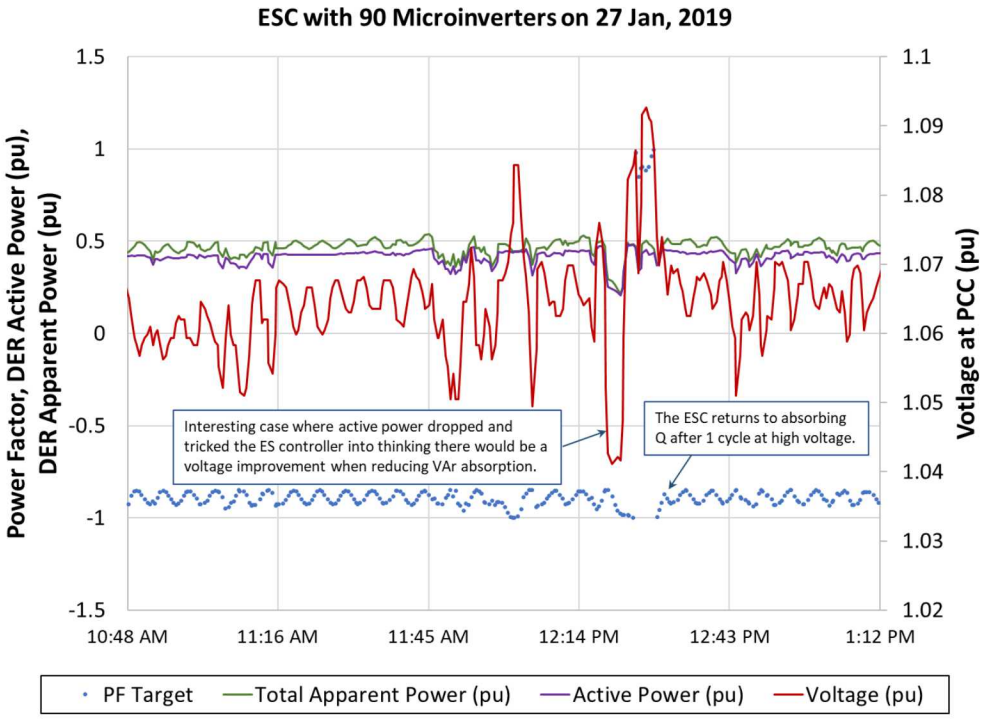

Figure 6-15: ESC results for a partly cloudy day on Jan 27th (detail view).

6.5.2. Field Demonstration

Based on the SunPower experiments and the RT simulations with the NG feeder model, a set of parameters (see set 1 in Table 6-2) were selected to verify the probing frequency, *f,* and amplitude, *a,* were appropriate for the field demonstration. Compared to the microinverter experiments, *J* was changed to be scalable based on the number of devices taking the measurements, and, if the equipment was connected at different voltage levels, the higher nominal voltage measurements would dominate the objective function. The results are shown in Figure 6-16. The probing signal is clearly visible for 8 cycles and the voltage is perturbed sufficiently to extract the objective function gradient—actually it was so large at the *a* parameter was reduced for the subsequent test cases. The objective function only used the PCC voltage to determine the objective function. To track the gradient, different integrator gains, *k*, were applied to track toward the optimal DER reactive power level. The response of the system is shown in Figure 6-17, wherein a second-order oscillation is clearly shown. Multiple attempts to dampen the second order oscillation were pursued (sets 3 and 4 in Table 6-2) where the low pass filter, *l*, objective function, and gain were adjusted, but it was not eliminated. This behavior could be recreated in simulation and is the source of further research. Essentially, by starting the probe so close to the optimum, the ESC algorithm cannot "see" which direction to travel because it is on the solution. This causes it to shift off the solution and backtrack repeatedly. In the case of the microinverter experiments, the ESC never reached the solution, so it did not experience these oscillations.

Table 6-2. ESC parameters for the NG field demonstration.

#	Model	J function	l	h	r_{comm}	Old Upton Rd PV Site (684 kW_{dc}, 672 kVA)			
						P	f	a	k
1	National Grid Field Demo	$\frac{1}{n}\sum_{i=1}^{n}\left(\frac{V_i - V_n}{V_n}\right)^2$	$\frac{1}{3000}$	$\frac{1}{3000}$	30 s	672 kVA	$\frac{1}{300}$	67.2 kVar	0
2	National Grid Field Demo	$\frac{1}{n}\sum_{i=1}^{n}\left(\frac{V_i - V_n}{V_n}\right)^2$	$\frac{1}{3000}$	$\frac{1}{3000}$	30 s	672 kVA	$\frac{1}{300}$	44.8 kVar	$-6.72\text{x}10^7$
3	National Grid Field Demo	$\frac{1}{n}\sum_{i=1}^{n}\left(\frac{V_i - V_n}{V_n}\right)^2$	$\frac{1}{6000}$	$\frac{1}{3000}$	30 s	672 kVA	$\frac{1}{300}$	44.8 kVar	$-7.18\text{x}10^8$
4	National Grid Field Demo	$\frac{1000}{n}\sum_{i=1}^{n}\left(\frac{V_i - V_n}{V_n}\right)^2$	$\frac{1}{3000}$	$\frac{1}{3000}$	30 s	672 kVA	$\frac{1}{300}$	33.6 kVar	$-7.18\text{x}10^8$
5	National Grid Field Demo	$\frac{1}{n}\sum_{i=1}^{n}\left(\frac{V_i - V_n}{V_n}\right)^2$	$\frac{1}{3000}$	$\frac{1}{3000}$	30 s	672 kVA	$\frac{1}{300}$	44.8 kVar	$-6.72\text{x}10^7$

Figure 6-16: Screenshot of the Connected Energy CNRG system with Parameter Set 1 during the process of tuning the probing signal for the ESC.

These probing parameters (*f*, *a*) were then used with a nonzero integrator gain, *k*, (parameter set 2) to track toward the optimal DER reactive power level. The response of the system is shown in Figure 6-17, wherein a second-order oscillation is clearly shown. After running additional simulations of the ESC, a couple of solutions were identified. The low pass filter could be adjusted to collect for this behavior.

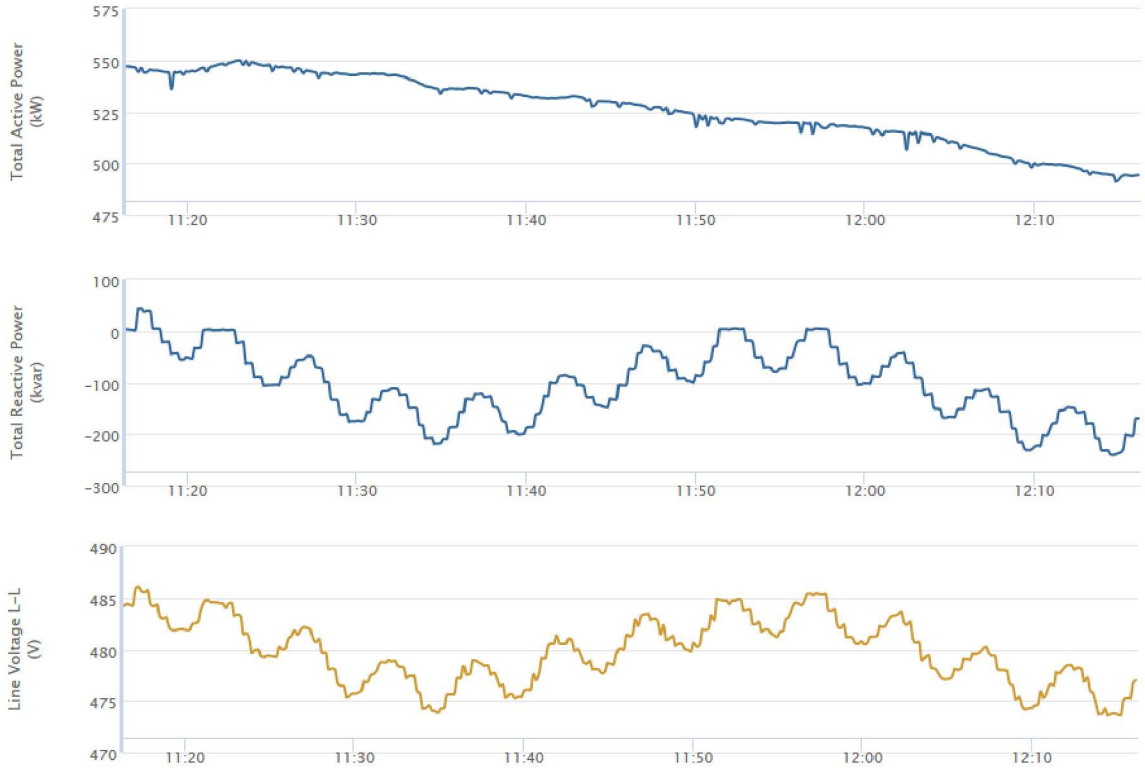

Figure 6-17: Second-order oscillation in the ESC control system with Parameter Set 2 caused by overshooting the optimal PF due to the ESC integrator.

After multiple attempts to remove the second-order oscillation shown in Figure 6-17, the parameters were reverted to parameter set 5 for the final demonstration. This demo produced the results shown in Figure 6-18. The 44.8 kVA probing signal produced ~0.0092 pu voltage changes and the ESC tracked to the optimal PF setpoint, overshot it and oscillated like an underdamped control system. The second-order oscillation initially decayed to produce a ~0.018 pu voltage deviations centered around the nominal voltage. Additional adjustments to the ESC parameters are expected to dampen the second-order oscillation further and produce a tighter voltage band. Ultimately, the ESC field demonstration showed that this approach has challenges when operating the system close to the optimal solution. It performs much better with more complicated objective functions, multiple DER systems, and when the initial conditions are farther from the optimum. The ESC struggles to determine the gradient when it is oscillating on the optimum. This was especially a problem for test cases that were initiated early in the morning when the voltage was extremely close to nominal. The ESC signal moved away from this target, only to track back to where it started (at unity PF).

6.6. PSO Experiments with Digital Twin

To issue optimal PF setpoints to the Old Upton Rd PV system, a particle swarm optimization (PSO) wrapped multiple OpenDSS time series simulations to find the best setpoints over the time horizon. Unfortunately, there were not enough field measurements to make the state estimation observable, so a RT "digital twin" was created that represented the power system and associated telemetry. This digital twin was the RT-Lab simulation coupled with the EPRI PV simulators. Simulated PMU data from RT-Lab was sent to a SEL-3373 PDC and transmitted to the WinIGS platform. The results of the state estimation, e.g., voltage and current phasors at each bus, were sent as a C37.118 stream to the PSO. OpenDSS active and reactive power load values were updated based on the phasor data to

represent current conditions. These values were persisted through the entire time series simulation. The Old Upton Rd PV forecast was used to update the expected production levels for all 31 PV devices in the OpenDSS time-series simulation to match the local irradiance.

The simulated PV systems were configured to provide full output (the irradiance was set to 1000 W/m^2) and the curtailment function was used to adjust the output of all the devices to match the production of the physical site. Spatial variability was not included, because there was no information about cloud fields or speed. A comparison of the Old Upton Rd power and the simulated PV system representing the site is shown in Figure 6-20. When the PSO was solved for the optimal PF for the Old Upton Rd site, this PF settings was issued to the physical site as well as the simulated PV system connected to Opal-RT.

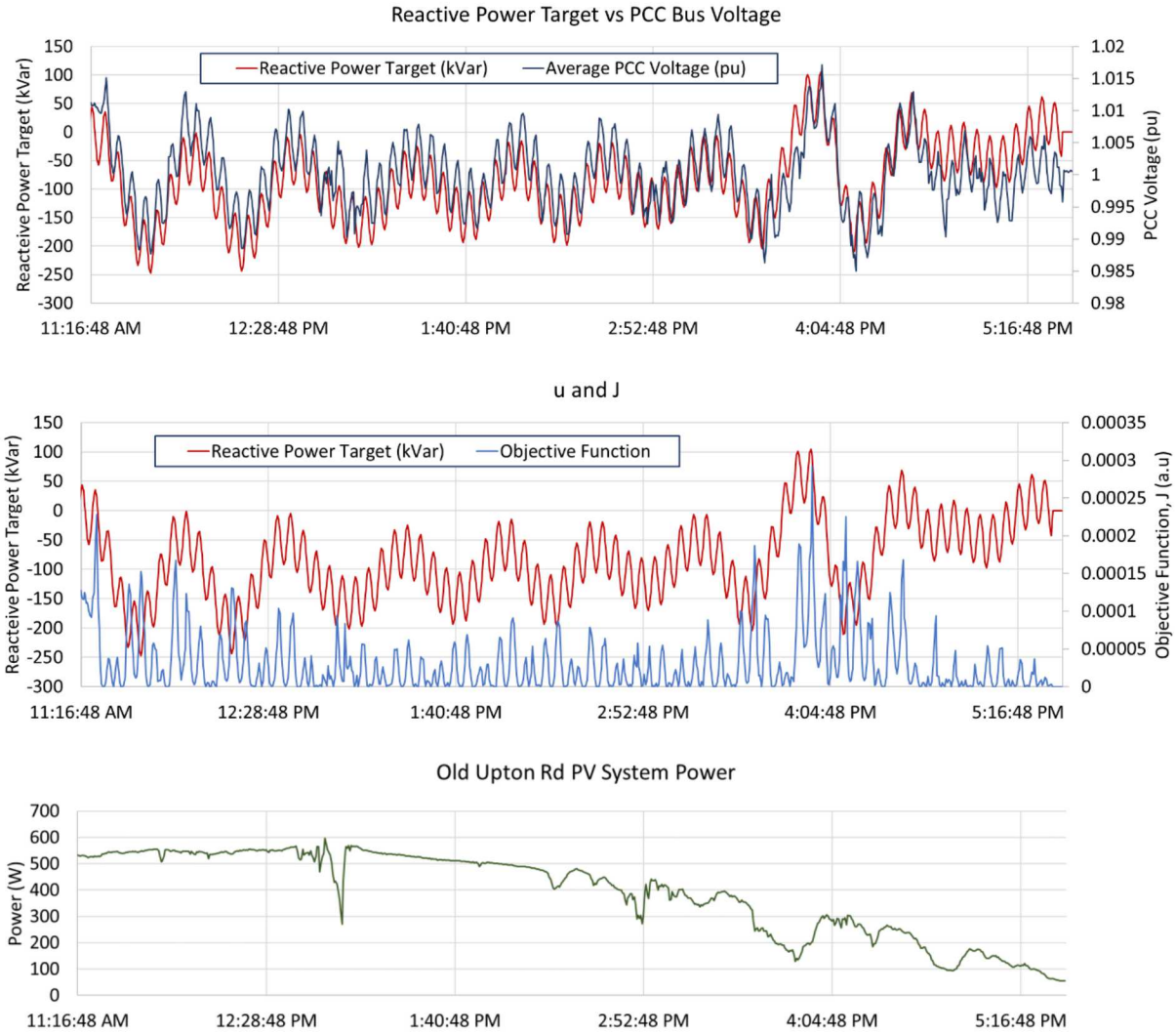

Figure 6-18: ESC results on the fielded system using parameter Set 5.

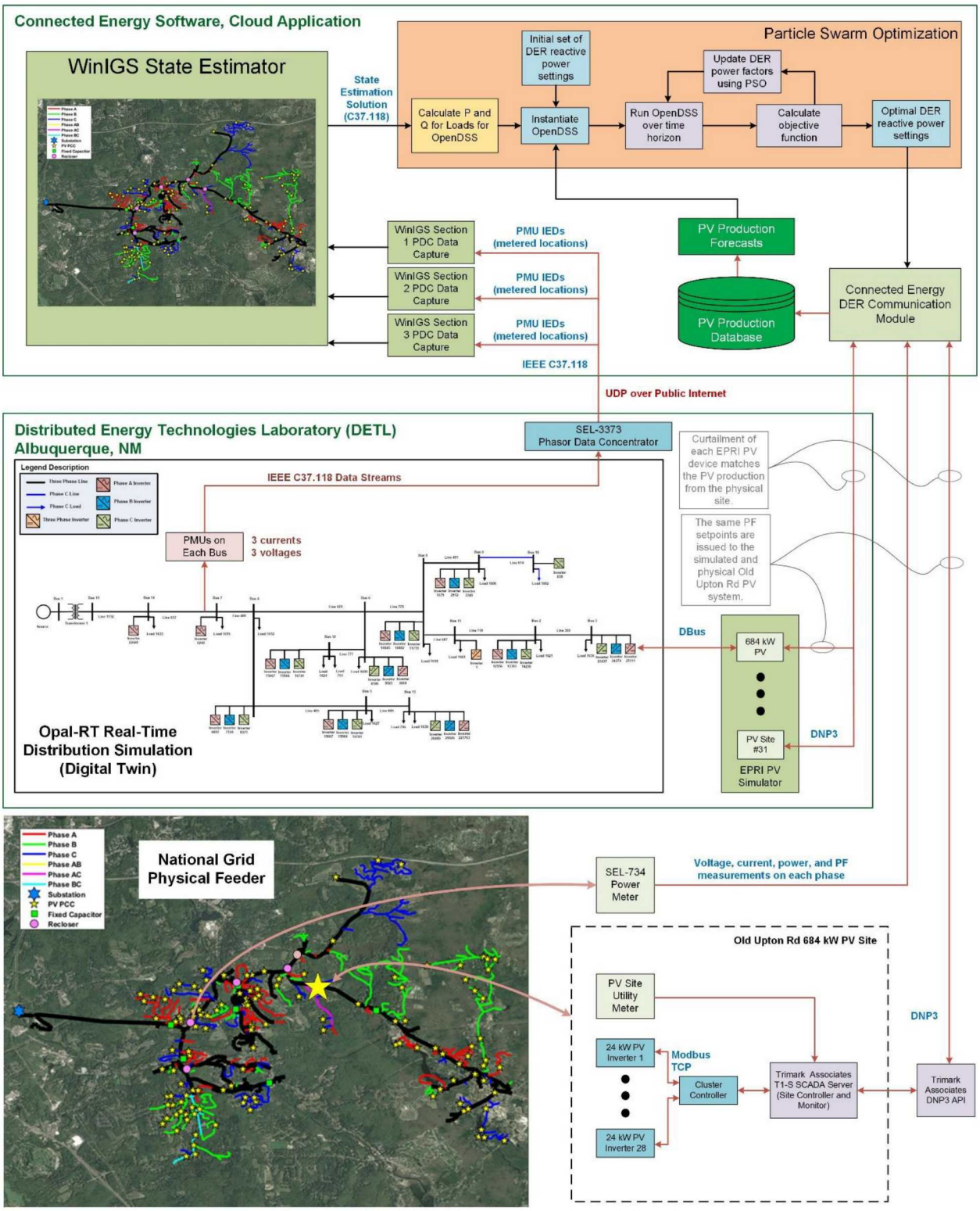

Figure 6-19. Digital twin experimental setup.

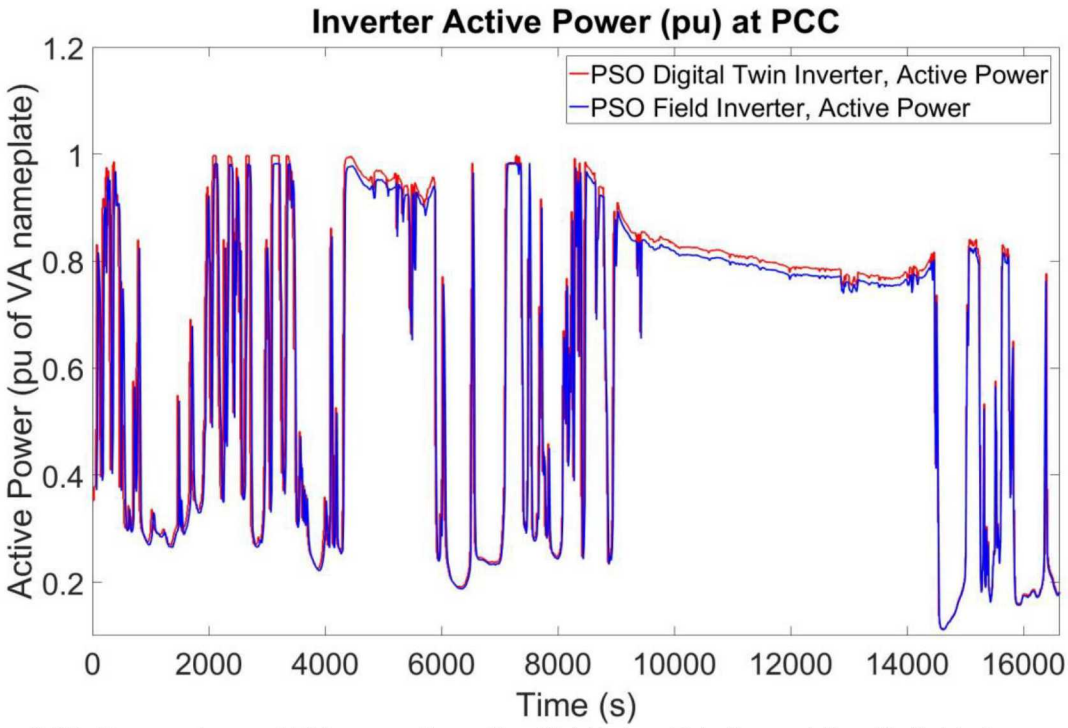

Figure 6-20. Comparison of PV power from the Old Upton Rd site and the digital twin represented by the curtailed EPRI PV simulator.

The reactive power provided by the physical and simulated Old Upton Rd PV systems is shown in Figure 6-21. The optimal PF values were very close to unity, shown in Figure 6-21, and only produced significant reactive power (>50 kVar) during the spike around 3000 seconds. Looking into the internal optimization states during that period, the PSO found a PF solution which improved the objective function but on the next loop that solution was no longer optimal and returned to the lower reactive power level. It is not clear what change in the OpenDSS initial conditions or simulation environment caused this deviation.

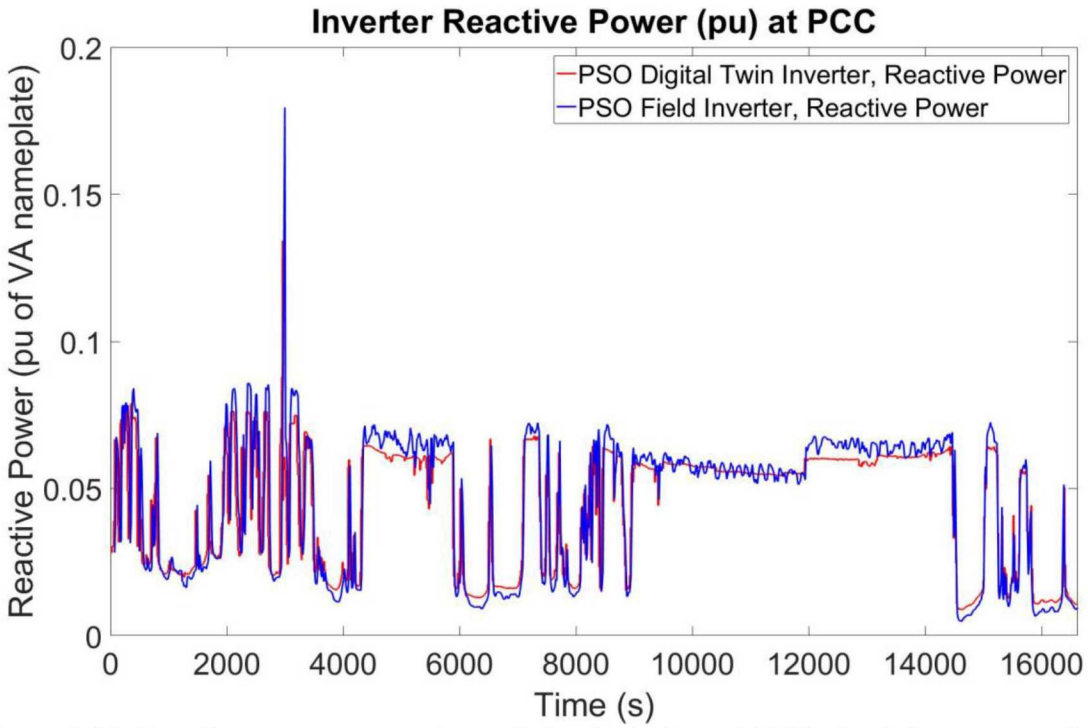

Figure 6-21: Reactive power comparison of physical site and EPRI simulator representing Old Upton Rd.

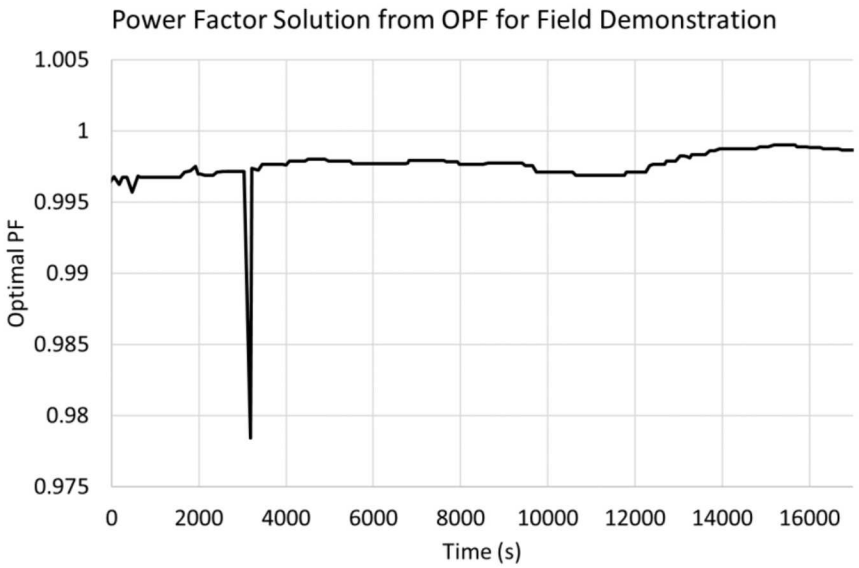

Figure 6-22: PF solutions from the PSO for the field demonstration.

Since the dynamic loads in the RT simulation did not represent the actual loads on the feeder, there were some differences in the feeder voltages and the measurements. The historical load data used in the simulation started at 09:00 (13:00 UTC) but the experiment began at 14:24 UTC, so there were some temporal differences in addition to seasonal and diurnal load profile changes. Additionally, the starting locations for the voltage regulation equipment was unknown, so the simulation was likely to deviate from the actual feeder. By comparing, the PV PCC voltage for the power simulation and the

field, the trends match reasonably well, but the magnitude of the response was different. As shown in Figure 6-23, the digital twin indicated that the average PCC voltage would swing much more significantly. This could be because of differences in the line model parameters (as an artifact of the circuit reduction process), the missing transformer at the Old Upton Rd site in the model, or the influence of other voltage regulation equipment on the feeder. The Simulink model of the substation voltage regulators did not include the line drop compensation programming but did include phase independent LTC operations with a deadband[28]. This could also contribute to some of the voltage differences.

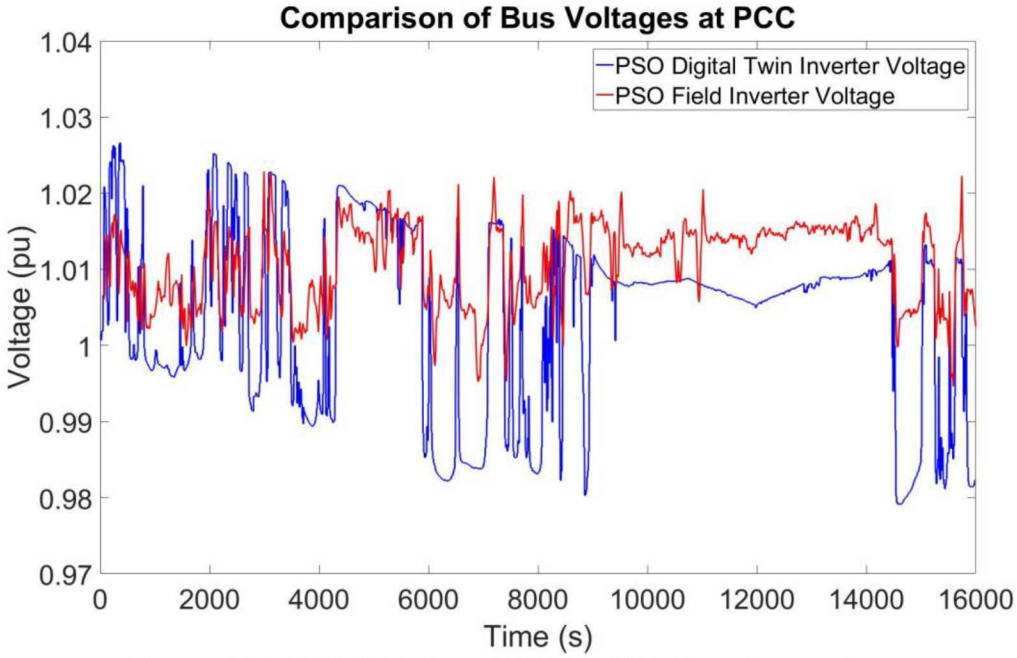

Figure 6-23: PCC RT-Lab and PCC Field Voltage Comparison.

The voltage at the PCC and feeder monitor, the PV production and forecast, and the reactive power contribution for the field demonstration are shown in Figure 6-24. As shown in the figure, the voltage trends from the baseline and other voltage regulation experiments are repeated for this experiment. As the PV power increases, the local voltage increases but the feeder monitor voltage decreases because of the line drop compensation. The PV forecast is seen lagging the irradiance changes but reasonably approximates the energy production. As the PV power changes, the reactive power produced by the site changes significantly. This produced the swings shown in Figure 6-22 and caused some of the voltage variability at the PCC and feeder monitor. Overall, the PSO operated near unity and could do little to help the voltage imbalance of the feeder—just like the other methods. Since Old Upton Rd only included three-phase inverters it was not possible to help the phase imbalance but did attempt to move the feeder voltages toward nominal. Without better field telemetry, it is uncertain if the digital twin PSO approach succeeded in doing so.

[28] W. H. Kersting, "Distribution Feeder Voltage Regulation Control," in *IEEE Transactions on Industry Applications*, vol. 46, no. 2, pp. 620-626, March-April 2010.

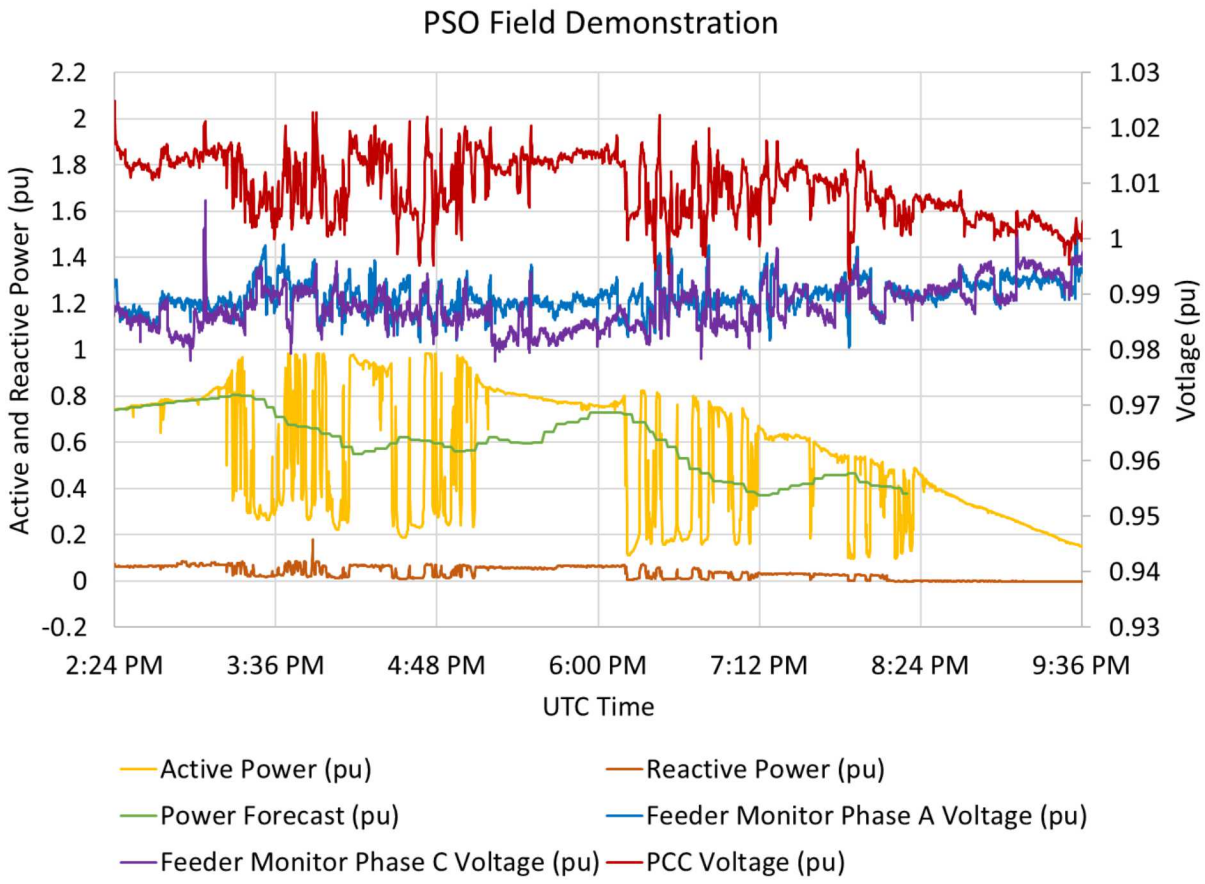

Figure 6-24: Feeder Monitor RT-Lab and PCC Field Voltage Comparison.

Some prior work indicated that, when providing voltage regulation from PV, line drop compensation should be disabled[29]. This would provide smoother temporal voltage operations and help the optimization track the best solution for the feeder. It would also reduce the number of relay or LTC tap operations. Perhaps, in the future, this could be considered for field demonstrations like the one presented in this work.

[29] J. Quiroz and M. Reno, "Detailed grid integration analysis of distributed PV," 2012 38th IEEE Photovoltaic Specialists Conference, Austin, TX, 2012, pp. 596-601.

7. CONCLUSIONS

Utilities and distribution system operators generally do not have the sensor infrastructure or DERMS communication network to execute centralized control of DER. However, as the number of measurement devices and interoperable DER increases, it will become possible to calculate power system states, calculate optimal DER setpoints to provide voltage regulation, and provide protection assurance on the system. These capabilities were demonstrated in this project with simulations and field demonstrations.

A dynamic state estimation solution was demonstrated in which state estimation data is compared to live power measurements. When deviations between measurements and the model appear, relay or other protection operations can be taken at the protection zone where the discrepancy appears within 1-2 cycles. This technology was demonstrated on the PNM model for two different fault cases in the Georgia Tech laboratory with rapid, subcycle mitigation of the fault.

This project investigated three voltage regulation approaches: volt-var, extremum seeking control, and particle swarm optimization. Each of the approaches were shown to help provide voltage support in a feeder with symmetrically elevated phase voltages. In the case of imbalanced feeder voltages, the approaches were ineffective when employed with three-phase inverters, but an aggregate of single phase devices were shown to improve feeder voltage profiles. This was demonstrated using RT simulations with simulated PV devices and power hardware-in-the-loop simulations with a 3 kW PV inverter. The extremum seeking control voltage regulation technique was shown to be effective at controlling groups of DER devices to improve feeder voltages, even in cases of phase imbalance. This is the first extensive demonstration of the technology and it showed promise in the RT and PHIL simulations. The particle swarm optimization approach worked well when the OpenDSS simulation that the PSO was optimizing matched the operating system. The technique incorporated live telemetry and PV forecast data to generate the optimal PF setpoints for a collection of PV systems over a fixed time horizon.

Field demonstrations of each of the approaches using a 684 kW_{dc} PV site were conducted on a live feeder in Grafton, MA. Each of the methods struggled to improve the feeder voltages because the feeder was imbalanced, but the average of the phases was close to nominal. As a result, it was difficult to compare the methods on the live system: VV provided little reactive power compensation; ESC produced a second-order oscillation around the optimal setpoint; and the PSO solution found the PF optimum close to unity. In future work, a feeder with higher or lower local voltages would be more effective at directly comparing voltage regulation approaches. It is also recommended that PV systems be developed that can provide zero and negative sequence currents so that phase imbalance can be corrected using three-phase PV systems.

DISTRIBUTION

Email—External

Name	Company Email Address	Company Name
Guohui Yuan	Guohui.Yuan@EE.Doe.Gov	U.S. Department of Energy
Kemal Celik	Kemal.Celik@EE.DOE.Gov	U.S. Department of Energy

Email—Internal

Name	Org.	Sandia Email Address
Jay Johnson	08812	jjohns2@sandia.gov
Abraham Ellis	08812	aellis@sandia.gov
Charlie Hanley	08810	cjhanle@sandia.gov
Ray Byrne	08813	rhbyrne@sandia.gov
Technical Library	01177	libref@sandia.gov

This page left blank

Sandia National Laboratories

Sandia National Laboratories is a multimission laboratory managed and operated by National Technology & Engineering Solutions of Sandia LLC, a wholly owned subsidiary of Honeywell International Inc. for the U.S. Department of Energy's National Nuclear Security Administration under contract DE-NA0003525.